Microsphere Flow Quantification and Bias Detection with a Porcine Coronary Model

Sinclair, Matthew David Maurice

Awarding institution:
King's College London

Microsphere Flow Quantification and Bias Detection with a Porcine Coronary Model

Doctoral Thesis

Author:
Matthew Sinclair

Supervisors:
Nicolas Smith, Ph.D
Tobias Schaeffter, Ph.D
Jack Lee, DPhil

A thesis submitted in fulfillment of the requirements for the degree of Doctor of Philosophy in the

Division of Imaging Sciences and Biomedical Engineering
School of Medicine
King's College London

September, 2014

Abstract

Cardiovascular disease (CVD) is the single largest cause of death in the world, accounting for nearly 30% of mortalities each year. Coronary artery disease (CAD) constitutes the largest category of CVD, and includes diseases caused by plaque formation in the coronary arteries resulting in a range of pathologies including coronary stenosis, ischemia, hibernating myocardium, infarct and heart failure.

Clinical dynamic contrast enhanced (DCE) MRI is an emerging non-invasive method for assessing the extent and severity of perfusion defects in the heart. Recently algorithms have been used to quantify myocardial blood flow (MBF) from excised porcine Langendorff hearts under normal flow, low flow, and stress conditions, with validation provided by the microsphere deposition technique. Microspheres of 15 micron diameter deposited within the myocardium were imaged with a fluorescent episcopic cryomicrotome after DCE-MRI acquisition, providing high-resolution images of the heart which were spatially co-registered to the MRI images. Previous validation studies involved physically sectioning hearts into segments for comparison to DCE-MRI. The presented method provided direct correspondence and hence higher accuracy of tissue segments used for the comparative calculation of MBF from DCE-MRI and microspheres. Results of the validation study in 8 pig hearts showed strong correlations at both 1.5T ($n = 4$) and 3T ($n = 4$) field strengths, and under all of the experimental flow conditions.

A question which has previously arisen regarding the distribution of microspheres in the coronary arterial circulation has been whether they undergo phase separation. Previous to this study geometric information of the coronary arterial structure has not been available for comparison to the distribution of microspheres to determine if this phenomenon plays a role in the observed bias of microspheres relative to a molecular tracer, IDMI. A Poiseuille flow model with an outlet flow boundary condition dependent on perfused tissue mass has been used to simulate flow distribution in a porcine coronary arterial network. The network reconstructed from cryomicrotome imaging data consisted of approximately 10^5 arterial and arteriolar vessel segments, with a minimum vessel diameter of 0.13mm. A

novel analysis using confidence intervals of a binomial distribution at every vascular bifurcation was used to determine the presence of phase separation in the coronary arteries and large arterioles, and to identify the most prevalent locations of phase separation within the network. It is known that phase separation of red blood cells and microspheres occurs in vessels of a diameter similar to that of the particles, namely the small arterioles and capillaries.

Results revealed that microsphere phase separation was most prevalent at bifurcations in the conduit coronary arteries, where branching asymmetry was highest. Phase separation prevalence was reduced at arteriolar bifurcations, where branching asymmetry was lower. This is the first study relating coronary arterial geometry with microsphere distributions and serves as an explanation for previously observed microsphere distribution bias in tissue regions of high flow. In future this bias may be corrected using a suitable model, but further work needs to be done to ascertain more accurate terminal vessel boundary conditions.

Acknowledgements

It has only been with the continuous support of many great academics, friends and family around me (and far away) that I have been able to complete this thesis. As Radek wisely pointed out near the beginning of this journey, "it is a marathon, not a sprint". Thank you for being a mentor, friend and colleague who has always led by example.

I am extremely grateful for the supervision of Prof. Nic Smith, for your guidance and patience particularly during times when the path was unclear. During the most difficult times, you always reminded me that careful methodical investigation could turn sources of frustration and ambiguity into insight and opportunity. Thank you for equipping me with the tools to approach greater challenges ahead with confidence. To my second supervisor Tobias, thank you for your invaluable insight into various aspects of my project, and for reminding me to keep my work within the context of a bigger picture. To Jack - I have been incredibly fortunate to have you as a supervisor. Your depth of knowledge and expertise across a range of topics and your persistent drive has always provided a source of inspiration. You have helped me tackle problems on so many levels throughout this project, and have always done so by providing a path of self-directed learning and self-improvement which I will always be thankful for.

To other members of the perfusion modeling group Andrew C, Simone, Eoin, Radek, Christian, Taha, Ayush, Lucas, Valentina and Lauren - you have provided a fun, stimulating and nourishing research environment. To my clinical collaborators at KCL Andreas, Amedeo, Nelly and Roman, it has been a pleasure and honour working with you, and to have been continuously reminded by your work, and indeed our work, of what is really important: helping those in need. To Pablo, it has been a great pleasure to work alongside you and to learn so much from your sharp insight, your synergistic team approach, and your contagious cheerfulness in the face of a challenge.

To my friends in KCL and London - you have pulled me out of the incessant waves

of coding, writing and over-thinking many a time and have made my experience here truly memorable. Special mention goes to my flatmates with whom many late nights were spent discussing both the trivial and important issues in life, ranging from the exact pronunciation of "pear" to the origins of the universe - Andrew, Bojan, Thomas and Dev you have been the best mates I could have hoped to share a flat with in London.

To all my friends in and out of the hospital - I owe you so much of my livelihood and happiness. Thanks for all the good times over lunch, on the squash court, basketball court and after work: Eoin, Simone, Myria, Fabrizio, Sara, Anastasia, Angela, Eric, Andrew C, Dave, Oleg, Christian, Andy, Devis, Ghislain, Christoph, Radek, Lucas, Sally, Pete, Gustau, Enrico, Elisabetta, Chris, Mike, Istvan, Catalina, Dan, Kev, Yolanda, Markus, Marcus, Kirsten, Alexis, Mazen, Ross, Marta, Valentina, Arian, Rui, Giulio, Julia, Des, Nika, Tanya, Federica, Alberto, big Nick; everyone in Cake Club (it has been a treat), the KCL basketball team, IAESTE, SSA, my climbing buddies; and a special mention goes to Carla who has kept me sane and smiling during the last year of my PhD.

To my NZ friends who ventured across to the UK - Bojan, Andrew W, Ally, Sunny and Soo, Penelope, T, Emma, DC, Terry, Karl, Reagan, Sulak, Holman, Tom, Andrew F - London wouldn't have been the same without you. Thanks for making it a home away from home with me. Friends around the world, I am so grateful for your support from afar, and thankful to be living in an era when we can communicate so easily and to continue traveling this journey together.

My deepest gratitude is reserved for my parents who have always been there for me with their unconditional love and support through the highs and lows. I could not have arrived here without you. From the dried fruits and nuts which have kept me going at my desk, to providing a nurturing home environment on many weekends away from London, and for everything else in between - I cannot thank you enough and love you both very much.

To the rest of my immediate family; Alex, thank you for your generous spirit and great company in London (and for all the invaluable cooking tips which I intend to put to good use once I submit). Chris and Olivia, thank you for your support from the other side of the world, and for your warm hospitality whenever I have been back in NZ. Claudia and Daniel, thank you for bringing so much joy into my life and reminding me how to stay young at heart - it has been incredible to see you both grow so much in the last four years. I'll always be there, and do my best, for all of you.

Contents

List of Figures

List of Tables

Symbols and Abbreviations

Chapter 1:	**Introduction**
CVD	Cardiovascular Disease
CAD	Coronary Artery Disease
CMD	Coronary Microvascular Disease
CT	Computed Tomography
SPECT	Single Photo Emission Computed Tomography
PET	Positron Emission Tomography
MRI	Magnetic Resonance Imaging
DCE-MRI	Dynamic Contrast Enhanced MRI
MBF	Myocardial Blood Flow
MPR	Myocardial Perfusion Reserve
AIF	Arterial Input Function
CMT	Cryomicrotome
FMS	Fluorescent Microspheres
BC	Boundary Condition
LCA	Left Coronary Artery
RCA	Right Coronary Artery
LAD	Left Anterior Descending
LCx	Left Circumflex
LM	Left Marginal
LV	Left Ventricle
RV	Right Ventricle
U	Strahler Order
D_U	Diameter of vessel in order U

μ_U	Mean diameter of vessels in order U
σ_U	Standard deviation of vessel diameters in order U
U_{vol}	Volume Order
V	Tissue fed volume
V_0	Theoretical terminal arteriole tissue fed volume
δ	Fed volume branching asymmetry

Chapter 2: Perfusion Quantification

BiV	Bi-Ventricular (segmentation)
PCA	Principal Component Analysis
PC	Principal Component
BP	Blood Pool (ventricular cavity)
Seg-PCA	Initial alignment based on PCA of LV segmentation
BP-PCA	Initial alignment based on PCA LV BP
DSC	Dice Similarity Coefficient

ξ_i	Local coordinate direction i
v_i	Coordinate direction i from *Seg-PCA* or *BP-PCA*
$\overline{r}_u$	Mean radius of BP in +ve PC1 direction
$\overline{r}_l$	Mean radius of BP in -ve PC1 direction
s_i	Components of scaling matrix S
P_{ap}	Coordinates of epicardial apex landmark
P_v	Coordinates of aortic (or mitral) valve landmark
P_{la}	Coordinates of basal LAD landmark
$\hat{v}_x, \hat{v}_y, \hat{v}_z$	Normalised coordinate vectors
R_{tar}	'Target' rotation matrix defined from MRI landmarks
R_{ref}	'Reference' rotation matrix defined from CMT landmarks
t_{tar}	'Target' translation defined from MRI landmarks
t_{ref}	Reference' translation defined from CMT landmarks
$\bar{x}_{cmt}$	CMT coordinates
$\bar{x}^a_{mri}$	Initial registered coordinates from CMT to MRI data
R_{man}	Manual rotation (in CMGUI)
t_{man}	Manual translation (in CMGUI)

$\bar{x}^b_{mri}$	Final registered coordinates from CMT to MRI data
N_i	Number of microspheres in tissue segment
M_i	Mass of tissue segment
Q_t	Total coronary network flow (ml/min)
Q_c	Controlled pump flow (ml/min)

Chapter 3: Vascular Reconstruction

MIP	Maximum Intensity Projection
$\mathcal{H}$	Hessian matrix
L	Image being filtered
$\mathbf{x}_0$	Centre of Hessian kernel
s	Scale of Hessian
$\hat{\mathbf{u}}_{s,k}$	Normalised Hessian eigenvector k at scale s
$\lambda_{s,k}$	Hessian eigenvalue k at scale s
$\mathcal{R}_\mathcal{A}$	First vesselness geometric ratio
$\mathcal{R}_\mathcal{B}$	Second vesselness geometric ratio
$\mathcal{S}$	"Second-order Structureness" term
$\mathcal{V}_0(s)$	Vesselness function
R_w	Poiseuille resistance-based graph edge weight
A	Area expansion ratio
S	Symmetry ratio
D_P	Parent vessel diameter
D_S	Smaller daughter vessel diameter
D_L	Larger daughter vessel diameters

Chapter 4: Coronary Flow Model

RD	Relative Dispersion
D	Fractal dimension
Q_m	Model flow (ml/min)
Q_f	FMS-derived flow (ml/min)
D_i^{NN}	Nearest-neighbour distance (terminal vessel i)
X_i	Distance of tissue voxel to terminal vessel i

r_i	Radius of terminal vessel i
ΔP	Pressure drop across vessel segment
R	Vessel segment resistance
Q	Flow through vessel
η	Blood viscosity
L	Vessel segment length
r	Vessel segment (mean) radius
$\eta_{0.45}$	Relative viscosity
H_D	Discharge haematocrit
C	Vessel segment conductance
q	log-log gradient for C versus U_{vol}
V_1	Smaller daughter fed volume
V_2	Larger daughter fed volume
V_{min}	Reference fed volume of terminal arteriole
V_t	Total segmentation tissue volume
N	Number of volume-order generations
R_S	Subtree resistance (geometric series)
Q_k	Outlet flow to terminal k
V_k	Tissue volume assigned to terminal k
d_i	Relative FMS deposition density
f_i	Relative regional perfusion (from model)
E_i	Absolute error (Q_f vs Q_m) in segment i
N_f^i	Number of FMS passing through segment i
U_2	Second volume order (using log10)
w_j	U_2 bin j
$\tilde{U}_2$	w_j bin midpoint value
n_j	Number of vessel segments in bin w_j
E_j^{rms}	RMS error in bin w_j
z	z-ratio (binomial distribution)
f	fraction of coronary flow
X_{95}	Number of FMS at binomial 95% upper CI limit
E_t	Theoretical binomial error
r	Correlation coefficient

m_0	Reference segment mass
$\bar{X}_i$	Mean FMS count for tissue aggregate level i
Q'_k	Perturbed terminal k outlet flow
$\tilde{\boldsymbol{Q}}$	Median original terminal flow
$\hat{Q}'_k$	Corrected, perturbed terminal k outlet flow

Chapter 5: Phase Separation Analysis

RBC	Red Blood Cell
HCT	Haematocrit
PMF	Probability Mass Function
CDF	Cumulative Distribution Function
PPD	Percentile Proportion Distribution
CI	Confidence Interval
CL	Confidence Level
Q^*	Bulk flow fraction
F^*	Particle distribution fraction (RBCs or microspheres)
N_{min}	Minimum no. of FMS
V_m^*	Fluid volume fraction of FMS
Q_c^*	Critical bulk flow fraction
H_D	Discharge haematocrit
b	Logistic function non-linearity constant
X	Random variable from binomial distribution
N	Number of FMS in parent vessel
p	Probability of FMS entering vessel (Q^*)
k	Number of FMS in daughter vessel
α	(1-α) gives confidence interval range
w_i	Percentile bin proportion of total bifurcations
F_i	Central percentile value of bin
M_i	Number of vessel segments in bin
β	Width (or range) of percentile bin
p_{LB}	Lower bound probability of CI
p_{UB}	Upper bound probability of CI

H_0	Null hypothesis
H_1^a	Skimming alternative hypothesis
H_1^b	Opposite alternative hypothesis
θ^*	Branching angle asymmetry
r_a^*	Fractional daughter radius ratio
r_b^*	Daughter-to-parent radius ratio
L_p	Parent vessel length
$S1$	H_1^a outliers where (Q^*<0.5, F^*<Q^*)
$S2$	H_1^a outliers where (Q^*>0.5, F^*>Q^*)
$S3$	H_1^b outliers where (Q^*<0.5, F^*>Q^*)
$S4$	H_1^b outliers where (Q^*>0.5, F^*<Q^*)
$S5$	All non-outlier vessels.

1 | Introduction

This chapter provides the motivation for the work carried out in this thesis, followed by a brief background and an outline of the thesis structure. The following four chapters of the thesis (Chapters 2-5) each contain an Introduction section providing more in-depth background relevant to each chapter's contents.

1.1 Motivation

Cardiovascular disease (CVD) is the single largest cause of death in the world accounting for nearly 30% of mortalities globally each year (Lopez *et al.* , 2006). Ischaemic heart disease constitutes the largest sub-category within CVD accounting for 12.8% of global deaths (Finegold *et al.* , 2013), and covers a range of conditions including coronary artery disease (CAD) and coronary microvascular disease (CMD). The most common manifestation of CAD is a narrowing of the coronary arteries (stenosis) due to the build up of atheromatous plaque, which can cause ischemia in the downstream myocardial tissue. CMD on the other hand is primarily the result of microvascular dysfunction, where resistance vessels in the coronary microcirculation fail to respond appropriately to changes in metabolic demand, also leading to ischemia (Camici & Crea, 2007).

Several techniques are commonly used in a clinical setting to detect and diagnose CAD and CMD, both invasively and non-invasively. Coronary X-ray angiography, one of the earliest introduced techniques, is still used routinely in the clinic (Proudfit *et al.* , 1966), and involves administration of a radio-opaque contrast

agent into the coronary circulation via invasive catheterisation during acquisition of X-ray (or CT) images. These images allow for the location of coronary arterial stenosis and severity of local narrowing to be assessed. Furthermore, catheters can also be used to provide pressure and flow measurements within the coronary arteries allowing for additional functional indices of stenosis severity to be computed (see Levine *et al.* , 2011, for comprehensive uses of coronary catheterisation).

A range of non-invasive imaging modalities have also come into clinical use in recent decades for the assessment of regional cardiac perfusion. These include single photon emission computed tomography (SPECT), positron emission tomography (PET), and magnetic resonance imaging (MRI) (Salerno & Beller, 2009). The passage through the myocardium of radiolabelled tracers in PET and SPECT or a gadolinium-based contrast agent in MRI is used to produce images of myocardial perfusion. Amongst these modalities dynamic contrast enhanced (DCE)-MRI produces images with the highest in-plane resolution, typically $1.2 \times 1.2\,\text{mm}^2$ in a 3 Tesla scanner (Lockie *et al.* , 2011) compared to between 2-3 mm and 6-8 mm for PET and SPECT images respectively (Salerno & Beller, 2009). The added diagnostic value of the higher-resolution MR images in the clinic lies in the information provided about the transmural extent of ischemia in the myocardium (e.g. delineating between a subendocardial versus subepicardial perfusion defect) which cannot be determined from PET or SPECT. Qualitative and semi-quantitative assessment of perfusion images from SPECT, PET and MRI have been used widely to guide the selection of patients for invasive coronary angiography and revascularisation therapy, saving time and cost while reducing risk (Salerno & Beller, 2009).

More recently the computation of quantitative perfusion, or myocardial blood flow (MBF), has been achieved with algorithms applied to the time-intensity curves of pixels within the PET and MRI images with a reference arterial input function. This quantitative approach provides an objective assessment of myocardial perfusion and myocardial perfusion reserve (MPR*), allowing regional severity of ischemia to be assessed in the heart more accurately. It also allows for disease progression to be objectively monitored in both cases of CAD and CMD, the latter

*MPR is defined as the ratio of perfusion under maximal vasodilation compared to at rest.

of which is difficult to assess by catheterisation alone (Camici & Crea, 2007).

Quantitative perfusion metrics were first derived from dynamic PET images by fitting a 2-compartment tracer kinetic model to the pixel time-intensity curves, while measuring an arterial input function (AIF) used as a reference from the blood pool (Kuhle *et al.* , 1992). Several years later a method for quantifying myocardial perfusion from DCE-MRI was proposed in (Jerosch-Herold *et al.* , 1998), where a Fermi-function model was used to fit to the time-signal curves in the myocardium. Several different models have since been proposed for perfusion quantification which are reviewed and compared in (Zarinabad *et al.* , 2013).

Validation of perfusion quantification from both PET and MRI was performed by comparison to microspheres, which are a gold-standard for intra-organ perfusion measurements. A type of deposition marker, microspheres have been widely used for organ and intra-organ perfusion measurements, for which clear experimental protocols have been established (Heymann *et al.* , 1977). Most studies historically have employed radioactive microspheres to measure perfusion, whereby organs were divided into tissue segments and flow to each segment was computed as a function of the measured radioactivity (see for example Rudolph & Heymann, 1967; Domenech *et al.* , 1969; Buckberg *et al.* , 1971; Dole *et al.* , 1982; Nose *et al.* , 1985; Chilian *et al.* , 1989; Christian *et al.* , 2004; Nekolla *et al.* , 2009). Motivated by a desire to avoid radioactivity, and provide longer lasting labels, and higher spatial resolutions, fluorescent (Hale *et al.* , 1986; Glenny *et al.* , 1993) and coloured microspheres (Kowallik *et al.* , 1991) have since been developed.

Previously validation methods were limited by requiring the dissection of an organ into tissue segments from which flow could be quantified from microspheres based on their radioactivity, fluorescence or simply count. Recent advances in high-resolution imaging have allowed for the 3D locations of microspheres to be accurately determined within an organ, allowing for more accurate anatomical correspondence of heart segments in perfusion images, and the flexibility to divide hearts in an unlimited number of ways. Specifically epifluorescent cryomicrotome (CMT) imaging has been used to image fluorescent microspheres (FMS), from

which the 3D locations within the heart can be determined (Kelly *et al.* , 2000). Similarly gold-coated X-ray opaque microspheres have been imaged with micro-computed tomography (micro-CT)(Marxen *et al.* , 2006), and iron oxide microspheres have been imaged with high-field MRI (Decking *et al.* , 2004). The 3D spatial coordinates of microspheres within the heart acquired using CMT imaging has allowed, for the first time, the direct comparison of measured perfusion (from microspheres) and perfusion quantified with algorithms from DCE-MRI in precisely corresponding myocardial tissue segments (Zarinabad *et al.* , 2013; Schuster *et al.* , 2014). The data acquired using this approach for this study is presented in greater detail in Section 2.2, and the methodology developed for quantifying perfusion from microspheres acquired with CMT imaging is presented in Chapter 2.

The visualisation of whole-heart coronary arterial networks is also possible with CMT imaging (Spaan *et al.* , 2005; van Horssen *et al.* , 2010) and micro-CT imaging (Beighley *et al.* , 1997; Lee *et al.* , 2007) (for large and small animal hearts respectively), following the injection of a vascular cast into the coronary arteries. The detailed 3D coronary geometry can be digitally reconstructed with appropriate algorithms to produce a computational network for analysis (Marxen *et al.* , 2006; Lee *et al.* , 2007; van den Wijngaard *et al.* , 2013; Goyal *et al.* , 2013). Thus with simultaneous reconstruction of vascular geometry and microsphere locations, the distribution of microspheres can be compared directly to features derived from the vascular network through which they have distributed.

This allows several unaddressed issues to be investigated. Firstly, the transit of microspheres through the coronary circulation is in theory proportional to blood flow and is subject to random variation, where deposition in a given tissue region has been approximated by a Poisson distribution (Buckberg *et al.* , 1971). However, studies have revealed a systematic overestimation of flow computed from microspheres in tissue regions of higher perfusion, and with preferential flow to the subendocardium over the subepicardium despite no significant difference in true underlying perfusion based on IDMI deposition patterns (Bassingthwaighte *et al.* , 1987, 1990). Furthermore a distinctly non-random deposition pattern was observed

from multiple samples of microspheres sequentially injected into the same organ, where clusters of microspheres had deposited in the same voxels, in clear contrast to areas of the tissue devoid of microspheres (Decking *et al.* , 2004). These effects have been hypothesised to be due to 'skimming'[†] of microspheres - a tendency for microspheres (as well as other particles) to preferentially enter a daughter vessel receiving a higher flow fraction at a bifurcation. Skimming becomes increasingly pronounced when flow distribution to daughter vessels at a bifurcation becomes more asymmetric[‡], when the diameter of the particles approaches the diameter of the vessel, and at lower particle concentrations (Chien *et al.* , 1985). Numerous *in vivo*, *in vitro* and *in silico* studies have been carried out to investigate influences of skimming, and a review can be found in Appendix A: Determinants and Models of Skimming.

No study to-date has examined how microspheres distribute through the highest generations of the coronary arterial circulation (namely through the epicardial and transmural conduit arteries), despite these vessels being probable sites of skimming leading to the previously mentioned deposition bias to regions of high flow (Bassingthwaighte *et al.* , 1987, 1990). Decking's observations of sequentially injected microspheres clustering in the same voxels is more likely the result of skimming in the arterioles of a similar diameter to the microspheres, at which scale the occurence of microsphere skimming has previously been confirmed (Ofjord & Clausen, 1983; Decking *et al.* , 2004). The simultaneous imaging of microspheres and coronary arterial network geometry provided by CMT (and micro-CT) imaging allows for an investigation into the prevalence of microsphere skimming in the higher generations of the coronary arteries, which could test Bassingthwaighte's hypothesis.

In order to ascertain the degree to which microsphere distribution deviates from blood flow distribution at bifurcations in the coronary arterial network, blood flow throughout the network can be simulated *in silico* to provide a comparison to

[†]The term skimming is used interchangeably with phase separation in literature and throughout this thesis.

[‡]Flow asymmetry is where one daughter vessel receives a greater fraction of flow from the parent vessel than the other daughter vessel.

microsphere deposition data. The Poiseuille model provides a simple relation between pressure drop and flow as a function of resistance in each vessel segment and is commonly used to simulate network flow by imposing conservation of mass at each junction (Beard & Bassingthwaighte, 2000; Marxen, 2004; Mittal *et al.* , 2005; Kassab, 2006; Huo *et al.* , 2009; Cookson *et al.* , 2012; Michler *et al.* , 2012; Hyde *et al.* , 2013a,b). Pressure and flow can be solved for intermediate vessel segments throughout a network provided that a pressure and flow are prescribed as boundary conditions (BCs) at the inlet of the network, and either pressure or flow is prescribed at all the network outlets.

While inlet pressure and flow can be measured (or even controlled) in the largest coronary arteries, it is impossible to measure all of the outlet pressures or flows of a truncated coronary arterial network. A common modeling assumption used to circumvent this issue is that pressure is relatively constant at the level of the capillaries. The arterial circulation downstream of each terminal vessel in a truncated network can be stochastically generated to the level of the capillaries based on morphometric data (Kassab *et al.* , 1993) in order to utilise this assumption at the terminal vessels of the network (Beard & Bassingthwaighte, 2000; Mittal *et al.* , 2005; Kassab, 2006; Huo *et al.* , 2009). Alternatively, *in vivo* pressure and vessel diameter measurements were acquired from beating cat hearts (Chilian *et al.* , 1989), providing measurements in coronary vessels less than $400\mu m$ in diameter. This data has been used to define outlet pressures in a truncated porcine vascular network (Hyde *et al.* , 2013a). A third way of addressing network outlet BCs was proposed by Marxen (2004), where downstream vascular resistance (to the capillary level) was estimated at each terminal vessel of a network based on an extrapolation of a power law between vessel resistance and terminal fed volume[§] from the vessels in the network. The downstream resistance was added to each terminal vessel and a constant capillary pressure was then applied at each outlet.

The accuracy with which these different outlet BCs are able to reproduce regional

[§]Terminal fed volume refers to the volume of tissue supplied by a terminal vessel in a truncated network, which is constrained by vessel radius, distance from neighbouring vessels, and a segmentation of the tissue supplied by the network. This is explained in detail in Chapter 4.

flows at different vessel scales in the network has not previously been assessed. Arguably, the boundary condition proposed by Marxen is the most physiologically realistic given that it utilises a scaling law based on assigned fed volumes and vessel resistances measured directly from the organ network under consideration - it is specimen-specific. By contrast, data used to parameterise the coronary model in (Hyde *et al.* , 2013a) was collected from another species/specimen, and in (Mittal *et al.* , 2005; Huo *et al.* , 2009) vessels downstream of a truncated coronary arterial network were 'pasted' from a limited database of measured bifurcation geometries. The only previous comparison of an arterial network flow model to microspheres was made by Marxen with his proposed volume-scaled resistance BC in a rat kidney network reconstructed from micro-CT images (Marxen *et al.* , 2006). Despite its use of a specimen-specific power law of resistance, comparing simulated flow to microspheres in the rat kidney arterial network produced no correlation of perfusion (ml/min/g) measured from the microspheres versus the model (Marxen *et al.* , 2006).

For the purposes of comparing model flow to microsphere distributions to determine the prevalence of skimming in the coronary arteries, it is important to also have confidence in the model's accuracy at the sites of interest. In the present study, accuracy of model flow (ml/min) rather than perfusion (ml/min/g) in each vessel segment is of importance for comparison to microsphere-derived flow. While it may not be feasible to accurately reproduce regional tissue perfusion values with current methods, this is likely to be unimportant for a comparison of model and microsphere flow in the larger coronary arteries. The reasoning for this is that tissue perfusion heterogeneity is known to reduce as a function of tissue sample volume, i.e. heterogeneity of perfusion computed from larger divisions of tissue is lower than that computed from smaller divisions of tissue (Bassingthwaighte *et al.* , 1989). This implies that higher generation arterial vessel segments (which supply larger tissue fed volumes) supply tissue regions which tend towards the mean perfusion of the myocardium*. With this in mind, another possible out-

*As a caveat, it must be taken into account that the left ventricular free wall has a higher perfusion than the right ventricle (Bassingthwaighte *et al.* , 1990) and septum (Muehling *et al.* , 2004)

let BC is one where flow is set proportional to terminal vessel tissue fed volume, i.e. a homogeneous perfusion BC, which while unphysiological at the micro-scale provides a control which produces increasingly accurate vessel flow values in the higher generations (larger vessels) of the coronary network.

1.2 Background

1.2.1 Coronary Anatomy and Function

In this thesis we are primarily concerned with the conduit and large resistance arteries in the pig heart, which is similar in structure and size to the human heart (Weaver *et al.* , 1986). Therefore this brief summary is provided to highlight relevant functional and structural components of the coronary arterial circulation. The coronary circulation is composed of a predominantly bifurcating arterial network feeding into a capillary bed (where oxygen is taken up by tissue) which is subsequently drained by a venous network. The arterial network originates at the coronary ostia located in the aortic wall just distal of the aortic valve, stemming into the left and right coronary arteries (LCA and RCA, respectively) which have a typical diameter in an adult pig of 4-5 millimetres (Ballesteros & Ramirez, 2008; Dombe *et al.* , 2012). The LCA and RCA predominantly supply networks feeding the left and right sides of the heart, respectively, although each network additionally supplies a smaller part of the opposing side.

The arterial circulation is composed of several structurally and functionally different vessel generations. Starting at the root of the coronary ostia, the LCA and RCA branch into several large epicardial vessels which extend longitudinally down the sides of and around the ventricles. Along their path transmurally oriented vessels branch off and penetrate the myocardium feeding vessel crowns, or subnetworks, that supply the myocardium (van Horssen *et al.* , 2014). The epicardial and transmural penetrating vessels are known as conduit vessels, generally considered as having a vessel diameter $> 300\mu m$, with the main purpose of transporting blood to feeding sites around the heart.

The conduit arteries feed into smaller arteries approximately 100-300μm in diameter and arterioles $< 100\mu m$ in diameter, both of which are under vasomotor control and are the sites of resistance changes. The greatest pressure drop observed in the coronary arterial network occurs in these vesels, where the small arteries respond primarily to changes in flow and intravascular pressure, and the arterioles respond primarily to metabolic changes (Camici & Crea, 2007). Autoregulation acts in response to two primary drivers: arterial pressure and myocardial oxygen demand. Resistance is adjusted to match blood flow to oxygen demand, which during exercise can increase approximately 5 to 6 times requiring a reduction in vascular resistance, brought about by vasodilation of the small arteries and arterioles and an increased arterial pressure (Duncker & Bache, 2008). Under exercise conditions additional capillaries are also recruited and myocardial oxygen extraction increases. Under constant myocardial oxygen demand however, it has been shown that coronary resistance changes to keep flow relatively constant even across a range of arterial pressures (Mosher *et al.* , 1964).

Pharmacologic vasodilation causes the coronary arteries to vasodilate beyond their physiological capacity under exercise, increasing myocardial blood flow during maximal exercise in swine by 15-26% despite arterial pressure being reduced significantly (Duncker & Bache, 2008). Standard pharmacological agents used in clinical stress tests include adenosine, dipyridamole and regadenoson which are all vasodilators, while another agent dobutamine is both a chronotrope and an inotrope which has similar effects to exercise. Stress testing is used to identify a decreased functional capacity in patients with suspected CAD or CMD. For example in a patient with a mild arterial stenosis, despite pharmacologically induced vasodilation the network downstream of the stenosis will receive limited flow, which can be detected with invasive coronary angiography pressure measurements and more recently non-invasive imaging such as perfusion MRI and PET (Morton *et al.* , 2012).

1.2.2 Network Ordering Schemes

Several vessel ordering methodologies have been proposed to define the relationship between vascular network geometric parameters and the different spatial vessel scales, or vessel generation. The prominent ordering schemes in the literature are the Strahler ordering scheme (Strahler, 1952), the diameter-defined Strahler ordering scheme (Kassab *et al.* , 1993), and more recently the volume-ordering scheme (Marxen & Henkelman, 2003, 2009). The Strahler ordering scheme was created to classify riverbed segments in terms of the area of land which they drained. The first capillaries fed by the terminal arterioles are assigned Strahler order $U = 0^*$. Moving up the arterial network, each parent vessel order is the maximum order of the daughter vessels, or if each daughter order is the same, U, the parent is assigned $U + 1$. This method works well when ordering the arterial network from the capillaries upwards, where terminal arterioles share common geometric scales. However for a truncated arterial network whose terminal vessel segments may vary greatly in diameter and length for example, the approach of assigning $U = 0$ to terminal segments results in less meaningful orders.

For this reason, Kassab introduced the diameter-defined Strahler ordering scheme with the aim of producing orders which contained vessels of non-overlapping ranges of diameters (Kassab *et al.* , 1993). To achieve this a network is first Strahler ordered. For each order U the mean and standard deviation of the diameters D_U are computed, μ_U and σ_U, respectively. Then each vessel segment with diameter D_i is reclassified into the order satisfying the following condition

$$\frac{(\mu_{U-1} + \sigma_{U-1}) + (\mu_U - \sigma_U)}{2} < D_i < \frac{(\mu_U + \sigma_U) + (\mu_{U+1} - \sigma_{U+1})}{2}. \tag{1.1}$$

After assignment of new vessel orders, μ_U and σ_U are recomputed. This process is iterated until the diameter ranges of successive orders no longer overlap.

Later, Marxen introduced an ordering scheme that provided independence of vessel order from diameter (Marxen & Henkelman, 2009). Specifically, they intro-

*Order will be referred to with U as in (Marxen *et al.* , 2006) instead of the more commonly used n to avoid confusion with another usage of n throughout this chapter.

duced the physiologically-based volume ordering approach, where order U_{vol} is determined by the volume of tissue which is perfused by a given vessel segment's downstream network, as in this study. The determination of the tissue volume perfused by vessel segments in the renal arteries was made possible by the availability of micro-CT images, from which the renal arterial network and the surrounding tissue were segmented. This is presented in greater detail in Chapter 4. Volume order is given by

$$U_{vol} = log_2 \left(\frac{V}{V_0} \right) + 1, \tag{1.2}$$

where V is the tissue volume supplied by a vessel, and the normalising factor V_0 approximates the tissue volume supplied by a terminal arteriole (i.e. an arteriole which supplies the capillary bed). This value is assumed to be constant throughout the tissue but is species- and organ-dependent and is estimated from literature based on recorded arteriole densities (Kassab *et al.* , 1993; Marxen, 2004). Volume order provided a new metric of vessel scale, which correlated more strongly than Strahler order with several geometric parameters including vessel diameter and conductance (Marxen, 2004).

An interesting finding of applying volume ordering to the renal artery was the observation that branching asymmetry, δ, at each bifurcation decreased towards lower vessel generations (i.e. further downstream vessels) (Marxen, 2004). Branching asymmetry was defined as tissue volume fed by the smaller daughter vessel at a bifurcation divided by the total tissue volume supplied by parent vessel. Thus symmetric branching is given by $\delta = 0.5$, and a highly asymmetric branching by $\delta \to 0$. This is consistent with the observation of increasingly symmetric daughter diameter ratio and length ratio in lower vessel generations (Van Bavel & Spaan, 1992; Kalsho & Kassab, 2004), and has implications for the heterogeneity of blood flow.

1.2.3 Reference to Additional Background Content

As briefly mentioned above, studies have shown that perfusion heterogeneity has a fractal relation to tissue volume size. This concept is presented in detail in the Introduction section of Chapter 4, in the context of metrics used to assess the coronary network flow model.

Microsphere skimming was also mentioned above, and the literature is reviewed in Appendix A, to which reference is made throughout Chapter 5 where key concepts of skimming are presented.

Finally several papers were co-authored during the preparation of this thesis, which are listed below with associated contribution:

Cookson *et al.* (2012)
: Creation of the LV finite element mesh; production of figures; running simulations for the multi-compartment Darcy model to determine suitable parameters for comparison to the Poiseuille model; scientific discussion and proof-reading.

Michler *et al.* (2012)
: Creation of the LV finite element mesh; production of figures; running simulations for the multi-compartment Darcy model; scientific discussion and proof-reading.

Lamata *et al.* (2013)
: Developed the robust initial alignment alignment algorithm; scientific discussion and proof-reading.

Hyde *et al.* (2013b)
: Creation of the LV finite element mesh for the porcine heart; scientific discussion and proof-reading.

Zarinabad *et al.* (2013)
: Provided microsphere perfusion quantification; scientific discussion and proof-reading.

Schuster *et al.* (2014)

Provided microsphere perfusion quantification; scientific discussion and proof-reading.

Sinclair *et al.* (2014)

Primary author, performed all analyses.

1.3 Aims and Structure of the Thesis

The validation of quantitative perfusion MRI for future use in the clinic is an on-going field of research where recent studies have addressed quantification at different spatial resolutions, under a range of flow conditions, and with different quantification algorithms (Hsu *et al.* , 2012; Zarinabad *et al.* , 2013). In this thesis microspheres imaged with the epifluorescent CMT were used to compute regional perfusion for the validation of quantitative perfusion algorithms applied to DCE-MR images (results can be found in Zarinabad *et al.* , 2013; Schuster *et al.* , 2014). A new methodology presented in Chapter 2 was created for the co-registration of CMT and MR image data and the quantification of perfusion from microspheres in tissue segments used to validate quantitative perfusion MRI.

The acquisition of coronary vessel architecture and microsphere deposition in the same organ allows for a comparison of a Poiseuille network flow model to microsphere distribution as described above. A necessary step towards this goal is the reconstruction of the coronary vascular anatomy as a network of vessel segments with defined connectivity and vessel parameters. The reconstruction of the left coronary arterial (LCA) network from one pig heart is presented in Chapter 3. Following the network reconstruction, a Poiseuille flow model was solved in the LCA network using both Marxen's proposed outlet BC method and an outlet BC with the assumption of homogeneous perfusion throughout the LV. The comparison of each network flow solution to the distribution of microspheres is presented in Chapter 4.

Finally microsphere skimming was investigated in the LCA network. A novel sta-

tistical method using binomial distribution confidence intervals was introduced to assess the proportion of bifurcations in which model flow distribution and microsphere distribution differed significantly. Skimming prevalence was also characterised in relation to vessel generation and vessel properties, which is presented in Chapter 5.

Each Chapter is additionally supplemented with a brief Introduction section, followed by Methods, Results, Discussion and Conclusion. Finally Chapter 6 contains conclusions and future work for the presented research.

2 | Perfusion Quantification

2.1 Introduction

This chapter presents a novel method for validating quantitative DCE-MRI with microspheres from cryomicrotome images, with the aim of demonstrating the accuracy of quantitative DCE-MRI under a range of flow conditions in explanted pig hearts. Previous comparisons of quantitative DCE-MRI with microspheres involved excision and subsequent sectioning of the LV into appropriate circumferential and radial segments for comparison to perfusion MR images acquired from the *in vivo* heart. Segments were chosen based on their relative position to anatomical landmarks, which provided approximate correspondence to points used to define segments from the perfusion MR images (Christian *et al.* , 2004; Hsu *et al.* , 2012). This correspondence of the physically sectioned myocardium and imaged myocardium however is at best an approximation, especially given that the hearts are sectioned after excision when the heart often deforms relative to its *in vivo* state due to removal from physiological conditions.

Pig hearts have often been used as a surrogate to human hearts in experimental studies. A study of the coronary anatomy of 65 pig hearts demonstrated that both distribution and structure of the circulation in pigs are very similar to that in humans (Weaver *et al.* , 1986) making them suitable for perfusion studies and validation of potential clinical imaging methods. The division of the pig coronary circulation into distinct perfusion territories makes them suitable for studying the effects on regional perfusion caused by occlusion of a coronary artery (Spaan *et al.* , 2005). Recently an MRI-compatible Langendorff apparatus was proposed (Schus-

ter *et al.* , 2010) to acquire dynamic contrast enhanced (DCE) MRI of explanted porcine hearts for the quantification of cardiac MBF (Zarinabad *et al.* , 2013; Schuster *et al.* , 2014). Scans were acquired under several different flow conditions with simultaneous injections of fluorescently-labeled microspheres for validation of quantitative DCE-MRI, as detailed in the Methods section. After MR image acquisition, hearts were frozen and subsequently imaged with a fluorescent episcopic cryomicrotome, providing high-resolution images of the whole heart with embedded vascular cast and fluorescent microspheres (van Horssen *et al.* , 2010). The cardiac geometry was then co-registered from the cryomicrotome to MRI images, providing accurate correspondence of segments used for microsphere and DCE-MRI quantification.

The segmentation of the left ventricular myocardium into circumferential and transmural segments was achieved using a cubic Hermite mesh representation of the LV, which was fitted to a segmentation of the LV geometry from the cryomicrotome images with an automated mesh fitting software tool (Lamata *et al.* , 2011, 2013). Below a workflow is presented involving automatic LV mesh fitting, image registration of cryomicrotome and MR images, and segmental microsphere quantification. Results of the microsphere MBF quantification were compared to MBF quantified from DCE-MRI of the same hearts, provided by Niloufar Zarinabad (Zarinabad *et al.* , 2013), to determine if quantitative DCE-MRI was accurate under a range of flow conditions. The results of this study serve as a step towards clinical application of quantitative DCE-MRI, providing a novel metric for assessing and comparing regional cardiac perfusion in patients.

2.2 Summary of Data

The work carried out in this chapter, and in the rest of this thesis, was made possible by the availability of a set of data acquired by collaborators at King's

College London* and the Academic Medical Centre in Amsterdam†. Details of the acquired data are summarised below.

Ten non-beating, explanted MR-compatible pig hearts were imaged with 3T Achieva TX and 1.5T Achieva CV scanners (see Schuster *et al.* , 2010, 2014). The system provided control over physiological conditions including blood oxygenation level, coronary perfusion pressure, left ventricular pressure and coronary blood flow. The left and right coronary arteries (LCA and RCA respectively) were cannulated separately for infusion of microspheres under three flow regimes: (1) resting flow, (2) low (50% resting) flow to simulate ischemia, and (3) adenosine-induced hyperemic flow.

First-pass DCE-MRI was acquired with a dual-bolus scheme using gadobutrol injections for 5 hearts at 3T with a spatial resolution of $1.3 \times 1.3 \times 8\,\text{mm}$, and for another 5 hearts at 1.5T with a spatial resolution of $1.9 \times 2.0 \times 10\,\text{mm}$ (full sequence details are given in Schuster *et al.* , 2014). In addition to the DCE-MRI, survey scans were acquired with a resolution of $2 \times 2 \times 5\,\text{mm}$ providing approximately 20 short-axis images of the myocardium.

Infusion using standard protocols (**?**) of approximately 10^5 fluorescent microspheres‡ was made at the same site of gadolinium injection under each of the three flow conditions (resting, low and hyperemic) immediately following DCE-MRI acquisition. After all MRI sequences had been acquired the coronary arteries were infused with a fluorescent cast replica material and left to set for 24 hours before freezing at -20 °C for serial sectioning using an epifluorescent imaging CMT (van Horssen *et al.* , 2010).

Hearts were sectioned from base to apex into somewhere between 1000 to 2000

*Collaborators involved in data collection at King's College London: Amedeo Chiribiri and Andreas Schuster.

†Collaborators involved in data collection at the AMC, Amsterdam: Pepijn Van Horssen, Jeroen Van den Wijngaard, Maria Siebes.

‡$15\mu m$ diameter microspheres, distinguishable by their unique emission/excitation frequencies (van Horssen *et al.* , 2010).

slices with a constant slice thickness between 60-100μm (see Appendix C for image dimension details of each heart). At each slice, up to 5 sets of 2000×2000 pixel images were taken with a digital camera together with combinations of excitation and emission filters to detect each of the 3 sets of microspheres with different fluorescent labels, the fluorescent vascular cast, and to acquire a bright light image providing the outline of the myocardium.

2.3 Methods

Figure 2.1 shows a workflow for computing microsphere MBF involving both CMT and MRI image data. The Methods section is split into the three indicated components: (a) Segmentation (3D) and Mesh Fitting, (b) Image Registration and (c) microsphere MBF Quantification. A total of 10 hearts were processed through this pipeline, 5 of which were imaged at 1.5T and the other 5 at 3T field strength.

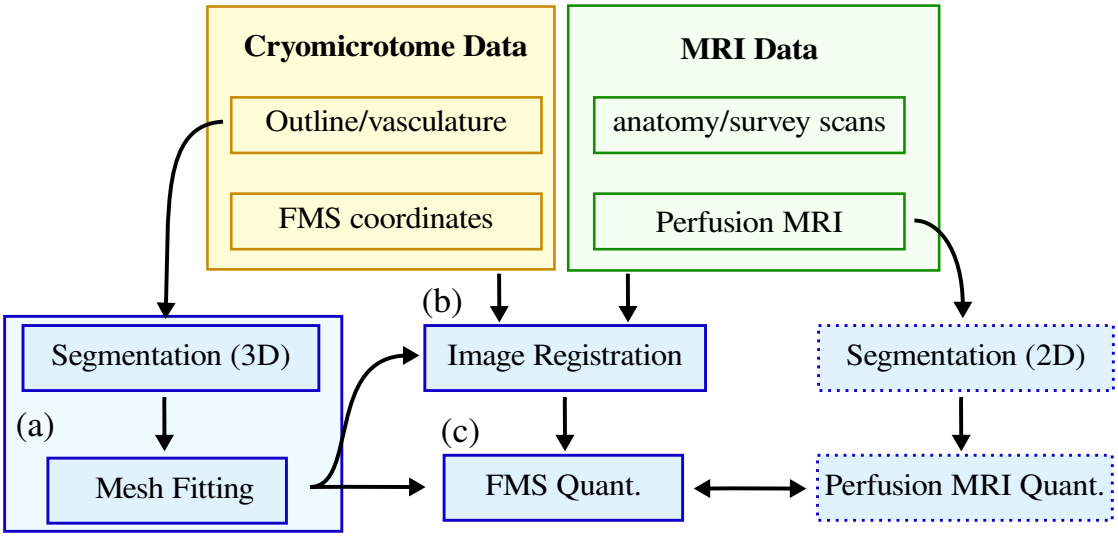

Figure 2.1: Perfusion quantification workflow. Step (a) involves segmentation of the LV myocardium from CMT images followed by mesh fitting. Step (b) involves image registration between the CMT and MRI images, using combinations of available image data. Step (c) involves definition of myocardial segments and quantification of MBF from microspheres. This quantification was then compared with DCE-MRI MBF (steps within dotted borders), provided by Niloufar Zarinabad (see Zarinabad *et al.* , 2013).

2.3.1 Segmentation and Mesh Fitting

The bright light CMT images of the heart outline were used for segmenting the LV myocardium. The high-resolution images were typically down-sampled by a factor of 50 for increased efficiency with the meshing pipeline (explained below) resulting in approximately 40 short-axis images for 3D segmentation, which was performed with the open source software ITK-SNAP (Yushkevich *et al.* , 2006). The 40 short-axis slices still provided sufficiently high-resolution detail for an accurate segmentation of the LV myocardium, excluding papillary muscles and following the inner contour of the epicardium. Furthermore, mesh fitting smoothly interpolates the LV ROI between segmented slices, and for the purposes of comparison to the much lower-resolution MR images this down-sampling of CMT images still provides a higher-resolution segmentation.

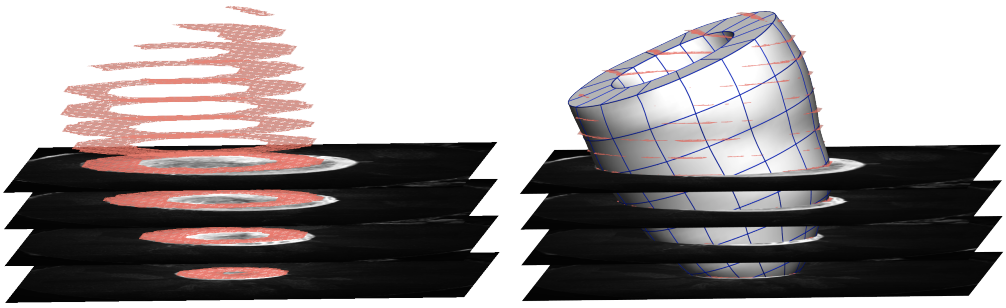

(a) (b)

Figure 2.2: Segmentation and fitted LV mesh. Segmentation of the LV geometry from the down-sampled CMT images (a), and a cubic Hermite mesh (silver) fitted to the LV segmentation (b).

In order to provide a local coordinate system for dividing the segmentation into transmural layers, a cubic Hermite mesh was fitted to each segmentation using rapid cardiac mesh fitting software, detailed in (Lamata *et al.* , 2011). This software tool fits a smooth LV ellipsoid template mesh with a truncated base to a LV cardiac segmentation (also with a truncated base) as shown in Figure 2.2. The fitted ellipsoid has three material coordinate directions, ξ_1, ξ_2 and ξ_3, as shown in Figure 2.3. The material coordinate direction ξ_3 varies linearly from 0 to 1 along the arc-length of each element in the transmural direction, allowing for transmural

segments of the fitted cubic Hermite mesh to be defined for quantification of microsphere density. For more detail on cubic Hermite meshes see (Hunter & Pullan, 2001; Smith *et al.* , 2004).

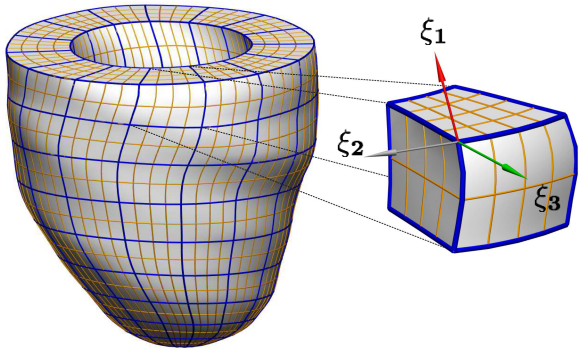

Figure 2.3: Fitted ellipsoid local coordinates. Each hexahedral element is marked with blue borders, local coordinates ξ_1, ξ_2 and ξ_3 vary from 0 to 1 in an apex-to-base, clockwise cirumferential, and endocardial-to-epicardial direction respectively. To illustrate how elements can be divided using the local coordinates, the golden lines mark $\xi_3 = 0.25, 0.5, 0.75$, $\xi_2 = 0.25, 0.5, 0.75$, and $\xi_1 = 0.5$ within an element. Divisions along ξ_3 produce transmural segments, used later for microsphere quantification.

Robust Initial Alignment

The mesh fitting process performs a non-rigid image registration between binary formats of the mesh and segmentation followed by a warping of the mesh nodal parameters. The geometric accuracy of the mesh fitting depends on the initial alignment of the ellipsoidal template binary and the LV segmentation. The correct orientation and tailoring of the template mesh geometry to the segmentation is essential for an accurately fitted mesh. The closer the template is to the segmentation in these respects, the more likely the fitting will be geometrically accurate (i.e. have a high percentage overlap with the segmentation), and additionally be more computationally stable for mechanics simulations (Lamata *et al.* , 2013).

There was a need to automate the initial alignment process in order to reduce user-interaction time and to deploy an automated web-based mesh fitting service (see Lamata *et al.* , 2013). Prior to this work, a time-consuming manual alignment and template generation process was the only way to ensure adequate mesh and

segmentation alignment before mesh warping. Another available alternative was Principal Component Analysis (PCA) applied to a mesh template and a segmentation point cloud (referred to in the text as the *Seg-PCA* method), where the three largest Principal Components (PCs) were used for scaling and aligning the template mesh to the segmentation. The new method proposed in this thesis first finds the LV (and RV) blood pool(s) from the segmentation, then uses PCA to find the major axis of the LV blood pool for orienting the mesh and segmentation (referred to in the text as the *BP-PCA* method). Methods were developed for both LV and BiV (bi-ventricular) mesh fitting, although in this chapter only the LV algorithm is discussed. Details on the alignment algorithm for BiV mesh fitting can be found in (Lamata *et al.* , 2013). A flowchart depicting the differences in the *Seg-PCA* and *BP-PCA* approaches is shown in Figure 2.4.

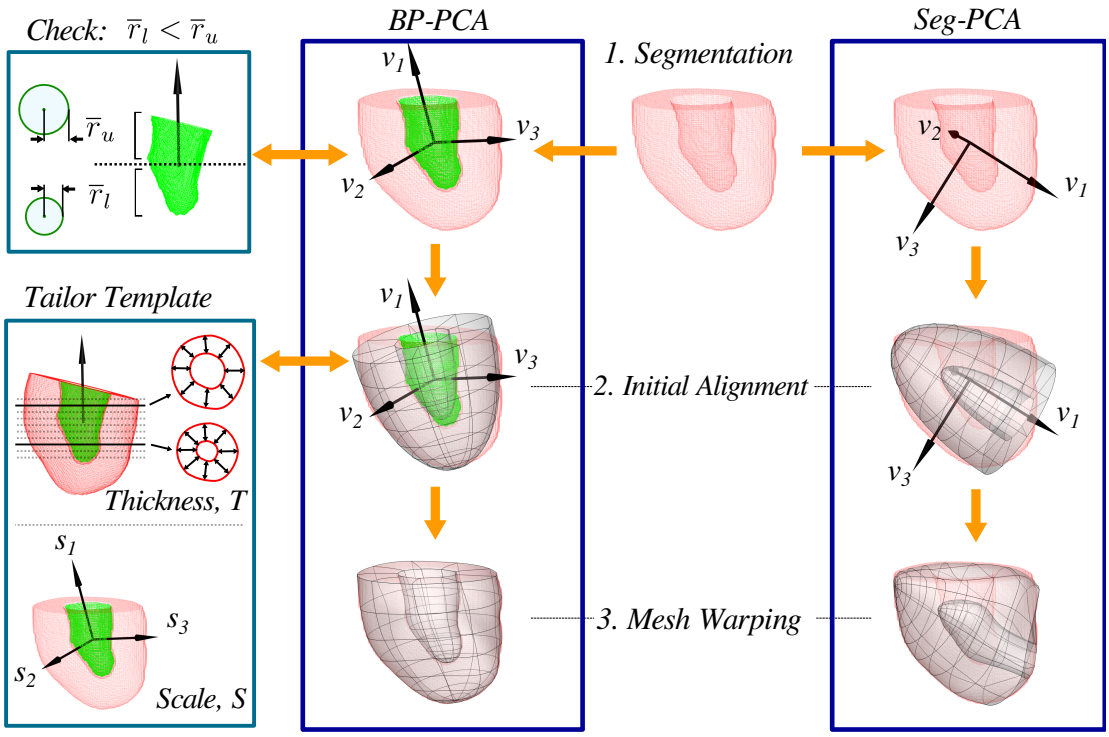

Figure 2.4: The *BP-PCA* and *Seg-PCA* alignment methods. Starting from a LV segmentation (1), the proposed *BP-PCA* method produces a more robust initial alignment (2) than the *Seg-PCA* method resulting in a correct mesh fitting (3). In the *Seg-PCA* method, PCA performed on the LV segmentation point cloud results in a coordinate system completely misaligned with the long-axis of this particular LV segmentation. Further details are given in the text.

The *BP-PCA* method is explained briefly as follows. A convex hull is computed from the point cloud of a LV segmentation followed by iterative morphological erosions to obtain the 3D geometry of the LV blood pool (shown in green in Figure 2.4). PCA is then performed on the blood pool point cloud and the three largest principal components are used to define a coordinate system. The axes of the coordinate system correspond to the long-axis of the LV blood pool and two orthogonal directions, represented by the unit vectors v_1, v_2 and v_3 respectively as shown in the *BP-PCA* panel in Figure 2.4. To ensure the v_1-axis defined by PC1 is oriented from apex to base, the LV BP point cloud is transformed into radial coordinates centred about v_1. A requirement of the segmentation for mesh fitting is that it is truncated at the base below the heart valves. Thus the width of the

LV BP is less at the apex than at the base. The mean radius of points at the endocardial surface is computed from the upper and lower halves of the LV BP from its centre of mass according to v_1, $\overline{r}_u$ and $\overline{r}_l$ respectively. If $\overline{r}_u > \overline{r}_l$ then the v_1-axis retains its orientation, otherwise it is switched (to point in the apex-to-base direction). The v_2 and v_3 axes given by PC2 and PC3, are modified if necessary to maintain a right-hand coordinate system.

The variance of the whole segmentation point cloud in the direction of each vector v_1, v_2 and v_3 is used to define a scaling, S, used to tailor the size of the template mesh. A constant wall thickness for the template mesh, T, is estimated from the distance between endocardial and epicardial contours of the LV along v_1. The template ellipsoid is initially oriented with its long-axis pointing in the positive z-direction, centred at the centre of mass of the LV BP. Thus the matrix $[v_3\ v_2\ v_1]$ specifies the rotation and the centre of mass of the segmentation LV BP provides the origin for a translation to align the template with the segmentation for fitting.

A study was performed to test the performance of the *BP-PCA* method compared to the alternative *Seg-PCA* method. The *Seg-PCA* method uses the three largest principal components from PCA performed on the entire LV myocardial segmentation to align and scale the template mesh to the segmentation.

The Dice Similarity Coefficient (DSC), introduced in (Zou *et al.* , 2004), is used to measure the overlap of the mesh and segmentation after initial alignment and mesh warping (steps (2) and (3) respectively in Figure 2.4). A mesh is binarised using the image stack dimensions and resolution of the segmentation for calculation of the DSC. The DSC expressed as a percentage is given by:

$$DSC(B_1, B_2)\frac{2\,\mathrm{Vol}(B_1 \cap B_2)}{\mathrm{Vol}(B_1) + \mathrm{Vol}(B_2)} \times 100 \tag{2.1}$$

Values of the DSC lie in the range $[0, 100]$ where 100% is complete agreement between two binary images B_1 and B_2, and a value of 0 indicates no overlap.

2.3.2 Image Registration

In order to more accurately quantify microsphere deposition in myocardial segments defined from the DCE-MR images, the CMT images were registered with the MRI images. Multiple MRI sequences were acquired for each heart, which included long-axis slices and DCE-MRI slices providing geometric information about the heart. Given the sparsity and varying intensity of the MRI image data it was not possible to automate the image registration. Therefore rigid registration was performed after scaling each image stack to physical units (i.e. millimetres). The rigid registration involved data transformation from CMT coordinate space into MRI coordinate space, performed in two steps:

1. Landmark-based rigid registration
2. Fine-tuning manual rotation and translation

Landmark-based rigid registration

This step required corresponding anatomical landmarks to be identified in each of the two image stacks, i.e. in the CMT image stack and in the MR images. Points which were usually identifiable include:

- Tip of the epicardial LV apex, P_{ap};
- Centre of the aortic (or mitral) valve, P_v;
- Centre of the Left Anterior Descending (LAD) artery near the base, P_{la}.

To aid in the selection of these landmarks multiple MR image sequences were simultaneously viewed, which was achieved by parsing DICOM[§] header information to visualise multiple image planes in CMGUI[¶]. A rotation matrix and origin was

[§]DICOM - Digital Imaging and Communications in Medicine - is the international standard for medical images and related information (ISO 12052).

[¶]CMGUI is a 3D visualisation software commonly used for manipulating finite element models and related imaging data (website: http://www.cmiss.org/cmgui).

then defined from these landmarks, namely R_{ref} and t_{ref} from the CMT landmarks, and R_{tar} and t_{tar} from the MRI landmarks. These were defined as follows:

$$v_z = P_v - P_{ap}; \tag{2.2a}$$
$$\hat{v}_z = \frac{v_z}{|v_z\|}; \tag{2.2b}$$
$$v_{temp} = P_{la} - P_v; \tag{2.2c}$$
$$v_y = (v_z \times v_{temp}) \times v_z; \tag{2.2d}$$
$$\hat{v}_y = \frac{v_y}{\|v_y\|}; \tag{2.2e}$$
$$\hat{v}_x = v_y \times v_z \tag{2.2f}$$

where each coordinate direction $\hat{v}_i$ is a 3×1 column vector, and are used to define the rotation matrices as:

$$R_{ref} = [\hat{v}_x^{ref}\ \hat{v}_y^{ref}\ \hat{v}_z^{ref}]; \tag{2.3a}$$
$$R_{tar} = [\hat{v}_x^{tar}\ \hat{v}_y^{tar}\ \hat{v}_z^{tar}] \tag{2.3b}$$

The CMT images as well as the LV mesh and microspheres were then transformed to MRI coordinate space with

$$\bar{x}_{mri}^a = R_{tar} R'_{ref} (\bar{x}_{cmt} - t_{ref}) + t_{tar} \tag{2.4}$$

where $\bar{x}_{cmt}$ is an $n \times 3$ matrix of coordinates (of microspheres and LV mesh) in the CMT images with physical units, and $\bar{x}_{mri}^a$ is the output $n \times 3$ matrix of the transformed coordinates.

The resulting overlay of CMT image data with the MRI images was then examined. Since the low resolution and sparse images sometimes made it difficult to accurately identify anatomical landmarks, the resulting rigid registration could often be visibly be improved.

Fine-tuning manual rotation and translation

Visual inspection of the position of the LV mesh and microspheres overlaid with the different planes of MR images in CMGUI allowed for manual rotation and translation to be applied using tools within the software to improve the registration. Correspondence between the LV mesh and microspheres with MR images was achieved by matching the LV mesh apex to the tip of the long-axis MR images and matching epicardial contours with each short-axis image. Figure 2.5 shows a LV mesh registered to the cardiac geometry in MRI coordinate space. The horizontal green lines mark the positions of the short-axis DCE-MRI slices.

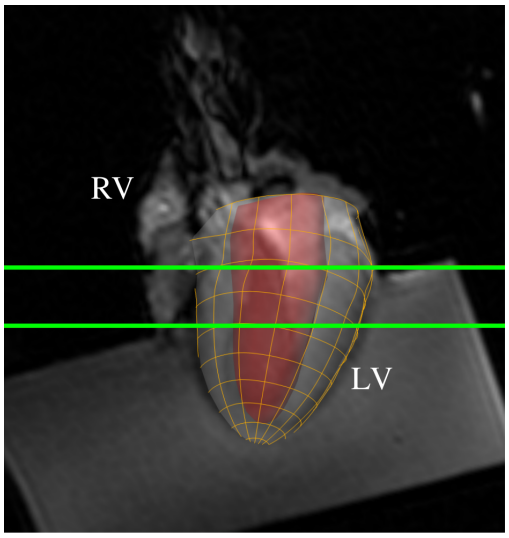

Figure 2.5: The LV mesh (fitted to a CMT segmentation) registered to MR images of the porcine heart in the Langendorff apparatus, shown from an anterior view. The orange lines trace the epicardial surface of the LV mesh with the red endocardial surface enclosed. In the background is a long-axis MR image (Schuster *et al.* , 2010), and the tilted rectanglular structure is the water-bath within which the heart was suspended. The horizontal green lines mark the basal and mid-cavity DCE-MRI slices.

To further constrain the manual registration, the boundaries of an induced myocardial infarct was used. Each heart was induced with a complete occlusion of either the left circumflex artery (LCx) or left anterior descending artery (LAD) after imaging the heart in a healthy state. The subsequent infarcted myocardial territory appeared dark in first-pass DCE-MR images acquired after this stage.

Microspheres injected into the coronary system at this point did not enter the occluded vessel. Thus, additional geometric correspondence could be gained between the CMT and MRI images by aligning the boundaries of the infarct as indicated by both the microspheres and first-pass DCE-MRI images, as shown in Figure 2.6(b).

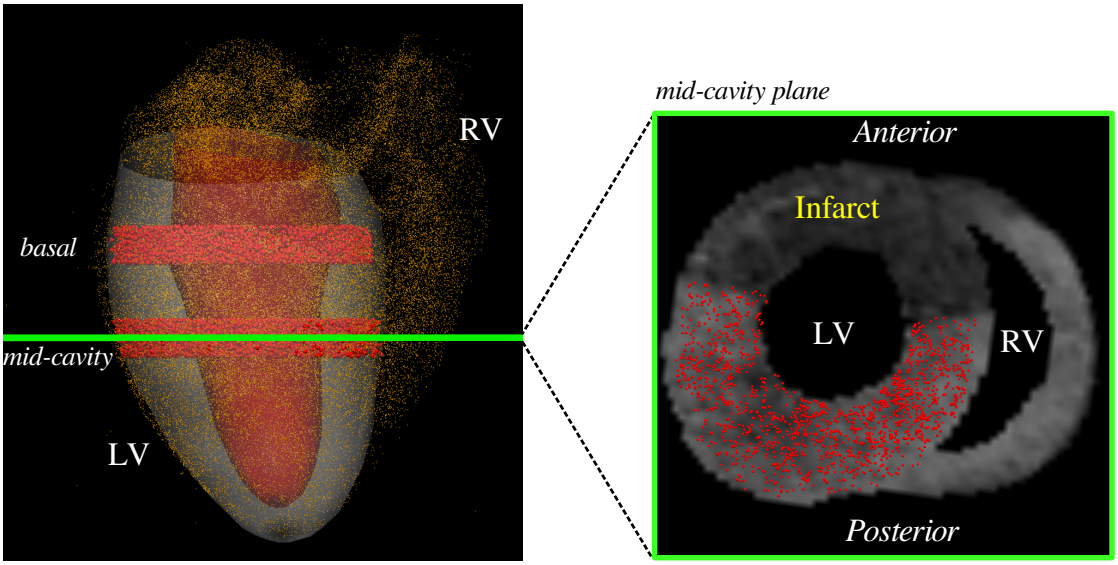

Figure 2.6: The LV mesh and microspheres shown from a posterior view. Microspheres injected into the heart distribute across both ventricles, indicated by the faint orange points (left). The larger microspheres shown in red are within the LV mesh and also within the 8mm width of the mid-cavity and basal DCE-MR image slices. A short-axis base-to-apex view of the microspheres within the mid-cavity DCE-MRI slice (marked in green on the left) shows the boundaries of the ischemic region provide correspondence between the microspheres and the DCE-MR image. (Note that the LV and RV cavities and the surrounding water bath have been manually removed for clarity.)

The final coordinates of the registered mesh and microspheres, $\bar{x}^b_{mri}$, were obtained from the landmark-based registered coordinates, $\bar{x}_{cmt}$, by applying this manual rotation, R_{man}, and translation, t_{man},

$$\bar{x}^b_{mri} = R_{man}\,\bar{x}^a_{mri} + t_{man} \tag{2.5}$$

2.3.3 Segmental Microsphere Flow

With the LV mesh and microspheres registered to the MR images, myocardial segments were defined from the DCE-MR images to quantify microsphere deposition for comparison to quantitative DCE-MRI. Standard AHA segments (Cerqueira *et al.* , 2002) were used to define circumferential segments in the base, mid-cavity and apical DCE-MRI slices for each heart (where available). These segments are shown in Figure 2.7, with slices viewed from apex-to-base.

Three transmural segments, namely subendocardial, midwall, and subepicardial, were defined by dividing the cubic Hermite mesh along the ξ_3 material direction at $\xi_3 = 0.33$ and $\xi_3 = 0.66$, as discussed above. Circumferential segments were defined by first marking in each DCE-MRI slice the centre of the LV cavity and the anterior interventricular sulcus, at the epicardial junction of the LV and the RV. Then segments were defined circumferentally every $60\,^\circ$ and numbered according to the AHA segments in Figure 2.7.

To quantify myocardial blood flow MBF in units of $(ml/min/g)$ from microsphere deposition in a segment i, the following equation was used

$$\mathrm{MBF}_i = \frac{N_i \cdot Q_t}{M_i \cdot N_t} \tag{2.6}$$

where N_i is the number of microspheres in segment i, M_i is the myocardial mass (g) of the segment, Q_t is the total flow (ml/min) entering the LV myocardium, and N_t is the total number of microsphere deposited in the LV myocardium. LV mass was computed from the volume of the cubic Hermite mesh multiplied by the mean myocardial tissue density, 1.05 (Vinnakota & Bassingthwaighte, 2004). Volume of each segment was computed from a binarisation of the mesh with a resolution of $50 \times 50 \times 50\,\mu\mathrm{m}^3$. After set up of the Langendorff apparatus a steady flow, Q_c, was supplied via a roller pump to the coronary arteries, and was adjusted for the three flow conditions mentioned earlier (normal flow, 50% flow, and adenosine induced hyperemia). Total flow to the LV myocardium, Q_t, was determined as the fraction of the microspheres within the LV mesh relative to the total number of microspheres in the heart, multiplied by the controlled inlet flow Q_c.

Bassingthwaighte noted in experiments performed with 11 sheep hearts that subendocardial segments had higher microsphere deposition density than subepicardial segments and hypothesised this was a result of microsphere skimming (Bassingthwaighte & Bever, 1991). Differences were tested for between MBF in the subendocardium, midwall and subepicardium as well as MBF in basal, mid-cavity, and apical regions. Normality was tested for with the D'Agostino-Pearson's test. Normally distributed MBF groups were compared with paired t-tests to check if there was a significant difference in group means, if $p < 0.05$. For non-normally distributed groups a Kruskal-Wallis test was used.

The absolute flow computed in each myocardial segment was compared to that from quantitative DCE-MRI. DCE-MRI flow quantification results were provided by a collaborator Niloufar Zarinabad[‖] who compared four methods: (1) Fermi function constrained deconvolution, (2) deconvolution with an exponential basis, (3) deconvolution with a B-spline basis, and (4) an autoregressive moving average model; further details of these analyses can be found in (Zarinabad *et al.* , 2013).

2.4 Results

2.4.1 Mesh Fitting

Meshes were automatically fitted with a 100% success rate (correct initial alignment and mesh warping) using the (*BP-PCA*) method for all 10 pig hearts. The mean DSC for fitted meshes using the *BP-PCA* alignment method was 92.9%. Figures 2.8 and 2.9 show the fitting results of all ten pig hearts, comparing the fitted meshes after initial alignment using the *Seg-PCA* method, and the *BP-PCA* method. The template mesh was only correctly oriented for 1 out of 10 hearts using the *Seg-PCA* method. DSC was higher for the *BP-PCA* method for all hearts compared to the *Seg-PCA* method.

[‖]Niloufar Zarinabad (at time of writing) is a collaborator in the Division of Imaging Sciences and Biomedical Engineering, King's College London, St. Thomas' Hospital, London, UK

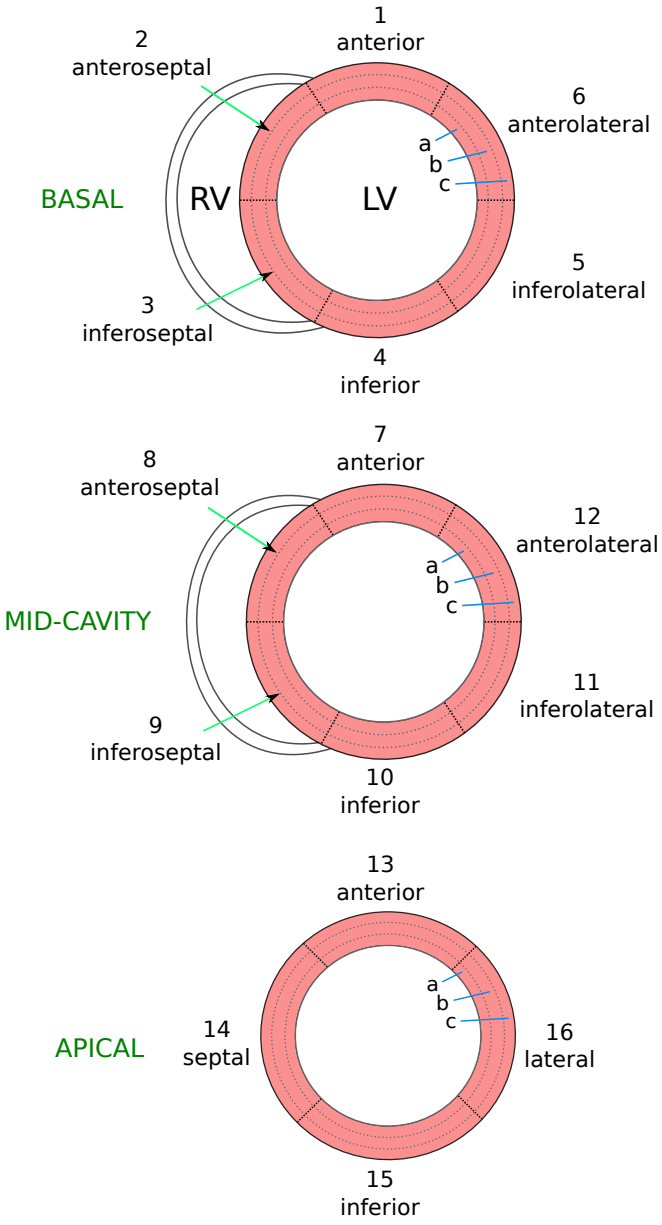

Figure 2.7: The division of the short-axis LV slices into circumferential segments (labeled according to their AHA number) with three transmural layers: (a) subendocardium, (b) midwall, and (c) subepicardium.

The mean DSC for the fitted mesh using the *Seg-PCA* alignment method was 85.3%. However given that the orientation was incorrect in 9 out of the 10 cases, the meshes would not have been useful for the subsequent microsphere quantification since the local ξ_3 coordinate was not representative of the segmentation transmural direction, and the mesh cavity intersects the LV wall at some point. The correct orientation of the LV meshes to segmentations using the *BP-PCA* method were crucial for the following microsphere quantification step.

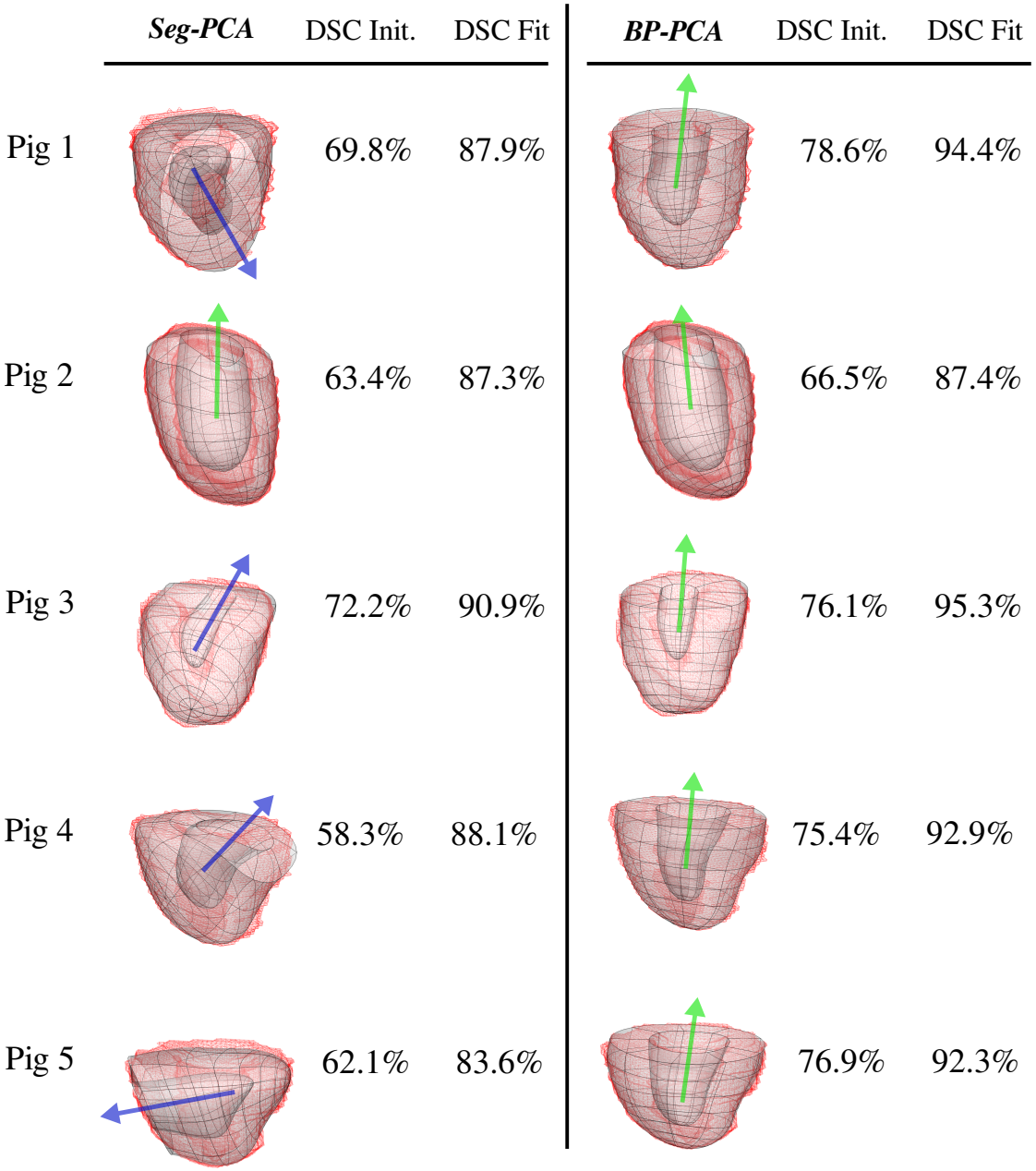

Figure 2.8: LV meshes fitted to segmentations of pig hearts 1 to 5 resulting from the *Seg-PCA* (left column) and *BP-PCA* (right column) alignment methods. Thin black lines mark the basal, endocardial and epicardial surfaces of the fitted mesh, superimposed on the segmentation (red). Segmentations are aligned the same way in both columns, with their long-axis in a vertical orientation. The DSC is given as a percentage for the overlap of mesh and segmentation after initial alignment (DSC Init.) and after mesh warping (DSC Fit). Arrows show the first principal component direction from each method which determines the long axis orientation of the mesh template with the segmentation. Green arrows indicate a good alignment of the mesh with the LV segmentation resulting in an accurate mesh fitting, and blue arrows indicate an inadequate initial alignment.

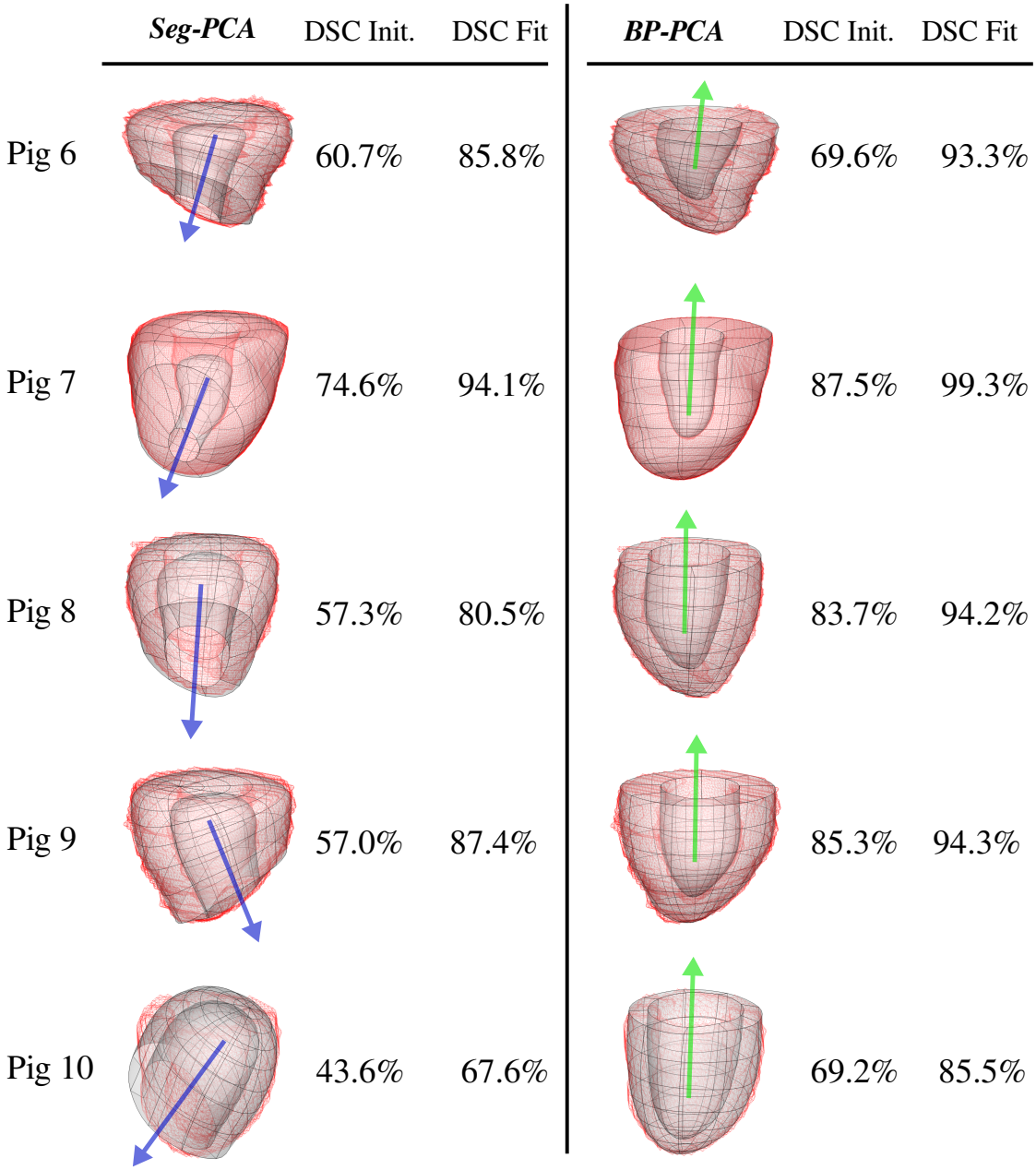

Figure 2.9: LV meshes fitted to segmentations of pigs 6 to 10 resulting from the *Seg-PCA* (left column) and *BP-PCA* (right column) alignment methods. Thin black lines mark the basal, endocardial and epicardial surfaces of the fitted mesh, superimposed on the segmentation (red). Segmentations are aligned the same way in both columns, with their long-axis in a vertical orientation. The DSC is given as a percentage for the overlap of mesh and segmentation after initial alignment (DSC Init.) and after mesh warping (DSC Fit). Arrows show the first principal component direction from each method which determines the long axis orientation of the mesh template with the segmentation. Green arrows indicate a good alignment of the mesh with the LV segmentation resulting in an accurate mesh fitting, and blue arrows indicate an inadequate initial alignment.

2.4.2 Microsphere Quantification

After manual rigid registration of fitted meshes and microspheres for each pig heart from cryomicrotome image coordinates to MRI image coordinates, microsphere flow was quantified in (1) AHA segments and (2) AHA segments divided into three transmural layers. Four of the ten hearts had all three perfusion planes acquired, i.e. basal, mid-cavity and apical slices. The remaining six hearts had just two perfusion slices acquired, four of which had basal and mid-cavity slices acquired and two of which had mid-cavity and apical slices acquired. A total of 448 AHA segments, or 1,344 radial segments, were available for analysis.

The number of microspheres deposited in each heart varied with a mean $\pm 1SD$ of $66,729 \pm 44,973$. Buckberg showed that microsphere deposition could be modelled with a binomial distribution, and that approximately 400 microspheres are required in a given tissue segment to have approximately 95% confidence of being within 10% of the true underlying flow distribution (Buckberg *et al.* , 1971). Using this approximation, for a heart segmented into 16 AHA and 3 transmural regions, approximately $16 \times 3 \times 400 = 19,200$ microspheres in total need to be deposited in the AHA regions for the above accuracy in quantification.

A total of 27 microsphere infusions were made across the 10 hearts, of which 4 infusions resulted in a deposition count considerably lower ($< 13,000$) than the suitable 19,200 within the LV mesh. One of the hearts removed from the analysis had all three perfusion slices imaged, and the other just two. For the 23 microsphere infusions made in the remaining 8 hearts, the mean $\pm 1SD$ number of microspheres deposited in the LV was $38,597 \pm 23,085$, or 804 ± 481 per radial AHA segment.

Mean LV MBF for each heart was computed from experimental flow rate divided by heart weight, which at normal, low and adenosine-induced hyperemic flow were 0.89 ± 0.18, 0.45 ± 0.1 and 1.47 ± 0.16 ml/min/g, respectively. The mean MBF to subendocardial, midwall and subepicardial segments was 1.43 ± 1.59, 1.23 ± 1.27, and 0.87 ± 0.80 ml/min/g respectively (each computed from 180 segments). The

distributions were non-normal, and the Kruskal-Wallis test showed that subendocardial MBF was significantly higher than subepicardial MBF but not midwall MBF, and midwall MBF was significantly higher than subepicardial MBF. Boxplots are shown in Figure 2.10. Note that these values were computed from 23 microsphere infusions at different flow rates, both with and without a coronary occlusion.

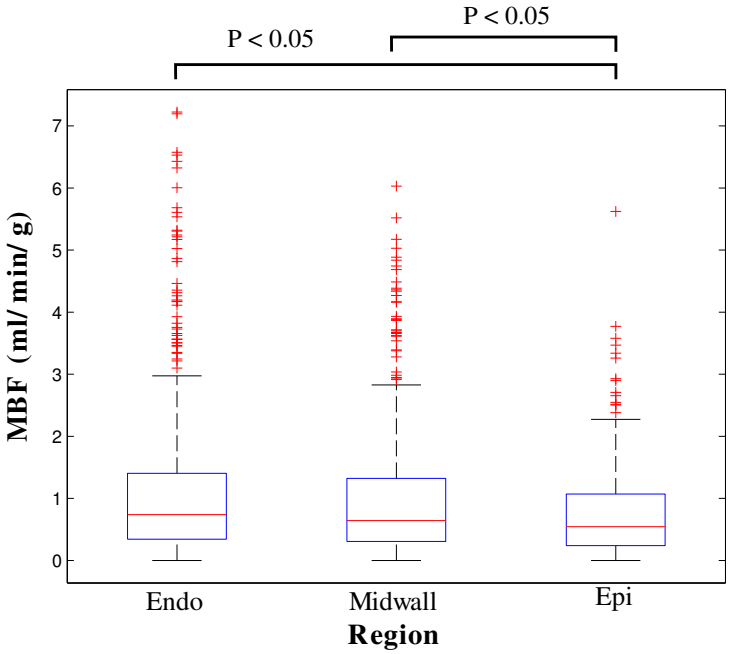

Figure 2.10: Transmural MBF differences shown in terms of boxplots visualised for 180 segments in each of the subendocardium (left), midwall (centre) and subepicardium (right). There is a significantly higher median MBF in the endocardium vs the epicardium, as well as in the midwall vs the epicardium.

To examine differences in MBF between the basal and apical regions, mean $\pm 1SD$ was calculated in basal, mid-cavity and apical slices from the three hearts in which all three perfusion slices were available (with a total of 5 microsphere infusions), yielding 0.38 ± 0.18, 0.43 ± 0.18, and 0.56 ± 0.20 ml/min/g respectively (computed from 90, 90 and 60 segments respectively). MBF in each transmural layer was normally distributed, and paired t-test analysis showed that MBF in the base was significantly lower than in the apex but not significantly different from MBF in the mid-cavity, and mid-cavity MBF was not significantly different from the apical region. Boxplots are shown in Figure 2.11. The values of MBF computed in these

longitudinal regions are lower than those computed above for transmural segments since only three hearts with all three imaging slices were considered, for which microspheres were only available at lower than average flows than some of the hearts used for the comparison of transmural regions.

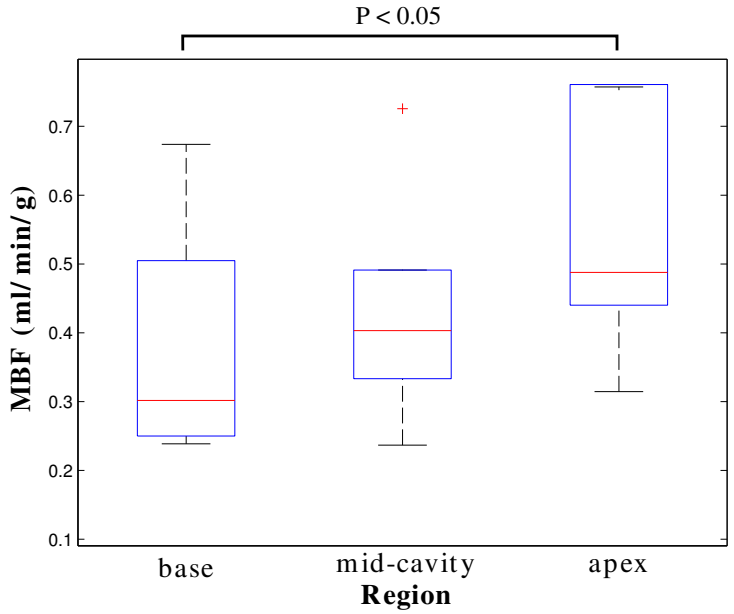

Figure 2.11: Longitudinal MBF differences shown in terms of boxplots visualised for 90 segments in the basal and mid-cavity slices and 60 segments in the apical slice.

AHA segmental MBF computed from the microspheres was compared to MBF quantified from DCE-MRI using 4 hearts imaged with a 1.5T scanner and 4 hearts imaged with a 3T scanner, results of which are presented in (Schuster *et al.* , 2014). Linear least-squares fits and paired t-tests showed statistically significant correlations for comparisons at both field strengths with all 4 DCE-MRI quantification methods. The Fermi function deconvolution method produced superior results to the other three methods at both 1.5T ($r = 0.93$, $p < 0.001$) and 3T ($r = 0.9$, $p < 0.001$). Figure 2.12 shows the 1.5T results and Figure 2.13 shows the 3T results.

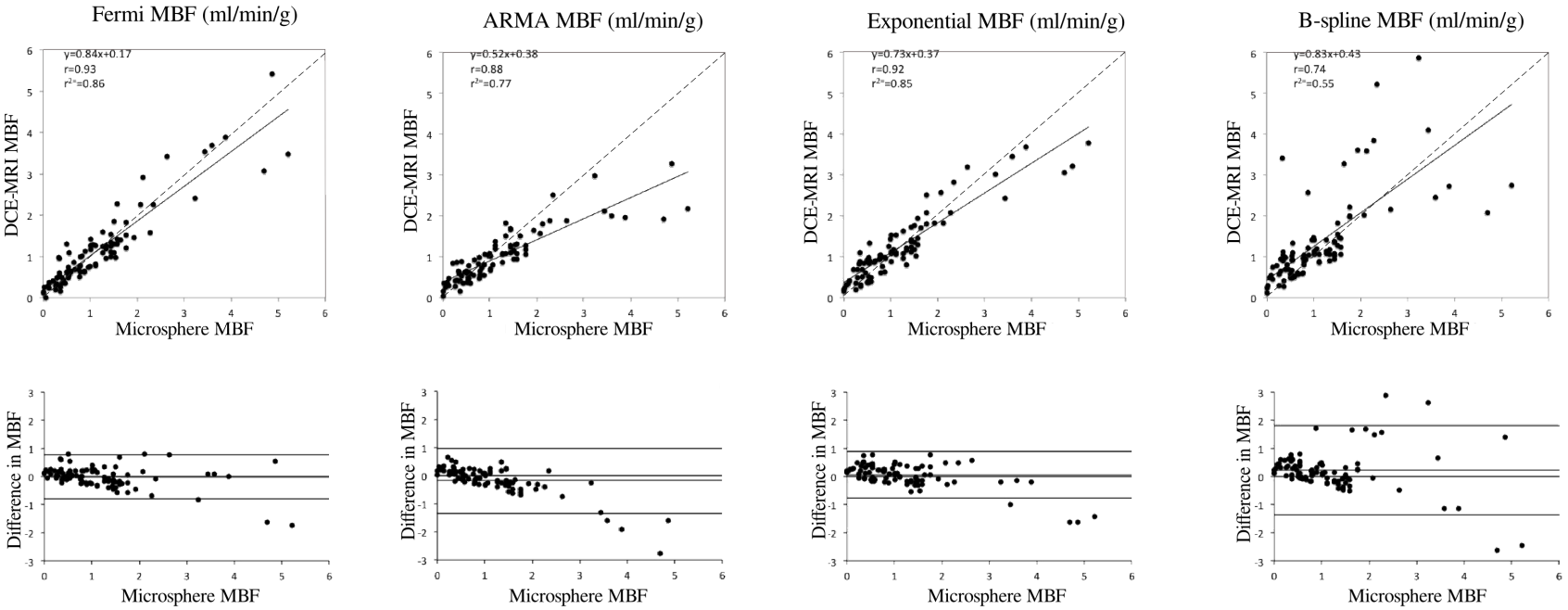

Figure 2.12: Microsphere validation of quantitative 1.5T DCE-MRI in AHA segments using the Fermi, ARMA, Exponential basis and B-spline basis methods. Linear-least squares regression in the top row and Bland-Altman plots in the bottom row show strong correlations for all methods with microsphere MBF. There is a trend for microsphere MBF to overestimate DCE-MRI MBF (adapted with permission from Schuster *et al.* , 2014).

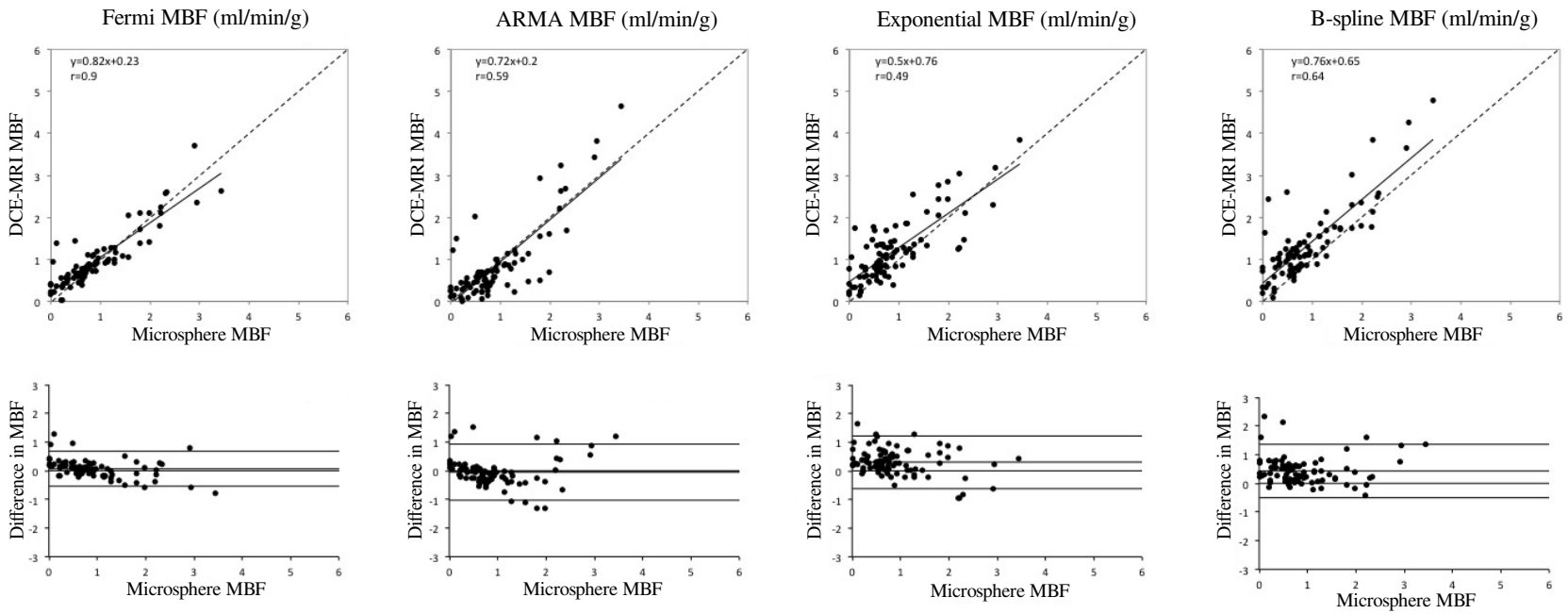

Figure 2.13: Microsphere validation of quantitative 3T DCE-MRI in AHA segments using the Fermi, ARMA, Exponential basis and B-spline basis methods. Linear-least squares regression in the top row and Bland-Altman plots in the bottom row show strong correlations for all methods with microsphere MBF (adapted with permission from Schuster *et al.* , 2014).

Interestingly there was a tendancy for DCE-MRI MBF to underestimate microsphere MBF in segments with high flows, particularly with the 1.5T results. Figure 2.14 shows a comparison of microsphere and DCE-MRI MBF in the three transmural layers: subendocardial, midmyocardial (midwall) and subepicardial. There is a clear trend for MBF from DCE-MRI to underestimate microsphere MBF in high flow regions. Figure 2.15 shows results at 3T with no evident overestimation of microsphere MBF.

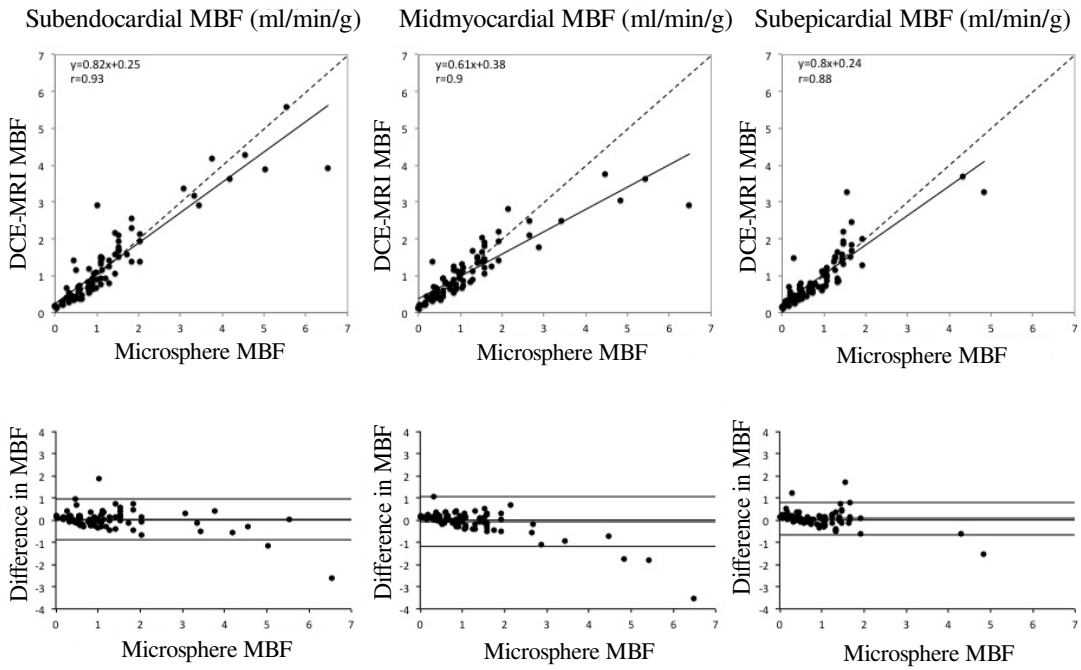

Figure 2.14: Comparison of MBF from microspheres and 1.5T DCE-MRI in subendocardial, midmyocardial and subepicardial layers using the Fermi function deconvolution method. Higher flow segments tend to result in an underestimation of MBF from DCE-MRI. (unpublished, courtesy of Andreas Schuster).

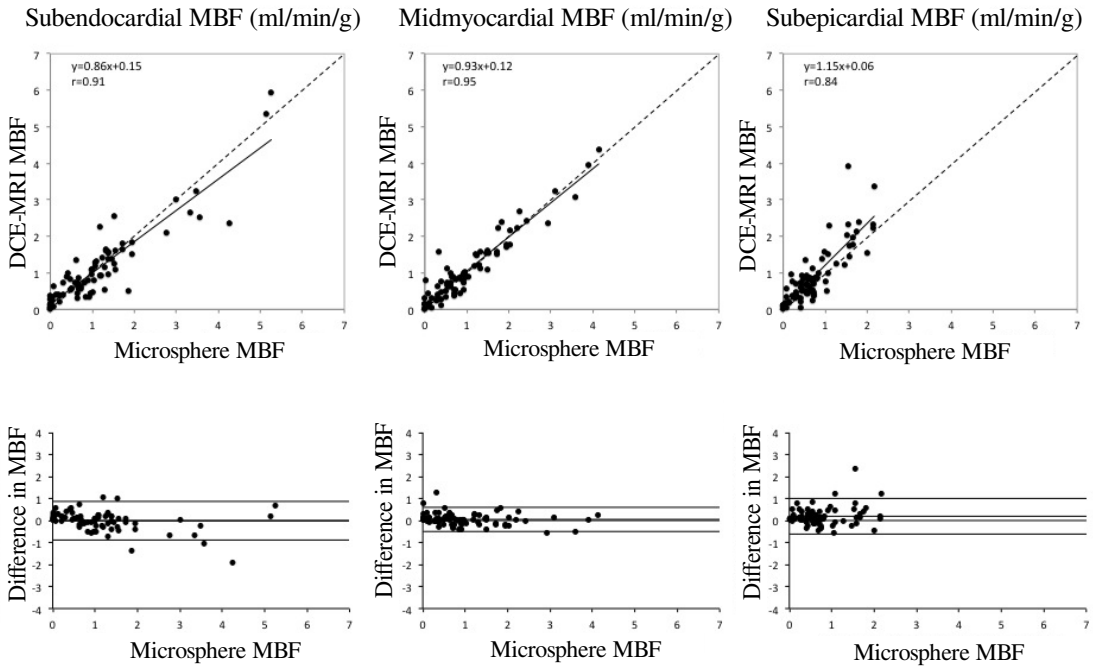

Figure 2.15: Comparison of MBF from microspheres and 3T and 3T DCE-MRI in subendocardial, midmyocardial and subepicardial layers using the Fermi function deconvolution method. Higher flow segments do not tend to result in an underestimation of MBF from DCE-MRI. (unpublished, courtesy of Andreas Schuster).

2.5 Discussion

A new approach has been implemented for quantifying MBF from microspheres for comparison to quantitative DCE-MRI. This method improves the accuracy of microsphere tracer to image comparisons by providing direct correspondence between microsphere locations and DCE-MR images via image co-registration. Furthermore a fitted LV mesh was used to accurately represent transmural position of microspheres and to quantify tissue volume in each segment for the accurate computation of microsphere MBF.

Previous methods for flow quantification validation with microspheres required physical sectioning of the heart into tissue segments corresponding to those selected from perfusion MRI images and relied on anatomical landmarks including papillary muscles and the interventricular sulcii (Jerosch-Herold *et al.* , 2003;

Christian *et al.* , 2004; Hsu *et al.* , 2012). This approach comes with several inherent errors; firstly the geometry of the heart deforms when excised due to a loss of intracavity pressure, cell death, and removal from the pericardium. Secondly, a dependence on using the relative position of myocardial segments to just a few anatomical landmarks further adds to potential error in segment definition. This was illustrated in this study by the need for additional manual adjustment of the cryomicrotome-to-MRI image registration after an initial rigid registration between the two image sets based on anatomical landmarks.

The ability to apply manual rigid transformations allowed for more accurate alignment of the cryomicrotome and MR images. Furthermore, since hearts were imaged with DCE-MRI in a Langendorff set-up, the geometry of the heart was virtually unchanged when frozen for cryomicrotome sectioning. The use of multiple MR image planes allowed for more geometric features of the heart to be used to guide the image registration, where correspondence of the RV geometry and LV apex were used to ensure correct alignment, as well as correspondence of ischemic regions in the LV between DCE-MRI and microsphere locations. Multiple MR image projections of varying contrast and resolution and different data types (microsphere spatial locations and fitted mesh) were necessary to accurately co-register the two image sets manually. An automated method for image registration would have required considerable time and effort. In future a high resolution cardiac anatomical MRI acquisition would allow for established, automated image registration methods to be used, relying solely on cardiac geometry from bright-light cryomicrotome images and the anatomical MR images. Non-rigid registration could be applied to account for any potential deformation in heart geometry between MRI and cryomicrotome image acquisition for example (Crum *et al.* , 2004).

The fitted LV mesh provided a region of interest (ROI) for microsphere quantification, where after image registration the resulting in-plane cross-section of the LV myocardium from the mesh and DCE-MR images was used for computation of MBF from microspheres and compared to DCE-MRI-derived MBF. Fitting an LV mesh for all 10 hearts was automated using a novel method for initialising the alignment of a template mesh and segmentation of the LV prior to mesh warp-

ing (Lamata *et al.* , 2013). PC1 obtained from the *BP-PCA* method was always oriented along the long axis of the blood pool, ensuring accurate alignment with the predefined long-axis of an LV template mesh. PC1 obtained from *Seg-PCA* was less reliable since the segmentation of the myocardium is more spherical than the blood pool and is subject to variable wall thickness, both of which affect the resulting PCA. In a study performed on biventricular geometries, the *BP-PCA* method was augmented to accommodate analysis of the RV blood pool as well, resulting in 84% success of automated mesh fitting to 36 BiV segmentations (using additional metrics of 'success' for the purposes of producing stable meshes for mechanics simulations) (Lamata *et al.* , 2013).

Microsphere MBF quantified in AHA regions showed strong correlations with all quantitative DCE-MRI methods in a total of 8 hearts. In segments of high MBF there was however a consistent under-estimation of MBF using all quantitative DCE-MRI algorithms in hearts imaged with a 1.5T scanner. This is consistent with previous studies where in tissue regions with higher MBF, quantitative DCE-MRI underestimated MBF computed from microspheres (Hsu *et al.* , 2012), and MBF from PET (Pärkkä *et al.* , 2006; Fritz-Hansen *et al.* , 2008; Morton *et al.* , 2012; Miller *et al.* , 2014). While it remains unclear why this discrepancy occurs when comparing quantitative DCE-MRI to PET, the discrepancy with microsphere MBF may in part be due to a slight over-estimation bias of MBF from microspheres in higher MBF tissue segments, as compared to the gamma-emitting molecular tracer IDMI, explained below (Bassingthwaighte *et al.* , 1987, 1990).

While this validation shows promise for future use of quantitative DCE-MRI in the clinic, this study was performed with non-pumping excised hearts sustained in a Langendorff apparatus (see Schuster *et al.* , 2010). A beating *in vivo* heart is subject to additional factors influencing blood flow, such as systolic flow impediment. A necessary further step towards clinical application would be to perform experiments to compare microsphere distribution *in vivo* with simultaneously acquired DCE-MRI to determine wether a similar correspondence could be achieved.

Interestingly in this study there were microsphere deposition gradients in both

longitudinal and radial directions, favouring flow towards the apex and subendocardium, respectively. The increase in perfusion from the subepicardium to the subendocardium is consistent with a study of 7 excised canine hearts injected with radioactive labelled microspheres under maximal vasodilation (Wüsten *et al.* , 1977) as well as a study with 7 rabbit hearts (Bassingthwaighte *et al.* , 1987) and 11 sheep hearts (Bassingthwaighte *et al.* , 1990). Bassingthwaighte's findings showed an increase in perfusion measured from microspheres towards the subendocardium in both small and large animal hearts, but no significant difference with IDMI. It was hypothesised that the 'skimming' phenomenon (the preference of particles to enter daughter vessels with a higher flow fraction) was possibly responsible for a higher subendocardial microsphere deposition density. Bassingthwaighte rationalised that microspheres had a preference to continue along the transmural conduit arteries which penetrate the myocardium towards the subendocardium rather than split off into smaller side branches. He showed that both tissue regions of higher flow and those towards the subendocardium had a correlation with increased microsphere deposition. The theory that microsphere deposition is influenced by skimming at bifurcations with disparate flow fractions resulting in preferential subendocardial deposition would also seem consistent with recent findings of transmural structure of vessel crowns. Specifically, epicardial vessels which penetrate the myocardium to feed the subendocardium are less frequent than those which feed the subepicardium, and as a corollary they also each supply a larger region of the myocardium hence would carry more blood than epicardial vessels supplying the subepicardium (van Horssen *et al.* , 2014). It has also been established that there is a larger volume of resistance vessels feeding the subendocardium than the subepicardium (Wüsten *et al.* , 1977). This is apparently to counter the effects of myocardial contraction which impedes flow in the subendocardium during exercise by remaining preferentially dilated relative to the resistance vessels supplying the subepicardium (Camici & Crea, 2007).

No overt investigation was made by Bassingthwaighte into base-to-apex differences of microsphere deposition density, although no significant difference was observed in individual canine hearts in his study. Using the same rationale as for the subendocardial microsphere deposition preference, it is plausible that microspheres tend

to remain in the large coronary arteries (with high flow fractions) descending the epicardial surface of the heart, rather than entering smaller side-branches, especially at low particle concentrations as is the case with microsphere injections. By contrast, skimming of red blood cells appears to become insignificant in vessels greater than about 30 microns in diameter (Pries *et al.* , 1989), although the concentration of RBCs is typically around 45% (compared to $\ll 1\%$ for microspheres). Particularly at the base of the heart where the left and right coronary arteries stem from the coronary ostia, flow fractions at bifurcations between large epicardial and small side branches show the greatest disparity. This is because the large epicardial vessels must supply a very large fraction of the myocardial mass compared to side-branches which supply tissue regions near the base. The findings of such preference for microsphere deposition in the apex and in the subendocardium would have implications for validation studies, and ideally in the future could be quantified and corrected for to improve the accuracy of the microsphere method. The relation between microsphere deposition and flow through the coronary tree is examined in the remaining chapters. An algorithm for coronary vascular segmentation from cryomicrotome images is presented in Chapter 3, followed by the comparison of a Poiseuille flow model to microsphere distributions in Chapter 4, and finally the prevalence of microsphere distribution bias relative to the model is investigated in Chapter 5.

2.6 Conclusions

Quantitative perfusion MRI has been validated in explanted pig hearts using fluorescent microspheres, a gold standard deposition marker. A novel, accurate approach for microsphere MBF quantification for comparison to quantitative perfusion MRI has been implemented using image registration of cryomicrotome and MRI image data. A new method for automatically aligning a LV mesh template with LV segmentations in order to initialise mesh fitting was created and successfully tested on 10 pig heart LV segmentations. The comparison of microsphere MBF and quantitative perfusion MRI MBF yielded strong correlations, providing promising results for future clinical application of perfusion MRI flow quantifi-

cation. Finally microsphere deposition gradients were identified from the base-to-apex and from the subepicardium-to-subendocardium suggesting microsphere deposition bias, which will be further investigated in the remainder of this thesis.

3 | Vascular Reconstruction

3.1 Introduction

Coronary vascular geometry plays a crucial role in the delivery of oxygenated blood to the myocardium. Integral to understanding this role is the study of the relationship between coronary structure and function across the range of vessel scales in the coronary network ($8\mu m - 5mm$ diameters), which additionally will help guide the treatment of coronary-related diseases (Camici & Crea, 2007). Computational modeling provides a framework for linking anatomical vascular geometry and the physics governing blood flow to study this relationship, with the further advantage of its ability to integrate biophysical measurements from multiple sources (Marxen *et al.* , 2006; Huo *et al.* , 2009; Lee & Smith, 2008; Waters *et al.* , 2011; Lee & Smith, 2012; Nolte *et al.* , 2013; Hyde *et al.* , 2013a).

Before the recent development of high-resolution imaging modalities for the visualisation of whole-heart coronary vasculature, coronary geometry and connectivity were measured manually and quantified in terms of statistical morphometry data most often from porcine coronary networks (Van Bavel & Spaan, 1992; Kassab *et al.* , 1993, 1994; Kassab & Fung, 1994). This morphometric data has since been used to reconstruct numerous representations of the coronary circulation in a non-beating configuration and has identified scaling laws relating a range of vascular parameters, including vessel radii, vessel length, vascular volume, tissue volume, flow rate, and vessel resistance (Van Bavel & Spaan, 1992; Beard & Bassingthwaighte, 2000; Kaimovitz *et al.* , 2005; Mittal *et al.* , 2005; Kassab, 2006; Choy & Kassab, 2008; Huo *et al.* , 2009; Huo & Kassab, 2012). These stochastically gen-

erated models however lack information about the 3D distribution of the vascular tree, which has been shown to demonstrate spatial compartmentalisation (Spaan *et al.* , 2005), and distinct differences in terms of vessel volume density and stem-crown* frequency between the subepicardium and subendocardium (van Horssen *et al.* , 2014). Biophysical models of coronary blood flow should ideally utilise the geometric information as part of the vascular anatomy to study flow distribution, which has been afforded by more recent advances in coronary vascular imaging and network reconstruction algorithms.

Current clinical imaging modalities provide only coarse anatomical detail of the coronary vasculature due to limitations in imaging resolution. Specifically, recent advances in clinical CT provide epicardial vessel anatomy at an image resolution of $0.6 \times 0.6 \times 1\text{mm}^3$ in patients injected with a radio-opaque contrast agent (Wischgoll *et al.* , 2009; Huo *et al.* , 2013). By contrast, micro-CT has been used to image whole vascular networks filled with cast in rat kidneys (Garcia-Sanz *et al.* , 1998; Marxen, 2004) and rat hearts (Beighley *et al.* , 1997; Jorgensen, 1998; Lee *et al.* , 2007) with a resolution of approximately 20μm. An advantage of micro-CT is that *in-vivo* imaging is possible (Ritman, 2011), thus observations can be made under physiological conditions. However for the larger porcine heart which has more structural and functional similarities to the human heart, micro-CT is unable to capture whole-heart geometry due to size limitations. Recent advancements in cryomicrotome imaging has allowed for the imaging of whole-heart arterial vascular networks in larger animals including pigs and canines with a resolution of 25μm (van Horssen *et al.* , 2010; van den Wijngaard *et al.* , 2013; van Horssen *et al.* , 2014). The method can separately image fluorescent cast embedded in the vasculature and fluorescent microspheres deposited in microvessels using appropriate combinations of excitation and emission filters. Such data has been used to identify compartmentalisation of vascular territories in the pig heart (Spaan *et al.* , 2005), the development of collaterals both in the ischemic borderzone and in distant vascular territories after ischemia in pigs (van den Wijngaard, 2011), and the transmural organisation of vascular crowns stemming from the epicardium in canines (van Horssen *et al.* , 2014).

*A 'crown' refers to all of the downstream vessels supplied by a 'stem' vessel.

A wide range of approaches for segmenting the coronary vasculature from micro-CT, cryomicrotome images and other imaging modalities has been proposed for the purposes of analysing vascular structure and simulating blood flow (Nordsletten *et al.* , 2006; Lee *et al.* , 2007; Lesage *et al.* , 2009; van den Wijngaard *et al.* , 2013; Goyal *et al.* , 2013). Methods generally follow a pipeline of pre-processing images to filter out noise with gradient or morphological filters, followed by vessel tracking with active contour or region growing approaches, often followed by vessel skeletonisation and radius estimation to represent a vascular network topology as a geometric model (Lesage *et al.* , 2009). Many different approaches have been proposed based on characteristics of the different imaging modalities with which vascular anatomy is imaged.

Reconstructed vascular topologies have been used for a range of modeling studies. One study used a Poiseuille flow simulation performed with segmented whole-organ vasculature to compare to the distribution of microspheres (Marxen *et al.* , 2006), revealing the difficulties in prescribing accurate terminal boundary conditions for the model to accurately reproduce regional perfusion. Anatomical whole-heart vascular structure has also formed the basis for recent advancements in porous perfusion modeling involving the parameterisation of a continuum multi-compartment Darcy perfusion model for whole heart flow simulations (Hyde *et al.* , 2013a). Simulation of time-dependent coronary blood flow and non-Newtonian rheology using a 1D flow model with considerations of varying viscosity (Pries & Secomb, 2005) in a reconstructed rat coronary network demonstrated a self-stabilising effect of varying vessel hematocrit (Lee & Smith, 2008). When coupled with contractile myocardial mechanics, computational models of flow have provided a means for investigating the effects of "cross-talk", the interaction of myocardial contraction and coronary network blood flow (Smith, 2004). More recently a poro-mechanical model incorporating myocardial mechanics and perfusion has been coupled with a 1D Navier-Stokes model of blood flow in the coronary vessels to investigate the etiology of coronary waves (Lee *et al.* , 2014).

In this chapter we present the reconstruction of a topological network of the left

coronary arterial circulation from cryomicrotome imaging data of a porcine heart, provided by collaborators at the AMC, The Netherlands[†] (van Horssen *et al.* , 2010). The processing steps presented in this chapter are based on the workflow presented in (Goyal *et al.* , 2013), although unique challenges related to the specific dataset and chosen methodologies are explored in greater depth. The presented pipeline is a step towards automatic whole-heart vascular model reconstruction, although currently several steps of the process require manual interaction.

The reconstructed left coronary artery network is used in Chapter 4 to perform a Poiseuille simulation, reflecting the non-beating state of the *ex vivo* Langendorff pig heart from which images were acquired (Schuster *et al.* , 2010), for comparison to the distribution of microspheres. In Chapter 5 the flow model is compared to the distribution of microspheres throughout the LCA network to determine the prevalence and location of microsphere skimming. For the purposes of comparing a flow model in the LCA network to microspheres, certain requirements should be met by the reconstructed network. It has been suggested that approximately 400 microspheres need to arrive in a region of tissue for 95% confidence that the flow measurement is within 10% of the true flow (Buckberg *et al.* , 1971). Thus, since approximately 100,000 microspheres were injected into the LCA an approximation can be made to the number of vessels through which at least 400 microspheres pass. Assuming that the network is dichotomously branching and that microspheres are split evenly at each junction, there should be approximately 250 unique vessel paths through which 400 microspheres pass. A crown with 250 terminal vessels corresponds to the 500 largest vessel segments in the coronary circulation, in which phase separation can be analyzed with 95% confidence that the microsphere-derived flow is within 10% of the true flow. It is in these 500 largest vessels that accurate reconstruction of vessel geometric properties (radii, lengths, branching angles) is most important. In vessels further downstream (through which fewer and fewer microspheres pass), there is greater error in a comparison between model flow and microsphere-derived flow due to the high statistical variability associated with low microsphere counts. However, the spatial distribution of these small ves-

[†]Department of Biomedical Engineering and Physics, Academic Medical Center, University of Amsterdam, Amsterdam, The Netherlands

sels is important for the correct demarcation of perfusion territories and hence the determination of tissue volume and number of microspheres assigned to upstream vessels used in the particle skimming analysis.

3.2 Methods

The network of a porcine coronary LCA was reconstructed from a CMT image stack with x, y, z dimensions of $1875 \times 1875 \times 1280$ and $64\mu m$ isotropic voxel size. The image stack had been pre-processed with deconvolution using the point spread function of the imaging system to reduce blurring effects of the vascular cast (see van Horssen *et al.* , 2010, for details). As outlined above, the pipeline described in this section for the reconstruction of a 3D vascular network consisting of 1D vessel segments from CMT imaging data is based on (Goyal *et al.* , 2013). The updated pipeline applied in this study is shown in Figure 3.1, with several changes employed to improve the efficiency of the code and accuracy of the reconstruction. Specifically manual adjustment of network reconstruction parameters were required at stages of image thresholding (step (b)), and connected component selection (step (c)); a simple method for calculating mean vessel segment radius was introduced for Poiseuille simulations (part of step (e)); and an iterative vascular pruning algorithm was introduced for removing false vessels (in step (f)).

3.2.1 Frangi Filtering

The first step in the pipeline involved applying the Frangi 'vesselness' filter to distinguish vessel-like structures in the 3D image stacks from globular structures or noise. The code used was a Matlab mex implementation by Dirk-Jan Kroon, available on Matlab Central[‡]. The Frangi filter involves the assessment of the eigenvalues of a second-order directional derivative (the Hessian $\mathcal{H}$) filter applied

[‡]Hessian based Frangi Vesselness Filter website:
http://www.mathworks.co.uk/matlabcentral/fileexchange/24409-hessian-based-frangi-vesselness-filter

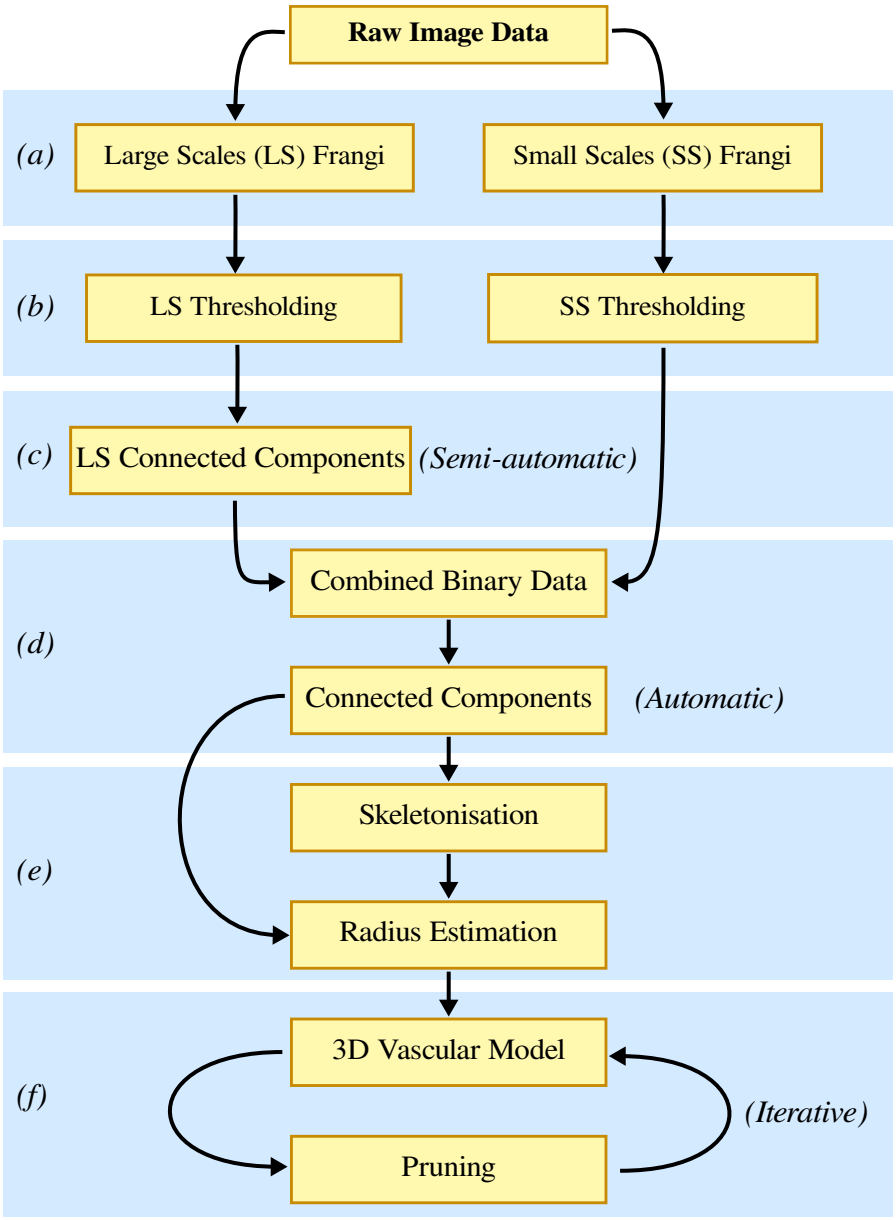

Figure 3.1: Vascular network reconstruction pipeline.

to the image L (see Frangi *et al.* , 1998, for full details). The Hessian of an image L centred at $\mathbf{x}_0$ with scale s is

$$\delta\mathbf{x_0}^T\mathcal{H}_{0,s}\delta\mathbf{x_0} = \left(\frac{\partial}{\partial\delta\mathbf{x_0}}\right)\left(\frac{\partial}{\partial\delta\mathbf{x_0}}\right)L(\mathbf{x}_0, s) \tag{3.1}$$

where the differentiation of L is given as a convolution with the (second-order) derivative of a Gaussian (see Frangi *et al.* , 1998). The scale s defines the size of the probe kernel produced from the second-order derivative of a Gaussian at scale s, which in the case of 3D image data corresponds to a voxel range $(-s, s)$ in each coordinate direction x, y and z. Eigenvalue analysis of the Hessian yields the k^{th} (normalised) eigenvector $\hat{\mathbf{u}}_{s,k}$ and corresponding eigenvalue $\lambda_{s,k}$ according to,

$$\hat{\mathbf{u}}_{s,k}^T\mathcal{H}_{0,s}\hat{\mathbf{u}}_{s,k} = \lambda_{s,k}. \tag{3.2}$$

The first three eigenvalues at scale s, $\lambda_{s,1}$, $\lambda_{s,2}$, $\lambda_{s,3}$ (ordered from smallest to largest), in an ideal tubular structure will satisfy the following relations

$$|\lambda_1| \approx 0, \tag{3.3}$$

$$|\lambda_1| \ll |\lambda_2|, \tag{3.4}$$

$$|\lambda_2| \approx |\lambda_3|. \tag{3.5}$$

These conditions can be explained intuitively. The three eigenvectors $\hat{\mathbf{u}}_{s,1}$, $\hat{\mathbf{u}}_{s,2}$, $\hat{\mathbf{u}}_{s,3}$ are orthogonal to each other, and the largest eigenvalue corresponds to the eigenvector which points in the direction of the greatest change in the gradient of voxel intensity. A vessel structure in the CMT images typically has a flattened cross-sectional Gaussian intensity profile, with maximum intensity in the centre transitioning to zero at the outer edges of the vessel wall. Voxel intensity along the long-axis of the vessel is approximately constant. Thus λ_1 corresponds to the eigenvector of the Hessian which points along the longitudinal axis of the vessel, while λ_2 and λ_3 define the magnitudes of the eigenvectors pointing from the centre in orthogonal radial directions towards the vessel wall.

A vesselness function is constructed from two geometric ratios, $\mathcal{R}_\mathcal{A}$ and $\mathcal{R}_\mathcal{B}$, and

a measure of "second-order structureness", $\mathcal{S}$, where

$$\mathcal{R}_{\mathcal{A}} = \frac{|\lambda_2|}{|\lambda_3|} \tag{3.6}$$

$$\mathcal{R}_{\mathcal{B}} = \frac{|\lambda_1|}{\sqrt{|\lambda_2 \lambda_3|}} \tag{3.7}$$

$$\mathcal{S} = \|\mathcal{H}\|_F = \sqrt{\sum_{j \leq D} \lambda_j^2} \tag{3.8}$$

$\mathcal{R}_{\mathcal{A}}$ distinguishes between plate-like and line-like structures by comparing the magnitude of the larger 2 eigenvalues, which is close to one for a line-like structure. $\mathcal{R}_{\mathcal{B}}$ determines how blob-like a structure is, reaching its maximum value when a structure is most blob-like. $\mathcal{S}$ determines whether the part of the image in question is part of the background (when its value is low) or part of a physical structure (when its value is high). The vesselness function is given by

$$\mathcal{V}_0(s) = \begin{cases} 0 & \text{if } \lambda_2 > 0 \text{ or } \lambda_3 > 0, \\ \left(1 - \exp\left(-\frac{\mathcal{R}_{\mathcal{A}}{}^2}{2\alpha^2}\right)\right) \exp\left(-\frac{\mathcal{R}_{\mathcal{B}}{}^2}{2\beta^2}\right) \left(1 - \exp\left(-\frac{\mathcal{S}^2}{2c^2}\right)\right) & \text{otherwise} \end{cases} \tag{3.9}$$

The first row indicates $\mathcal{V}_0(s) = 0$ when $\lambda_2 > 0$ or $\lambda_3 > 0$ since these values indicate a structure composed of background voxels, as opposed to a bright structure where $\lambda_2 < 0$ and $\lambda_3 < 0$. The weights α, β and c are set to 0.5 as this has been shown to produce reasonable results (Frangi *et al.* , 1998). The multiplicative form of Equation (3.9) ensures that $\mathcal{V}_0$ is only large when all three criteria are well satisfied. The output images $\mathcal{V}_0(s)$ contain voxel intensities that reflect the probability-like estimates of vessel structures. Another important feature of this function is that $\mathcal{V}_0$ is scale invariant, and will be maximum at scale s when a vessel-like structure of similar radius to s is detected. Finally vesselness measures applied to image L at different scales s can be combined as

$$\mathcal{V}_0(\gamma) = \max_{s_{min} \leq s \leq s_{max}} \mathcal{V}_0(s, \gamma) \tag{3.10}$$

The whole-heart vascular image stack was processed with two sets of scales, small

scales $\mathbf{s}_s$ and large scales $\mathbf{s}_l$, corresponding to step (a) in Figure 3.1,

$$\mathbf{s}_s = [1,\ 1.2,\ \ldots\ 1.8,\ 2] \tag{3.11}$$

$$\mathbf{s}_l = [3,\ 4,\ \ldots\ 39,\ 40] \tag{3.12}$$

The smallest scale in s_s of 1 (voxel) corresponds to the smallest radius identifiable in the images, i.e. $64\mu m$. The largest scale of 40 (voxels) corresponds to approximately the largest vessel in the dataset at the root of the LCA network, approximately $2.5mm$. The purpose of the separation into two sets of scales was to remove regions of cast leakage which were detected in the filtered large scale images, but physically were only connected to the coronary network through the small terminal vessels, detected in the filtered small scale images. Thus after large scale filtering (step (a) in Figure 3.1) and thresholding (b), a connected components analysis (c) allowed for the separation of the true coronary network from the leaked cast in the large scale vessels. This is illustrated with a series of maximum intensity projections (MIPs) of the large scale vessels in Figure 3.4.

3.2.2 Thresholding and Connected Component Selection

Since the Frangi filter produces output images with intensities that are scale-invariant, a manual voxel intensity threshold was determined by trial and error to binarise both the large scale and the small scale images in order to retain true vessel structures (step (b) in Figure 3.1). A common false vessel structure was manifested as 'rings' detected with the small scale filtering and appearing around the circumference of large vessels (e.g. 10+ voxel diameter). This was due to voxel saturation in the larger vessels such that the vessel cross-sectional profile had a steep drop-off from maximum voxel intensity to zero within just a few voxels near the vessel wall. Small scale filtering in this region produced noticeable rings in $\mathcal{V}_0$, but the intensity of $\mathcal{V}_0$ in these regions was still lower than true vessels at the same scales. Hence a manual threshold for the small scales was chosen to remove the false 'rings' from the segmentation while retaining visibly real vessels.

Step (c) in Figure 3.1 not only allowed for regions of leakage to be removed from the large scale vessel binary, but also identified major subnetworks in the vasculature which were disconnected from the largest connected component tree of the LCA. The cast filling these subnetworks was not continuous with the cast in the main network due to an apparent clipping of the vascular tree at the base of the image stack. After thresholding and retaining relevant connected components of the large scale vessels, the binaries of the small and large scale vessels were combined into a single image stack. The single largest connected component from the combined binary image was then retained (step (d)), removing noise and small disconnected vessels from the resulting network.

3.2.3 Skeletonisation and Radius Estimation

After thresholding, in step (e) of the pipeline of Figure 3.1 binary thinning was applied to obtain the vessel centre-lines. The code used for skeletonisation was the Skeletonize3D plugin implemented in FIJI[§] and involves iterative symmetric erosion of binary structures to their centre-lines using a decision tree method (Lee *et al.* , 1994). The connectivity (or degree[¶]) of centre-line voxels was then determined to be either (i) an endpoint (degree = 1), (ii) a junction (degree $\geq$ 3), or (iii) a mid-point (degree = 2). Each physical vessel segment was then represented by a node chain: the vessel's centre-line voxels consisting of mid-point voxels between a junction-endpoint voxel pair, or between a junction-junction voxel pair. The connectivity of each vessel to upstream/downstream vessels in the network was then determined based on which vessels shared each junction node.

Radius was estimated using the local thickness plugin (Dougherty & Kunzelmann, 2007) in FIJI, which operates by fitting a sphere around each voxel such that it is completely enclosed within non-zero voxels (Hildebrand & Rüegsegger, 1997). At each centre-line voxel in the skeleton network the local thickness was computed from the binary of the combined vessel scales.

[§]FIJI is an open-source image processing toolbox described in (Schindelin *et al.* , 2012)
[¶]Degree refers to the number of vessel segments connected at a node.

3.2.4 3D Vascular Model and Pruning

A network with linear 1D representations of each vessel segment was produced in step (f), where radius, r, and spatial coordinates, $[x\ y\ z]$, were linearly interpolated between the start and end node of each vessel segment, corresponding to values at the first and last node of each node chain. This representation was used for visualisation purposes. To perform a Poiseuille flow simulation with the network (see Chapter 4), a single radius value was required for each vessel segment. This value was chosen to be the mean radius computed from nodes in each vessel segment's node chain, excluding radius measurements at the nodes lying within one radius of the parent node, as illustrated in Figure 3.2.

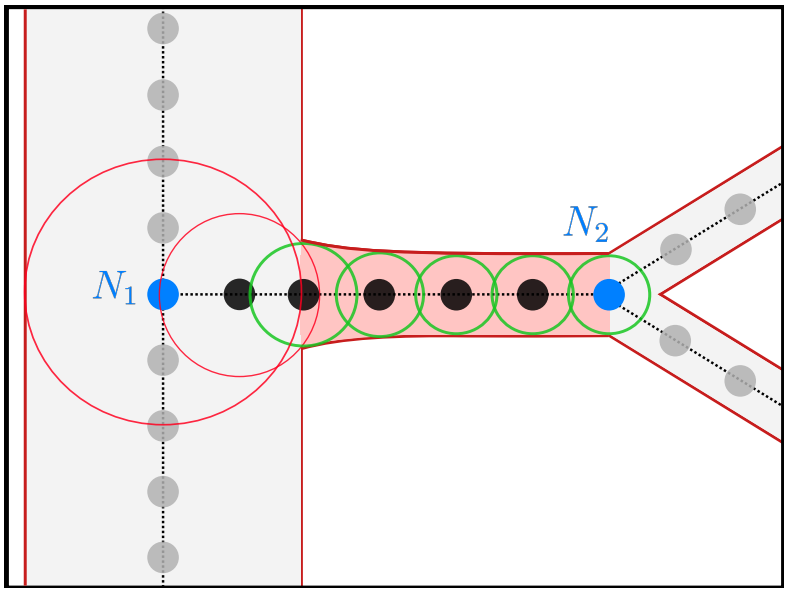

Figure 3.2: Calculation of mean radius in a side-branch in a 2D representation. The dashed black lines represent the centre-lines of each vessel segment. The smaller, filled circles represent the node chain voxel centre-points, emboldened for the side-branch with parent and daughter junction nodes marked N_1 and N_2 respectively. The rings around each node represent the local thickness measure, where green rings are those used to compute the mean radius for the side-branch.

From this start-and-end node representation of each vessel segment, spurious branches and loops were removed from the network based on geometric considerations. The criteria determined for the removal of spurious branches was determined after trial and error of criteria values and visual assessment of the resulting

vascular network. The criteria listed below are applied to each vessel segment, containing a start and end node each with a radius estimated as depicted in Figure 3.2.

Spurious Branch Pruning Criteria

1. One of the vessel segment's nodes was (degree = 1) (ie. a terminal vessel),
2. if either
   (a) radius at either vessel node was more than twice that of the other node *and* radius of either node was greater than 4 voxels (0.256mm),
   (b) vessel length was less than vessel diameter *and* radius of either node was greater than 4 voxels (0.256mm),
   (c) radius at both nodes was greater than 5 voxels (0.32mm).

These criteria were chosen to target clearly visible vessel 'stubs' stemming from the larger diameter vessels, while avoiding the removal of small-scale vessels. This form of pruning was important for the allocation of terminal vessel fed-volumes which was radius-dependent, as explained in Chapter 4. The resolution of the CMT images was $64\mu m$ in each dimension. This was the smallest discernible vessel radius, and also the expected radius of all terminal vessels in the network if (1) the vascular cast reached the same depth of the vasculature (beyond the image resolution) throughout the heart, and (2) the reconstruction algorithm captures all of these vessels accurately.

Cycles (or loops[‖]) in the network were removed since almost no collaterals are assumed to be present in healthy pig hearts (van den Wijngaard, 2011), meaning detected loops were assumed to be artifacts of the reconstruction process. Loops were identified and discarded using Dijkstra's algorithm to find the path of least resistance between each terminal node and the root node of the network. Poiseuille resistance without unnecessary constants, R_w, provided the edge weights,

[‖]A loop occurs when there is a non-unique path between node A and node B in the network.

$$R_w = \frac{L}{r^4}. \tag{3.13}$$

Thus for multiple paths between each terminal node and the root node of the network, vessel segments corresponding uniquely to higher resistance vessel paths were discarded. Figure 3.3 illustrates the nested iterative pruning process for discarding spurious branches and loops from the network.

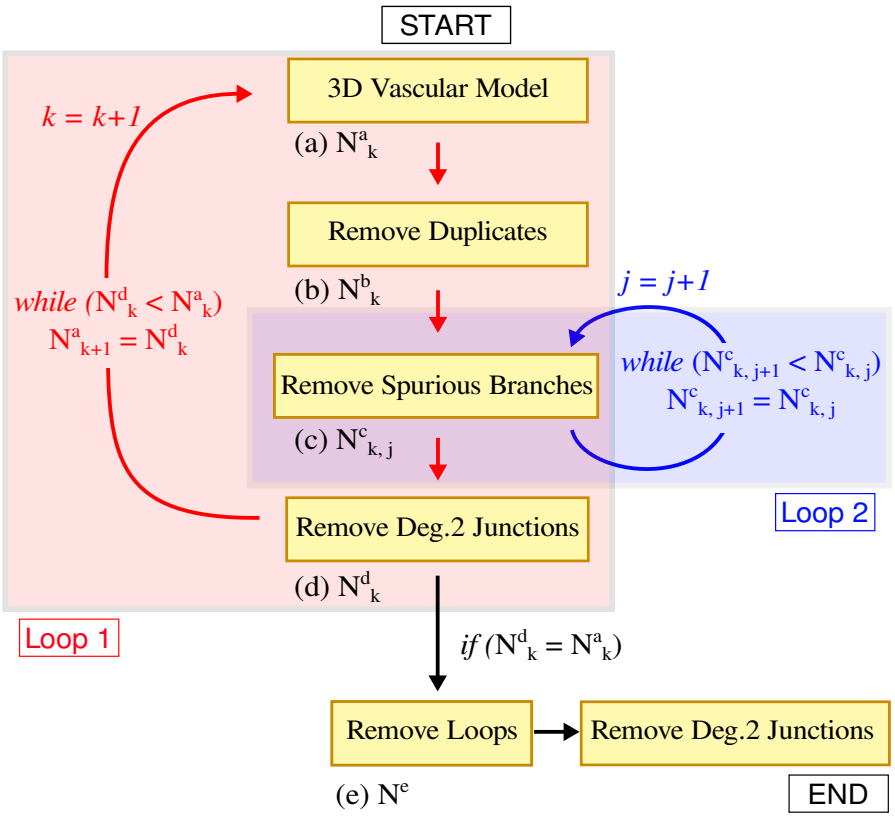

Figure 3.3: Iterative pruning algorithm schematic. The input is the 3D vascular model at (a) with N_k^a vessel segments at iteration $k = 1$. Duplicate segments (two or more segments which share the same start and end nodes) are reduced to just one segment leaving N_k^b vessel segments at (b). Spurious branches are pruned in a nested iterative loop (loop 2), removing a maximum of one spurious branch along each terminal-to-root vessel path per iteration j, leaving $N_{k,j}^c$ vessel segments at (c). Then any vessel segments connected by (degree = 2) junction nodes are combined to form a single vessel segment (d), leaving N_k^d segments. This entire process from steps (a) to (d) is repeated (loop 1) until no further segments are removed from the 3D vascular model. Finally false collateral vessels (or loops) are removed from the network at (e) leaving N^e vessel segments, and any resulting (degree = 2) junctions are removed.

3.3 Results

3.3.1 Large Vessel Processing

Whole heart maximum intensity projections (MIPs) show the result of large scale filtering (step (a)), followed by binarisation (step (b)) and connected component selection (step (c)) in Figure 3.4. The three largest connected components were retained after visual inspection as comprising three valid subtrees which were disconnected due to absence of cast in the most basal slices of the image stack. All three subtrees appeared to lie along the path of a single vessel extending along the base of the heart as part of the LCx artery. This vessel was therefore manually recreated with care to match the diameter of upstream and downstream vessels connected to it. The blob-like structures of leaked cast in Figure 3.4(b) are clearly removed after the connected component selection in Figure 3.4(c).

3.3.2 Small Vessel Processing

MIPs in Figure 3.5 illustrate the result of small scale filtering (step (a)) and thresholding (step (b)), as well as combining this with the large scale binary image stack and selection of the single largest connected component (step (d)). A considerable number of small vessels were discarded between images in Figure 3.5(c) and 3.5(d) which is addressed in the Discussion.

3.3.3 Skeletonisation and Radius Estimation

MIPs in Figure 3.6 show the output images of skeletonisation and radius estimation. The reconstructed 3D network of linear 1D vessel segments is also shown, viewed along each image coordinate axis in the same way the MIPs were created.

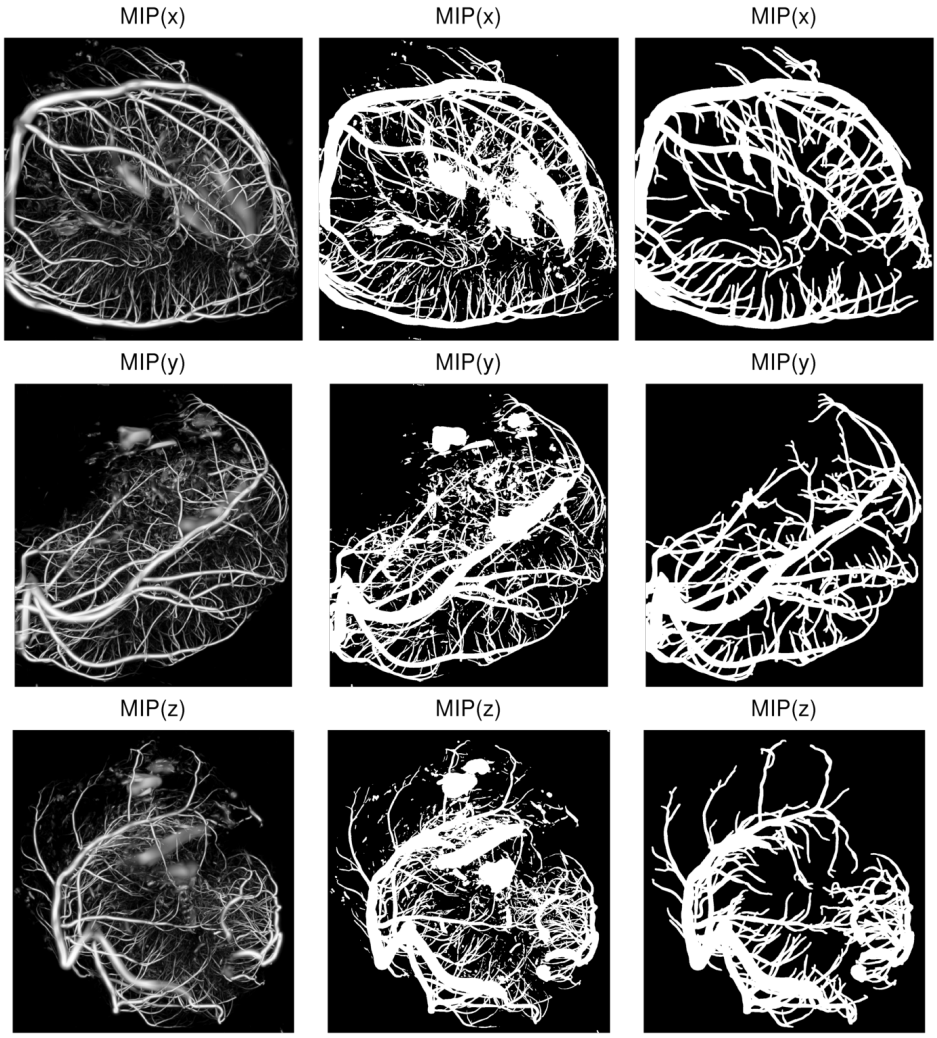

Figure 3.4: MIPs are shown in the x direction (top row), y direction (middle row) and z direction (bottom row) of large scale combined vesselness filtering (a), thresholding (b), and the three largest connected components (c).

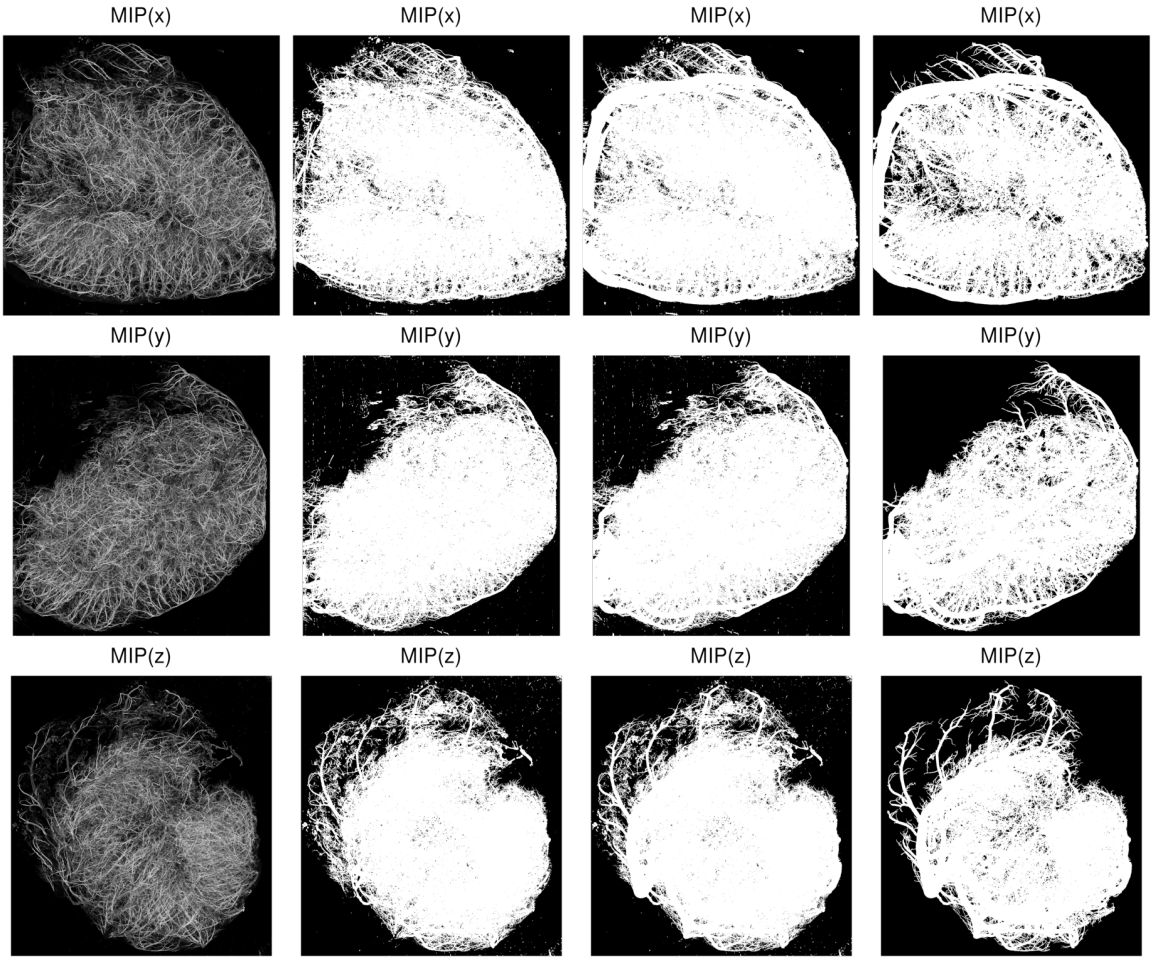

Figure 3.5: MIPs are shown in the x direction (top row), y direction (middle row) and z direction (bottom row) of small scales combined vesselness filtering output (a), thresholded small scale vessels (b), combination with large scales binary (c), and the single largest connected component (d).

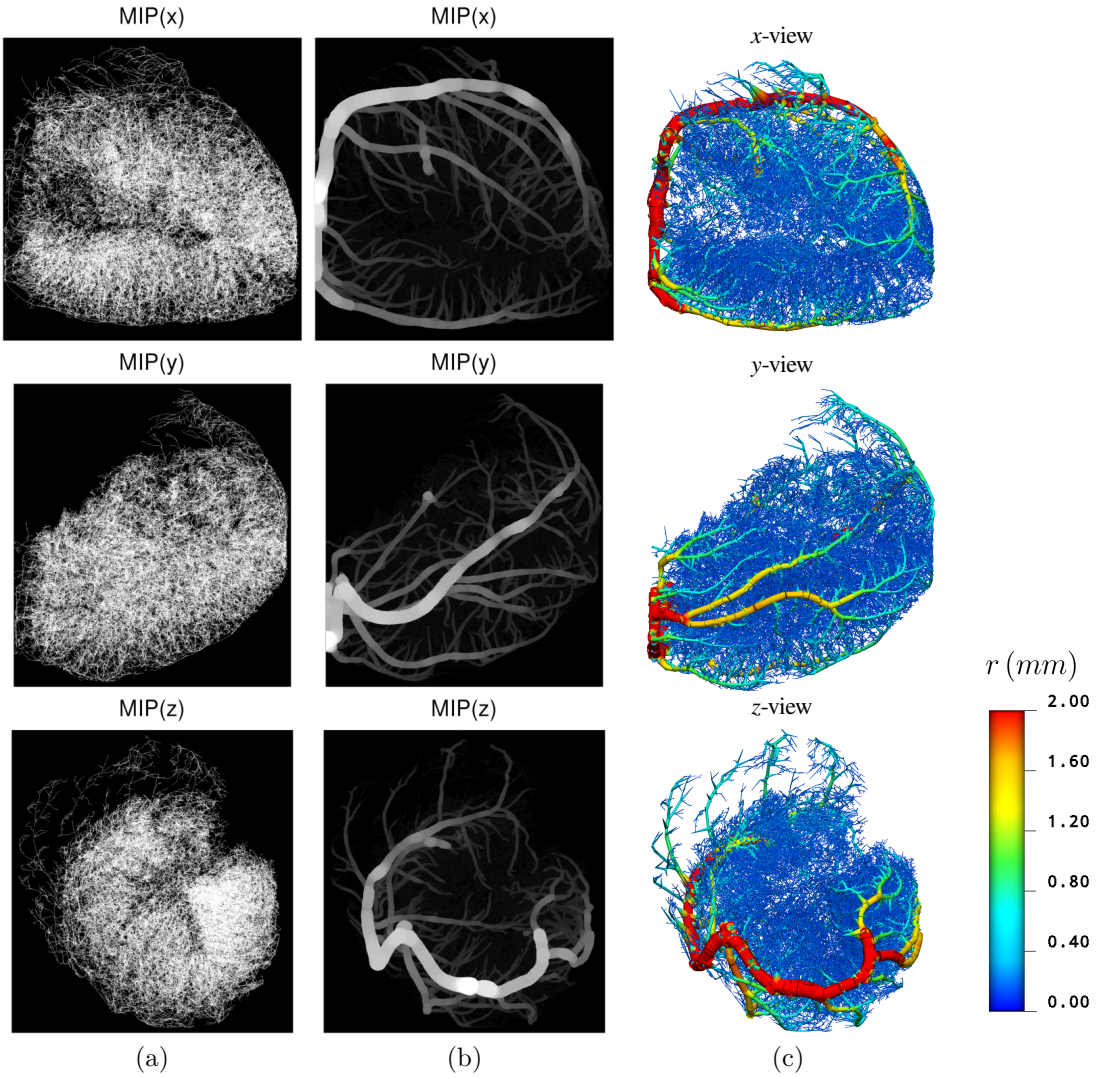

Figure 3.6: MIPs are shown in the x direction (top row), y direction (middle row) and z direction (bottom row) of the skeletonized network (a), local thickness-based intensity (b), and the reconstructed 3D vascular tree colour-coded by radius (c).

3.3.4 Pruning and 3D Model

Close-ups of two regions in the 3D network are shown in Figure 3.8 to illustrate the effects of the iterative pruning algorithm. Obvious spurious branches, or 'stubs', (green vessels) were removed after the first iteration of pruning of spurious branches (the result of step (c) in Figure 3.3), but before joining segments connected by (degree = 2) junctions (grey vessels) corresponding to the result of step (d) in Figure 3.3. After iterative pruning loops (or cycles) in the network were removed, resulting in the final network shown in red in Figure 3.8. A total of 1660 spurious vessel segments and 3316 vessel segments associated with loops were removed. Pruning was completed after 2 iterations of loop 1, within which there were 5 and 3 iterations of loop 2 respectively (see Figure 3.3). The vast majority of the segments associated with loops in the network were found in the microcirculation, with examples shown in Figure **??**.

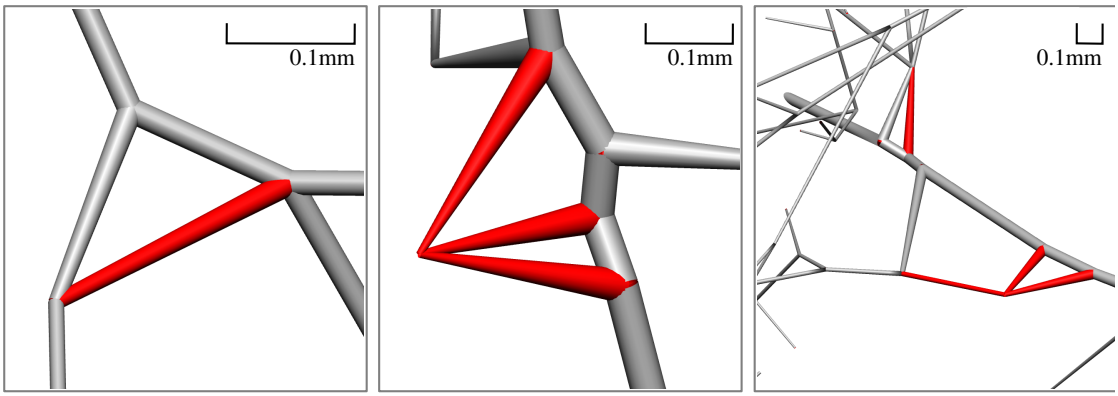

Figure 3.7: Examples of vessel segments associated with loops (red) in the network. Note that vessel radius has been scaled to 10% of the measured radius for clarity, but the distance scale refers to the unchanged spatial coordinates.

3.3.5 Vascular Network Statistics

The final pruned 3D vascular network contained 97,500 vessel segments of which 51,836 were terminal vessels. Of the 96,914 nodes in the network, 45,078 were junction nodes whose connectivities are listed in Table 3.1 with their respective percentage of the total. Note that junctions with (degree = 3) correspond to bifurcations, (degree = 4) to trifurcations, and so on. Junctions with connectivity

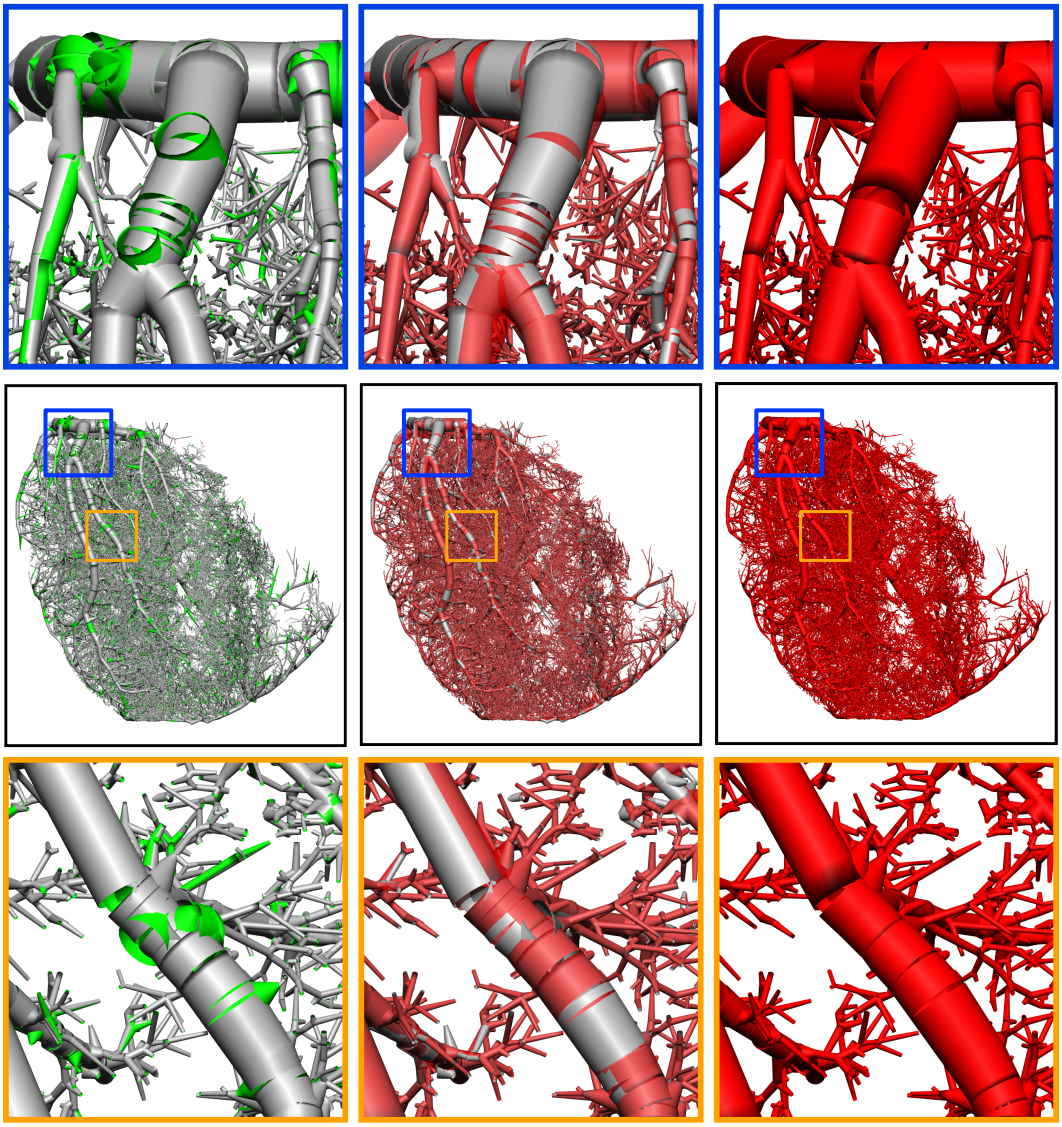

Figure 3.8: Iterative network pruning results - the middle row shows a posterior view of the LCA network with two boxed regions, a basal region (blue box) corresponding to the close-up in the top row and an LCX sub-branch (orange box) corresponding to the close-up in the bottom row. The first column compares the initial unpruned network (green vessels) and after the first pruning operation of spurious branch removal (grey vessels). The second column compares the first pruning operation (grey) with the final iteration of pruning (transparent red vessels), with just the final network shown in the third column. (Note that vessels appear sparse in the top and bottom rows because vessels further from the foreground are hidden for clarity.)

as high as (degree = 9) were detected from the vascular cast, and an unexpectedly high percentage of junctions had a connectivity of (degree ≥ 4).

Table 3.1: Post-pruning network junction connectivity.

Degree	Number of Junctions	Percentage of total, %
3	39261	87.1
4	5003	11.1
5	704	1.6
6	98	0.2
7	10	0.02
8	1	0.002
9	1	0.002

Van Bavel and Spaan examined relationships between several geometric parameters in two porcine coronary networks (Van Bavel & Spaan, 1992). These included the parent-to-daughter diameter ratio at bifurcations (comparing parent vessel diameter, D_p, to the larger, D_L, and smaller, D_S, daughter vessel diameters), area expansion ratio A and symmetry ratio S, defined by

$$A = \frac{D_L^2 + D_S^2}{D_p^2}, \tag{3.14}$$

$$S = \frac{D_S}{D_L}. \tag{3.15}$$

The area expansion ratio A represents whether the cross-sectional area increases or decreases from a parent vessel to its daughter vessels, and the symmetry ratio S the diameter ratio of the smaller and larger daughter vessel radii. Parent-to-daughter diameter comparisons show similar characteristics in the 39,261 bifurcations of the reconstructed LCA compared to Van Bavel's results, as depicted in Figure 3.9. Large daughter diameter is much closer to parent diameter than small daughter diameter and shows less variance. Furthermore, daughter diameters are almost always lower than parent vessel diameter, and there is increasing variance towards

smaller vessel diameters. Quantization of smaller vessel diameters is evident, reflecting the effects of the radius estimation method and lack of accuracy in the smaller vessels.

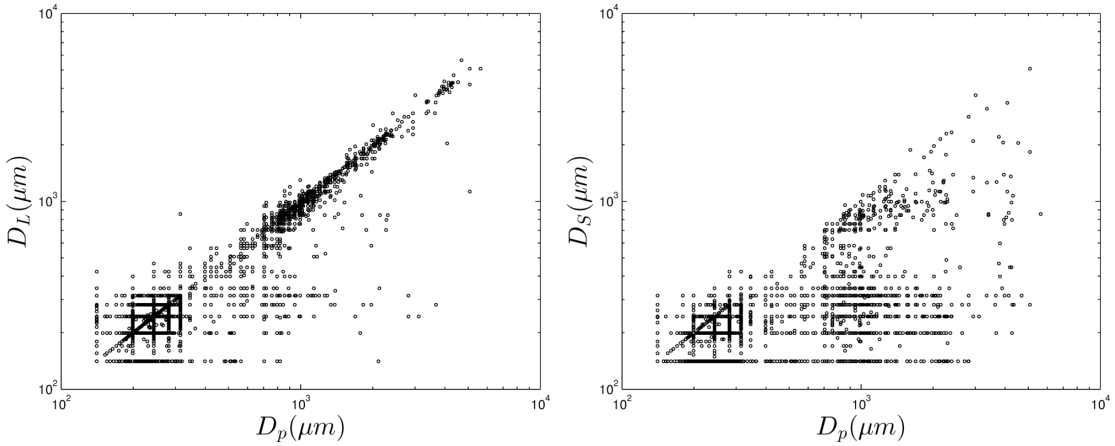

Figure 3.9: A comparison of large daughter diameter with parent diameter (a), and small daughter diameter with parent diameter (b) at 39,261 bifurcations.

Figure 3.10 compares the diameter ratios of D_S/D_p and D_L/D_p, indicating a clustering of bifurcations where the area expansion ratio $A = 1$, similar to Van Bavel's results (see Van Bavel & Spaan, 1992). A far larger degree of scatter is present in this data however due to limitations of radius estimation in the smaller vessels.

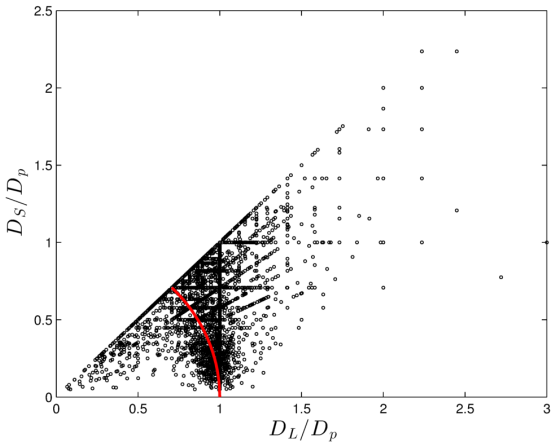

Figure 3.10: A comparison of parent-to-daughter ratios of the large (x-axis) and small (y-axis) daughter diameters with parent diameter. The red line marks an area expansion ratio $A = 1$.

From the 39,261 bifurcations in the reconstructed LCA, the mean±1SD values were $A = 1.47 \pm 0.56$, and $S = 0.80 \pm 0.21$. Van Bavel's measurements taken from 1,663 bifurcations from two porcine hearts (with a diameter range of approximately $10\mu m$ to $4 \times 10^3 \mu m$) yielded both lower area expansion and symmetry ratios with $A = 1.12 \pm 0.30$ and $S = 0.51 \pm 0.24$. The microvasculature was not represented in its entirety but was instead sampled in their study since vessel segments needed to be examined individually with an inverted microscope; therefore the higher generation (larger) vessels had a disproportianate weighting on their computed mean values of A and S. Furthermore as shown in Figure 3.11, A and S vary with parent vessel diameter, both decreasing with larger parent vessel diameter.

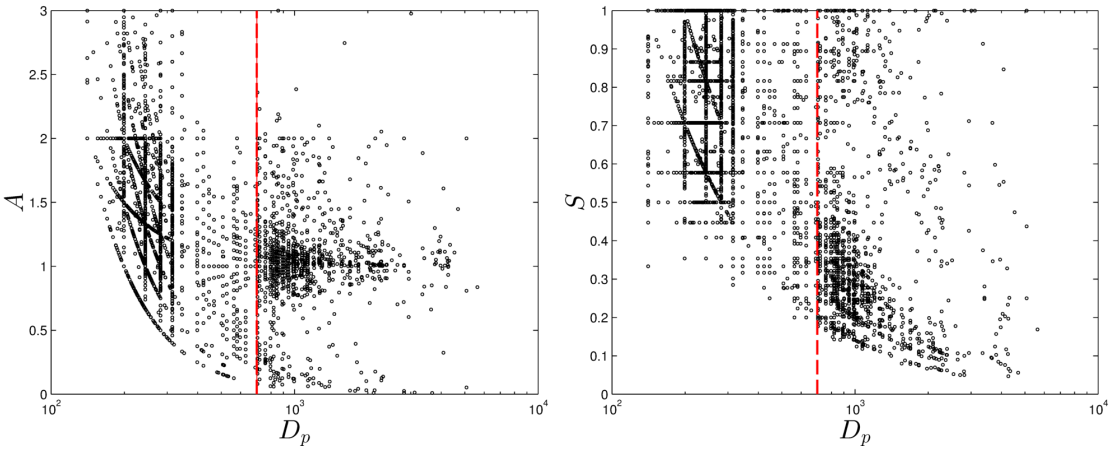

(a) (b)

Figure 3.11: Area expansion ratio A (a) and symmetry ratio S (b) as a function of parent diameter. The vertical red line marks a parent vessel diameter of 10 voxels, or equivalently $640\mu m$.

Approximately a 1 voxel error is expected in the estimation of vessel diameter using the local thickness measure since it is applied to a vessel binary and thus does not take into account cast signal drop-off at vessel walls. For a diameter measurement error no less than 10%, only vessels with a 10+ voxel diameter should be considered. Taking only bifurcations with a parent vessel diameter $D_p \geq 10$ voxels leaves 2,087 bifurcations, from which the computation of A and S are significantly lower than with all bifurcations, at $A = 1.05 \pm 0.37$ and $S = 0.38 \pm 0.23$. The vasculature highlighted in Figure 3.12 shows that these vessels make up mainly

epicardial and transmural conduit arteries. The value of A is much closer to that computed by Van Bavel, although S is considerably lower. This is a reflection of the fact that the epicardial arteries have many smaller branches stemming off in a transmural direction, resulting in greater asymmetry in daughter vessel diameters.

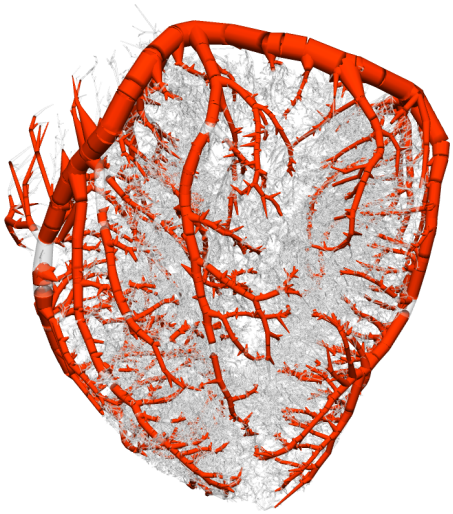

Figure 3.12: Vessels highlighted in red connected to bifurcations with 10+ voxel diameter parent vessels, from which $A = 1.05 \pm 0.37$ and $S = 0.38 \pm 0.23$ are computed. These bifurcations largely constitute epicardial and transmural conduit vessels.

3.4 Discussion

A 3D left coronary arterial network was successfully reconstructed from cryomicrotome image data down to terminal vessel segments with a radius of $64\mu m$. Several unexpected results highlight limitations in the reconstruction pipeline as well as in the data. First there were more than expected high connectivity junctions as shown in Table 3.1, with 11.1% trifurcations, and quadfurcations making up just under 1.6%. This is compared to Kassab's findings where 98% of junctions in the porcine coronary arterial circulation are bifurcations (Kassab *et al.* , 1993). Junctions with a degree of 8 or 9 were inspected and found to be connected with 7 and 8 terminating vessels respectively. Visualising the original image data at the location of these junctions revealed apparent micro-leakages of the cast. The degree 8

and 9 junctions were therefore removed from the network. The number of remaining 'high connectivity' junctions with (degree ≥ 4) were too numerous to inspect visually, so the number of terminal vessels connected to each of the remaining junctions was inspected instead. Unlike the degree 8 and 9 vessels, the majority of the remaining 'high connectivity' junctions supplied further downstream vessel subtrees, consisting of at least one further downstream junction. For the purposes of the study in Chapter 4 the 13% of 'high connectivity' junctions are not considered to affect the simulations and resulting conclusions as these junctions mostly occur in the microvasculature, which is used primarily to define the tissue volume subtended by upstream vasculature. Specifically, 90% of all (degree ≥ 4) junctions have a parent vessel radius of < 0.2mm, at which size the average number of microspheres passing through a junction is just 40 (see Chapter 4 for further details). In future an analysis of the source of these high connectivity vessels should be undertaken for studies which require greater accuracy in the microvasculature.

By retaining just the single largest connected component of the combined large and small scales binary network, numerous small scale vessel segments (as well as noise) were discarded from the final reconstructed network. This was due to a feature of the Frangi filter output where vessel junctions, due to their low vesselness, are typically suppressed in the output. To determine the number of vessels discarded, connected components consisting of 20 or more voxels which were disconnected from the retained LCA network (in step (d) of the pipeline in Figure 3.1) were counted. A total of 84,687 vessels made up these missing subtrees with a total intravascular volume of 1.12ml, which as a fraction of the 6.07ml intravascular volume (97,500 vessels) of the reconstructed LCA network is 18%. Figure 3.13 shows a cross-section of the mid-cavity with vasculature from 200 images superimposed on a cryomicrotome image of the vascular cast. The locations of the missing subtrees are diffuse throughout the myocardium, with some subtrees clearly a result of noise and other subtrees clearly produced by disconnections at suppressed vascular junctions (see Figure 3.13 caption). This issue may be resolved in future by testing recently proposed methods which combine the gradient filters (like the Frangi filter) to detect tubular objects with a morphological filter to enhance junctions (Tankyevych & Talbot, 2009; Verdú-Monedero *et al.* , 2009).

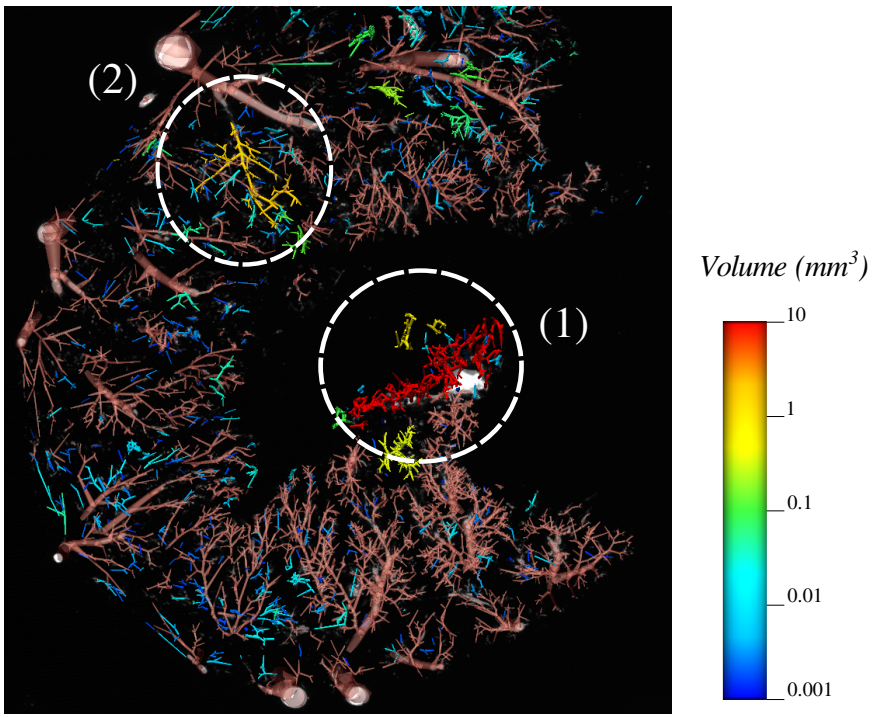

Figure 3.13: Missing subtrees colour-coded according to volume in a short-axis view of the LV consisting of 200 image slices, superimposed on a cryomicrotome image of the vascular cast. The translucent mauve vessels correspond to the pruned LCA network. The apparent red vessel subtree (1) in the centre of the LV corresponds to a region of leaked cast, as opposed to the orange subtree (2) which represents true vessels in the cast images disconnected from an upstream branch above it.

While the loss of smaller vessel subtrees is undesired, the effect on the flow model presented in Chapter 4 is not significant, particularly in the higher vessel generations. This is because these missing small scale vessels are primarily used for the model to define a myocardial region supplied by the upstream vessels. The effect of these small missing subtrees is that the spatial boundaries of tissue regions assigned to crowns of upstream stems become less well defined. However, given that the distribution of missing subtrees appears consistent throughout the myocardium, the overall volume of myocardial tissue assigned to stems further upstream in the LCA is likely to be unchanged, since total myocardial tissue volume is constrained by a segmentation of the myocardium. The myocardial segmentation method is presented in detail in the following chapter.

The high prevalence of loops in the network reflects issues with the reconstruction algorithm mainly in the microvasculature. The smallest detected vessels have lengths of only several voxels and radii of one or two voxels, which creates difficulties at multiple steps in the reconstruction pipeline. Furthermore, cast leakage in the microvasculature manifests itself not only in the form of large 'blobs' which were removed by separately filtering large and small scales, but also as more subtle smearing of small scale vessels in the cryomicrotome images. As a result there are several small vessel subtrees which do not represent presumably the true underlying vasculature, leading to some of the high-connectivity junctions, loops, and disconnected subtrees.

Another limitation of the reconstruction process is the use of the local thickness measurement to estimate vessel radius (Hildebrand & Rüegsegger, 1997) from the combined binarised Frangi outputs. This results in quantization of radius values in the smaller vessels since there is no gradient of signal intensity in the vessel cross-section. Use of the rayburst algorithm to estimate radius at vessel centreline voxels from the original cryomicrotome images would potentially provide more accurate radius estimation (Rodriguez *et al.* , 2006), although it would be more susceptible to any noisy vessel structures in the original images, and the issue of accurately determining vessel boundaries would persist. A solution to this would be to image phantom data with the CMT, specifically tubes of known diameter filled with fluorescent cast to validate any radius estimation approach. This may in the future need to be done for each heart processed since camera settings, lighting and cast properties (including shrinkage upon polymerisation) may vary from sample to sample.

The quantization of radii using the local thickness method is not a major concern for the study in the following chapters. While accuracy in radius estimation should be improved for future studies of the smaller arteries and arterioles, the vessels with a diameter of ≥ 10 voxels (or 0.64mm) suffer from errors of approximately 10% or less (based on a 1 voxel radius estimation error from visual comparison of the radius estimation output and original images). The model proposed to sim-

ulate blood flow in the network in Chapter 4 is not heavily dependent on vessel diameter either, which is addressed in the Discussion section of Chapter 4.

Finally, there is a clear sparsity of reconstructed vessels feeding the RV myocardium compared to the LV myocardium. While it is expected that vessel density in the RV is lower than in the LV (van Horssen *et al.* , 2014), both the reconstructed vasculature and cast appeared not to reach the same depth of the microvasculature as in the LV. However, as will be shown in Chapter 4, vessel stems/crowns of the LCA supplying the RV are discarded, which reduces the error between flow and microspheres throughout the network.

3.5 Conclusion

A pipeline proposed in (Goyal *et al.* , 2013) was tuned and improved with the addition of an automated pruning algorithm and used to reconstruct the LCA network of a porcine heart from CMT image data. Several limitations in the reconstruction pipeline have been highlighted for future improvement, but the resulting vascular network reproduces similar geometric and scaling properties to those reported in literature. The reconstructed LCA network is a step towards automatically converting high-resolution images of the coronary circulation in large animals into a model representation for anatomy and flow studies.

4 | Coronary Flow Model

You uncover what is when you get rid of what isn't.
– Richard Buckminster Fuller (1895-1983)

4.1 Introduction

The cryomicrotome data used in this chapter includes both microsphere locations as well as a coronary vascular cast in the same heart from which the three-dimensional LCA vascular network was reconstructed (presented in Chapter 3). This novel set of data allows for a direct comparison between network model flow and microsphere distribution which has not previously been performed in the heart. This allows for insight to be gained into the relationship between blood flow distribution and microsphere distribution *in vivo* throughout the coronary arterial network. In this chapter a Poiseuille flow model is solved on the coronary network and is compared to flow computed from the distribution of microspheres.

A major limitation of current coronary network flow models is a lack of data for prescribing boundary conditions (BCs) at the terminal vessel outlets. Previous models of coronary flow have aimed to reproduce a physiologically accurate relation between perfusion heterogeneity and tissue volume size, represented by the fractal dimension D in the range 1.15-1.3 (see Methods section below). Perfusion is the volumetric blood flow to a tissue segment divided by the segment mass (with units $mm^3/s/g$), and is known to be heterogeneous throughout the myocardium (Bassingthwaighte *et al.* , 1989), as well as locally correlated (Van Beek *et al.* , 1989; Bassingthwaighte & Bever, 1991). The fractal dimension D

relates increasing perfusion heterogeneity with decreasing tissue segment size, as measured from distributions of microspheres and IDMI (Bassingthwaighte *et al.* , 1989, 1990). Existing coronary flow models have reproduced values of D consistent with physiological calculations from the microsphere and IDMI distributions (Mittal *et al.* , 2005; Marxen *et al.* , 2006; Huo *et al.* , 2009). Only one study to-date however has compared regional microsphere deposition with perfusion computed from a Poiseuille model solved on the vasculature in the same organ (rat kidney) (Marxen *et al.* , 2006). The results however showed that regional perfusion computed from the model and from microspheres showed no correlation, despite the model reproducing a realistic value of D. The source of this discrepancy was most likely the fed-volume-scaled resistance terminal vessel BC used, which under initial consideration seemed quite reasonable (this will be explained in detail in the Methods section below).

Microspheres used as deposition markers are expected to distribute in proportion to blood flow and are subject to Poisson noise (Buckberg *et al.* , 1971; Polissar *et al.* , 2000). In this study the discrepancy between vessel segment flow (mm^3/s) computed from the distribution of the fluorescent microspheres, Q_f, and the Poiseuille model, Q_m, is used as a standard for model accuracy. This is important since in the following chapter microsphere skimming is investigated using the discrepancy between Q_f and Q_m at each bifurcation. Terminal vessel BCs for the model are prescribed independently of the microsphere distribution and the resulting error between Q_f and Q_m is compared at different scales, with previous experimental results comparing IDMI deposition with microspheres used for reference (Bassingthwaighte *et al.* , 1990). Two types of outlet BCs are used to solve for Q_m throughout the network, namely a heterogeneous perfusion BC adapted from (Marxen, 2004), and a proposed homogeneous perfusion BC.

Both of these BCs are defined based on a tissue volume assigned to the outlet of each terminal vessel. A method for segmenting the myocardial tissue region supplied by the LCA vasculature and dividing the segmentation into terminal vessel fed-volumes is first presented, which is similar to the approach in (Marxen, 2004). The fed-volumes assigned to each terminal vessel are then used to prescribe ter-

minal BCs for the solution of Poiseuille flow throughout the network. For the heterogeneous perfusion BC, the distal (or downstream) subtree resistance of each terminal vessel is estimated based on a power law of vessel conductance and tissue fed-volume, and assumes a constant exit pressure at the level of the capillaries (Marxen, 2004). For the homogeneous perfusion BC on the other hand terminal flows are proportional to the tissue volume subtended by each terminal vessel. This BC disregards experimentally observed perfusion heterogeneity but lends itself to increasing accuracy at higher network generations (vessels further upstream) where perfusion heterogeneity decreases (as discussed in the Introduction chapter).

The accuracy of Q_f at different scales of the network is limited by several considerations. Microsphere measurements are less reliable in lower generation vessels since there are fewer microspheres passing through each vessel, which makes the measurement subject to greater variance from Poisson statistics (Buckberg *et al.* , 1971; Polissar *et al.* , 2000). Furthermore microspheres are subject to phase separation effects as demonstrated with *in vitro* slit and tube models (Ofjord & Clausen, 1983; Chien *et al.* , 1985). Phase separation effects are known to become highly pronounced wheen the vessel diameter approaches that of the particle (Pries *et al.* , 1989), which in this study however is considerably smaller than resolution of the image data. The effects of phase separation on microsphere distribution throughout the coronary arterial network have not yet been characterised, although they are believed to be responsible for the systematic bias observed in excessive microsphere deposition in higher perfusion regions of the myocardium (Bassingthwaighte *et al.* , 1987, 1990).

The comparison of Q_m and Q_f provides a novel method for identifying regional errors in the vascular network reconstruction and experimental protocol. Specifically a monotonically decreasing error is expected between Q_m and Q_f moving up vessel generations, since higher microsphere counts result in lower Poisson noise in the calculation of Q_f, and since perfusion heterogeneity decreases such that the homogeneous perfusion BC model becomes increasingly accurate. Several alterations were made to the vascular network by enforcing this monotonically decreasing error relationship across vessel generations. Finally the comparison of Q_m and Q_f

provide an estimate for a suitable tissue segment size and a required number of microspheres for accurate microsphere flow quantification.

This chapter is structured as follows: firstly the Methods section details the procedure for segmenting the LCA myocardial territory and assigning terminal fed volumes. The Poiseuille flow model formulation is then presented along with the definitions of the heterogeneous and homogeneous perfusion BCs. The error metrics used for the comparison of Q_m and Q_f are then detailed, followed by a summary of the network alterations made, and details are given for a perturbation analysis used to test the effect of introducing random terminal perfusion heterogeneity on the network flow solution. Key findings are covered in the Results section with limitations and future prospects covered in the Discussion. The resulting LCA network and Poiseuille flow simulation which the analyses in this chapter yield are used for the assessment of microsphere skimming in Chapter 5.

4.2 Methods

4.2.1 LCA Myocardial Tissue Fed Volumes

A tissue segmentation of the LCA territory within the myocardium of the pig heart was defined in order to associate terminal vessels of the porcine network with a tissue fed volume. These fed volumes then provide the basis for prescribing boundary conditions and for counting microspheres at each terminal vessel. A stack of bright-light images of the myocardium acquired with the imaging cryomicrotome with dimensions $2000 \times 2000 \times 1280$ voxels and resolution $60 \times 60 \times 64 \mu m$ were processed for the segmentation. Several steps were required to segment the LCA myocardial territory which are detailed below.

Image Post-processing and Segmentation

The original bright-light images were first down-sampled by a factor of 4 in each dimension producing an image stack with dimensions $500 \times 500 \times 320$. A mid-cavity slice is shown in Figure 4.1(a).

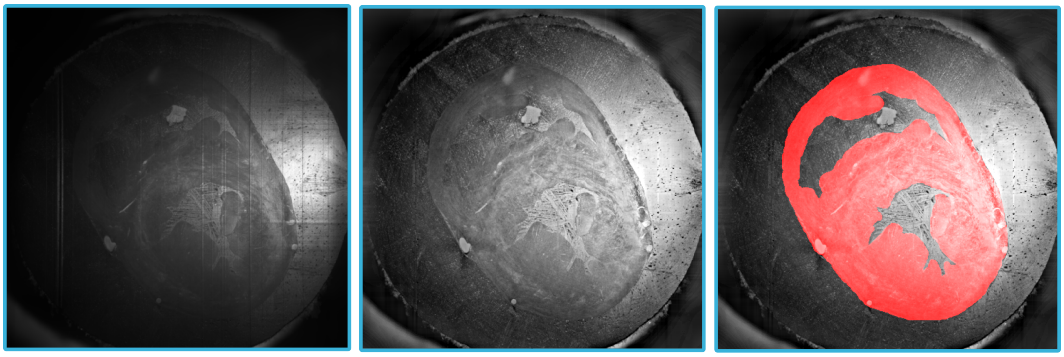

(a) (b) (c)

Figure 4.1: Enhancement of the bright-light myocardial images for tissue segmentation.

Subtraction of a Gaussian blurred image mask in each image of the stack was first used to reduce high-frequency noise. Periodic vertical bands were removed in the frequency domain after Fourier transformation, and contrast was enhanced by histogram normalisation leading to a cleaner outline of the myocardium as shown in Figure 4.1(b). Due to the lack of delineation between the myocardium and

surrounding medium in the images both in terms of signal intensity and structural features, automatic segmentation was not feasible. Thus the myocardium was manually segmented in every fifth image of the stack using the open-source software package FIJI (Schindelin *et al.* , 2012), taking care to trace the epicardial and endocardial surfaces accurately as shown in Figure 4.1(c).The segmented image slices were then interpolated to complete the segmentation for the full image stack. The segmented image stack was then resampled to match the vascular cast image stack with isotropic resolution of $64\mu m$ and image stack dimensions of $1875 \times 1875 \times 1280$.

To define the myocardial territory in the segmentation supplied solely by the LCA network the following image-processing steps were taken. Firstly a binary image stack mask was created from the extracted vascular network, where the nearest-neighbour Euclidean distance (in voxels), D_i^{NN}, from each voxel in the mask to each terminal vessel, i, was computed. A sphere of non-zero voxels around each terminal vessel's location was defined with radius $2 \times D_i^{NN}$, thus defining a preliminary, albeit possibly excessive, myocardial mask related to the LCA network. An **AND** operation was then applied to this mask with the whole-myocardium segmentation, resulting in a rough LCA territory mask (a), as shown in the mid-cavity image slice in Figure 4.2. Creating an LCA myocardial mask by defining non-zero voxel spheres around terminal vessels with half the aforementioned radius, D_i^{NN}, was also tested but was found to result in an LCA myocardial mask with many holes since spheres did not sufficiently overlap, essentially losing much of the myocardial tissue within the LCA region.

Mask (a) still contained missing regions of the myocardial segmentation clearly within the LCA territory of the whole-heart segmentation, mostly near the subendocardium and subepicardium. To recover these missing regions, mask (a) was subtracted from the original myocardial segmentation resulting in mask (b) which essentially represents the RCA tissue region along with the missing LCA tissue regions. The single largest connected component binary region was retained from mask (b) resulting in mask (c), the RCA tissue region *without* missing LCA tissue regions. However the spherical binary mask criterion for each terminal vessel with

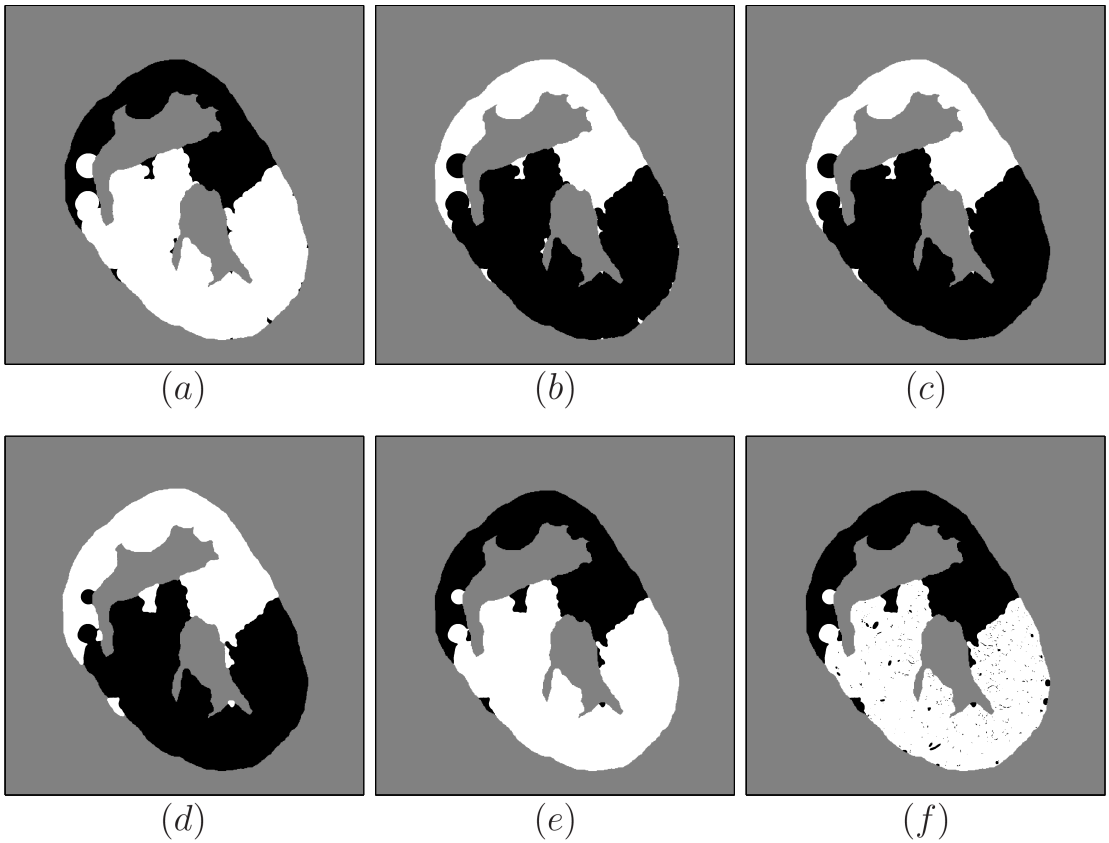

Figure 4.2: A mid-cavity image slice showing the binary masks in the LCA myocardial territory definition process (see text for explanation). The mask at each stage is shown in white, the background in grey and the remainder of the whole-heart myocardial segmentation in black. The final segmentation of the LCA myocardial territory in (f) appears speckled after the subtraction of a binary image mask of the LCA vasculature.

radius equal to $2 \times D_i^{NN}$ overestimates the LCA myocardial territory near the border zone with the RCA myocardial territory. Therefore the RCA territory mask (c) was dilated by the average terminal vessel nearest-neighbour distance producing mask (d). Then to recover the LCA territory with the missing regions from mask (a) and with a more realistic boundary zone with the RCA territory, mask (d) was subtracted from the original myocardial segmentation resulting in mask (e). Finally a binary image stack of the extracted vasculature was subtracted from mask (e) leaving just myocardial tissue in the LCA territory, as shown in mask (f).

Terminal Fed Volume Allocation

The LCA myocardial territory of mask (f) was then divided into tissue fed volumes between all of the terminal vessels of the LCA vascular tree. Each voxel in the LCA territory was assigned to a terminal vessel based on the radius scaled distance to each terminal vessel end-point, introduced in (Marxen, 2004), given by

$$min\left(\frac{X_i}{r_i}\right) \tag{4.1}$$

where r_i is the radius of a terminal vessel i, and X_i is the distance from a given voxel to the end-point of that terminal vessel. For the situation where a voxel is the same distance from two terminal vessel end-points, this weighting preferentially assigns the voxel to the terminal vessel with the larger radius. The voxels assigned to each terminal vessel are then summed to compute the tissue fed volume of each terminal vessel. For a constant density of terminal vessel end-points throughout the myocardial segmentation, this criterion results in larger tissue fed volumes for terminal vessels of larger radii. The resulting terminal fed volumes are depicted in Figure 4.3.

The number of microspheres in each terminal vessel fed volume, as well as the fed volumes themselves, were progressively summed at upstream junctions. This provided microsphere distributions at each junction throughout the entire LCA network, and volume order U_{vol} could be calculated for each vessel segment.

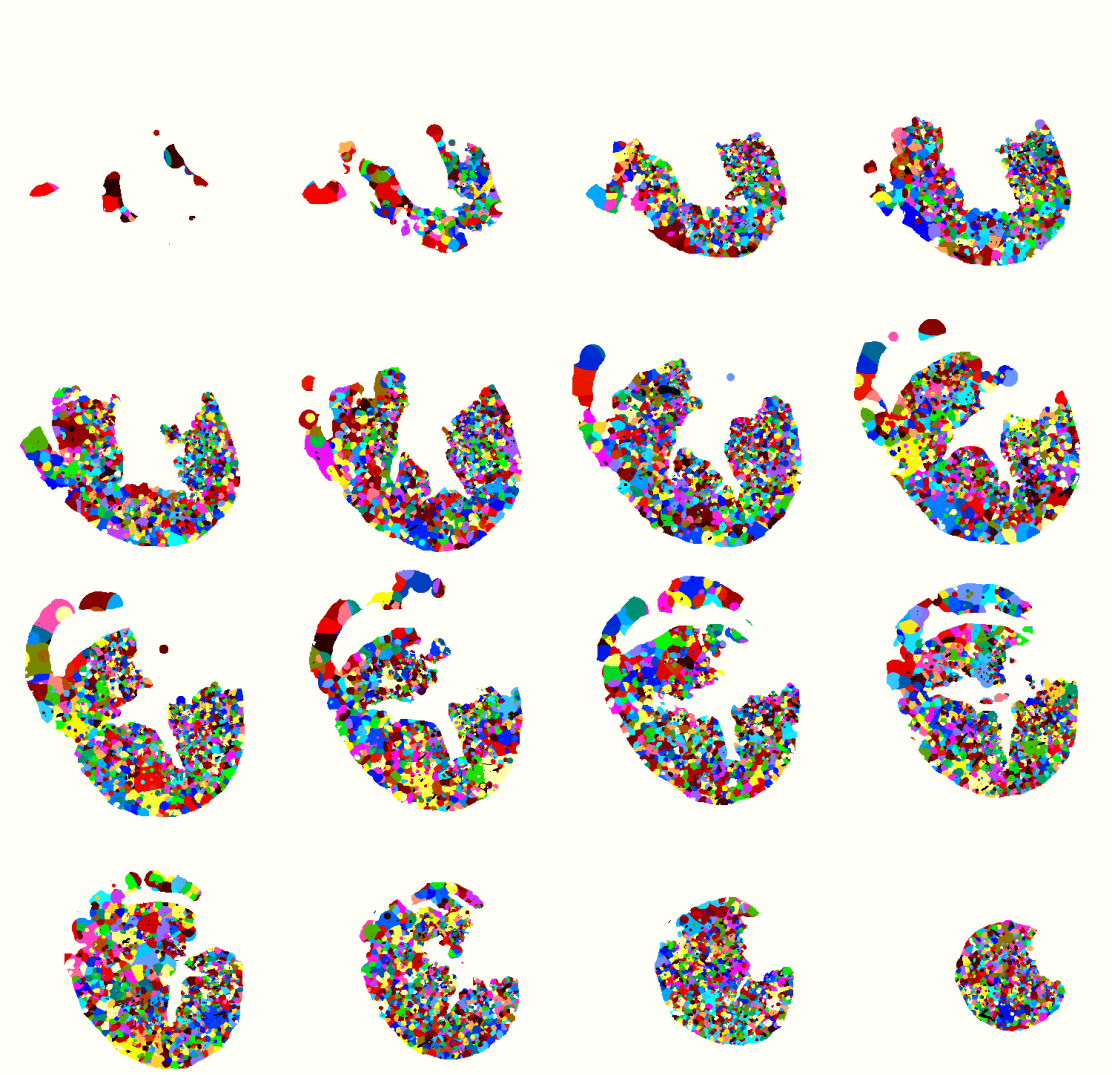

Figure 4.3: Assigned terminal vessel fed volumes for the LCA territory are indicated by the different colours where short-axis images of the segmentation progressing from base to apex are shown in the order of left-to-right and top-to-bottom.

4.2.2 Coronary Network Flow Model

The Poiseuille model was used to simulate blood flow in the coronary network since data were acquired from a non-beating, isolated porcine heart. The Poiseuille flow model assumes laminar, steady flow through axisymmetric 1D tubes and provides a relation between pressure drop, ΔP, blood flow, Q, and resistance, R,

$$Q = \frac{\Delta P}{R} \tag{4.2}$$

where

$$R = \frac{8\eta L}{\pi r^4}. \tag{4.3}$$

L is vessel segment length, r mean vessel radius, and η blood viscosity. Pries and Secomb found that *in vivo* dynamic blood viscosity differed from *in vitro* glass tube viscosity measurements as a function of diameter and haematocrit, but lost significance in vessel diameters greater than $30\mu m$ (Pries *et al.* , 1994). For vessels above $50\mu m$ in diameter an *in vitro* viscosity law matched the *in vivo* viscosity well and represents the well-known Fahraeus-Lindqvist effect (Fåhræus & Lindqvist, 1931), which demonstrates a noticeable reduction in blood viscosity with decreasing tube diameter, an effect observed in tubes up to $300\mu m$ in diameter. The *in vitro* viscosity law proposed in (Pries *et al.* , 1992) is

$$\eta = 1 + (\eta_{0.45} - 1) \cdot \frac{(1 - H_D)^C - 1}{(1 - 0.45)^C - 1} \tag{4.4}$$

where $\eta_{0.45}$ is the relative viscosity for a fixed discharge haematocrit $H_D = 0.45$, given by

$$\eta_{0.45} = 220 \cdot e^{-2.6r} + 3.2 - 2.44 \cdot e^{-0.06(0.5r)^{0.645}} \tag{4.5}$$

where r is vessel radius in micrometres. In our model a fixed discharge haematocrit $H_D = 0.45$ is assumed so Equation (4.5) alone is used to compute vessel viscosity, which in turn is used to compute vessel resistance from Equation (4.3). There is a maximum drop in viscosity of 19% in the smallest vessels of the network compared to vessels with diameter$> 300\mu m$ in which viscosity is approximately constant.

4.2.3 Boundary Conditions

Poiseuille flow and pressure can be solved throughout a branching vascular network computationally with the provision of appropriate boundary conditions (BCs) by enforcing mass conservation at each junction. BCs employed are typically either where (1) Q is prescribed at both the inlet and outlets and P is fixed at the inlet, or (2) P is fixed at the inlet and outlets and Q is fixed at the inlet. Previous simulated network flow models have employed both (1) (Karch *et al.* , 2003) and (2) (Kassab *et al.* , 1997; Beard & Bassingthwaighte, 2000; Marxen & Henkelman, 2003; Marxen *et al.* , 2006; Marxen & Henkelman, 2009; Mittal *et al.* , 2005; Huo *et al.* , 2009; Hyde *et al.* , 2013a) depending on the application.

A current limitation of coronary network flow data is the inability to measure pressure or flow in the smaller vessels of the network and thus accurately prescribe terminal vessel BCs. Previous studies have used stochastically reconstructed vascular networks based on morphometric data from (Kassab *et al.* , 1993) to the level of the capillaries where a constant terminal vessel outlet pressure of 26mmHg is assumed (Kassab *et al.* , 1997; Beard & Bassingthwaighte, 2000; Mittal *et al.* , 2005; Huo *et al.* , 2009). The study of Huo demonstrated a very close fractal dimension D relating perfusion RD and sample volume using the Poiseuille flow model compared to D computed from microsphere deposition in separate animal experiments.

Another approach for prescribing terminal boundary conditions in a truncated network was proposed in (Hyde *et al.* , 2013a) where anatomical canine and porcine coronary vasculature had been reconstructed from imaging data. Terminal vessel outlet pressures were prescribed based on a fitted sigmoidal function to pressure measurements in vessels less than $400\mu m$ in diameter collected by Chilian in anesthetized cats (Chilian *et al.* , 1989). The focus of this study however was a comparison of an anatomically parameterised porous Darcy model of coronary flow with a spatially averaged Poiseuille model solved in the 1D vasculature which showed good agreement. None of the above studies made a direct comparison of a Poiseuille flow model with microsphere deposition.

Marxen reconstructed the spatially superimposed 3D microsphere locations and vascular geometry from micro-CT images of rat kidneys and was the first to make a comparison between microsphere distribution and a simulation of Poiseuille flow in the same organ (Marxen *et al.* , 2006). Using a tissue segmentation of the kidney cortex which was fed by the vascluar tree, he sought to account for regional perfusion heterogeneity by estimating downstream resistance and then prescribing a constant 25mmHg pressure boundary condition at the level of the extrapolated capillaries. Specifically, an additional resistance at each terminal vessel of the network was computed based on a power law relation of vessel segment conductance with volume order. The comparisons drawn between the flow model and microspheres were of flow heterogeneity, in terms of D, and of perfusion in 500 segments with the largest number of associated microspheres. Although a physiologically realistic value of D was reproduced, dispersion of perfusion measured from microspheres was far more than measured from the model, and there was no correlation of regional perfusion between the model and microspheres. This approach, being the only existing approach for prescribing terminal boundary conditions based on terminal fed volume, is considered in this study and is presented in greater detail in the next section.

In another study outlet flow BCs were prescribed in an *in silico* branching network (generated with constrained constructive optimization) which were proportional to tissue fed volume (Karch *et al.* , 2003). Tissue fed volume in this case was defined by Voronoi polyhedra volumes associated with each terminal vessel. Flow at each outlet vessel was set as proportional to fed volume i.e. the fed volume of a terminal vessel as a fraction of the entire domain multiplied by the total inlet flow. This model assumes a homogeneous perfusion (and thus tissue metabolism to which it is associated(Decking *et al.* , 2004)) and naturally did not reproduce a physiologically meaningful fractal dimension D since perfusion by definition is flow divided by tissue volume.

This homogeneous perfusion BC however yields a suitable control network flow model for comparison with microsphere distributions for two reasons. Firstly no network flow model to-date has reproduced accurate regional perfusion compared

to a deposition tracer - favourable comparisons have always been made based on whole-organ characteristics, such as the fractal dimension D. Secondly, the typical physiological range of values of D (between approximately 1.1 and 1.3 in baboon hearts (Bassingthwaighte *et al.* , 1989)) reflects a decrease in perfusion heterogeneity, given by relative dispersion RD, when the heart is divided into fewer large tissue segments compared to many smaller tissue segments; this implies a reduction in the perfusion heterogeneity of higher compared to lower generation vessels, since they supply larger and smaller tissue regions respectively.

In baboon hearts the relative dispersion of perfusion in segments larger than 2g (or approximately 5% of myocardial mass) dropped below 8% (Bassingthwaighte *et al.* , 1990). Furthermore, several studies have shown that in a vasodilated state there is a reduction in perfusion heterogeneity across the heart (Gorman *et al.* , 1989; Bauer *et al.* , 2001; Chareonthaitawee *et al.* , 2001). This suggests for the current study that a homogeneous perfusion BC may be appropriate. Such a terminal vessel BC also entails that flow within vessels of the network are highly dependent on the fed volume allocation algorithm. The heterogeneous and homogeneous perfusion BCs are presented in more detail in the following sections.

The Heterogeneous Perfusion BC

As discussed briefly above, Marxen proposed a power law relationship between vessel segment conductance and volume order to derive additional resistances at network terminal vessels representing the distal vascular resistance down to the level of the capillaries. This approach successfully reproduced whole-kidney flow heterogeneity observed in experiments (Bassingthwaighte *et al.* , 1989), as determined by the value of the fitted fractal dimension D in Equation (4.27) (see Section 4.2.6). For the purposes of the current study however, flow heterogeneity at the scale of the whole organ is not of interest, but rather terminal boundary conditions that most accurately reproduce regional flows to reduce model error when comparing to microsphere distributions. The heterogeneous BC has been shown to reproduce a physiologically consistent fractal dimension D, but did not reproduce accurately local perfusion heterogeneity compared to microspheres (Marxen *et al.*

, 2006).

Following the assignment of fed volumes to terminal vessels of the renal arterial tree Marxen was able to fit the relationship between fed volume (Equation (1.2)) and resistance with a power law:

$$log_2(C) = L + q.U_{vol}, \tag{4.6}$$

where conductance C is computed from the Poiseuille flow relation in equation (4.3) as $1/R$. The parameter q was estimated by a linear least-squares regression on a log-log plot of vessel segment conductance C versus volume order U_{vol} for a reconstructed kidney vascular network. Marxen fitted this relation for volume orders above 7 in 2 mice and above 12 in 2 rats, producing an average value of $q = 0.845 \pm 0.034$, with R values for each fit of 0.99. This relation was then used to determine conductance values for generated bifurcating subnetworks distal to each terminal vessel of the kidney vascular tree. Briefly, the tissue fed volume assigned to each terminal was iteratively subdivided and assigned to daughter vessels of consecutive bifurcations based on an asymmetry ratio δ

$$\delta = \frac{V_1}{(V_1 + V_2)}, \tag{4.7}$$

where V_1, V_2 are daughter vessel fed volumes and $V_1 \leq V_2$. The value of δ for each generated bifurcation was sampled from a normal distribution with mean 0.5 (i.e. equal division of fed volume) and a standard deviation calculated from the terminal bifurcations of the original network. A conductance was then assigned to each daughter vessel by sampling a normal distribution with mean given by the extrapolated value from the fitted relation in Equation (4.6) of the assigned volume (V_1 or V_2), and standard deviation computed from the terminal vessels of the existing reconstructed network. These distal bifurcations were generated iteratively until the fed volume assigned to a daughter vessel was less than a threshold V_{min} (corresponding to $U_{vol} \approx 1$) determined to be approximately equal to the fed volume supplied by terminal arteriole based on morphometric data (Kassab *et al.* , 1993). These generated subtrees provided a surrogate for the distal vasculature down to the level of the capillaries, where a constant outlet pressure was then used

as a boundary condition for the Poiseuille flow model (Marxen, 2004).

A limitation with this approach is that sampling normal distributions for δ and C disregards underlying local, physiological determinants of distal network conductance, which is dependent on local branching patterns and metabolic demand. Furthermore the standard deviation of low generation vessel segment conductances from reconstructed network data is high, where at $U_{vol} = 7$ used for fitting in the mouse kidney in (Marxen & Henkelman, 2009), segment conductances spanned approximately two orders of magnitude. Performing a linear least-squares fit for conductances in $U_{vol} \geq 7$ for the porcine LCA network yields a relatively poor fit ($R^2 = 0.497$), where in fact a quadratic polynomial yields a better fit ($R^2 = 0.533$). Figure 4.4 shows these fitted curves along with bounds of 95% confidence intervals, which for the $U_{vol} = 7$ spans more than 2 orders of magnitude (on the y-axis).

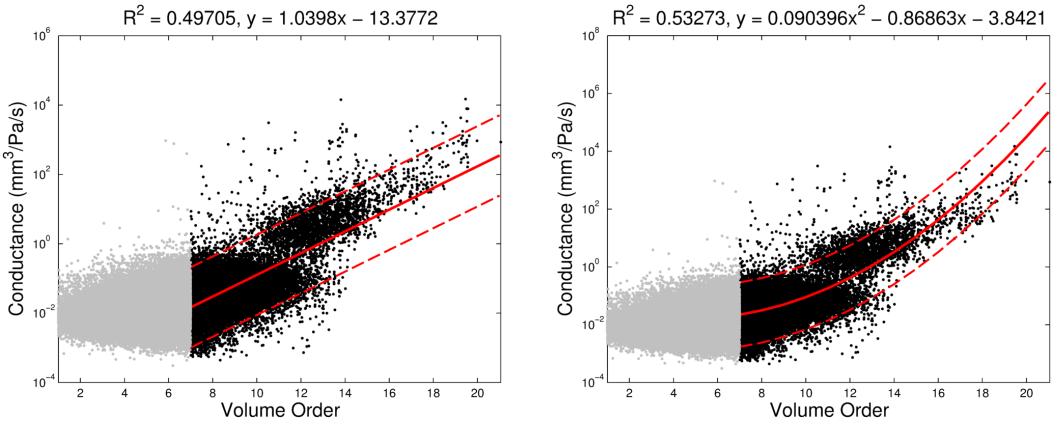

(a) (b)

Figure 4.4: Least-squares fits using a linear (a) and quadratic (b) polynomial for $log_2(C)$ versus U_{vol} are shown with the solid red line for volume orders ≥ 7. Lower volume order vessel segments not used for the fitting are shaded out. 95% confidence intervals are represented with dashed red lines.

In this study heterogeneity of flow is of less concern than accuracy of terminal outflows. Therefore there is little need to adopt a method for sampling δ and C using normal distributions and thus adding a random component to the model outlets. A simplification can be made by assigning $\delta = 0.5$ to all generated subtree bifurcations and C can be computed from the fitted relation in Equation (4.6). A

further simplification now due to symmetric bifurcations, $\delta = 0.5$, is that the number of extrapolated generations for each terminal vessel is a function of the volume order, U_{vol}. Since $U_{vol} = 1$ is the target for the most distal extrapolated vessels, and since successive generated bifurcations are given $U_{vol}(k+1) = U_{vol}(k) - 1$, the number of generations in a given generated subnetwork at each terminal vessel, T, can be approximated by

$$N = \text{round}[U_{vol}(T)] - 1, \tag{4.8}$$

such that for example a terminal vessel with $U_{vol}(T) = 3.3$ or $U_{vol}(T) = 2.7$ will have 2 extrapolated generations of symmetric bifurcations added to it. Each daughter vessel at a generated bifurcation will have a conductance, C_d, as a function of the parent vessel conductance, C_p, from Equation (4.6),

$$C_d = 2^q.C_p \tag{4.9}$$

and similarly for the resistance,

$$R_d = 2^{-q}.R_p. \tag{4.10}$$

Resistance of a daughter vessel at a generation i distal to the terminal vessel (counting each added generation of bifurcations as $1 \ldots N$ from proximal to distal), is given by

$$R_i = 2^{-i.q}.R_T(U_{vol}), \tag{4.11}$$

where $R_T(U_{vol})$ refers to the terminal vessel resistance calculated from Equation (4.6) based on its volume order and is not the terminal vessel's actual resistance. The resistance of the entire generated subtree can be derived and is given by the following geometric series

$$R_S = \sum_{i=1}^{N} 2^{-i(q+1)} \cdot R_T(U_{vol}). \tag{4.12}$$

Subtree resistance R_S is computed and added to each terminal vessel in the network, and a constant pressure BC is applied at each terminal corresponding to

pre-capillary pressure ($25mmHg$). An illustration is shown in Figure 4.5 of a generated subnetwork. For simulating Poiseuille flow in the porcine LCA, $q = 1.04$ was taken from the linear least-squares fit shown in Figure 4.4a. This is in line with (West *et al.* , 1997) where for non-pulsatile flow the value of $q = 1$ was proposed, which would lead to proportionality between vessel resistance and volume scale and thus a linear drop in fluid pressure with volume order for a symmetrically branching network (Marxen, 2004). This particular BC provides one approach to solving flow using the Poiseuille model in order to provide a comparison with microsphere distributions and is compared to a homogeneous perfusion BC in the Results of section 4.3.

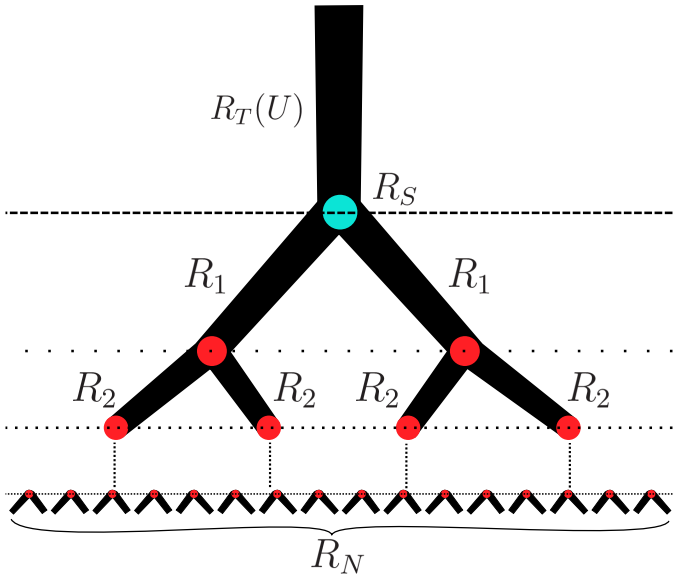

Figure 4.5: An extrapolated subnetwork. The light blue dot indicates the terminal vessel end-node, and successive generations of added bifurcations are separated by dashed lines. Each generation contains vessel segments of equal resistance: R_1 in generation 1 down to R_N in the final generation N. R_S is computed according to Equation (4.12).

The Homogeneous Perfusion BC

The homogeneous perfusion boundary condition prescribes outlet flow as proportional to tissue fed volume, specifically the outlet flow to terminal vessel k is

$$Q_k = Q_t \left(\frac{V_k}{V_t} \right) \tag{4.13}$$

where Q_t is the total flow entering the network (as controlled in the experiment),

V_k is the tissue fed volume assigned to terminal vessel k, and V_t is the total myocardial mass of the LCA territory. A similar such BC was used in an *in silico* study where Voronoi tesselations were instead used to define tissue volume subtended by a vessel subtree (Karch *et al.* , 2003).

Given that there is no reliable method for determining true outlet flow, the homogeneous perfusion BC provides a control where the mean perfusion is effectively prescribed throughout the whole network. This entails that the error between model and microsphere flows will decrease in higher vessel generations as perfusion heterogeneity decreases (Bassingthwaighte *et al.* , 1989).

Furthermore, in the present experiment the pig heart was in a state of maximal coronary vasodilation for the injection of microspheres and cast, under which conditions regional flow becomes more homogeneous. Bauer demonstrated with high-resolution MRI that coronary vasodilation in isolated rat hearts caused a decrease in the fractal dimension D (see Equation (4.27)) indicating a more homogeneous perfusion distribution (Bauer *et al.* , 2001). Other studies have also demonstrated a reduction in flow heterogeneity in a vasodilated state in guinea pigs using microspheres (Gorman *et al.* , 1989) and in humans using positron emission tomography (Chareonthaitawee *et al.* , 2001). In addition to the maximally dilated vasculature, a low intra-cavity pressure may further reduce heterogeneity transmurally in the LCA territory in this study.

Finally, it should be noted that despite terminal vessel perfusion being prescribed as homogeneous, terminal vessel flow is dependent on terminal vessel radius, and on the distance of nearest-neighbour terminal vessels as described in Section 4.2.1. This dependence preferentially assigns tissue to larger radius terminal vessels, under the assumption that larger vessels supply larger tissue regions. A relationship between vessel radius and supplied tissue volume has yet to be determined experimentally at the spatial scale of the coronary arterioles, although one study found a 3/4 power law relationship between flow and myocardial mass for major epicardial vessels of eight pig hearts (Choy & Kassab, 2008).

4.2.4 Flow Error Metrics

Bassingthwaighte assessed differences in perfusion measured between 16.5μm diameter microspheres and molecular tracer IDMI depositions in order to determine whether there was significant bias in the microsphere method in 11 sheep hearts (Bassingthwaighte *et al.* , 1990). Relative deposition density*, d_i, in 2789 tissue segments (from all 11 hearts) with mass 217±100mg was used to compare the two methods. An average error of 12.6±13.7% between the two methods was found, with a preferential deposition of microspheres in higher IDMI density regions. In the current study relative deposition density of fluorescent microspheres is calculated as

$$d_i = \left(\frac{N_i}{M_i}\right) / \left(\frac{N_H}{M_H}\right) \tag{4.14}$$

where N_i and M_i are microsphere count and mass respectively of tissue segment i, and N_H and M_H are microsphere count and mass of the whole LCA region. The equivalent calculation for relative regional perfusion from the Poiseuille model, f_i, is

$$f_i = \left(\frac{Q_i}{M_i}\right) / \left(\frac{Q_H}{M_H}\right) \tag{4.15}$$

For the homogeneous BC flow solution the value of f_i is 1 in all segments since flow is set proportional to mass and so this comparison has little meaning. For the heterogeneous BC, Marxen showed that although the fractal dimension D for flow heterogeneity computed from the model was similar to experimental results with microspheres, relative model perfusion showed no correlation to microsphere distribution densities. Therefore comparing relative perfusion to microsphere densities in this way has limited value, except to compare the errors of the homogeneous and heterogeneous BCs. A more meaningful comparison that can be made given the limitations of the BCs for comparing perfusion is to compare Poiseuille flow in each vessel segment to microsphere flow. The absolute percentage error between the fluorescent microsphere distribution, Q_f, and the Poiseuille model flow, Q_m, is calculated in each vessel segment, i, according to

*Relative deposition density is equal to relative perfusion.

$$E^i = \sqrt{\left(\frac{Q_f^i - Q_m^i}{Q_m^i}\right)^2} \times 100 \tag{4.16}$$

where microsphere flow Q_f^i is given by

$$Q_f^i = \frac{N_f^i}{N_f^T} Q_m^T \tag{4.17}$$

where N_f^i denotes number of microspheres which have passed through segment i, Q_m^T denotes the total model flow at the root of the network, and N_f^T the total number of microspheres at the network root. Although Q_m is solved for using Poiseuille's relation throughout the network for the heterogeneous perfusion BC, the homogeneous perfusion BC leads to the following relation of flow and cumulative tissue volume

$$Q_m^i = \frac{V^i}{V^T} Q_m^T \tag{4.18}$$

where V is the sum of the fed volumes assigned to all of the downstream terminal vessels. After some manipulation E^i can be written for the homogeneous BC just in terms of the number of microspheres and tissue volume,

$$E^i = \sqrt{\left(\frac{N^i}{V^i}\frac{V^T}{N^T} - 1\right)^2} \times 100, \tag{4.19}$$

Flow error can be assessed in relation to vessel generation defined in terms of tissue volume. Rather than using the previously introduced value of U_{vol} however, which requires an additional computation to represent in terms of physical units mm^3, a second representative volume order is defined as

$$U_2 = log_{10}(V) \tag{4.20}$$

Vessel segments throughout the network are grouped into 20 bins covering the range of fed volumes from $10^0 - 10^5 \text{mm}^3$, or equivalently $0 \leq U_2 \leq 5$. Thus the U_2 volume order coverage of each bin w_j span the values

$$\tilde{U}_2(w_j) - 0.1 < U_2(w_j) < \tilde{U}_2(w_j) + 0.1 \tag{4.21}$$

and the fed volumes of each bin span the values

$$10^{\tilde{U}_2(w_j)-0.1} < V(w_j) < 10^{\tilde{U}_2(w_j)+0.1} \tag{4.22}$$

where $\tilde{U}_2(j)$ is the central value of U_2 in bin w_j. Each bin w_j contains n_j vessel segments which have a fed volume in the range specified by $V(w_j)$. The root mean squared error (E_j^{rms}) of all vessel segments in bin w_j can be calculated as

$$E_j^{rms} = \sqrt{\frac{\sum_i^{n_j}(E_j^i)^2}{n_j}} \tag{4.23}$$

For a physiologically realistic flow, plotting E_j^{rms} vs w_j should produce a monotonically decreasing relation representing decreasing model-microsphere flow distribution error towards the higher generations of the network. When this relation is not monotonically decreasing, two consecutive bins, w_j and w_{j+1}, can be compared in terms of the cumulative frequency of the *ordered errors* of their constituent vessel segments. On the y-axis the cumulative frequency of vessels in bin w_j spans the values of 0 to 1, and on the x-axis the segment error E_j^i of each vessel in bin w_j is ordered from lowest to highest. The ordered error curve of bin w_{j+1} is expected to mostly be above the ordered error curve for bin w_j, i.e. to have a higher frequency of lower error vessel segments. When the ordered error curves intersect or cross, this allows for the identification of particular vessel segments in bin w_{j+1} with unexpectedly high errors, and these segments can be visualised in the 3D coronary vascular network.

4.2.5 Theoretical 95% Confidence Limit Error

The distribution of microspheres to a region of tissue within the myocardium has been considered to follow a binomial distribution (i.e. it either deposits in that region or not) (Buckberg *et al.* , 1971). A theoretical error at the 95% confidence limit of a binomial distribution based on this assumption was proposed by Buckberg, and is modified herein for the current data. Within the heart a given tissue segment can be expected to receive a fraction of the total coronary flow given by f. Since microsphere distribution is expected to be proportional to flow, the number of microspheres expected to reach a tissue segment is $f.X_t$ where X_t is

the total number of microspheres. The standard deviation for this distribution is $\sqrt{X_t.f.(1-f)}$, assuming X_t is large. The z-ratio can be used to determine if the observed number of microspheres that reach a tissue segment, X, is significantly different from $f.X_t$ as expected by random variability,

$$z = \frac{X - f.X_t}{\sqrt{X_t.f.(1-f)}} \tag{4.24}$$

The number of microspheres at the 95% upper confidence limit expected to reach the tissue region, X_{95}, can be computed by setting $z = 1.96$, substituting $X = X_{95}$ and rearranging the above,

$$X_{95} = 1.96\sqrt{X_t.f.(1-f)} + f.X_t \tag{4.25}$$

The percentage error between X_{95} and $f.X_t$ microspheres arriving in a tissue region can be computed for different values of f,

$$E_t = \frac{X_{95} - f.X_t}{f.X_t} \tag{4.26}$$

This theoretical error E_t can be compared to segment flow error computed from the data with Eq. (4.16) to see if segment error E_i is within the 95% confidence limits under the assumption that the model flow is equivalent to the expected number of microspheres arriving in a tissue segment.

4.2.6 Coronary Flow Heterogeneity

An important functional characteristic of the coronary circulation is the heterogeneity of myocardial blood flow (units ml/min) and tissue perfusion (units $ml/min/g$, "millilitres of blood per minute per gram of tissue"). Regional perfusion heterogeneity has been characterised as following a fractal relationship with tissue segment size in the myocardium of dogs, rabbits, sheep, and baboons using both radionuclide microspheres and the high-accuaracy radionuclide 'molecular' tracer IDMI (Yipintsoi *et al.* , 1973; King *et al.* , 1985; Bassingthwaighte *et al.* , 1987, 1989, 1990; Bassingthwaighte & Bever, 1991; Austin *et al.* , 1990). Many studies have been performed to determine the underlying causes of this heterogene-

ity, with evidence that regional tissue metabolism (Franzen *et al.* , 1988; Caldwell *et al.* , 1994; Sonntag *et al.* , 1996; Deussen, 1997; Decking *et al.* , 2001; Alders *et al.* , 2004) and vascular anatomical structure (Van Beek *et al.* , 1989; Van Bavel & Spaan, 1992; Beard & Bassingthwaighte, 2000) play important roles. Several studies have demonstrated a proportionality between regional flow and metabolic activity, where local flow increases were linked with increased glucose uptake (Sonntag *et al.* , 1996), and enhanced glucose metabolism (Deussen, 1997). Decking showed a threefold difference in local flow was concomitant with a 3.4-fold increase in local Kreb's cycle turnover (Decking *et al.* , 2001). Several studies have also explored spatial heterogeneity of organ vasculature as an explanatory factor for flow heterogeneity, where branching asymmetry has been shown to result in heterogeneous flow in simulated models (Van Beek *et al.* , 1989; Van Bavel & Spaan, 1992; Kassab *et al.* , 1997; Marxen & Henkelman, 2003; Beard & Bassingthwaighte, 2000).

Bassingthwaighte showed that perfusion heterogeneity follows a fractal relationship with tissue segment size in baboon, rabbit and sheep hearts (Bassingthwaighte *et al.* , 1989). Sheep hearts were perfused with radionuclide-labeled microspheres and were dissected into approximately 200 equal-sized tissue segments. Relative deposition density, d, was computed for each tissue segment as the local tissue segment tracer density divided by the whole-heart tracer density. Given that microspheres are distributed in proportion to flow, this is equal to relative perfusion. Relative dispersion, RD, was calculated using d from all the tissue segments as the standard deviation over the mean, $RD(d) = SD(d)/\bar{d}$. Segments were progressively aggregated to form larger approximately equal-mass tissue segments with mean mass m_i, and RD_i was computed from d of all the tissue segments at each aggregation level, i. The following function was then fit to the data,

$$log\left[\frac{RD_i}{RD_0}\right] = (1 - D) \cdot \left[\frac{m_i}{m_0}\right], \tag{4.27}$$

where RD_0 and m_0 are the relative dispersion and tissue segment mass of a reference segment size, which was chosen as $1g$ in Bassingthwaighte's experiments. The variable D is the fractal dimension and represents the fractal change of RD with

tissue mass m. D also reflects the correlation of perfusion in neighbouring tissue segments (Van Beek *et al.* , 1989), and is related to the correlation coefficient r of adjacent segments by the equation

$$r = 2^{3-2D} - 1. \tag{4.28}$$

A value of $D = 1.2$ gives $r = 0.52$ suggesting a moderate correlation of neighbouring tissue segments. For $D = 1$, $r = 1$ indicating uniform (constant) perfusion across all tissue segments, and $D = 1.5$ indicates completely random, uncorrelated local perfusion with $r = 0$. Note that r is constant for every tissue segment size, indicating that correlation of perfusion in adjacent tissue segments is constant at different tissue sizes. Bassingthwaighte's study computed D from microsphere distributions in 10 baboons, 11 sheep and 6 rabbit LVs producing an average value of $D = 1.21 \pm 0.04$ with $RD_0 = 13.5\%$ for $m_0 = 1g$ (Bassingthwaighte *et al.* , 1989).

Polissar demonstrated that to achieve an accurate measure of perfusion heterogeneity from microsphere deposition, Buckberg's theoretical minimum number of microspheres required per tissue segment of 400 was unnecessarily high (Polissar *et al.* , 2000). It was shown that the computation of RD from microspheres, given that their deposition theoretically follows a Poisson distribution, should be corrected for Poisson noise (particularly at low microsphere counts) with the equation

$$\hat{RD}_i = \sqrt{RD_i^2 - \frac{1}{\bar{X}_i}} \tag{4.29}$$

where $\bar{X}_i$ is the mean number of microspheres for tissue aggregate level i.
In addition to this fractal relation being demonstrated *ex vivo* with tracers, more recently D has been fitted using PET perfusion data (Kuhle *et al.* , 1992) and perfusion MRI data (Jerosch-Herold *et al.* , 1998, 2003; Bauer *et al.* , 2001). This fractal relation has been used for the validation of realism of some coronary computational flow models based on stochastically generated networks (Van Beek *et al.* , 1989; Beard & Bassingthwaighte, 2000; Karch *et al.* , 2003; Marxen & Henkelman, 2003) and in flow simulations with vascular networks completely or partially generated from morphometric data (Van Bavel & Spaan, 1992; Kassab *et al.* , 1997;

Smith, 2004; Mittal *et al.* , 2005; Marxen *et al.* , 2006; Huo *et al.* , 2009).

4.2.7 Network Alterations Based on Error Metrics

The RMS flow error E_j^{rms} is expected to decrease at higher generation volume bins, w_j, due to (1) a reduction in perfusion heterogeneity from the microsphere distributions, and (2) an increase in the number of microspheres passing through higher generation vessels. It is shown in the Results section that the expected monotonic reduction in E_j^{rms} with w_j was not initially observed, which led to the identification of underlying errors in the LCA myocardial segmentation, network reconstruction process (Chapter 2) and experiment. The particular problems which were corrected are listed below:

1. Removal of the right ventricle (RV) feeding vessels, to which tissue volume was over-prescribed (section 4.3.2);

2. Normalisation of microsphere flow by the inlet flow of each of the major sub-networks: the Left Circumflex (LCx), Left Anterior Descending (LAD), and Left Marginal (LM) arteries (section 4.3.2);

3. Removal of two high-error subtrees: one stemming from the LCx and another stemming from the LAD feeding the apex (section 4.3.2). This was done by comparing ordered error plots of neighbouring volume bins w_j and w_{j+1}.

After the above corrections, an almost monotonically decreasing relationship was found between E_j^{rms} and w_j. Using this relationship an approximate minimum tissue volume required for an accurate estimate of flow could be determined, as well as a corresponding minimum number of microspheres. Previous studies have shown that approximately 384 microspheres are required in a given tissue segment to have 95% confidence that the flow estimate is within 10% of the true value according to a Poisson distribution (Buckberg *et al.* , 1971; Nose *et al.* , 1985; Bassingthwaighte *et al.* , 1987, 1990).

4.2.8 Terminal Perfusion Perturbation Analysis

Finally, in order to determine the sensitivity of the Poiseuille flow solution using the homogeneous perfusion BC to randomly added perfusion heterogeneity at the terminals, a perturbation analysis is carried out using a Monte Carlo approach. Keeping terminal fed volumes constant, random perturbations in outlet flow were introduced producing heterogeneity in outlet perfusion (flow/tissue volume), while conserving total flow throughout the network. Specifically flow is perturbed at each terminal vessel, k, according to

$$Q'_k = \begin{cases} 0 & \text{if } (Q_k + X_k \tilde{\boldsymbol{Q}} \leq 0) \\ Q_k + X_k \tilde{\boldsymbol{Q}} & \text{otherwise} \end{cases} \tag{4.30}$$

where Q'_k and Q_k are the perturbed flow and the original flow at terminal k respectively, and $\tilde{\boldsymbol{Q}}$ is the median original terminal flow (which is explained further below). X_k is a random variable sampled from a normal distribution with standard deviation σ and a mean of 0,

$$X_k \sim N(0, \sigma^2) \tag{4.31}$$

The value σ is chosen to reflect a desired perfusion heterogeneity in the terminal vessels, and is set to 20%, 40%, 60% and 80% for comparison. The sum of the perturbed flows at each terminal is then corrected in order to match the sum of the original (unperturbed) flows, Q_t,

$$\hat{Q}'_k = Q'_k \left(\frac{Q_t}{Q'_t} \right) \tag{4.32}$$

where $\hat{Q}'_k$ is the corrected, perturbed flow at terminal k, and Q'_t is the sum of all perturbed flows from equation (4.30). The median terminal vessel flow $\tilde{\boldsymbol{Q}}$ is used in Equation (4.30) since the original terminal flows Q_k are non-uniform and span several orders of magnitude (as do the terminal fed volumes to which they are proportional). The logarithm of the terminal fed volumes are approximately normally distributed, as shown in Figure 4.6. It has been established that perfusion heterogeneity (given as a measure of relative dispersion, RD) decreases with increasing tissue segment size (Bassingthwaighte *et al.* , 1989) or equivalently vol-

ume order (Marxen, 2004). This entails that terminal vessels with larger flows (and volumes) should be perturbed by a smaller fraction than those with lower flows (and volumes) in order to produce the appropriate perfusion heterogeneity. Using $\tilde{\boldsymbol{Q}}$ is a simplistic approach for representing this dynamic.

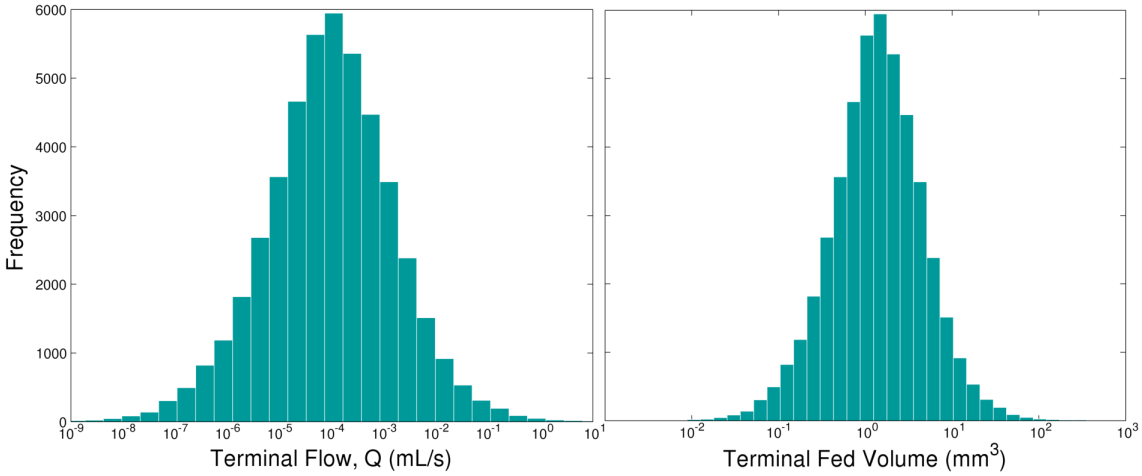

Figure 4.6: Terminal flow (left) and fed volume (right) distributions related by the homogeneous perfusion BC.

A thousand trials are performed for the analysis at each value of σ, where a single trial consists of the perturbation of all terminal flows in the network. RMS errors between the perturbed Poiseuille model and microsphere flows, $\hat{E}_j^{rms}$, are computed from Equation (4.23) in each volume generation bin w_j for each trial. Considering all 1000 trials the maximum and the minimum values of $\hat{E}_j^{rms}$ in each bin w_j define the flow error limits of the perturbation. These limits are then superimposed on the homogeneous perfusion BC flow error E_j^{rms} in each volume bin to assess sensitivity of flow errors in the higher vessel volume generations with different levels of terminal flow perturbations, specifically where $\sigma = 20\%$, 40%, 60% and 80%.

4.3 Results

4.3.1 Homogeneous vs Heterogeneous Perfusion BC

The Poiseuille model is solved on the LCA network with the heterogeneous and homogeneous perfusion BCs for comparison. The heterogeneous BC results in greater errors between the model and microsphere flows across all but the highest three volume bins w_j (not shown). Since the RMS error value E_j^{rms} is sensitive to low model flows Q_m, the w_j versus E_j^{rms} relation is not plotted as values tend to infinity for the heterogeneous BC model in most vessel generations. A vastly greater spread of Q_m across lower orders of magnitude is associated with the heterogeneous BC compared to the homogeneous BC as illustrated in the Q_f versus Q_m scatter plots in Figure 4.7.

The terminal $log_{10}(Q_m)$ distributions produced by the two BCs along with that of a Poiseuille model solved *without* additional terminal resistances but with a constant terminal pressure are shown in Figure 4.8. Unlike the fairly normally distributed homogeneous BC terminal flows in Figure 4.8(a), the distribution of heterogeneous BC terminal flows is negatively skewed with a tail of very low flow values (Figure 4.8(b)). The constant pressure BC model terminal flow distribution is yet more negatively skewed. This result suggests that the added terminal resistances in the heterogeneous BC model help mitigate the errors of a constant terminal pressure BC where terminal vessels do range across several vessel generations. However errors between the model and microsphere flows are still much higher than expected with the heterogeneous BC model (not displayed but can be inferred from Figure 4.7) and considerably higher than the homogeneous BC model. In light of this result only the homogeneous BC model will be considered in the remainder of the Results, with the heterogeneous BC model and the constant pressure outlet solution revisited in the Discussion.

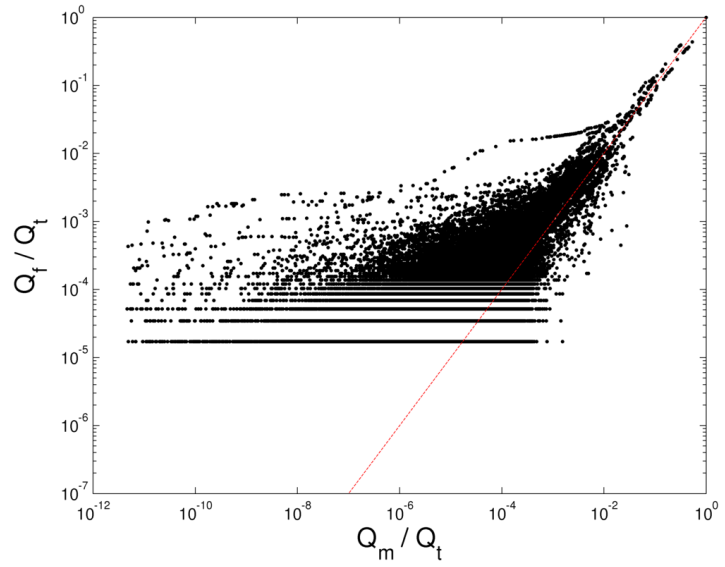

(a)

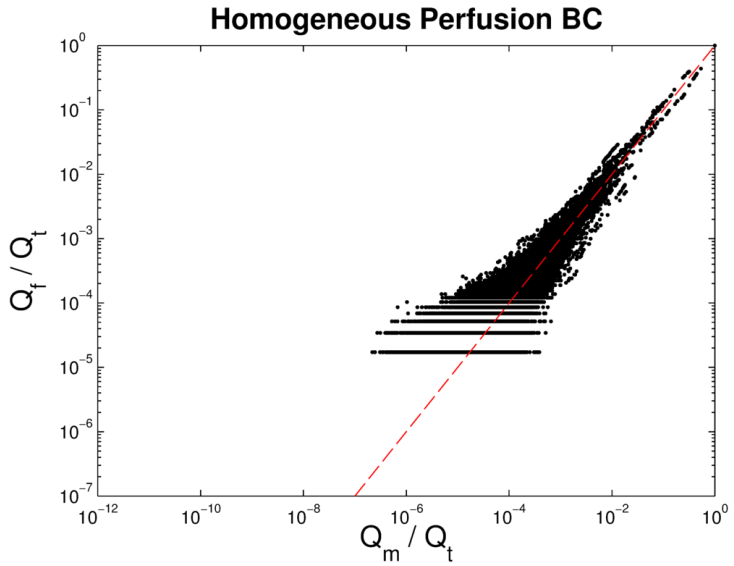

(b)

Figure 4.7: Log-log scatter plots of Q_m (model flow) versus Q_f (microsphere-derived flow) normalised by Q_t (total coronary inlet flow) for the heterogeneous (a) and homogeneous (b) perfusion BCs. Q_m matches Q_f more closely at higher generations, but is considerably worse for the heterogeneous perfusion BC at lower generations (a). The line of identity is indicated by the dashed red line, along which Q_m and Q_f are equal.

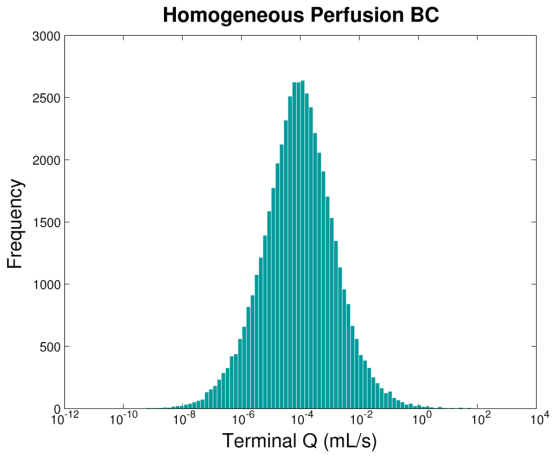

(a)

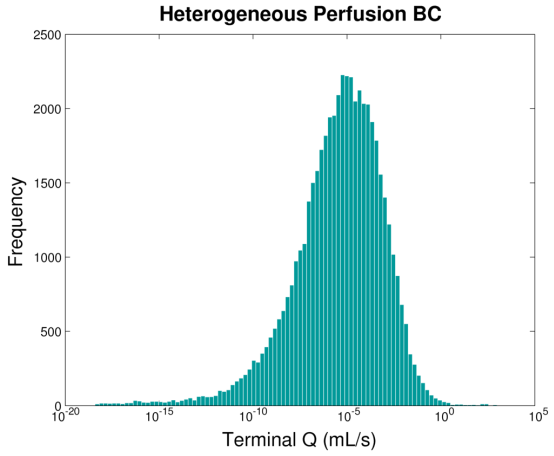

(b)

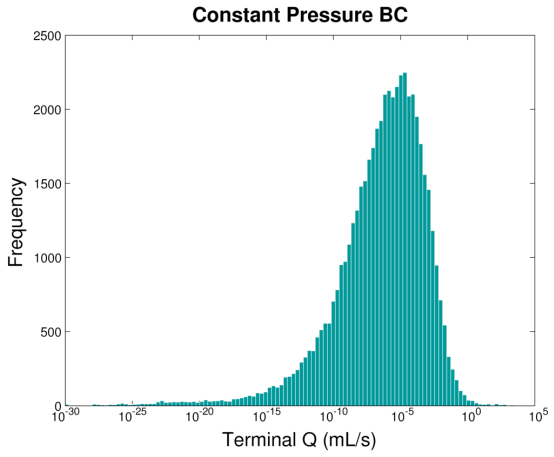

(c)

Figure 4.8: Terminal Q_m distributions for the homogeneous perfusion (a), heterogeneous perfusion (b) and constant pressure (c) BCs, shown with a log_{10} scale.

4.3.2 Network Alterations

RV Feeding Branches

A relationship between volume bins w_j and E_j^{rms} is plotted in Figure 4.9 for the homogeneous perfusion BC model. Bins are numbered on the upper x-axis, and fed volume in mm^3 is plotted on the bottom x-axis for ease of interpretation.

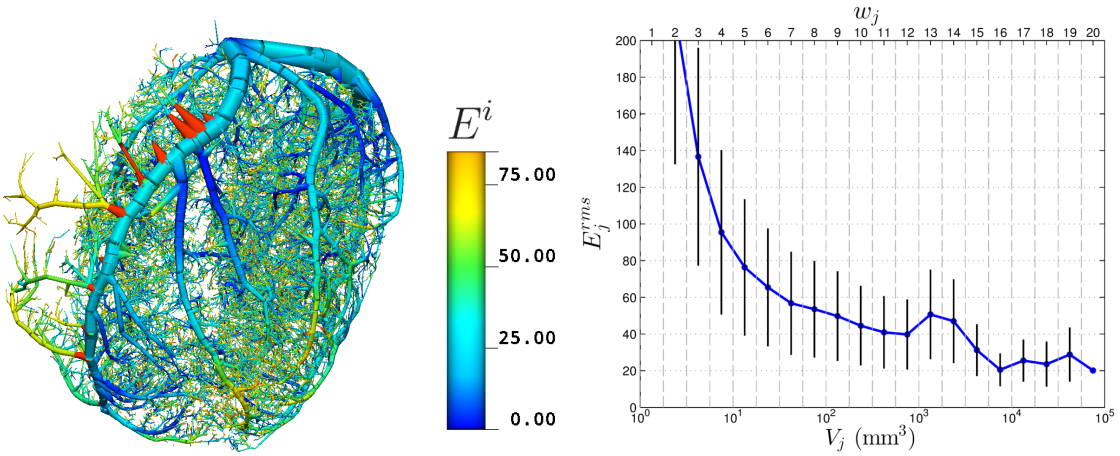

Figure 4.9: Segment flow errors E^i are shown in the 3D LCA coronary network (left) (note only vessels with an error $< 75\%$ are shown). Highlighted in red are the root elements of the RV vessels which are later removed. E_j^{rms} is plotted against bins w_j (right), with the vertical bars corresponding to $\pm 1SD$ displayed for each bin. There is a clear local peak in E_j^{rms} at fed volumes greater than 10^3mm^3 (in bin w_{13}).

Figure 4.9 shows that the relationship between E^{rms} and V is non-monotonically decreasing. There is an increase in E^{rms} from w_{12} to w_{13} bins, just larger than $10^3 mm^3$, and even in the highest volume bin w_{20} the value of E_{20}^{rms} is above 20%. This error corresponds to the large epicardial vessel segments in light blue in the left figure. It is also evident that the errors between Q_m and Q_f are high in the subtrees which feed the RV, whose root elements are highlighted in red and whose terminals are green or yellow indicating segment flow errors E^i greater than 50%. This is most likely due to the sparsity of the vasculature feeding the RV which results in a much larger tissue volume being assigned to those terminal vessels relative to other terminal vessels. Not only are these RV-feeding terminal vessels assigned unequal proportions of microspheres compared to tissue fed volumes

(since mean RV perfusion is much lower than mean LV perfusion), but they also distort the overall flow error in the network, causing excessive model flow to supply the LAD relative to the LCx artery. Therefore the RV-feeding terminal vessels were removed from the analysis, which involved removing their associated microspheres and tissue volumes, and scaling the input network flow by the fraction of the total remaining tissue volume.

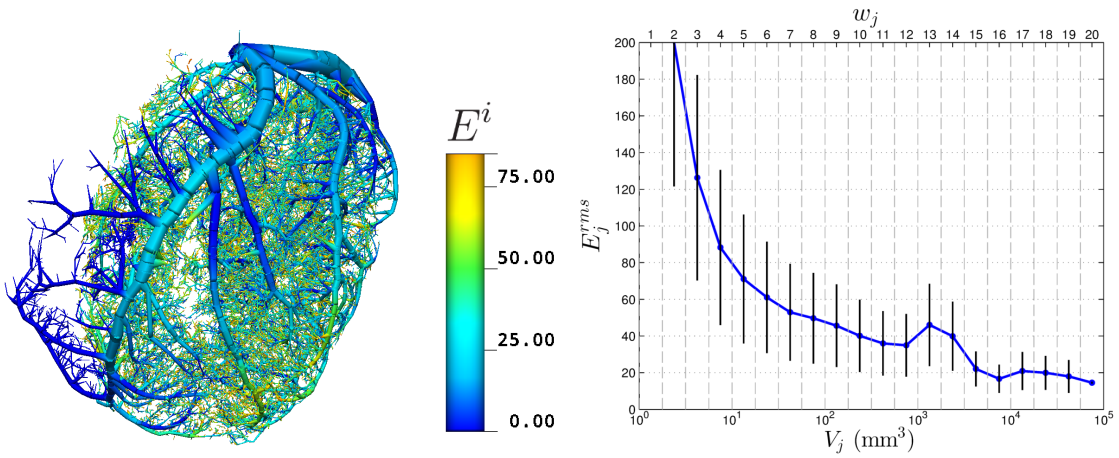

Figure 4.10: Segment flow errors E^i in the 3D LCA network (left) after removing the RV-feeding terminal vessels (note only vessels with an error $< 75\%$ are shown). E_j^{rms} versus w_j is plotted on the right.

Figure 4.10 shows that the removal of the RV vessels reduced the overall error in the vasculature. However, in the largest volume generation w_{20} the flow error is still remarkably high, just below 20%.

Subtree Q_f Normalisation

To investigate the high errors in the large vessels the absolute differences between Q_f and Q_m were compared for the three major subtrees in the network: the left coronary circumflex (LCx), left marginal (LM) and left anterior descending (LAD) arteries. This comparison revealed that model flow in the LAD artery considerably overestimated microsphere flow, and vice versa in the LCx and LM arteries, as shown in Figure 4.11. At the proximal roots of the LCx and the LM arteries Q_f overestimated Q_m by 23.5% and 18.2% respectively, whereas in the LAD Q_m

overestimated Q_f by 18.8%. This indicates that the LAD was assigned disproportionately fewer microspheres relative to tissue volume compared to the LCx and LM arteries. This was most likely due to lower perfusion in the tissue fed by the LAD artery, which consists largely of the RV and septum whereas the LCx and LM arteries supply the LV which is known to have a higher perfusion. This is explained in more detail in the Discussion.

To circumvent these errors, the microsphere flows Q_f, which up to this point were given as a fraction of the total input flow rate to the entire LCA, were recalculated as a fraction of the Poiseuille flow at the root of the LCx, LAD and LM arteries. The values of Q_m throughout the tree are unchanged and only Q_f values are adjusted on an individual subtree basis from Equation (4.17), where Q_m^t is taken as the inlet model flow for each of the three subnetworks. Thus each subtree has a constant perfusion which is different from each of the other subtrees. Flow errors arising from each subtree are shown in Figure 4.12, where values of E^{rms} in the largest volume bins w_j are below 20% for all subtrees.

Removing High Error Subtrees

Errors for the whole LCA network after subtree flow normalisation are considered together; E^{rms} is plotted against volume in Figure 4.13(a). Clearly E^{rms} is still not monotonically decreasing with increasing tissue volume although is lower than before subtree normalisation.

Both plots in Figure 4.13 illustrate that the E^{rms} increases from bin w_{12} ($E_{12}^{rms} = 28\%$) to bin w_{13} ($E_{13}^{rms} = 36\%$). This increase is illustrated in Figure 4.13(a) by the hump around $V = 10^3 mm^3$, and in Figure 4.13(b) by the w_{13} (pink dashed) line traversing the w_{12} (dark blue dotted and dashed) line at a segment flow error of 40%, or in the highest 15% of the w_{13} segment errors. The ordered error line for w_{14} vessel segments in Figure 4.13(b) follows a very similar profile to the w_{13} line, and also crosses over the w_{12} line for a significant fraction of its ordered segment errors.

Plotting for just w_{12} and w_{13} ordered error curves as points in Figure 4.14, it

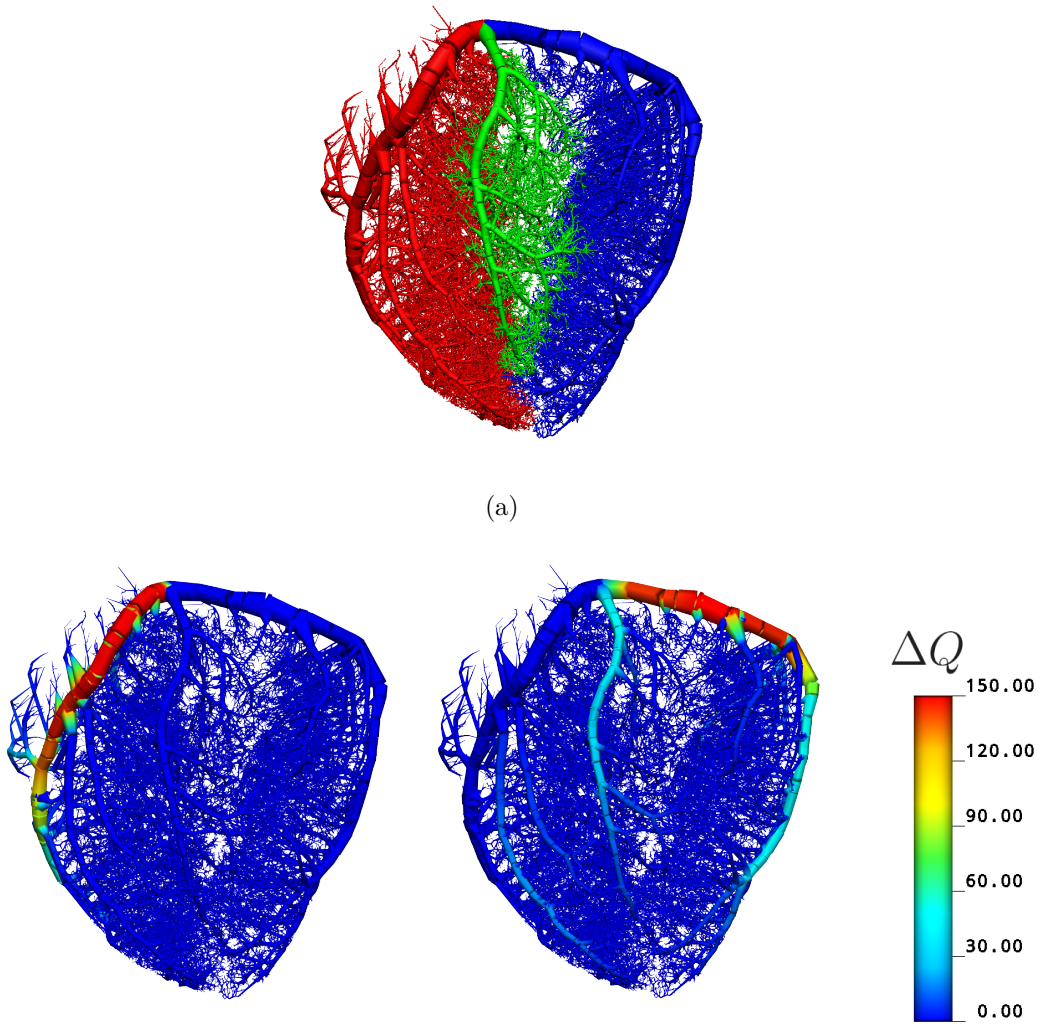

(a)

(b) $\Delta(Q) = Q_m - Q_f$

(c) $\Delta(Q) = Q_f - Q_m$

Figure 4.11: The LCA is colour-coded showing the LAD (red), LM (green) and LCx (blue) sub-networks in (a). The difference in flow favours Q_m in the LAD subnetwork (b), and favours Q_f in the LCx and LM subnetworks as shown in (c). The colourbar refers to flow errors indicated in the figure captions, given in units of $mm^3 s^{-1}$.

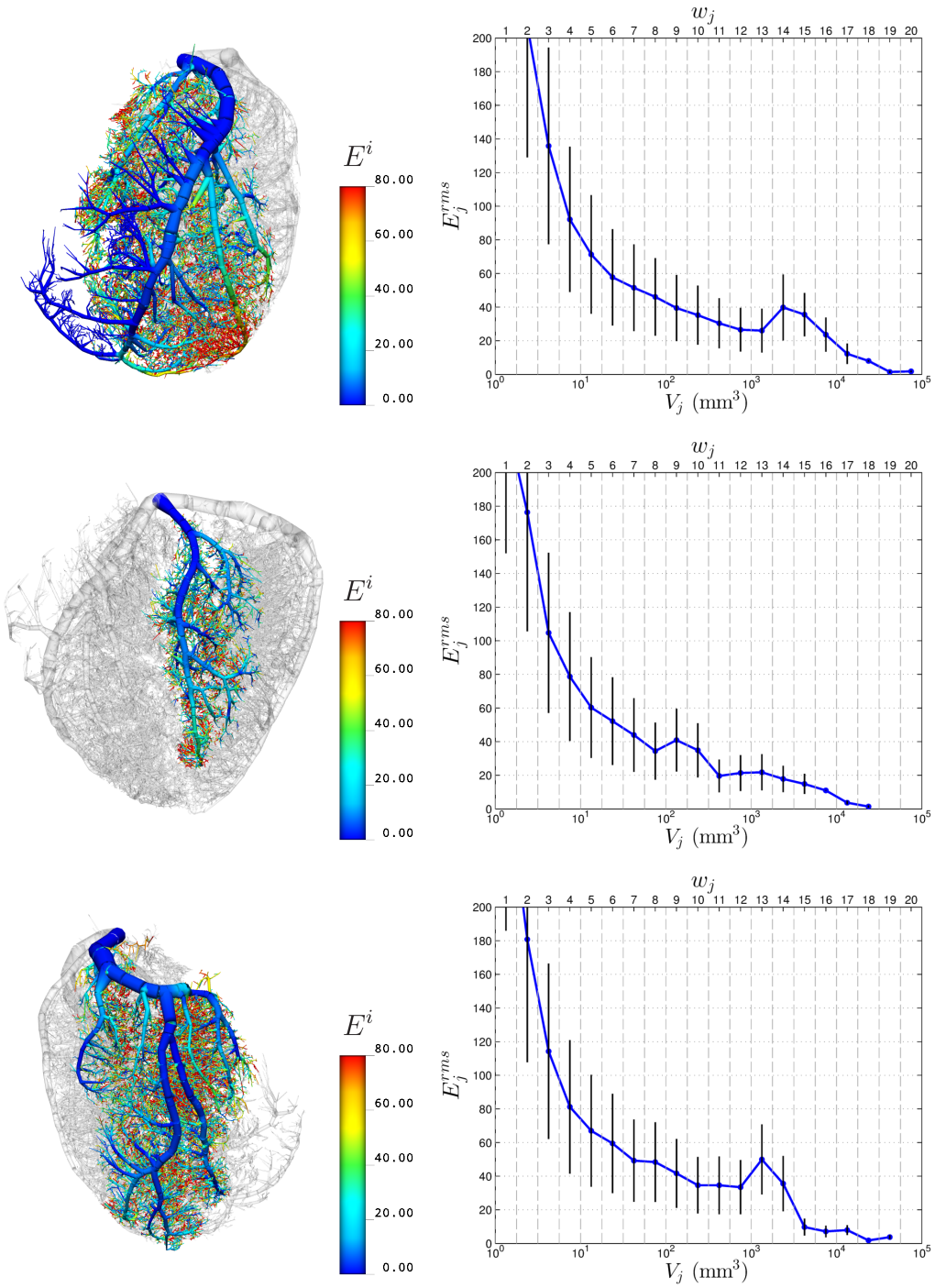

Figure 4.12: The three major subtrees with Q_f normalised to the root flow rate of each subtree are displayed with their respective errors (Eq. (4.16)), here displayed between 0% to 100% (left column). The E^{rms} vs w_j plots are shown to the right for the LAD subtree without RV vessels (top), the LM subtree (middle) and the LCx subtree (bottom).

becomes clear that a cluster of outlier segments have errors of around 90% in bin w_{13}, which is responsible for E_{13}^{rms} being greater than E_{12}^{rms}. The spatial location within the 3D vascular network of vessel segments in bins w_{12} and w_{13} are displayed in Figure 4.15, with w_{13} vessel segments with $> 80\%$ flow error rendered in red.

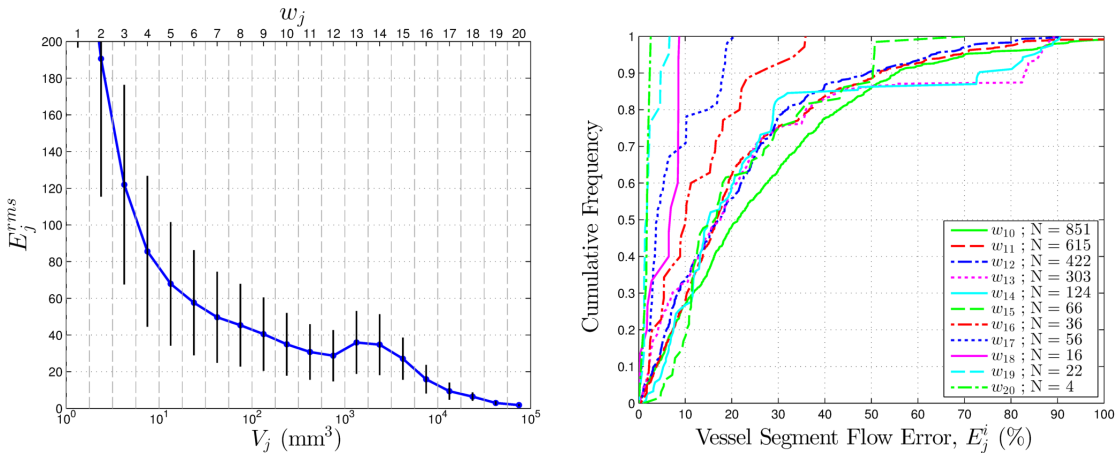

(a) (b)

Figure 4.13: E^{rms} versus volume plotted for the combined 3 subtree flow-normalised LCA network (a). The ordered errors of all vessel segments in bins $w_{10} - w_{20}$ are shown in (b). The legend indicates volume bin w_j and the corresponding number of vessel segments in the bin is indicated by N.

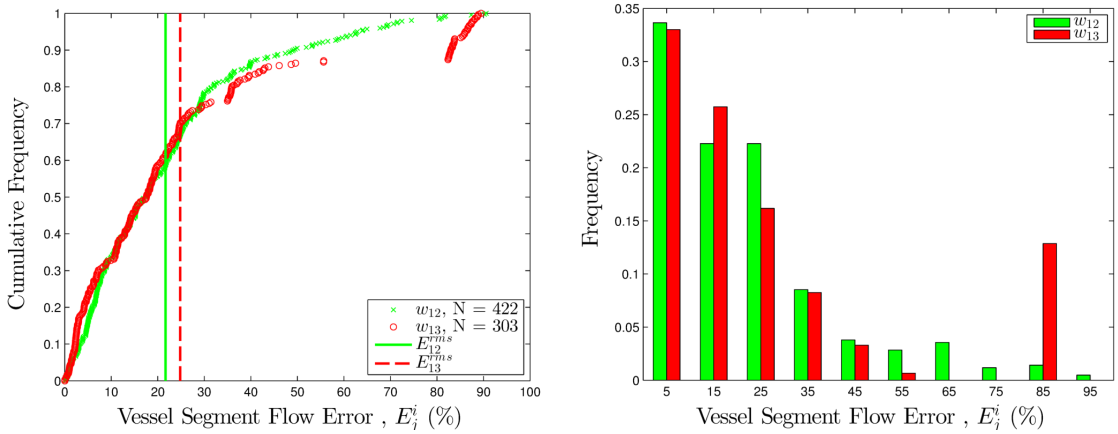

(a) (b)

Figure 4.14: Bin w_{12} and w_{13} ordered errors (a), and histogram (b).

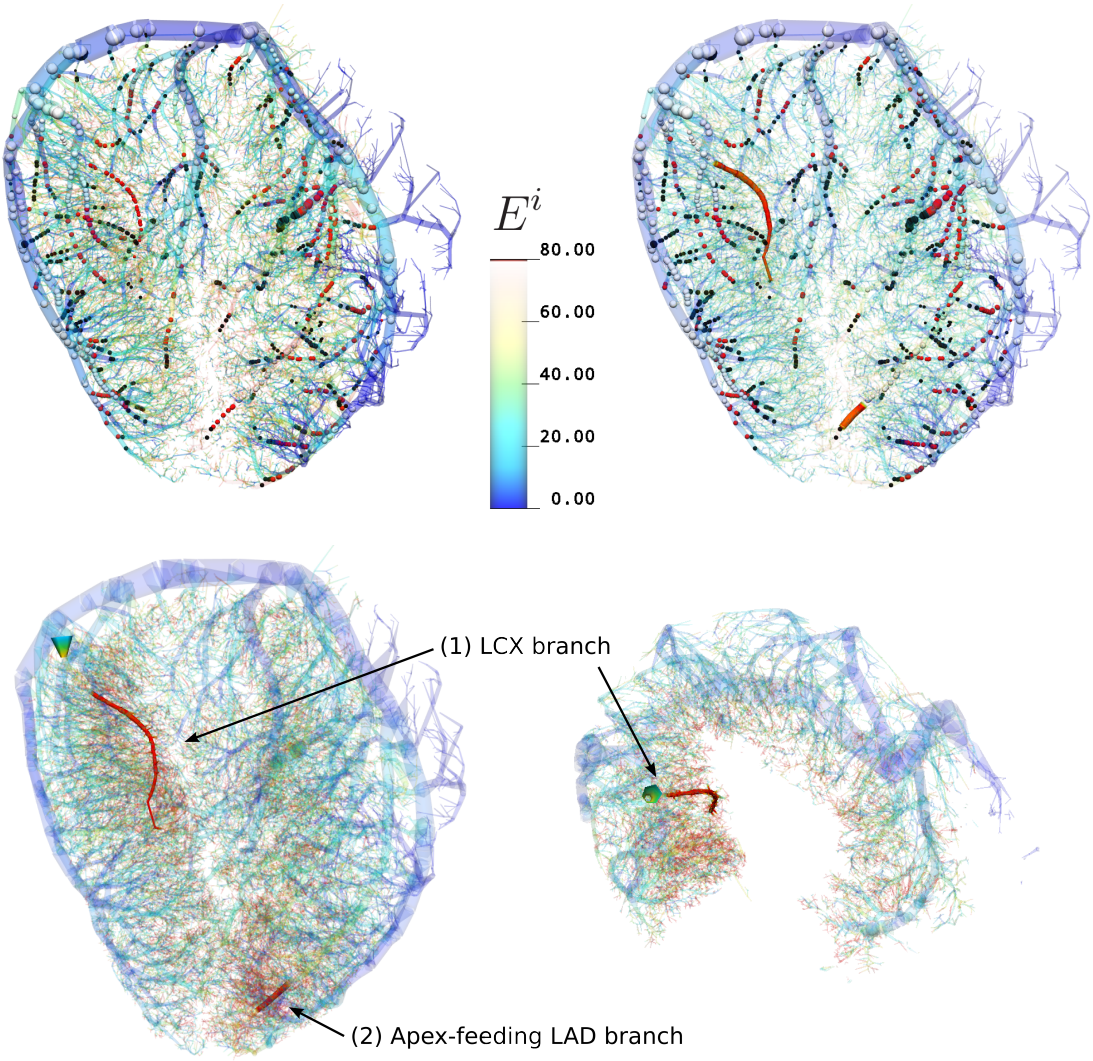

Figure 4.15: Vessel segment end nodes of bins w_{12} and w_{13} are marked with black and red spheres respectively (top row), and white spheres correspond to vessel segment nodes in bins w_{14} to w_{20} (nodes for vessels in bins w_1 to w_{11} are not displayed). The spheres are superimposed on the LCA vasculature displaying the flow errors with scale given in the colour bar. Bin w_{13} vessel segments with $> 80\%$ error are displayed in red (top right, and bottom row), indicating two regions: (1) a branch in the LCx subtree and (2) a branch near the apex stemming from the LAD subtree. These two branches are shown alone for clarity superimposed on the LCA vasculature in the bottom row. The opaque green cone is the root vessel segment of the high error w_{13} branch stemming from the LCx subtree. A short axis MIP (bottom right image) shows that this branch descends along the subendocardium.

There are two clear subtrees with unusually high errors shown in Figure 4.15, one branching from the LCx trunk and one near the apex branching from the LAD trunk. Examining firstly the subtree branching from the LCx trunk reveals an error in the connection point of an apparent terminating vessel, shown in Figure 4.16. A distal portion of the high-error subtree (shown in blue below) contains a terminating vessel with an unusually large radius. It appears that this large-radius terminal vessel should instead have stemmed from another nearby large-radius terminating vessel, but has falsely been connected in the network reconstruction process to the high-error subtree via distal microvasculature.

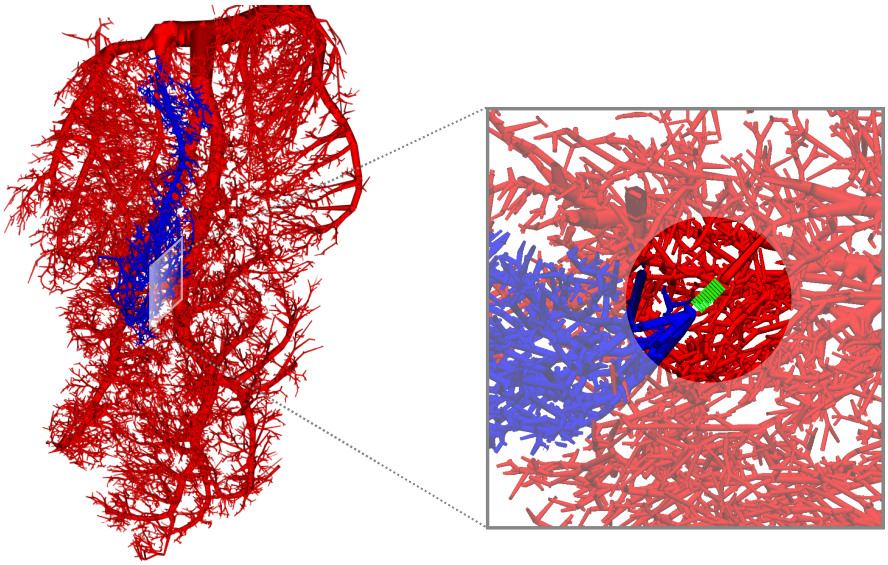

Figure 4.16: A section of the LCx network is displayed (in red) with the endocardial side facing out of the page (left). The high-error branch identified in Figure 4.15 and all of its downstream vessels are shown in blue. The cross-section window in the lower part of the subtree is shown zoomed in (right), and contains a large-radius terminating vessel. A banded green line indicates where a connection should have been made with the network reconstruction algorithm.

Removal of this high-error branch from the whole-network analysis causes the E^{rms} from bin w_{12} to w_{13} to decrease, as shown in Figure 4.17. The results of the updated network however still contain an increase in E^{rms} between bins w_{13} and w_{14}, again due to high-error outliers identified in the ordered error plots shown in Figure 4.18.

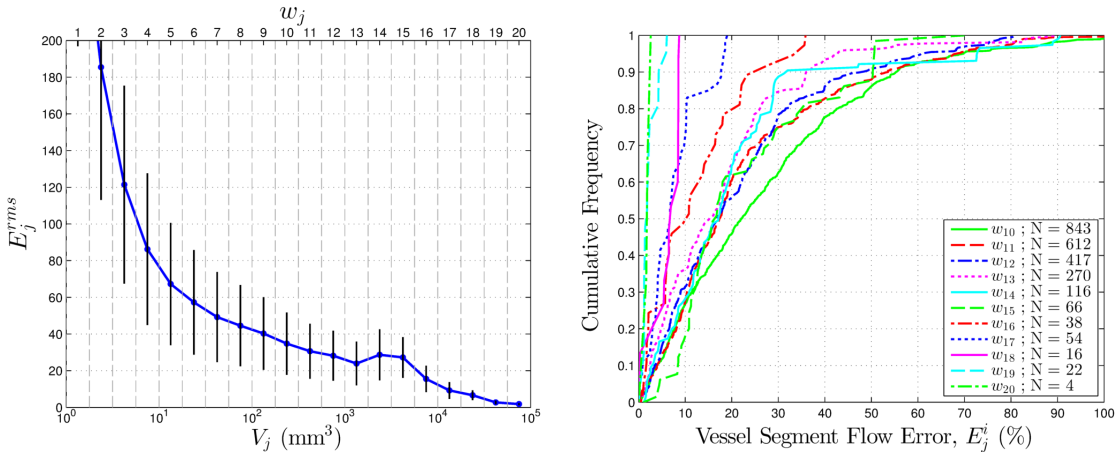

(a) (b)

Figure 4.17: E^{rms} versus volume plotted for the combined 3 subtree flow-normalised tree with the removed subtree stemming from the LCx trunk (a). The ordered errors of all vessel segments in bins $w_{10} - w_{20}$ are shown in (b), where volume bin and number of constituent vessel segments are given in the legend.

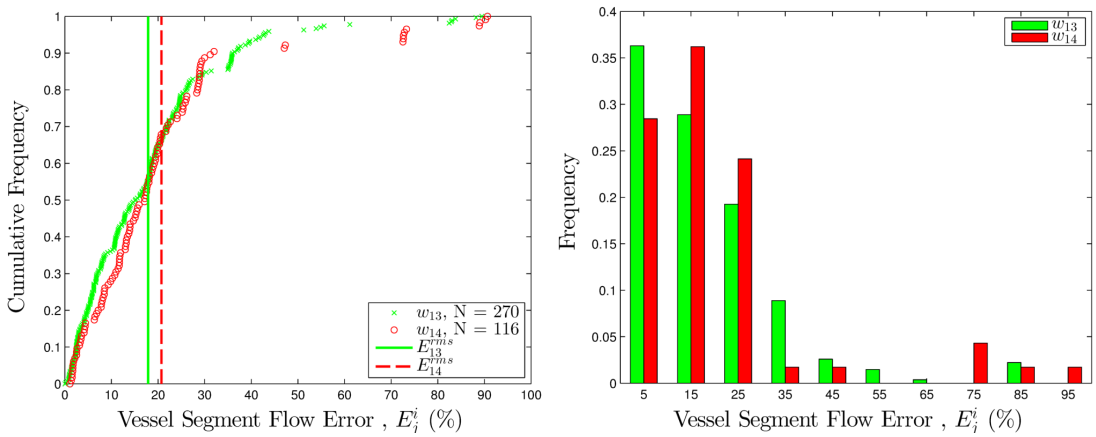

(a) (b)

Figure 4.18: Ordered vessel segment errors for bins w_{13} and w_{14} after excludusion of the high-error LCx subtree plotted in order of magnitude (a) and as a histogram (b).

The vasculature containing vessel segments in bin w_{14} with $E^i > 70\%$ are visualised on the 3D LCA network in Figure 4.19 revealing the high-error region corresponds to an apex-feeding subtree branching from the LAD trunk, which was also identified before in Figure 4.15.

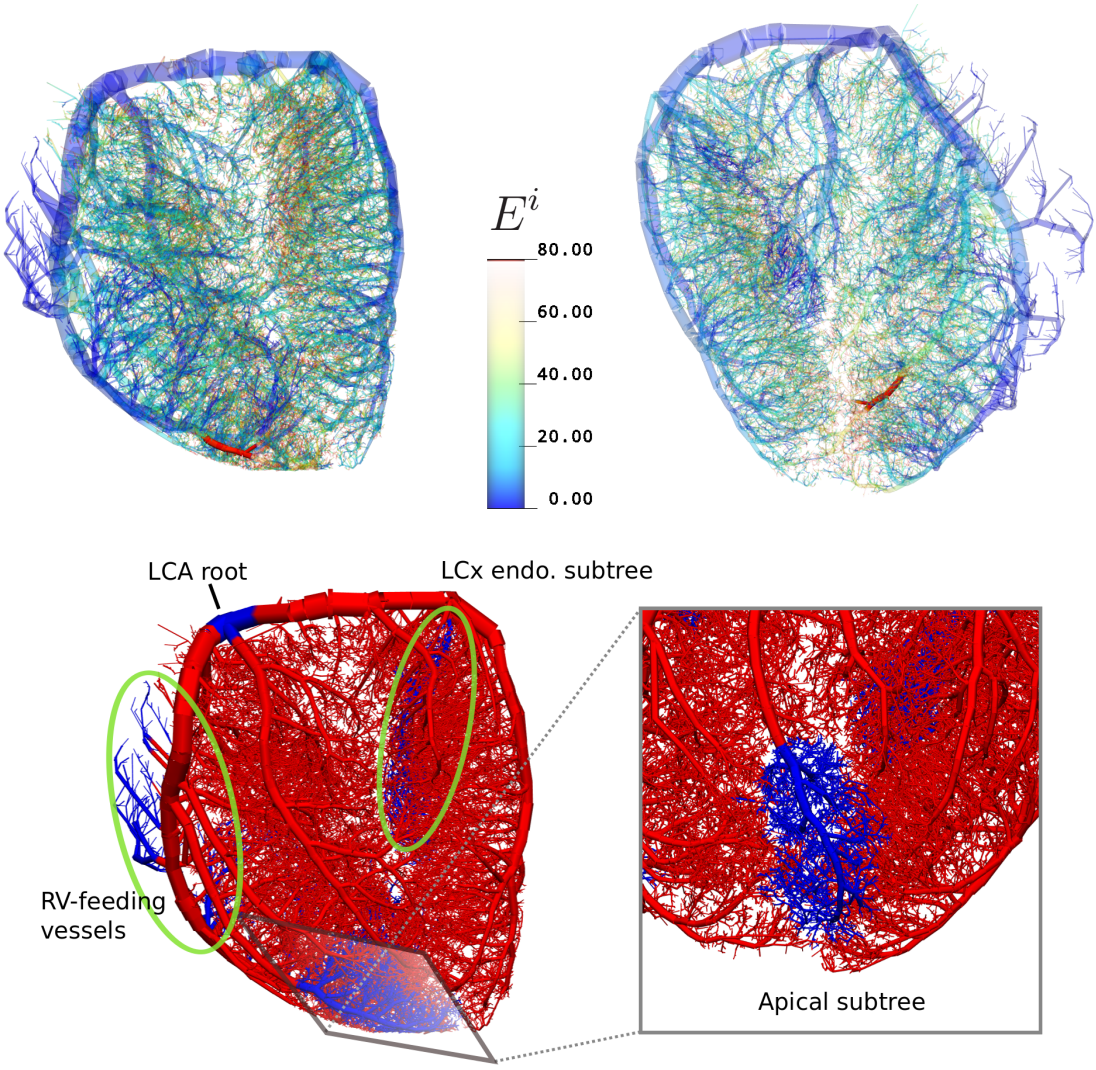

Figure 4.19: The vessel segments in bin w_{14} with a flow error $E^i > 70\%$ are highlighted in red (top row), superimposed on the LCA vascular tree with segment flow errors corresponding to the colour bar. An antero-lateral view (top left) and a posterior view (top right) of the vascular network are shown. All associated downstream vessels of the apex-feeding branch are shown in blue from an anteroinferior view of the apex (bottom right); all vessel segments which were removed from the flow error analysis are shown in blue (bottom left); these include the apical subtree, the RV-feeding vessels, the LCx endocardial subtree and the root of the entire LCA where Q_f was normalised for each individual major subtree (LCx, LAD and LM).

The model flow Q_m underestimates Q_f in the apical subtree quite significantly. The apical subtree therefore is provisionally excluded from the analysis, which

reduces the E^{rms} significantly in the volume range of $10^3 - 10^4 mm^3$, leading to an almost monotonically decreasing E_j^{rms} vs w_j relationship as shown in Figure 4.20(a). This is also illustrated in the ordered vessel segment errors plot in Figure 4.20(b) where the overlap of error lines from one bin to the next is small compared to the ordered error plots from before the removal of the apical subtree (Figure 4.17).

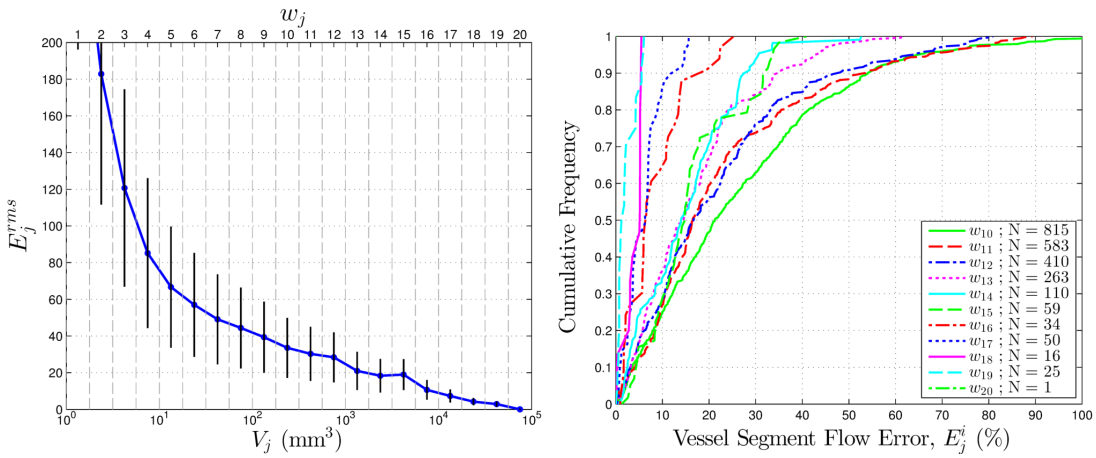

(a) (b)

Figure 4.20: Error versus FV plot for the combined 3 subtree flow-normalised tree with the removed LCx and apical subtrees (left). Ordered bin errors are shown on the right, where the bin 15 error line traverses the bin 14 line.

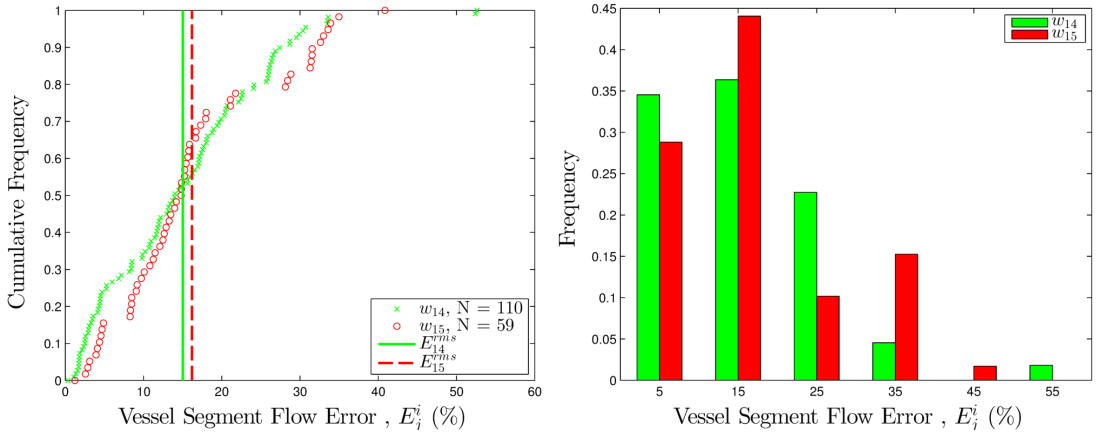

(a) (b)

Figure 4.21: Ordered vessel segment errors for bins w_{14} and w_{15} after excludusion of the high-error LCx and apex-feeding subtrees plotted in order of magnitude (a) and as a histogram (b).

However there is still a slight increase in E^{rms} between bins w_{14} and w_{15} (as shown in Figure 4.21). The vessel segments in bin w_{15} with $E^i > 30\%$ make up a greater proportion of vessel segments than those in bin w_{14} with $E^i > 30\%$. Visualising this on the vascular network identifies another, parallel branch stemming from the LAD and feeding the apex, which is highlighted in red in Figure 4.22. Removal of this subtree from the analysis however did not significantly improve the E^{rms} versus w relationship. For this reason no further subtrees are removed from the network. A mathematical relationship between removed microspheres and tissue volume with error in subtrees of the remaining network is presented in Appendix A.

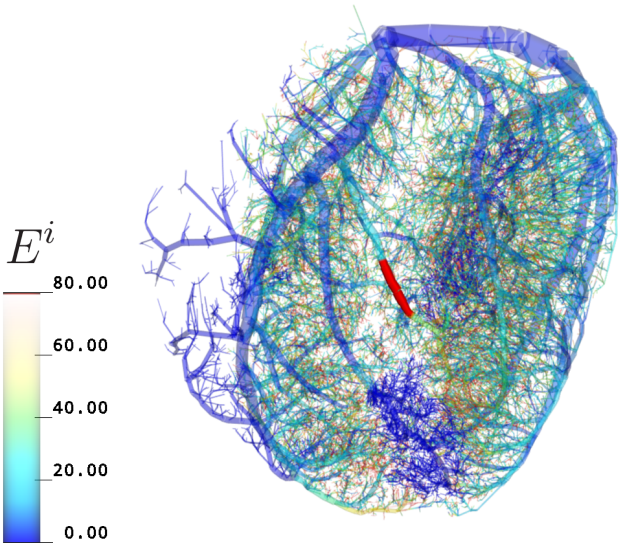

Figure 4.22: An anterior view of the LCA shows the vessel segments with $E^i > 30\%$ in bin w_{15} highlighted in red. The colourbar shows flow errors in the vascular network. Note the dark blue distal subtree near the apex corresponds to the removed apical subtree.

The final network contains a total of 51,442 microspheres distributed to 46,820 terminal vessels, and an LCA tissue fed-volume of $146.6cm^3$. For comparison, before removal of any vessel subtrees a total of 58,154 microspheres were distributed to 51,817 terminal vessels with a total LCA tissue fed-volume of $171.5cm^3$.

4.3.3 Terminal Flow Perturbation Analysis

A perturbation analysis was carried out where terminal vessel perfusion was perturbed randomly at different levels of heterogeneity, specified by a standard deviation of terminal flows, σ = 20%, 40%, 60% and 80%. Figure 4.23 shows that differences between the homogeneous perfusion BC model and perturbed perfusion BC model decrease rapidly in higher volume bins, w_j. From bin w_7 upward, differences between the maximum and minimum perturbed BC model flow errors $\hat{E}_j^{rms}$ in each bin w_j and the unperturbed BC model flow errors E_j^{rms} are minimal, between approximately 1%-2% for all levels of heterogeneity as shown in Figure 4.24. This corresponds to fed volumes greater than approximately $100mm^3$, or 0.1g. Thus introducing terminal perfusion heterogeneity does not significantly affect the flow errors in higher generation vessels, in which the comparison of Q_f and Q_m is more meaningful since Q_f is subject to lower Poisson noise (due to higher numbers of microspheres).

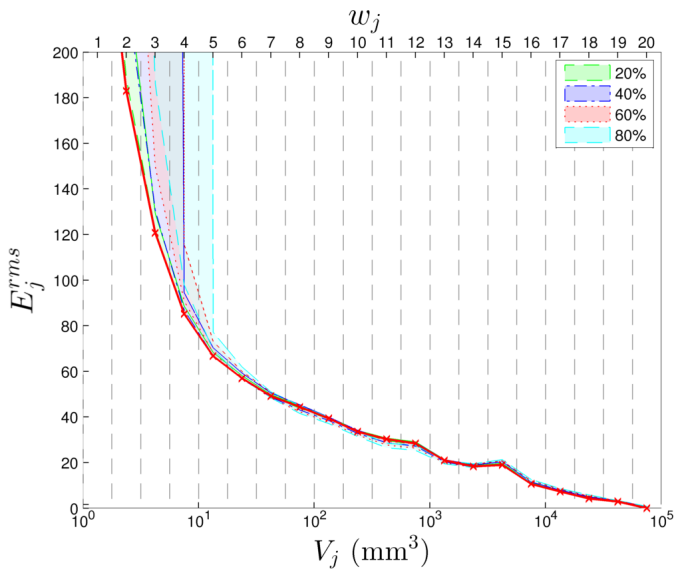

Figure 4.23: E_j^{rms} vs w_j from the perturbation analysis with 1000 trials at terminal flow heterogeneities sampled with σ = 20%, 40%, 60% and 80%, indicated in the legend. The homogeneous perfusion BC model error curve is marked with a red line and crosses. Shaded regions correspond to the area between the minimum and maximum RMS error values, $\hat{E}_j^{rms}$, in each w_j bin from the 1000 trials at each heterogeneity level, σ.

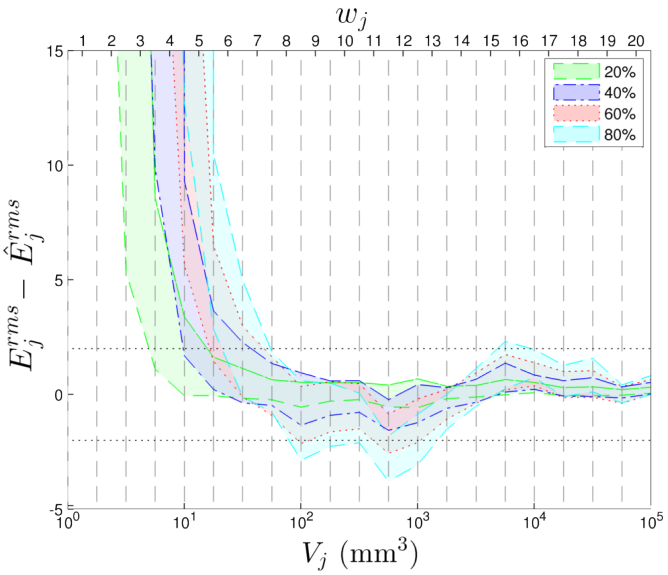

Figure 4.24: $E_j^{rms} - \hat{E}_j^{rms}$ vs w_j from the perturbation analysis with 1000 trials at heterogeneity levels $\sigma = 20\%$, 40%, 60% and 80%, indicated in the legend. The difference between the homogeneous BC model errors and the max/min perturbed BC model errors, E_j^{rms}-$\hat{E}_j^{rms}$, in each bin w_j is plotted. Dashed horizontal lines indicate a difference of $\pm 2\%$.

The fractal dimension D computed from the linear fitted relation of RD and tissue size for the four levels of terminal vessel perfusion heterogeneity provide insight into the effects of such perturbations on perfusion heterogeneity in the upstream network. For each volume bin w_j, vessel segments upstream of other vessel segments in the same bin were discarded for the computation of RD to ensure only unique tissue territories were considered. This ensured that the computation of RD was not biased towards perfusion in any particular tissue region.

Figure 4.25 shows RD plotted against fed volume at each level of heterogeneity, where datapoints correspond to RD computed in volume bins w_1 to w_{17} (which are shown only in terms of fed volume for simplicity). RD in each bin w_j is the average RD from 100 perturbation trials for a given terminal perfusion heterogeneity level σ. The bottom plot shows a fitted linear function across all fed volumes $1 - 10^4 mm^3$ and indicates that increasing σ increases RD, and reduces the value of D from 1.46 at $\sigma = 20\%$ to 1.33 at $\sigma = 80\%$. RD computed from the microspheres in the same vessels (additionally correcting for Poisson noise) shows a higher RD

at all fed volumes compared to the model even at $\sigma = 80\%$, with a lower fractal dimension $D = 1.18$.

Since perfusion heterogeneity was introduced randomly at the terminal vessels, one would expect the fitted values of D to reflect this. The top plot in Figure 4.25 shows that fitting a linear function between RD and fed volume for the smaller half of the tissue fed volumes, $1 - 100mm^3$, produces values of $D = 1.5$, 1.49, 1.47 and 1.46 for terminal perfusion heterogeneity levels of $\sigma = 20\%$, 40%, 60% and 80%, respectively. These values are all close to 1.5 indicating uncorrelated perfusion of neighbouring tissue regions, as is expected for introducing random perturbations of terminal vessel perfusion (Van Beek *et al.* , 1989).

However fitting a linear function between RD and fed volume in the larger half of the tissue fed volumes, $100 - 10^4mm^3$, produces values of $D = 1.41$, 1.30, 1.24 and 1.22 at $\sigma = 20\%$, 40%, 60% and 80%, respectively. These values are closer to physiological values observed in baboon hearts in the range of 1.1-1.30 (Bassingthwaighte *et al.* , 1989), which are considered to have moderate correlation of local perfusion. This suggests that despite terminal vessel perfusion perturbations being random, the higher generation vessels of the network feeding tissue regions of greater than approximately $100mm^3$ in volume seem to have more correlated neighbouring tissue segment perfusion.

Furthermore higher values of σ result in higher RD values and lower values of D, approaching the values obtained from the microspheres. At a tissue volume of 10^3mm^3 (or $\approx 1g$ mass) $RD = 26\%$ for the microspheres, which is similar to observations in sheep, baboons and rabbits in the same tissue size (Bassingthwaighte *et al.* , 1989). The fitted relation between RD and fed volume produced values of $D = 1.18$ across the full range ($1 - 10^4mm^3$), $D = 1.23$ in the smaller half of fed volume bins ($1 - 10^2mm^3$), and $D = 1.13$ in the larger half ($10^2 - 10^4mm^3$). Despite the decrease of D when computed from the larger fed volume bins, these values are both within a physiological range.

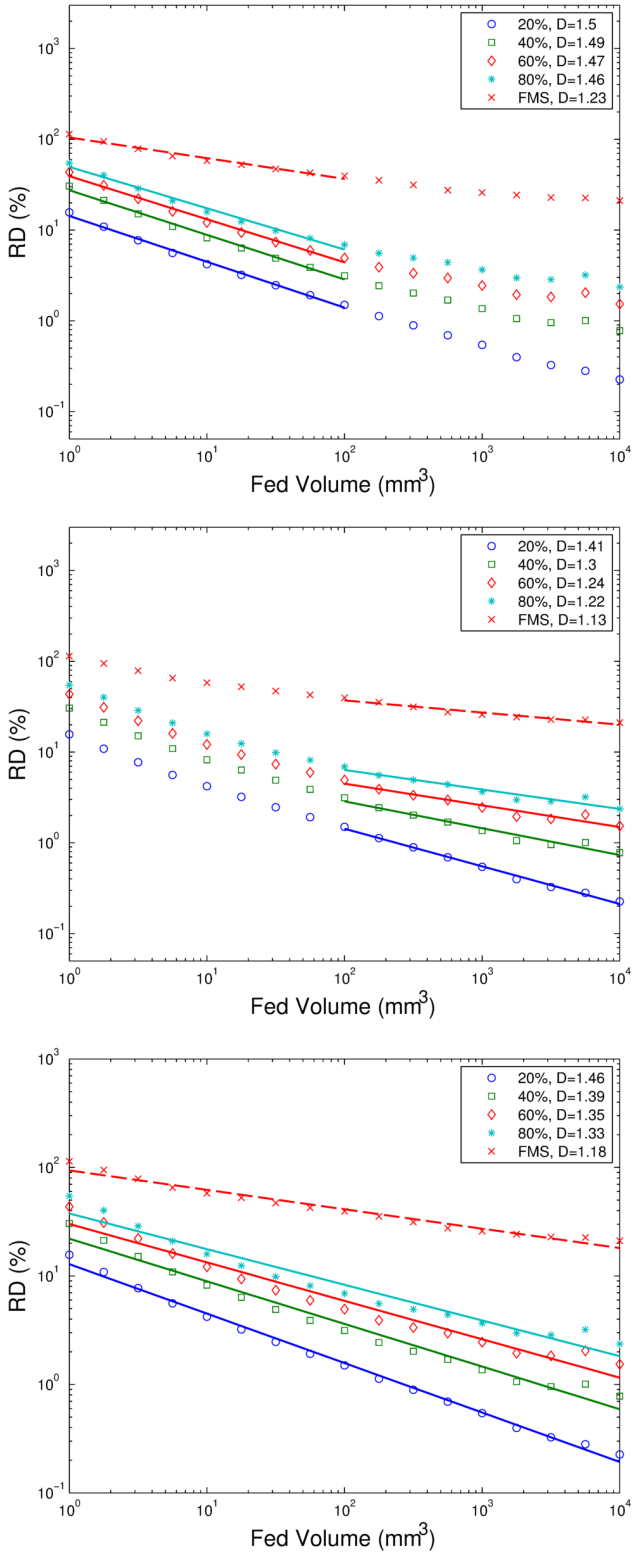

Figure 4.25: *RD* versus fed volume with perturbed terminal perfusion at heterogeneity levels of $\sigma = 20\%$, 40%, 60% and 80%, along with the relation obtained from the microspheres. The relation is fitted for segment sizes from $1 - 100mm^3$ (top), $100 - 10,000mm^3$ (middle), and $1 - 10,000mm^3$ (bottom).

4.3.4 Fed Volume and Microsphere Accuracy Limits

In Figure 4.26 the theoretical error, E_t, between the upper 95% confidence limit and the expected number of microspheres $f.X_t$ reaching a tissue segment is plotted, assuming microsphere deposition to a tissue segment follows a binomial distribution (see Section 4.2.5). The relationship of E_i and the actual number of microspheres N passing through vessel segments in the network is plotted, both in individual segments (grey dots) and as the mean $E_{i,j}$ in bins j of microspheres N (black line and dots). The mean flow errors exceed the theoretical error for most of the range of N. This is explored further in the Discussion.

In light of the perturbation analysis results, the E_j^{rms} versus w_j relation for the model using the homogeneous perfusion BC can be used to estimate a minimum fed volume to obtain microsphere results with a desired accuracy. Figure 4.27(a) shows that for microsphere deposition measurements to be within approximately 20% of the model flow, a tissue size of at least 1g needs to be used. This corresponds to a minimum requirement of approximately 400 microspheres for the same flow accuracy as shown in Figure 4.27(b).

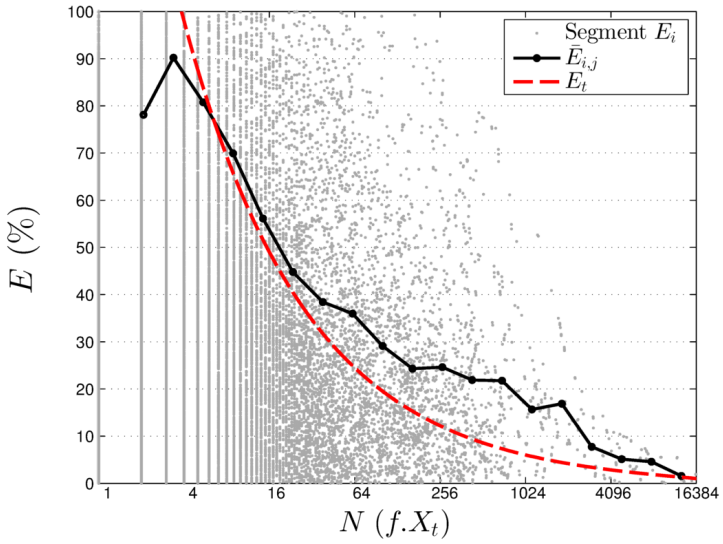

Figure 4.26: Flow error plotted against microsphere count, N. Grey dots represent segment flow errors E_i, the black line and dots are mean segment errors $E_{i,j}$ for bins j of microsphere counts N. The theoretical error E_t at the 95% confidence limit for expected number of microspheres $f.X_t$ according to a binomial distribution is given by the dashed red line.

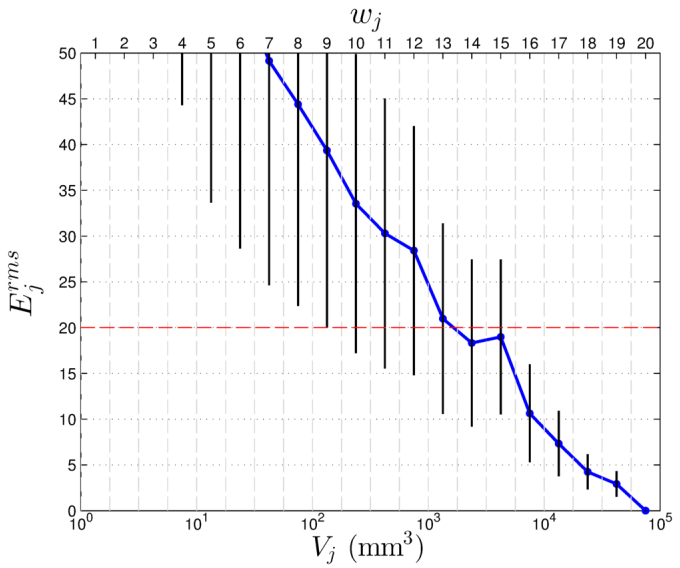

(a)

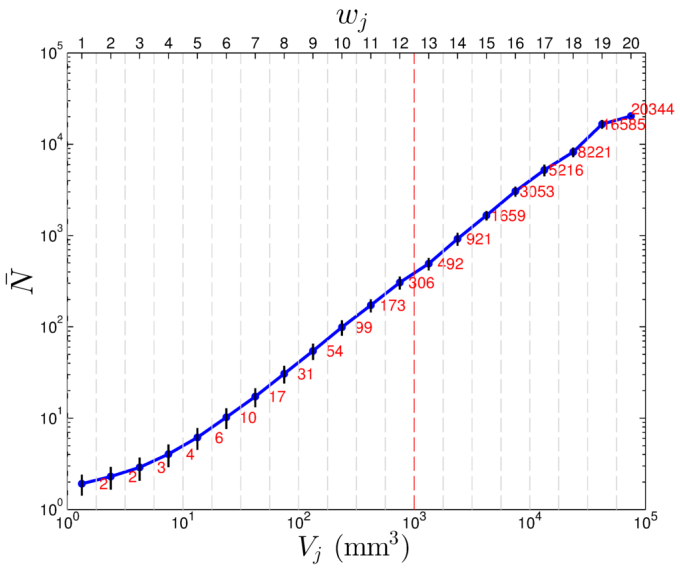

(b)

Figure 4.27: The E_j^{rms} vs fed volume plotted for the final pruned network, indicating that tissue segments of approximately 1g mass are required for microsphere flow quantification accuracy within 20% of true flow, (marked with a horizontal dashed red line) in (a). A tissue mass of 1g is marked with a vertical dashed red line in (b) and corresponds to an approximate minimum number of microspheres of 400, where mean microsphere count, $\bar{N}$ is listed for each volume bin in red. Vertical black lines indicate $\pm 1SD$ of y-axis variables.

4.4 Discussion

The primary goal of this study was to relate flow error between a Poiseuille model and microsphere distribution as a function of tissue fed volume. This comparison allowed for several sources of error to be identified. Firstly an over-allocation of tissue fed volume to the terminal vessels in the RV was identified. The terminal vessels of the LAD artery were notably allocated a larger average total tissue fed-volume than the LCx and LM artery terminal vessels. The mean tissue volume assigned to LAD terminal vessels was $3.57mm^3$ (after removal of the RV-feeding vessels) compared to $2.49mm^3$ in the LCx. The larger fed-volumes assigned to the LAD terminal vessels was due to a higher spatial sparsity of terminal vessels compared to those in the LCx subtree. As shown in Figure 4.28 the RV territory contained a disproportionately large myocardial tissue volume for the number of local terminal vessels relative to the rest of the LCA territory. In future this may be partially rectified by obtaining images with cast in both the LCA and RCA, which when bounded by a whole-heart myocardial segmentation would provide more realistic tissue boundaries for each arterial tissue region. After removal of the RV vessels from the analysis, overall flow error in the network was reduced by between 4-10% in the highest 10 volume bins w_j.

Secondly, an unexpectedly large flow error in the major arterial subtrees of the LAD versus the LCx and LM arteries was identified. This was accounted for by normalising microsphere flow by the total Poiseuille flow at the root of each subtree. The LAD artery supplied a tissue territory with approximately 30% lower microsphere density (equivalent to perfusion) than the LCx/LM arteries. The tissue allocated to the LAD territory mostly lies in the RV and septum as shown in Figure 4.28. The RV is known to receive a lower perfusion than the LV, shown for example in rabbit and sheep hearts (Bassingthwaighte *et al.* , 1987, 1990), and the septum is known to receive lower perfusion under stress-testing in humans (Muehling *et al.* , 2004). Normalising microsphere flow by the inlet flow of each subtree matched the mean microsphere perfusion with the model perfusion in each subtree which in turn brought the flow error to zero at the inlet of each individual subtree. Subtree root normalisation reduced flow error in the highest 10 volume

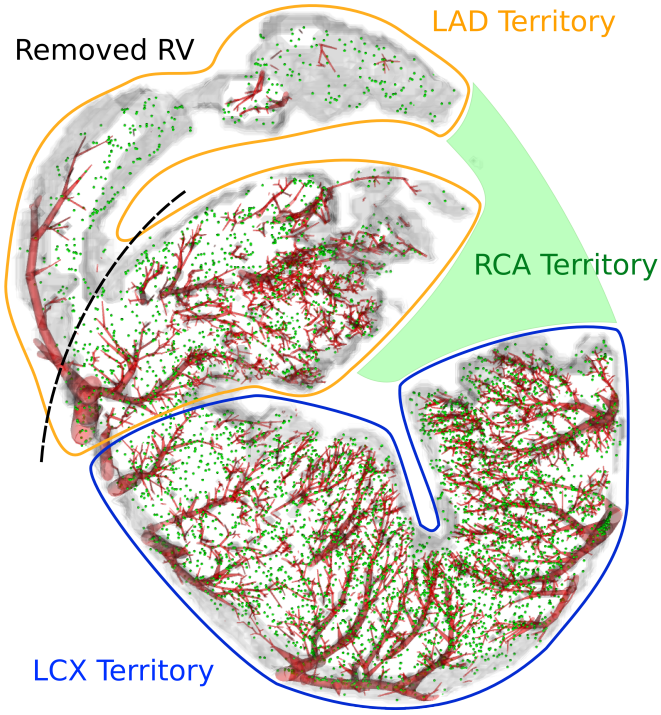

Figure 4.28: A short-axis MIP from 100 images of the LCA vasculature (red), microspheres (green) and LCA myocardial territory (grey outline). Perfused territories of the LAD and LCx arteries are labeled (orange and blue respectively); the dashed black line demarcates the RV and LV tissue fed by the LAD artery, which was excluded from the study; the missing RCA myocardial territory is shaded in green.

bins w_j by approximately 7% on average.

The use of ordered error plots comparing flow errors of vessels in different volume bins w_j provided a way of identifying errors in the vascular reconstruction. Specifically a high-error subtree branching from the LCx was identified, and an apex-feeding subtree stemming from the LAD. The high-error subtree branching from the LCx was the result of a falsely connected terminal vessel which had a large radius. This terminal vessel should not have been one at all, but should instead have been part of a feeding arteriole connected to another subtree branch stemming from the LCx artery (see Figure 4.16 on page 127), which was confirmed upon examination of the image stack of the vascular cast as shown in Figure 4.29. It appears that the large radius terminating vessel was not connected to the correct upstream vessel in the reconstruction due to a discontinuity of the vascular cast

where it terminated.

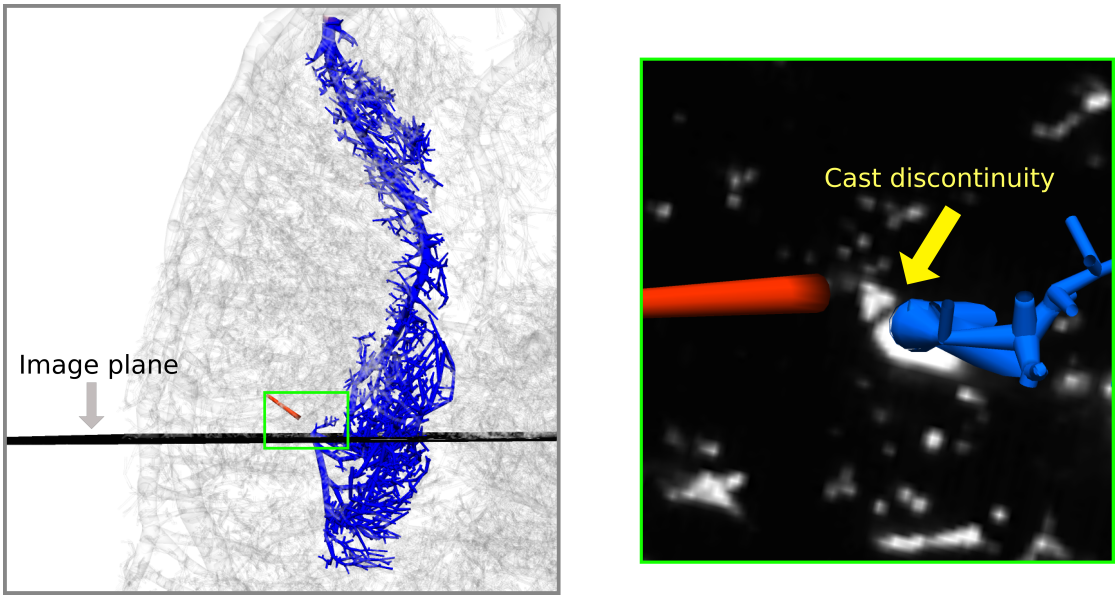

Figure 4.29: The whole high-error subtree stemming from the LCx artery is shown in blue in the left image, where a red vessel segment stemming from another LCx subtree is shown. The red segment appears it should have connected with the large-radius downstream terminating vessel in the high-error subtree, intersecting with the image plane in the green box. In the right image a view into the image plane reveals a discontinuity in the vascular cast adjacent to the terminating large radius vessel (blue) where the other (red) vessel seems should have connected.

After removal of this high-error subtree stemming from the LCx, another high-error subtree feeding the apex was identified stemming from the LAD. In the apex-feeding subtree Q_f significantly overestimated Q_m, where perfusion to the subtree myocardial territory was 70% higher than the average perfusion in the LAD myocardial territory. This subtree supplied a myocardial territory bordering the LCx territory and indeed may have been assigned some of the tissue territory that in reality was supplied by the LCx, which has a higher perfusion than the LAD territory. Removing this subtree was not the ideal solution for reducing overall network flow error as other subtrees consequently had an increased flow error (see Appendix A for an explanation). This is ultimately a limitation of the homogeneous perfusion BC (normalised for each major LCA subtree), where local perfusion heterogeneity is disregarded. Ideally terminal vessel perfusion should be estimated based on a molecular tracer which does not suffer the same inaccuracies

as microspheres in small tissue regions (Bassingthwaighte *et al.* , 1987). Currently however there are not any such tracers reported in the literature for simultaneous imaging with microspheres using the cryomicrotome.

Another unexpected result was the large discrepancy between the heterogeneous and homogeneous perfusion BC models in terms of flow errors across volume generations. One possible cause for such high errors obtained from the heterogeneous perfusion BC is the wide range of terminal fed volumes spanning several orders of magnitude (see Figure 4.7 on page 118). Since terminal fed volume is determined by radius-weighted distance of each voxel from each terminal vessel, a constant fed volume amongst all terminal vessels would be achieved if spatial terminal vessel density and radius were constant, which is not the case.

Marxen's results for a rat renal network flow model parameterised with the heterogeneous BC did not show the same magnitude of errors between Q_f and Q_m as in this study (see Figure 2 in Marxen *et al.* , 2006). A number of factors may have contributed to the higher errors including inaccuracy of terminal vessel radius estimation, disconnected vessel subtrees, and pruning of large radius terminal vessels (all discussed in the previous chapter). Each of these factors would have affected the terminal vessel fed volume allocation. While for the homogeneous BC these errors were likely to cancel out in higher vessel generations, for the heterogeneous BC the added downstream resistance R_S was dependent on an estimated terminal vessel resistance R_T according to its volume order (see eq. 4.12 on page 105). The high variability in the relation between vessel segment conductance and volume order (see Figure 4.4 on page 104) suggests that estimating terminal resistance based on its fitted relationship with fed volume is not an ideal approach. Vascular volume density is significantly higher in the subendocardium relative to the subepicardium (van Horssen *et al.* , 2014); such distribution heterogeneity suggests that scaling laws cannot be applied globally to the coronary circulation.

It is possible that the heterogeneous BC model would perform better when applied to a truncated network whose terminal vessels' radii and fed-volumes were within the same order of magnitude. However truncating the vascular network at an

upstream level to ensure greater radius accuracy for this purpose would have the negative effect of losing information about the spatial domain of the downstream network, which is important when comparing to microsphere distributions. In the future a more accurate radius estimation algorithm should be used. Firstly radius estimation should ideally be performed directly on the CMT imaging data (as opposed to thresholded filtered data) such as the Rayburst algorithm (Rodriguez *et al.* , 2006), and secondly validation studies should be performed with phantom data to account for imaging parameters of the fluorescent CMT. This second step could be achieved by simultaneously imaging various sized tubes of known diameter filled with the same fluorescent cast used for the vasculature.

Previously experiments were performed to test the approximation of microsphere deposition by a Poisson distribution by comparing two simultaneously injected samples of microspheres (Buckberg *et al.* , 1971). Buckberg showed that the error between the perfusion measured from the two samples could be explained by the random variation of the Poisson Distribution approximation, that for tissue samples with at least 400 microspheres errors between the two measurements seldom exceeded 20%. In this study the difference between the model flow (Q_m) and microsphere-derived flow (Q_f) was determined as a function of tissue fed volume, i.e. the downstream volume supplied by each vessel segment. Figure 4.27 illustrates that the relationship between fed volume (V_j) and (a) the binned RMS error (E_j^{rms}), and (b) mean number of microspheres in each bin $\bar{N}$. It shows that vessel segments with fed volumes of approximately 1g ($\approx 10^3 \text{mm}^3$) and higher on average have less than a 20% error E^{rms}, and also have approximately 400 or more microspheres downstream. This is in line with previous experimental findings and demonstrates that the homogeneous perfusion BC solution gives as good a prediction of flow between two samples as would be approximated by a Poisson distribution (Buckberg *et al.* , 1971; Nose *et al.* , 1985). Relating this tissue segment size to recent perfusion CMR methodologies (Schuster *et al.* , 2010), imaging resolution in perfusion MRI sequences can be as small as $1 \times 1 \times 8\text{mm}^3$, which means approximately 125 pixels would be required for meaningful validation of perfusion quantification with microspheres in a given myocardial tissue segment. Increasing the number of microspheres injected would lead to higher microsphere

density and in turn would mean a smaller myocardial segment size that could be used for accurate microsphere flow quantification. Previous studies have used up to 30 to 50 million microspheres per kilogram of bodyweight in dogs and sheep for higher resolution of tissue segments without loss of accuracy due to vessel blockages (Bassingthwaighte *et al.* , 1990; Oosterhout *et al.* , 1995).

The random perturbation of terminal flows of the homogeneous BC model to produce perfusion heterogeneity resulted in only very small changes in vessel flow errors at higher vessel generations. This provides confidence that the homogeneous perfusion terminal BC provides a good estimate for flow in the network, and is insensitive to random perturbations of terminal vessel perfusion. However, heterogeneity has been shown to be locally correlated in the myocardium (Van Beek *et al.* , 1989), which is inconsistent with the approach of introducing uncorrelated, random perturbations at terminal vessels. The value of $D \approx 1.5$ is found from fitting a linear function between RD and fed volume in the smaller half of vessel fed volumes $(1 - 100mm^3)$, reflecting the randomness of the perturbations. However fitting a linear function to RD versus fed volume in the higher half of the vessel fed volume $(100 = 10^4 mm^3)$ yields values of D near 1.2 and 1.3 suggesting correlation of perfusion in neighbouring tissue regions despite locally uncorrelated perfusion heterogeneity at the terminals. This suggests that perhaps the branching structure of the network somehow is responsible for locally correlated perfusion heterogeneity. Careful investigation in the future into the link of correlated local perfusion and geometric parameters such as branching angle, parent-to-daughter radius and length ratios could shed some light on this finding.

Another possible contribution to the increasingly physiological value of D with increasing heterogeneity is that terminal vessel flow perturbations were introduced with an additive term that was a fraction of the median terminal flow value. As a result flow and hence *perfusion* (flow/tissue volume) in the lower-flow terminal vessels would have been changed by a greater fraction than in the high-flow terminal vessels. It is not unlikely that the low-flow and high-flow daughter vessels are spatially arranged in a particular way such that the method used to perturb terminal flows might in fact cause locally correlated changes in perfusion. It is

known that there is a higher density of arterioles ($< 150\mu$m in diameter) in the subendocardium relative to the mid-myocardium or sub-epicardium for example (van Horssen *et al.* , 2014), where as a result of the homogeneous perfusion BC results in lower flows on average for terminal vessels in the subendocardium with our model. Thus by perturbing perfusion at terminal vessels in the subendocardium more than in the subepicardium, it is possible that this resulted in some level of local perfusion correlations leading to physiological values of D.

Another comparison was made where vessel flow errors were binned according to the number of microspheres entering them and compared to a theoretical error using binomial statistics. Errors from the model exceeded the theoretical error at the 95% confidence limit for bins of vessels with 10 or more microspheres passing through them. This discrepancy is due to a combination of errors arising from the homogeneous perfusion BC, and an actual underlying discrepancy between coronary blood flow and microsphere distribution through the network due to skimming effects. Bassingthwaighte previously proposed that skimming effects may play a role in microsphere deposition after observing in 11 sheep hearts a significant increase in microsphere deposition density in the subendocardium versus the subepicardium (Bassingthwaighte *et al.* , 1990). This observation contrasted with a statistically insignificant difference in flow between the subendocardium and subepicardium computed from the molecular tracer IDMI in the same hearts, although heterogeneous IDMI density was observed from some 1800 myocardial tissue segments considered.

Bassingthwaighte proposed a model to fit a relationship between relative microsphere deposition density and perfusion computed from IDMI deposition as a function of three variables: (1) the IDMI perfusion, (2) deviation of microsphere deposition density from that predicted by the IDMI perfusion (an indication of particles to preferentially enter higher perfusion regions), and (3) the depth of the tissue region in the myocardial wall (0 to 1 from epicardium to endocardium). All three terms had a significant effect on predicting the deviation of microsphere perfusion from IDMI perfusion and suggested that microspheres were likely to preferentially follow along the large transmural conduit arteries than distribute to smaller side-

branches, and thus preferentially deposit in the subendocardium. However a limitation of Bassingthwaighte's study is that without the native coronary structure with which to delimit perfused tissue regions, flow reaching a tissue segment in his studies came from several separate perfusion territories (Spaan *et al.* , 2005; van Horssen *et al.* , 2014). Skimming is the result of geometry and flow fraction at each bifurcation where the daughter vessel receiving a lower flow fraction receives an even smaller fraction of the microspheres passing through the parent vessel (Chien *et al.* , 1985). A flow path through a vascular network which follows consecutive low-flow fraction daughter vessels leads to a continuous reduction of downstream particle concentration, a phenomenon coined as the network Fahreaus Effect (Pries *et al.* , 1986). The next chapter examines skimming at bifurcations throughout the network to see if there is a significant effect on microsphere distribution.

4.5 Conclusions

A detailed left coronary arterial tree and its associated myocardial tissue were segmented and used to set up a Poiseuille flow model with (1) a homogeneous terminal perfusion BC and (2) a volume-scaled resistance terminal perfusion BC for the comparison of simulated blood flow to microsphere-derived flow. The homogeneous perfusion BC model resulted in lower flow errors as compared to the microspheres than the previously proposed volume-scaled resistance BC in the porcine LCA network. The assumption of a monotonically decreasing RMS flow error with fed volume allowed for the iterative identification and pruning of erroneous vessel subtrees, up to the point where no further pruning was useful in error reduction. This is a novel approach for correcting vessel network segmentation and in future could be fed back into the network segmentation pipeline.

Assessing the final pruned LCA network, microsphere-derived flow deviated from the model flow on average less than 20% in vessels with $1g$ or larger fed volumes, corresponding to a mean of approximately 400 or more microspheres in the subtended tissue. These figures are consistent with literature and demonstrates that the homogeneous perfusion BC model produces a network flow solution which is comparable to the error between simultaneously injected deposition markers.

The flow RMS error in higher generation vessel segments was shown to be relatively insensitive to terminal perfusion heterogeneity as evidenced with a perturbation analysis. This provides some confidence in the values obtained in higher generation vessels for the purposes of identifying vessel segments in which skimming occurs in the following chapter. Finally the vessel flow RMS errors binned according to the number of downstream microspheres overestimates the theoretical error determined from a Poisson distribution at the 95% confidence level in higher vessel generations containing more microspheres (shown in Figure 4.26). This discrepancy is most likely due to a combination of errors stemming from the modelling assumption of homogeneous perfusion, and possible systematic bias of microsphere distribution from the network flow solution. The prevalence of skimming and its characterisation as a systematic bias tied to underlying branching and flow parameters is investigated in the following chapter.

5 | Phase Separation Analysis

5.1 Introduction

In this chapter we investigate the extent to which phase separation occurs across the multiple scales of the porcine vascular tree and whether its occurence can be explained by various parameters including daughter-to-parent branching angle, daughter-to-daughter radius ratio and fractional daughter flow, given by the Poiseuille flow model with homogeneous flow boundary conditions. To perform this analysis a novel statistical approach has been proposed in order to address issues of limited observability and the following considerations.

Previous experiments that were conceived to analyse phase separation have always involved controlling the range of certain parameters in order to study their effects. For example *in vitro* experiments such as (Ofjord & Clausen, 1983; Dellimore *et al.* , 1983; Fenton *et al.* , 1985; Chien *et al.* , 1985) involved single bifurcations with fixed tube diameters while parent vessel haematocrit and particle diameter was controlled, allowing for a logistic function (see Appendix Section A.2) to be fitted to the resulting Q^* vs F^* data. Q^* and F^* correspond to the fluid and microsphere fractions, respectively, entering a daughter vessel at a bifurcation. This approach allowed for the importance of particle to vessel diameter ratio, λ, and flow profile to be identified. The *in vivo* experiments which have been performed were restricted to capillary and arteriolar networks where vessel diameters were limited to approximately one order of magnitude, haematocrit was within a physiological range, and flow fractions between daughter vessels at bifurcations could be systematically controlled in a step-wise manner by progressively occluding distal vessels

(Svanes & Zweifach, 1968; Schmid-Schönbein & Skalak, 1980; Klitzman & Johnson, 1982; Pries *et al.* , 1989). Pries' approach was to fit a logit function (Equation (A.7)) to the Q^* vs F^* data separately at each bifurcation for a range of imposed Q^* steps, then compute average values for the logit function parameters across all 65 bifurcations considered. By contrast the current data has a single value of Q^* and F^* at each vessel. Considering values from all bifurcations to fit a logit function results in a huge degree of scatter due to the wide range of uncontrolled parameters, as demonstrated in section 5.2.1.

Another unique feature of this dataset is the issue of observability; the number of terminal vessels (51,820) in the LCA network is approximately equivalent to the number of microspheres (51,442) distributed through the network. The majority of the 35,463 bifurcations which could be potentially used to assess flow bias have a very low number of microspheres passing through them. As shown in Figure 5.1 just over 50% of bifurcations contain fewer than 5 microspheres, just over 25% of bifurcations have 10 or more microspheres, and approximately 17% contain no microspheres at all.

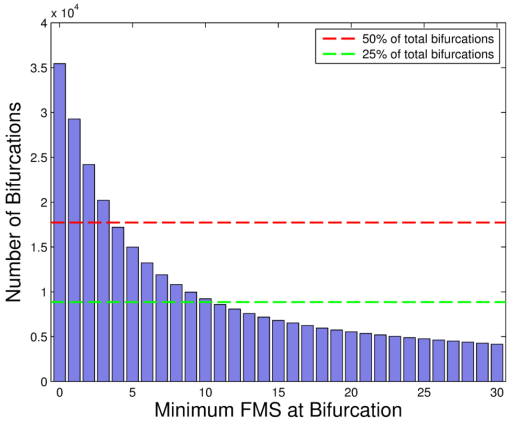

Figure 5.1: Numbers of bifurcations containing a minimum number of microspheres, N_{min}. The x-axis is limited to $N_{min} = 30$ (left) showing the 50% (upper red dashed line) and 25% bifurcation proportions correspond with approximately 4 and 10 microspheres.

Such low microsphere counts at bifurcations in the more distal circulation, compounded with any error in the flow model introduced by using homogeneous flows at the terminal vessels, make both Q^* and F^* considerably less reliable in the more

distal circulation. Conventional analysis of flow bias by fitting a logit function to the Q^* vs F^* data therefore is only suitable for the bifurcations with a sufficiently large number of microspheres. In previous phase separation studies the statistical power of observations at a bifurcation was not an issue - since blood flow was continuous the number of particles passing through a junction could be counted until deemed sufficient for recording F^*.

The porcine dataset provides the entire LCA network geometry down to a vessel diameter of $128\mu m$, allowing for analysis of phase separation effects of microspheres in both the conduit arteries and a large proportion of the resistance arterioles which has never previously been performed. The conduit vessels are distinct from arterioles and capillaries in several important ways. They are generally considered to be greater than $500\mu m$ in diameter in humans (Camici & Crea, 2007), and similarly in pigs, with the primary purpose of transporting blood from the coronary ostia to resistance vessels spread around the heart.

Figure 5.2: Conduit arteries of the LCA from the extracted porcine network.

The conduit arteries consist of the epicardial vessels which transport blood generally in the base-to-apex direction and feed into transmural vessels which transport blood in an epicardial-to-endocardial direction. Since blood needs to be supplied to the whole heart, regions of tissue that are supplied by side branches more proximal to the root of the conduit arteries (i.e. closer to the coronary ostia) will be apportioned a smaller fraction of the blood flow from the conduit artery than a

branching vessel supplying a tissue region requiring the same supply of flow more distal along the large conduit artery. Disparate flow fraction into a daughter vessel of a bifurcation is a primary determinant of phase separation, but whether phase separation occurs with microspheres at the large diameter scale of the conduit arteries has not previously been investigated.

The determinants of phase separation in Table A.1 allow hypotheses to be formed about the occurence of phase separation in the coronary vessels from our dataset. The volume fraction of RBCs suspended in plasma is known as the haematocrit (HCT), and similarly microspheres make up a certain volume fraction of the blood. A lower HCT has been shown to result in more pronounced phase separation and scatter in the F^* vs Q^* relation due to a greater wall layer thickness (Ofjord & Clausen, 1983; Fenton *et al.* , 1985) and possibly due to a greater particle profile asymmetry especially following flow disturbance at upstream bifurcations (Pries *et al.* , 1989; Carr & Wickham, 1990). The fluid volume fraction of the microspheres V_m^* is in the order of 10^{-5}-10^{-6} based on the microsphere injection procedure. This is miniscule relative to physiological HCTs that are typically used in experiments (in the range of 0.2-0.6) when analysing phase separation of RBCs. Fenton demonstrated that with 20% and 40% HCT values of blood travelling through *in vitro* channels, skimming of RBCs was pronounced in $20\mu m$ channels (significantly more so at 20% than 40%), and that while skimming was not present at 40% in $100\mu m$ channels, with 20% HCT skimming was observed. Thus we can reasonably assume that microspheres of a considerably lower volume fraction than 20% would also exhibit skimming in $100\mu m$-wide channels, and the possibility that microspheres exhibit skimming in larger vessels of the coronary network seems plausible.

The vessels of the extracted LCA network have a diameter range of 0.128mm at the terminals to 5.6mm at the root of the LCA, and since microsphere diameter is $15\mu m$, λ ranges between 0.00268-0.1173. In a single junction slit model using microspheres, a comparable value of V_m^* to the current study was used (5×10^{-5}) and phase separation was observed at $\lambda = 0.083$ but no lower than $\lambda = 0.0291$ (Ofjord, 1981). The lowest flow fraction Q^* imposed in Ofjord's experiments how-

ever was 0.02, which was likely to be too high to observe phase separation at $\lambda = 0.0291$. Other studies demonstrated the existence of a critical flow fraction Q_c^* which causes all particles to enter the higher flow daughter vessel receiving $1 - Q_c^*$, and is a function of particle diameter and dividing streamline distance from the parent vessel wall (Yen & Fung, 1978; Pries *et al.* , 1989). This suggests that at a value Q_c^* closer to zero, phase separation could very well have occured with the smallest microspheres considered in Ofjord's experiments. In the current LCA network bifurcations contain a range of values $0 < Q^* < 1$. Figure 5.3 shows that only considering bifurcations with a minimum number of microspheres passing through them, N_{min}, approximately 2.4% of vessels whose parent has $N_{min} = 1$ receives a non-zero flow fraction $Q^* < 0.01$. As N_{min} is increased, the proportion of the bifurcations with disparate flow fractions increase. Higher values of N_{min} correspond to higher generation vessels as shown in Figure 5.4, and therefore higher generation vessels demonstrate higher mean flow asymmetry.

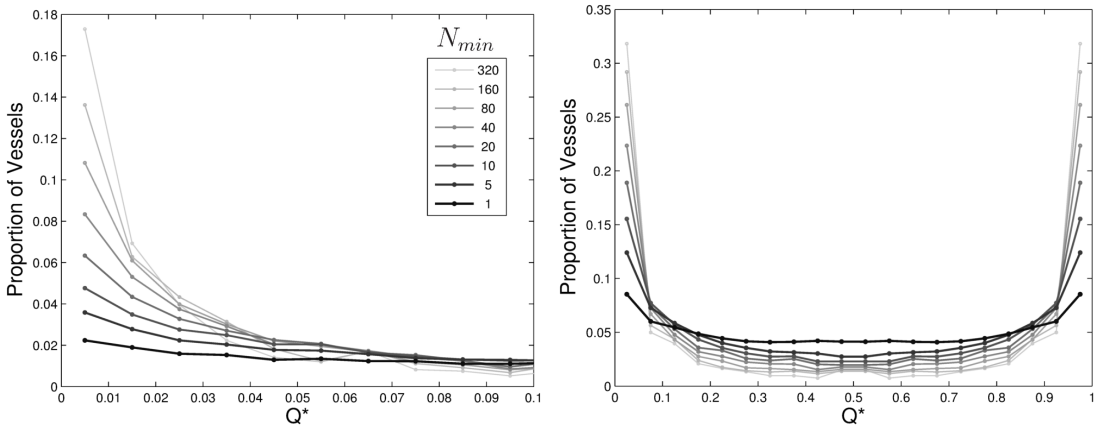

Figure 5.3: The proportion of vessels with different values of Q^* for bifurcations limited by $N_{min} = 1$, 5, 10, 20, 40, 80, 160 and 320. Values of Q^* in the range 0 to 0.1 at bin increments of 0.01 (left) indicate an increasing proportion of bifurcations with $Q^* \to 0$ (although note that Q^* is always greater than zero). Values of Q^* between 0 and 1 at bin increments of 0.05 (right) show an increasingly skewed profile at higher values of N_{min} reflecting increasing flow asymmetry.

Given the above observations in the data, it is hypothesised that phase separation may indeed occur, and the question becomes where and to what extent it can be observed. The difficulties of assessing phase separation using the approach of

fitting a logit function are presented in the following Section 5.2.1. An alternative method for assessing phase separation is then proposed in Section 5.2.2 where the microsphere flow fractions at each bifurcation are considered in the context of a binomial distribution and confidence intervals can be used to identify outlier bifurcations for which differences in terms of branching parameters to non-outliers are then assessed. The findings of the analysis presented in the Results section indicate the prevalence and spatial location of phase separation throughout the vascular network.

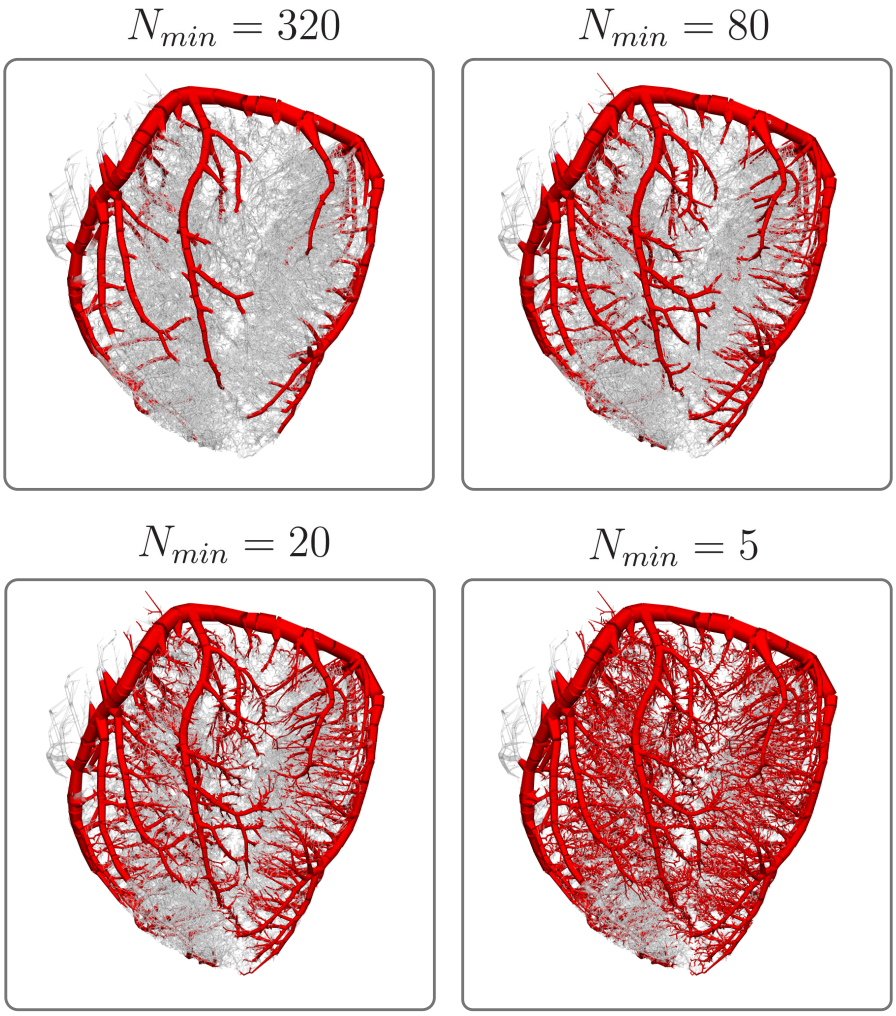

Figure 5.4: The extent of the vascular network, shown in red against a grayed out distal network, when limited by N_{min} = 320, 80, 20 and 5. The increasing flow distribution asymmetry associated with bifurcations limited by a higher value of N_{min} (illustrated in Figure 5.3) is reflected by a transition to the conduit arteries in the vascular tree. This is consistent with observations of increased branching asymmetry in more proximal vessels of the kidney cortex circulation (Marxen, 2004).

5.2 Methods

5.2.1 Logistic Function Fitting

As discussed briefly before, assessment of phase separation in the coronary network by fitting a logit function has several limitations. Due to single measurements for Q^* and F^* being available at a bifurcation, each of which may experience different flow disturbances and has different geometric features, the variability in the plotted Q^* vs F^* relation across all bifurcations is limiting. The single parameter logistic function (Eq. (A.1)) of Klitzman is used instead of the 3 parameter logit function (Eq. (A.7)) of Pries to provide a simple fitting procedure for the sigmoidal parameter b, rewritten below for convenience,

$$\ln\left(\frac{1-F^*}{F^*}\right) = b \cdot \ln\left(\frac{1-Q^*}{Q^*}\right)$$

In Figure 5.5 (left) F^* vs Q^* is plotted for all bifurcations with $N_{min} = 1$. Scatter is progressively reduced when N_{min} is increased, where at $N_{min} = 100$ (right), only a weakly non-linear relationship between Q^* and F^* for the corresponding bifurcations is found where $b = 1.052$.

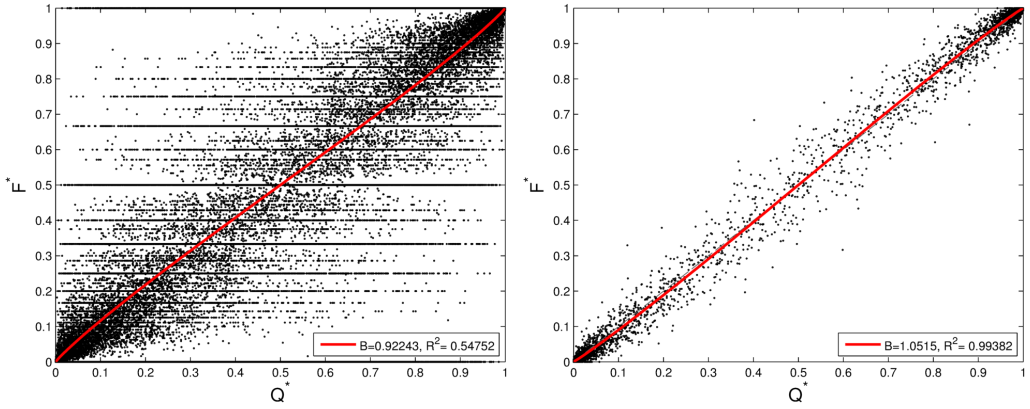

Figure 5.5: Least squares regression used to fit the logistic function to F^* vs Q^* for all bifurcations containing $N_{min} = 1$ (left) and $N_{min} = 100$ (right). The value of the fitted parameter b is 0.922 and 1.052 respectively, with the goodness of fit parameter R^2 equal to 0.548 and 0.994, reflecting a reduction in the scatter with a higher N_{min}.

As shown in Figure 5.6 the value of b for the fitted logistic function increases from 0.92 to 1.03 within the range $1 \leq N_{min} \leq 30$ and then fluctuates approximately between 1.04-1.06 when bifurcations are limited to $N_{min} > 30$. This relatively stable value of b at $N_{min} > 30$ suggests minor phase separation in the proximal circulation. R^2 values for this range of bifurcations also appears close to 1 despite evident scatter around the fitted line. This is mainly due to a high concentration of data points around $Q^* \approx 0$ and $Q^* \approx 1$ (see Figure 5.3), where consequently $F^* \approx 0$ and $F^* \approx 1$ respectively, such that the fitting error overall is artificially reduced since these points are already clustered around the ends of the fitted line. There is considerable deviation of data points from the fitted line across the range of Q^* which may reflect phase separation effects influencing particle distributions to different extents at individual bifurcations due to a combination of geometric parameters, upstream flow disturbances and flow fraction. The underlying error of the flow model is of course also a contributing factor, although this error is reduced in the higher vessel generations at larger values of N_{min}. An alternative approach needs to be taken to identify which bifurcations are subject to phase separation, and consequently which factors are influencing it. Such an approach is presented in the following section.

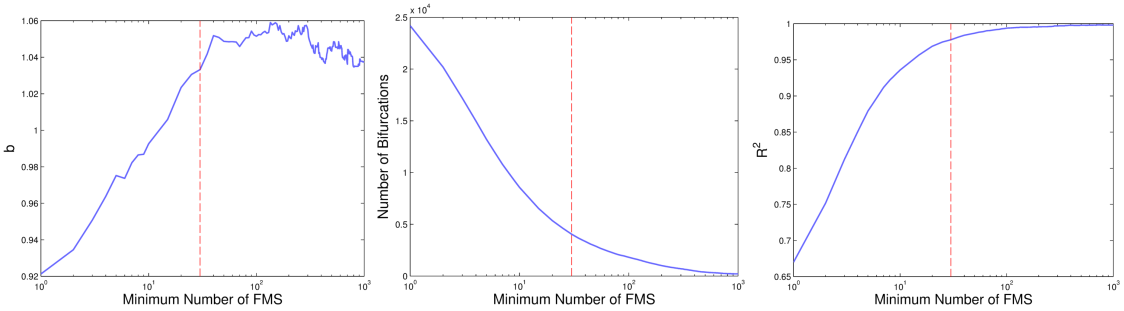

Figure 5.6: The relationship of b (left), number of bifurcations considered (middle), and R^2 (right) with N_{min} when fitting the logistic function to F^* vs Q^* data. $N_{min} = 30$ is indicated by the dashed red line.

5.2.2 Probabilistic Identification of Phase Separation

The underlying assumption of the microsphere method is that microsphere distribution is proportional to flow and is subject only to random variation, and not a systematic bias. This assumption can be used to test for phase separation in a probabilistic sense, ignoring at first the possibility of physical determinants of phase separation. For each bifurcation the distribution of microspheres to each daughter vessel can be assessed probabilistically with a binomial distribution denoted by

$$X \sim B(N, p) \tag{5.1}$$

where X is the number of microspheres entering a daughter vessel, N is the number of microspheres passing through the upstream bifurcation, and p is the probability of microspheres entering one of the daughter vessels, and $(1 - p)$ the probability of entering the complementary daughter vessel. In this study $p = Q^*$, which assumes that the fraction of microspheres, F^*, entering a daughter vessel is sampled from the binomial distribution around Q^* with N trials. The influence of other factors such as geometric parameters and flow profile disturbances are initially disregarded. This approach allows for bifurcations where F^* deviates sufficiently from Q^*, termed *outliers*, to be identified as those outside of desired confidence intervals, which once determined can be used to identify correlated parameters. Furthermore these outliers can also be spatially located within the network as shown in the Results.

To introduce the basic concepts of this approach, suppose idealistically that there is a large population of *identical* bifurcations, each with the same number of microspheres passing through the parent vessel, N, and each with an equal flow fraction (or probability of entering) into each daughter vessel, i.e. $p = Q^* = 0.5$. The number of microspheres that enter each daughter vessel is given by the random variable X which follows the binomial distribution $X \sim B(N, p)$. The probability of exactly k microspheres entering a vessel is given by the probability mass function

$$f(k;N,p) = Pr(X = k) = \begin{pmatrix} N \\ k \end{pmatrix} p^k (1-p)^{1-k} \tag{5.2}$$

where

$$\begin{pmatrix} N \\ k \end{pmatrix} = \frac{N!}{k!(N-k)!} \tag{5.3}$$

Suppose that $N = 30$, the probability mass function, PMF, can be illustrated in terms of X or in terms of X/N as shown below in Figure 5.7. The two representations will be used interchangeably where appropriate throughout the text.

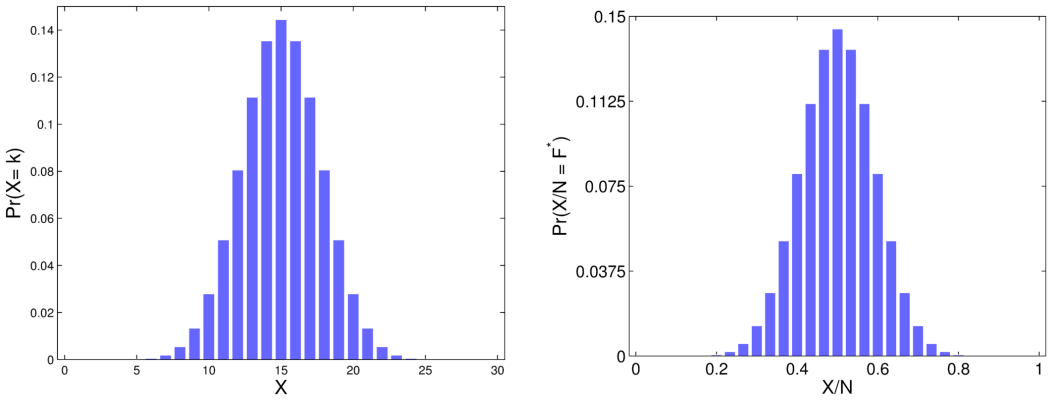

Figure 5.7: Two representations of a binomial PMF with $N = 30$ and $p = 0.5$ with either X (left) or X/N (right) on the x-axis. The latter option allows a direct relation to F^*, whereas the former is more intuitive when considering a discrete outcome of microspheres, k.

The cumulative distribution function, CDF, is given by

$$F(k;N,p) = Pr(X \leq k) = \sum_{i=0}^{k} \begin{pmatrix} N \\ i \end{pmatrix} p^i (1-p)^{N-i} \tag{5.4}$$

The cumulative probability of k microspheres entering a daughter vessel, $Pr(X \leq k)$, (or equivalently $Pr(X/N \leq F^*)$ where $F^* = k/N$) represents how often such an outcome is beneath a certain level. $F(k;N,p)$ for the outcome k can also be considered as the *percentile* of the outcome k - how often such an outcome is expected to occur if the same binomial distribution $X \sim B(N,p)$ were sampled many times. A confidence interval (CI) is a pair of bounds defined with a coverage

of $(1-\alpha)$ for the CDF that is used to determine the likelihood of an outcome based on whether the percentile of the outcome lies inside or outside of the CI bounds. The CDFs corresponding to the PMFs shown in Figure 5.7 are shown below in Figure 5.8 with the bounds of a two-tailed 90% CI ($\alpha = 0.1$). The outcomes outside of the CI bounds highlighted in red are all of the possible outcomes at a bifurcation where $Q^* = 0.5$ and $N = 30$ that would be considered as *outliers*.

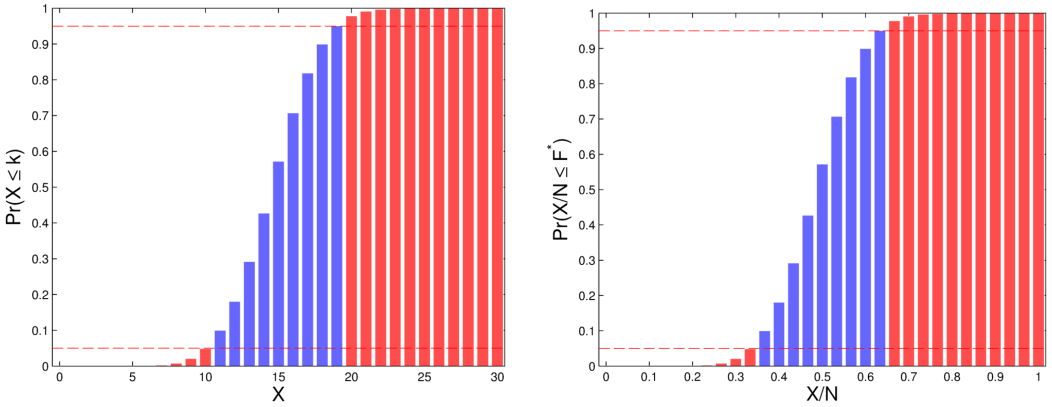

Figure 5.8: Two representations of a binomial CDF with $N = 30$ and $p = 0.5$ with either X (left) or X/N (right) on the x-axis. A two-tailed 90% CI is bounded by the upper and lower dashed red lines, where outliers are highlighted in red.

The two-tailed 90% CI bounds in Figure 5.8 are drawn at $(\alpha/2 = 0.05)$ and $(1 - \alpha/2 = 0.95)$ on the y-axis. The test for outliers at the two tails are

$$Pr(X \leq k) < \alpha/2 \tag{5.5}$$

for the lower tail, and

$$Pr(X \geq k) < \alpha/2 \tag{5.6}$$

for the upper tail. Coming back to the idealised example where a large population of bifurcations each have N microspheres passing through them and $Q^* = 0.5$, each daughter vessel can be represented with the binomial distribution $X \sim B(N, 0.5)$. Assume now that the number of microspheres entering each daughter vessel, k, is a random variate that is *sampled* from this distribution. If the percentiles of every daughter vessel outcome are computed, approximately $W\%$ of all computed

percentiles will have a percentile value that is $\leq W\%$. This can be represented with a histogram of a *percentile proportion distribution* (PPD). Each bar of the histogram represents the proportion, w_i, of vessels with computed percentiles within a fixed-width interval given by

$$w_i = \frac{\sum_j^{M_i}(F_i - \beta/2 < F_j < F_i + \beta/2)}{M} \tag{5.7}$$

where M is the total number of daughter vessels, β is the width of each interval ($\Delta F_i = \beta$), F_i is the central percentile value of each interval, and M_i is the total number of daughter vessels within each interval i. For the example where percentiles computed for each daughter vessel for a large population of bifurcations is sampled from the same binomial distribution, the PPD is flat; i.e. every percentile bin contains the same proportion of vessels. A PPD that is distinctly skewed on the other hand, given a large population of bifurcations, would suggest that there is a significant proportion of bifurcations where the microsphere distribution is not well represented by the binomial distribution at those bifurcations. It would indicate that F^* differs significantly from Q^* in part of the vessel population, identifying phase separation.

When applying the use of confidence intervals to bifurcations in the porcine network several considerations need to be taken into account. As demonstrated in Section 5.1 the value of Q^* throughout the porcine network varies across the range of $0 < Q^* < 1$ with a fairly even distribution when $N_{min} = 1$ (see Figure 5.3). The number of microspheres passing through each bifurcation also varies, decreasing with each successive branching generation. The PMF (and CDF) varies with both Q^* and N as illustrated in Figure 5.9. Notably at lower values of N the probability of any one outcome $Pr(X = k)$ is generally greater than at higher values of N, and the overall profile of the PMF is more spread out. Nonetheless, if the PPD is plotted for a large population of bifurcations with varying Q^* and N, the proportion of vessels in each percentile interval would still be approximately constant if the outcomes are sampled from the binomial distribution used for each daughter vessel.

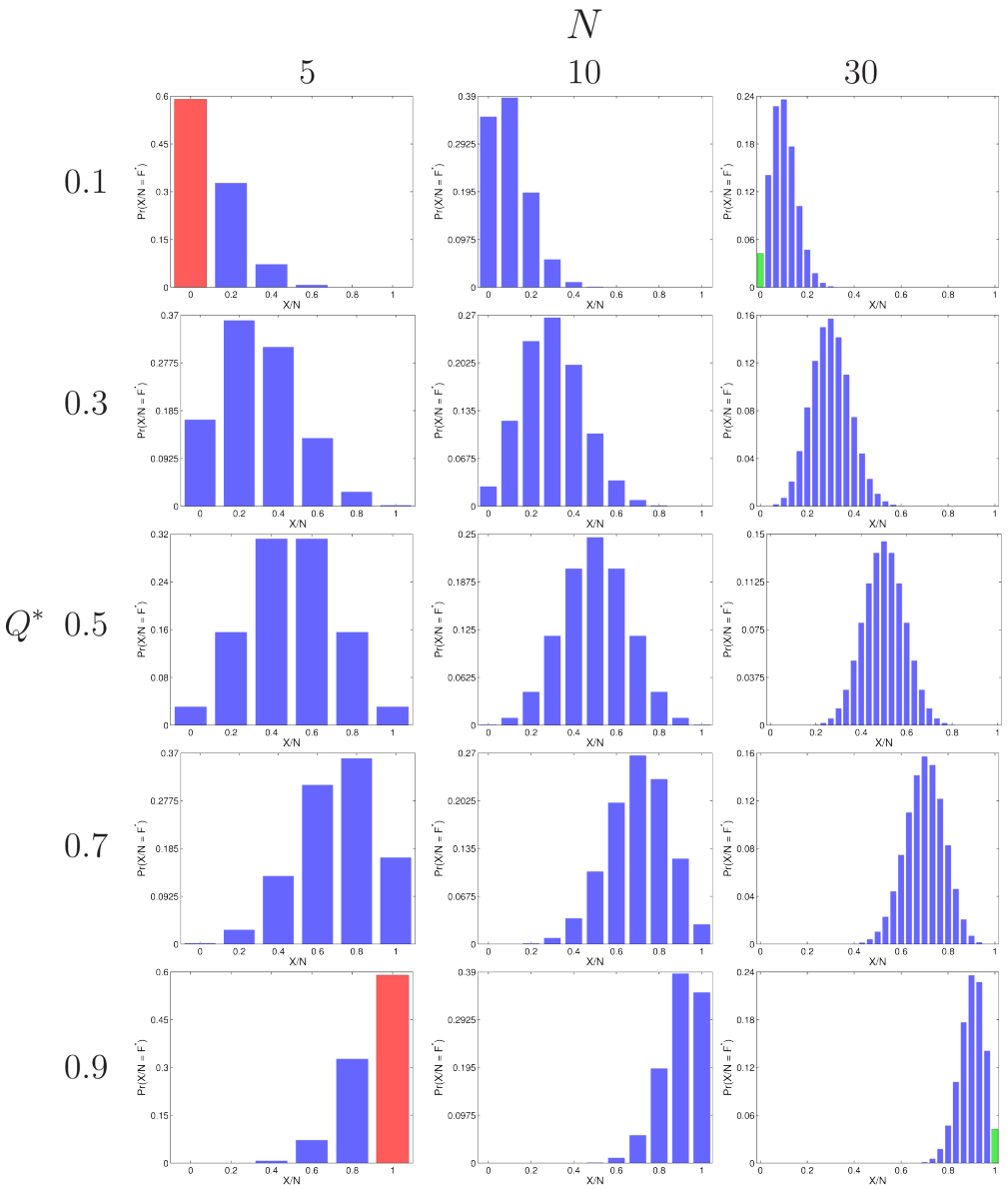

Figure 5.9: PMF variation with a range of values of Q^* and N. Note that the PMFs in the rows from the top are complemented by the PMFs in the rows from the bottom for flow fractions into daughter vessel pairs at a bifurcation. Bars highlighted in red indicate where for a given value of Q^* and N, the microsphere distribution to the vessel segment does not meet the observability criteria. The green bars indicate that an increase in N can result in the vessel meeting the observability criteria.

An important issue with using real data is that of *observability* at each bifurcation. Observability refers to whether it is possible to observe statistical outliers using a desired confidence level (CL) for a binomial distribution $X \sim B(N, p)$. Consider

a two-tailed test with a 90% CL, where the tail widths are $\alpha/2 = 0.05$. If the probability of exactly zero microspheres entering the daughter vessel $Pr(X = 0) > \alpha/2$, or conversely of all microspheres entering the daughter vessel $Pr(X = N) > \alpha/2$, then the binomial distribution for that daughter vessel has failed the test of observability. Essentially there is no way of telling if an outcome is outside of the desired CL. Observability improves for higher values of N and for values of p closer to 0.5, and at lower CLs. A relation can be drawn between α, N, and p to give a range where observability is satisfied, which is referred to as the *viable space* for a desired CL. Given N and α from a one-tailed test, the maximum and minimum possible values of p (or Q^* in a daughter vessel) which satisfy observability can be found using the binomial PMF in Equation (5.2) as

$$\begin{aligned} Pr(X = 0) = p_{min}^0(1 - p_{min})^N &= \alpha \\ \Rightarrow p_{min} &= 1 - \alpha^{\frac{1}{N}} \end{aligned} \tag{5.8}$$

and

$$\begin{aligned} Pr(X = N) = p_{max}^N(1 - p_{max})^0 &= \alpha \\ \Rightarrow p_{max} &= \alpha^{\frac{1}{N}} \end{aligned} \tag{5.9}$$

where only daughter vessels with $p_{min} \leq Q^* \leq p_{max}$ are in the viable space. For a two-tailed test confidence level, α in the above equations is replaced by $\alpha/2$. Figure 5.10 shows the viable zones for 60% to 99% two-tailed confidence intervals illustrating wider viable zones for lower confidence levels. In the top row of Figure 5.9 where daughter vessel PMFs are displayed with $Q^* = 0.1$, highlighted in red is $Pr(X = 0) = 0.59$ for a bifurcation with $N = 10$, and in green $Pr(X = 0) = 0.042$ for a bifurcation with $N = 30$. For a two-tailed 90% CI where $\alpha/2 = 0.5$, only the latter would be considered viable. A symmetric relationship results in the complementary daughter vessel where $Q^* = 0.9$, where in red $Pr(X = N) = 0.59$ for $N = 10$ and in green $Pr(X = N) = 0.042$ for $N = 30$. Thus both the daughter vessels branching from the bifurcation with $N = 10$ are outside of the viable space for a 90% CL, and those from the bifurcation with $N = 30$ are within the viable space.

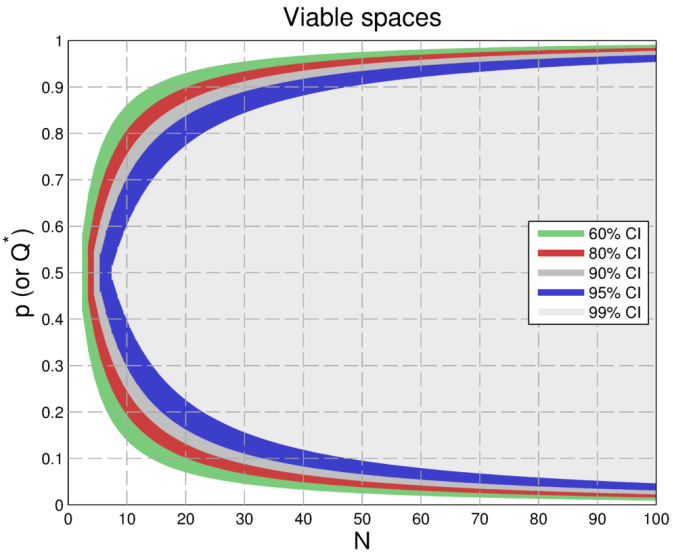

Figure 5.10: Viable spaces for two-tailed 60%, 80%, 90%, 95% and 99% confidence intervals in terms of N and p (or Q^*). The upper and lower bounds for each CI correspond to p_{min} and p_{max} from Equations (5.8) and (5.9) respectively. The x-axis is truncated at $N = 100$ as p_{min} and p_{max} of the viable spaces approach 0 and 1 respectively with higher values of N. Note that the 60% CI viable space encloses the other viable spaces.

Confidence intervals for binomial distributions can be computed using the Clopper-Pearson method (Clopper & Pearson, 1934). Given the discrete nature of the binomial distribution there is no guarantee that there will be outcomes from the distribution that lie exactly on the upper and lower bounds of a desired CI. The Clopper-Pearson CI estimate produces conservative upper and lower bounds for probability coverage of at least $(1 - \alpha)$ for every possible value of p (Agresti & Coull, 1998). Hypothesis testing is used to determine whether an outcome lies within a CI, and can be one-tailed or two-tailed. The two-tailed Clopper-Pearson CI with probability coverage of $p_{LB} < p < p_{UB}$ is considered an "exact" CI for p, which is a function of the number of trials N, the number of expected successes $x = N.p$, and the stated coverage of the interval $1 - \alpha$, i.e. $p_{UB} - p_{LB} \geq (1 - \alpha)$. For whole numbers of $x = 1, 2, ..., N - 1$ the lower bound p_{LB} can be found by inverting

$$Pr(X \geq x) = \sum_{i=x}^{N} \binom{N}{i} p_{LB}^{i}(1 - p_{LB})^{N-i} = \frac{\alpha}{2} \tag{5.10}$$

and for $x = 1, 2, ..., N - 1$, the upper bound p_{UB} is found by inverting

$$Pr(X \leq x) = \sum_{i=0}^{x} \binom{N}{i} p_{UB}^{i}(1 - p_{UB})^{N-i} = \frac{\alpha}{2} \tag{5.11}$$

where $p_{LB} = 0$ when $x = 0$, and $p_{UB} = 1$ when $x = N$. However x is not always a whole number in the porcine dataset since $p = Q^*$ is from the flow model and N is the number of microspheres passing through the parent bifurcation. Overcoming this issue and the issue of long numerical solve times associated with large values of N, Blyth derived a calculation for the CI bounds using the F-distribution which is well-defined for positive real values of x (Blyth, 1986),

$$p_{LB} = \left(1 + \frac{N - x + 1}{x \cdot F[1 - \frac{\alpha}{2}; 2x, 2(N - x + 1)]}\right)^{-1} \tag{5.12}$$

$$p_{UB} = \left(1 + \frac{N - x}{(x + 1) \cdot F[\frac{\alpha}{2}; 2(x + 1), 2(N - x)]}\right)^{-1} \tag{5.13}$$

where $F[c; v, w]$ is the $1 - c$ quantile from an F-distribution with parameters v and w. The probability coverage of a CI is at least $1 - \alpha$, which corresponds to a varying range of outcomes X depending on both N and Q^*. This is illustrated in Figure 5.11 below where *confidence belts* for 90% CIs (with tails of $\alpha/2 = 5\%$) are plotted for distributions of $N = 10$ and $N = 20$ in the range $0 \leq Q^* \leq 1$.

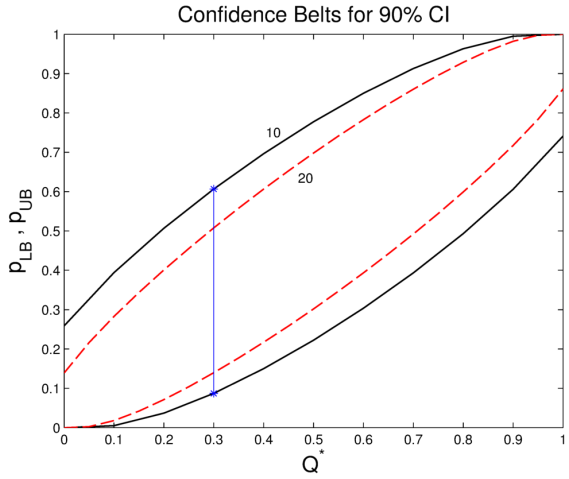

Figure 5.11: 90% confidence belts with lower (p_{LB}) and upper (p_{UB}) limits for $N = 10$ (solid line) and $N = 20$ (dashed red line). The blue line indicates the width of a confidence interval for $N = 10$ and $Q^* = 0.3$ for which $[p_{LB} \quad p_{UB}]$ is [0.087 0.61].

The narrowing of the confidence bounds for a given value Q^* at higher values of N is a reflection of the narrowing of the PMF, as illustrated earlier in Figure 5.7. Intuitively this occurs because with a larger number of trials N, there is greater confidence that the observed outcome k will lie closer to the expected outcome $p.N$.

In order to assess phase separation in the bifurcations retained within the viable space of a desired CL, two hypothesis tests are essentially considered. It has been observed experimentally that a disproportionately low microsphere fraction tends to enter daughter vessels with a low flow fraction (and disproportionately high microsphere fraction enters high flow fraction daughter vessels). The null hypothesis therefore is that the microsphere fraction and model flow fraction are the same; that the computed percentile at a bifurcation is within the specified CI bounds,

$$H_0 : F^* = Q^*$$

The two alternative hypotheses are

$$H_1^a : F^* < Q^* \quad \text{for} \quad Q^* < 0.5 \tag{5.14}$$

$$H_1^b : F^* > Q^* \quad \text{for} \quad Q^* < 0.5 \tag{5.15}$$

The first alternative hypothesis H_1^a states that the microsphere fraction F^* entering a daughter vessel which receives a flow fraction $Q^* < 0.5$ is significantly lower than the flow fraction Q^*. This is a test for the flow bias that has been observed in both *in vitro* and *in vivo* experiments with RBC's and microspheres as previously discussed. The second alternative hypothesis H_1^b states that the microsphere fraction F^* entering a daughter vessel which receives a flow fraction $Q^* < 0.5$ is significantly *higher* than the flow fraction Q^*. These vessels demonstrate the opposite bias effect to what is expected, but may indeed occur within the porcine network based on observed scatter (see Figure 5.5), and may be due to effects of flow disturbance. H_1^b serves as a type of control for unexpected effects in the analysis, compared to H_1^a which characterises classic skimming. The complementary

daughter vessel at each bifurcation receives $(1-Q^*) > 0.5$ and $(1-F^*)$ such that alternative hypotheses in the high flow fraction daughter vessels are equivalent and symmetric to the above Equations (5.14) and (5.15).

$$H_1^a : F^* > Q^* \quad \text{for} \quad Q^* > 0.5$$

$$H_1^b : F^* < Q^* \quad \text{for} \quad Q^* > 0.5$$

For a given two-tailed CI with coverage $(1-\alpha)$, The alternative hypothesis H_1^a is true for a daughter vessel, and indeed a bifurcation, if the following binomial tests are satisfied

$$Pr(X \leq k) < \alpha/2 \quad \text{for} \quad Q^* < 0.5,\ F^* < Q^* \tag{5.16a}$$

$$Pr(X \geq k) < \alpha/2 \quad \text{for} \quad Q^* > 0.5,\ F^* > Q^* \tag{5.16b}$$

where $Pr(X \leq k)$ is equivalent to $Pr(X/N \leq F^*)$. Note if either of these equations is satisfied at one daughter vessel the other will also be satisfied for the complementary daughter vessel. The alternative hypothesis H_1^b is true at a bifurcation if the following binomial tests are satisfied

$$Pr(X \geq k) < \alpha/2 \quad \text{for} \quad Q^* < 0.5,\ F^* > Q^* \tag{5.17a}$$

$$Pr(X \leq k) < \alpha/2 \quad \text{for} \quad Q^* > 0.5,\ F^* < Q^* \tag{5.17b}$$

A PPD can be constructed for each of the binomial tests above, restricted to the daughter vessels in the viable space of a desired CL. The smallest interval width β in a PPD which can be used for a given CL is $\alpha/2$. This is because certain bifurcations in the viable space of a high CL will not meet observability criteria in a lower CL (the banded regions in Figure 5.10). For example certain bifurcations in the viable space for an 80% CL are not in the viable space for a 90% CL, where outliers determined from these bifurcations will lie in the bottom 10^{th} percentile but not the bottom 5^{th} percentile due to lack of observability.

The width of β can however be set to any value greater than $\alpha/2$, which is useful

for comparing PPDs of bifurcations in the viable space of higher confidence levels to those of lower confidence levels. For example outliers for H_1^a within an 80% CL viable space are those bifurcations whose low flow daughter vessels have percentiles $< 10\%$ and which make up the proportion in the lowest interval of the PPD, w_1 where $0 < F_j < 0.1$. The outliers for a 90% CL have percentiles $< 5\%$ which make up the lowest interval $0 < F_j < 0.05$. Summing the proportions of the two lowest intervals for the 90% CL PPD would give a new proportion equivalent to that in the interval to w_1 for the 80% CL.

Finally since the binomial tests in Equations (5.16a) and (5.17b) each only apply to daughter vessels in which $F^* < Q^*$, the computed percentiles are almost always less than 0.5 so the PPD for these tests is displayed between 0 and 0.5. Similarly for the binomial tests in Equations (5.16b) and (5.17a) where vessels have $F^* > Q^*$, the PPD is displayed between 0.5 and 1 to reflect the fact that the proportions represent upper percentiles, computed as $(1 - Pr(X \geq k))$ for Eq. (5.16b) and $(1 - Pr(X \leq k))$ for Eq. (5.17a).

5.3 Results

5.3.1 Viable Space Bifurcations

A total of 29,268 bifurcations with at least 1 microsphere passing through them are available in the porcine network for analysis. Table 5.1 lists the number of bifurcations in each of the viable spaces associated with CLs between 60% and 99%. It also includes the options for PPD interval widths, β, indicating a common interval width of $\beta = 20\%$ to compare the results of each viable space. Figure 5.12 shows two scatter plots of Q^* vs N corresponding to the vessels within each viable space. The data is symmetric about $Q^* = 0.5$ due to pairs of daughter vessels receiving complementary flow fractions summing to 1. The majority of vessels in the network do not meet the observability criteria for the outlier analysis and are marked with dots; a total of 10713 bifurcations in the 60% CL viable space and 3788 bifurcations in the 99% CL viable space are retained for analysis.

Table 5.1: Viable space information.

Confidence Level, %	Viable Bifurcations	$\alpha/2$, %	β Options, %
60	10713	20	20
80	7982	10	10, 20
90	6344	5	5, 10, 20
95	5228	2.5	2.5, 5, 10, 20
99	3788	0.5	0.5, 2.5, 5, 10, 20

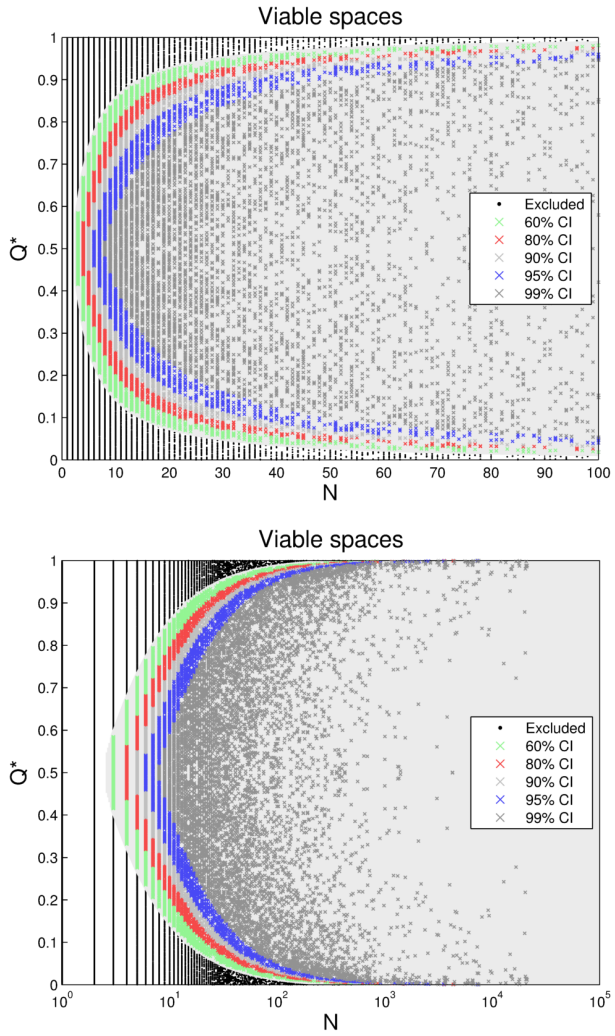

Figure 5.12: Viable spaces for analysis with 60%, 80%, 90%, 95% and 99% confidence intervals. Daughter vessels of all viable bifurcations have been marked with crosses and excluded vessels with black dots. The top figure with an x-axis limit of $N = 100$ matches Figure 5.10, and the full range of viable vessels is shown underneath with a log-scale x-axis. Note all points within the viable space of higher confidence levels also lie in the viable space of lower confidence levels.

5.3.2 Outlier Analysis and PPDs

The binomial tests for outliers using the available bifurcations in each viable space display significantly larger than expected proportions. The percentages of H_1^a outliers (the anticipated bias where for $Q^* < 0.5$, $F^* < Q^*$) and H_1^b outliers (the opposite bias where for $Q^* < 0.5$, $F^* > Q^*$) are listed in Table 5.2 for each con-

fidence level and graphed in Figure 5.13. The value of β corresponds both to the width of the confidence interval tail ($\alpha/2$) as well as the expected proportion of outliers in that tail.

Table 5.2: Outlier proportions (as %).

Confidence Level	β	H_1^a Proportion	H_1^b Proportion
60	20	23.06	17.79
80	10	16.06	11.39
90	5	11.77	8.14
95	2.5	8.82	5.99
99	0.5	5.49	3.43

H_1^a outlier proportions are consistently higher than the expected outlier proportion (β) for all confidence levels, with a higher factor increase at lower β. For example the proportion of H_1^a outliers is approximately $11 \times \beta$ when $\beta = 0.5\%$ (a 99% CL), and is just marginally more than expected at $1.15 \times \beta$ when $\beta = 20\%$ (a 60% CL).

H_1^b outlier proportions are greater than expected for 80% CLs and higher, and is marginally less than expected at a 60% CL. The proportion of H_1^a outliers is approximately $6.9 \times \beta$ when $\beta = 0.5\%$ (a 99% CL), and is $0.89 \times \beta$ when $\beta = 20\%$ (a 60% CL).

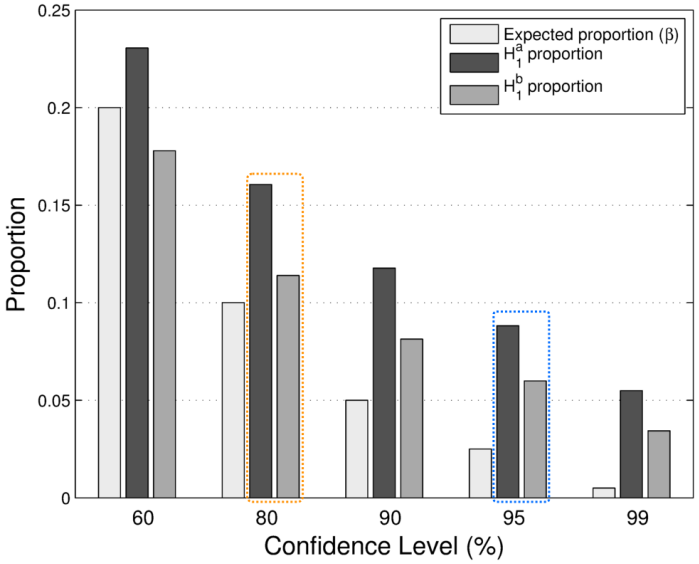

Figure 5.13: Outlier proportions for H_1^a and H_1^b at different CLs relative to the expected proportion, β. PPDs are plotted for the 80% CL (orange box) and the 95% CL (blue box) in Figures 5.15 and 5.14 respectively

The proportion of H_1^a outliers is greater than the proportion of H_1^b outliers at all CLs, indicating that there are more vessels with the anticipated form of phase separation than vessels with the opposite. The relative proportions of both H_1^a and H_1^b outliers with respect to β increase at higher CLs. All outliers identified with a higher CL (in its associated viable space) are still outliers at a lower CL (in its wider associated viable space). This suggests that the proportion of vessels beneath a certain percentile increases at lower percentiles, which is confirmed in the PPDs plotted for 80% and 95% CLs in Figures 5.14 and 5.15 respectively.

The outlier proportions of the 95% CL PPD have an interval width of 2.5% (Figure 5.14), but relative to other percentile bins are much greater than the outlier proportions of the 80% CL PPD with an interval width of 10% (Figure 5.15). Furthermore the percentile bins between 2.5% and 10% in the 95% CL PPD are only marginally above the expected proportion of $\beta = 2.5\%$, thus if the 2.5% width percentile bins were lumped into 10% width percentile bins to compare with the 80% CL PPD, most of the excess in that proportion would be due to vessels with percentiles under 2.5%.

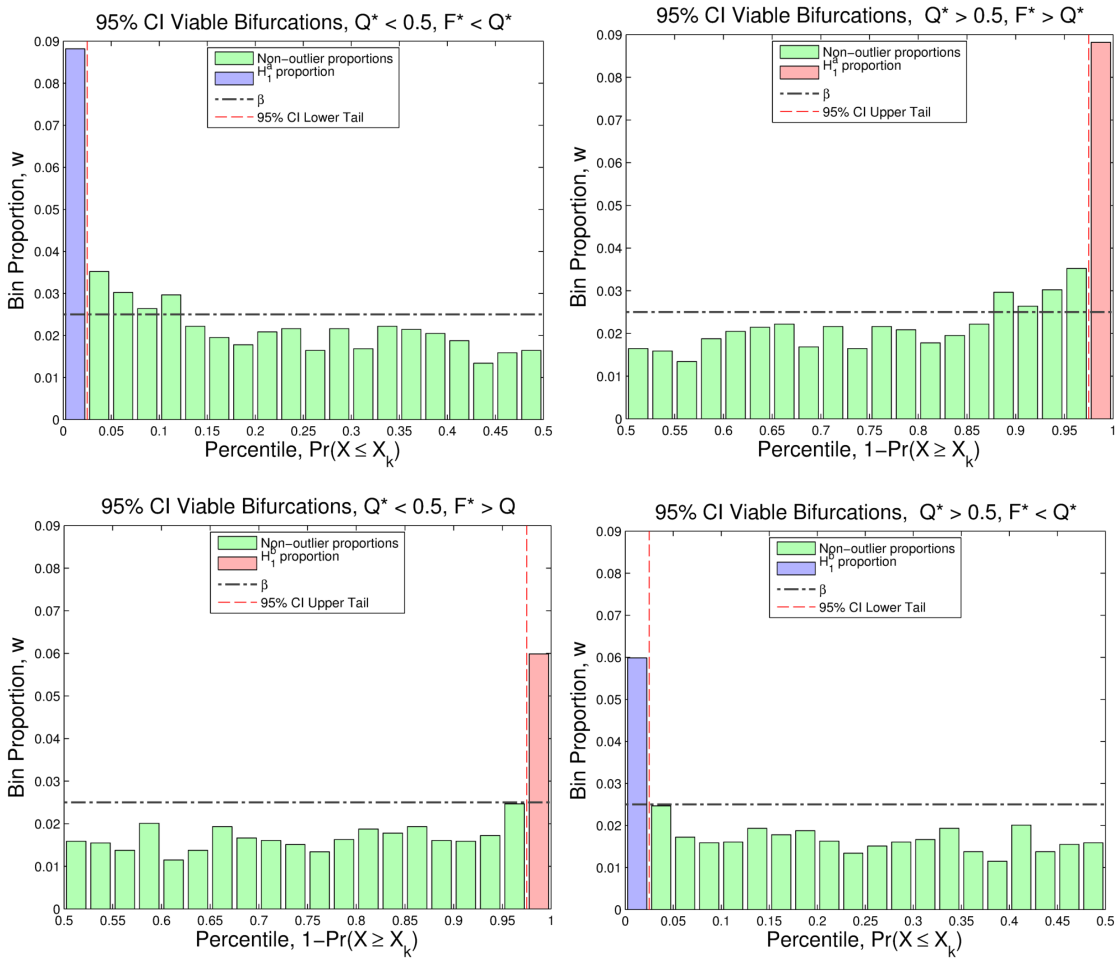

Figure 5.14: 95% CL viable space PPDs with interval width $\beta = 0.025$. The top row shows symmetric PPDs for daughter vessel pairs tested for the anticipated phase separation H_1^a with Equations (5.16a) and (5.16b). Outliers of these tests make up the proportions of the blue and red bars respectively. The bottom row shows symmetric PPDs for daughter vessel pairs tested for the opposite phase separation H_1^b with Equations (5.17a) and (5.17b). The outlier proportions of the two tests correspond to those enclosed in the dashed blue box in Figure 5.13.

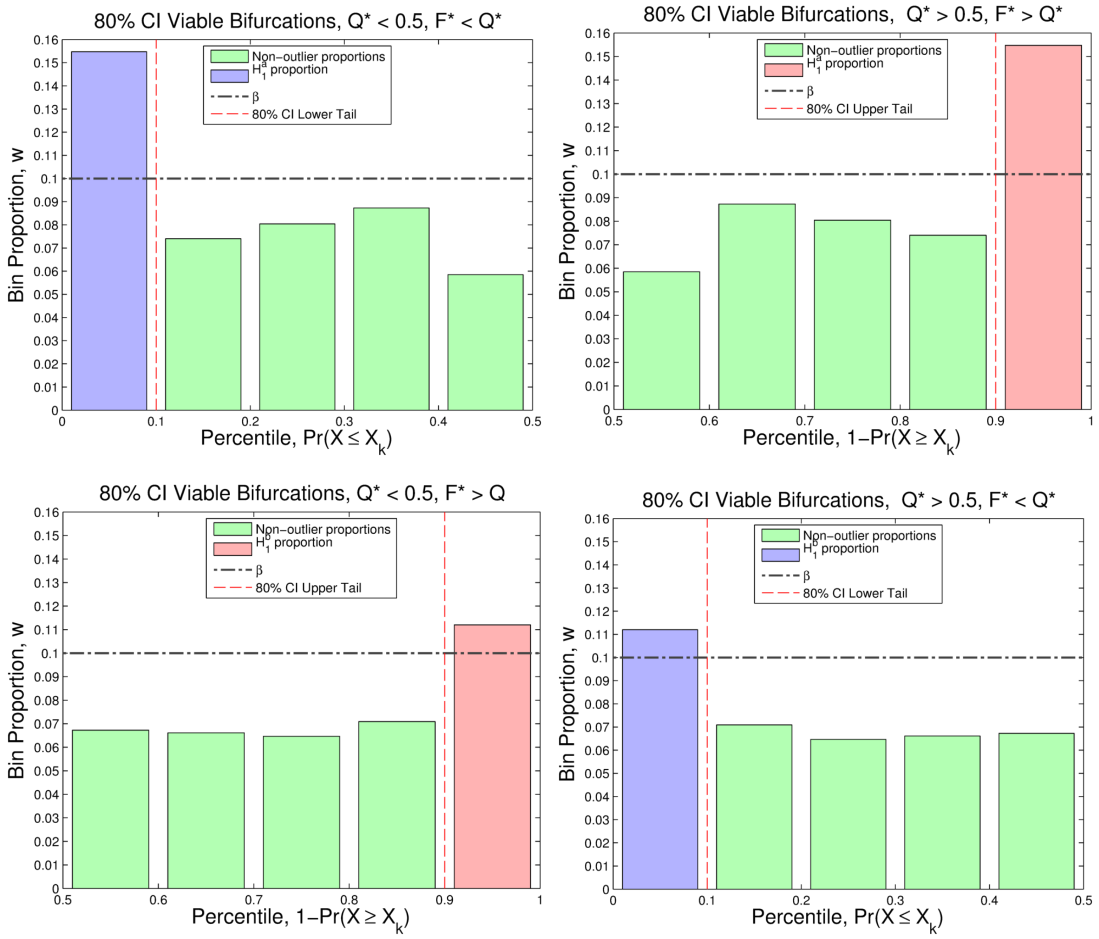

Figure 5.15: 80% CL viable space PPDs with interval width $\beta = 0.1$. The top row shows symmetric PPDs for daughter vessel pairs tested for the anticipated phase separation H_1^a with Equations (5.16a) and (5.16b). Outliers of these tests make up the proportions of the blue and red bars respectively. The bottom row shows symmetric PPDs for daughter vessel pairs tested for the opposite phase separation H_1^b with Equations (5.17a) and (5.17b). The outlier proportions of the two tests correspond to those enclosed in the dashed orange box in Figure 5.13.

In order to determine whether the additional bifurcations retained in the lower CL viable spaces contribute more or less to the outlier proportion, a comparison can be made between each set of viable spaces by considering outliers in the bottom 20^{th} percentile, $\beta = 0.2$. This is the same as lumping the percentile bins less than 20% in the PPDs of higher CL viable bifurcations into new proportions.

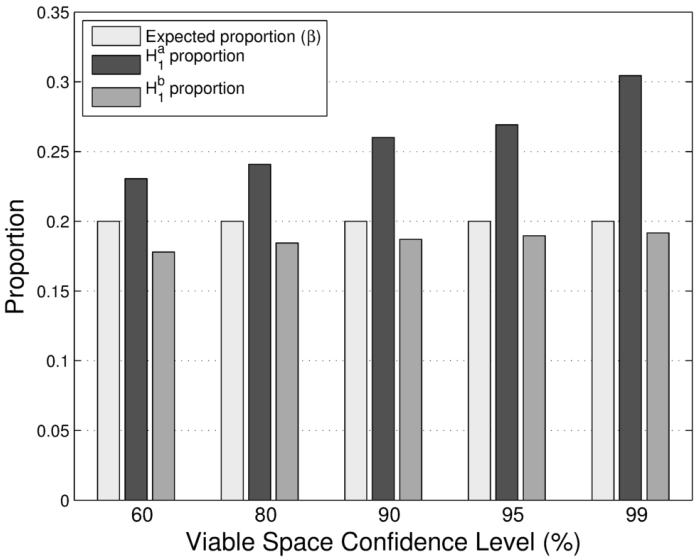

Figure 5.16: Outlier proportions for H_1^a and H_1^b when $\beta = 0.2$ for each of the viable spaces. There is a noticeable increase in the H_1^a outlier proportion for higher CL viable space bifurcations, whereas the H_1^b outlier proportion increases only slightly.

Figure 5.16 illustrates an increase in the H_1^a outlier proportion at higher CLs, and only a marginal increase in the H_1^b outlier proportion. This is possibly a reflection of the proportion distributions of Q^* values considered for each viable space, shown in Figure 5.17. Since in higher CL viable spaces there are a higher proportion of vessels with more extreme values of Q^*, namely those with $Q^* < 0.1$ and $Q^* > 0.9$, it is probable that those vessels are more susceptible to phase separation and thus contribute to greater outlier proportions. Another factor is that bifurcations retained in higher CL viable spaces have a higher minimum number of microspheres, N_{min} entering them. As shown earlier in Figure 5.4, increasing N_{min} corresponds to retaining more of the larger proximal vessels. Branching asymmetry in these larger vessels, in terms of daughter vessel diameter ratios, flow fraction, and branching angle, may have an effect on outlier proportions.

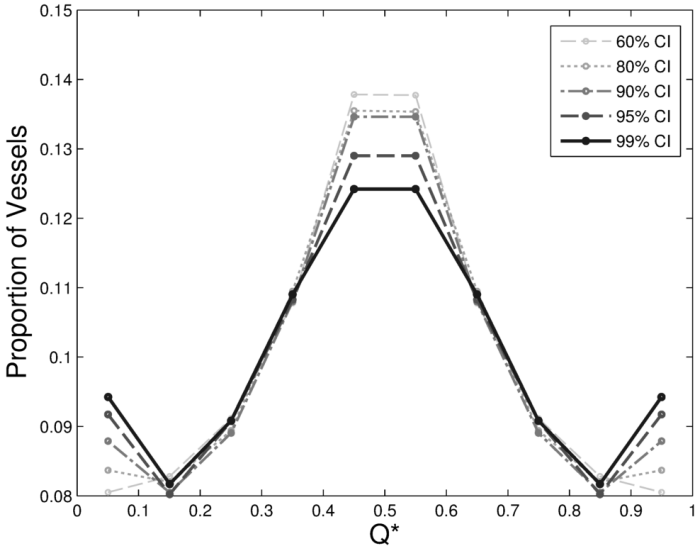

Figure 5.17: Q^* proportion distribution for each viable space with bin-widths of 0.1. In higher CL viable spaces the proportion of vessels with $Q^* < 0.1$ (or equivalently $Q^* > 0.9$) increases, and the proportion of vessels with $0.4 < Q^* < 0.6$ decreases.

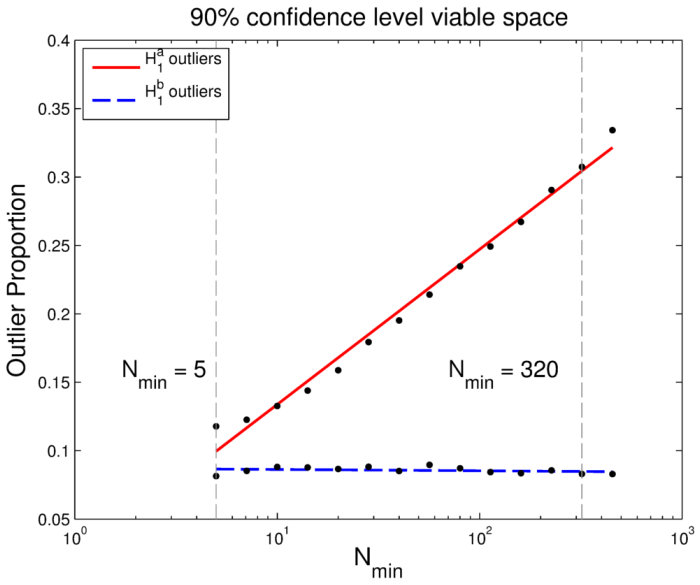

Figure 5.18: 90% CL viable space outlier proportions in relation to N_{min}. Linear least-squares fits are shown for the H_1^a outlier proportions with the solid red line, and for H_1^b with the dashed blue line. The dashed grey lines mark values of N_{min} for which PPDs are plotted in Figures 5.20 and 5.22 respectively.

5.3.3 Regional Phase Separation in Coronary Tree

In order to relate phase separation to vessel generation, the network under consideration can be restricted to bifurcations with a minimum number of microspheres passing through them, N_{min}, as first introduced in Figure 5.4. Outlier proportions for H_1^a and H_1^b are plotted as a function of N_{min} in Figure 5.18 for bifurcations of the 90% CL viable space. There is a positive and approximately linear relationship between H_1^a outlier proportion and $log_{10}(N_{min})$ (Figure 5.19 top), indicating a higher proportion of vessels with phase separation in the more proximal circulation. The H_1^b outlier proportion on the other hand remains approximately constant (Figure 5.19 bottom).
Plots relating H_1^a and H_1^b proportions with N_{min} for each CL viable space are shown in Figure 5.19 with the outlier percentile set to 20%. Trends are consistent for all CL viable space datasets indicating that exclusion of vessels in higher CL viable spaces does not distort this relation and thus phase separation is more prominent in the more proximal circulation. Furthermore with a 20% outlier percentile, H_1^b outlier proportions decrease with N_{min}, reflecting a reduction of vessels with the opposite phase separation effect in higher vessel generations. The PPDs at $N_{min} = 5$ and $N_{min} = 320$ for the 90% CL viable space are plotted in Figures 5.20 and 5.22 respectively. The H_1^a outlier proportions for $N_{min} = 5$ are clearly lower than those for $N_{min} = 320$. The increase in H_1^a outlier proportions are matched by a decrease in the non-outlier percentile proportions, comparing the bottom rows of Figures 5.20 and 5.22. These proportions consist of all the vessels tested for H_1^b, namely vessels which have $Q^* < 0.5$ and $F^* > Q^*$ (bottom left PPD) and their complementary daughter vessels which have $Q^* > 0.5$ and $F^* < Q^*$ (bottom right PPD). The decrease of these particular proportions relative to all others indicates fewer such vessels in the more proximal circulation, and less scatter in the Q^* vs F^* relation of these bifurcations.

Vessel segments corresponding to H_1^a outliers are shown in the 3D vasculature for the PPDs with $N_{min} = 5$ in Figure 5.21 and with $N_{min} = 320$ in Figure 5.23. The red segments are those which make up the H_1^a outlier proportion in the top right PPD where $Q^* > 0.5$ and $F^* > Q^*$, and the blue segments the outlier proportion

in the top left PPD where $Q^* < 0.5$ and $F^* < Q^*$. Figure 5.21 shows that the constraint $N_{min} = 5$ results in a network that includes all of the conduit arteries and many of the arterioles, in which almost 12% of vessels are H_1^a outliers. The prevalence of red segments along the main conduit arteries indicates that there is a clear preference for microspheres to continue along the main branches of the conduit arteries instead of entering a side-branch. Figure 5.23 shows that the constraint of $N_{min} = 320$ results in a coronary network consisting of effectively only epicardial vessels in which the proportion of H_1^a outliers is almost 31%. As illustrated earlier in Figure 5.3 there is greater flow asymmetry in these more proximal coronary arteries.

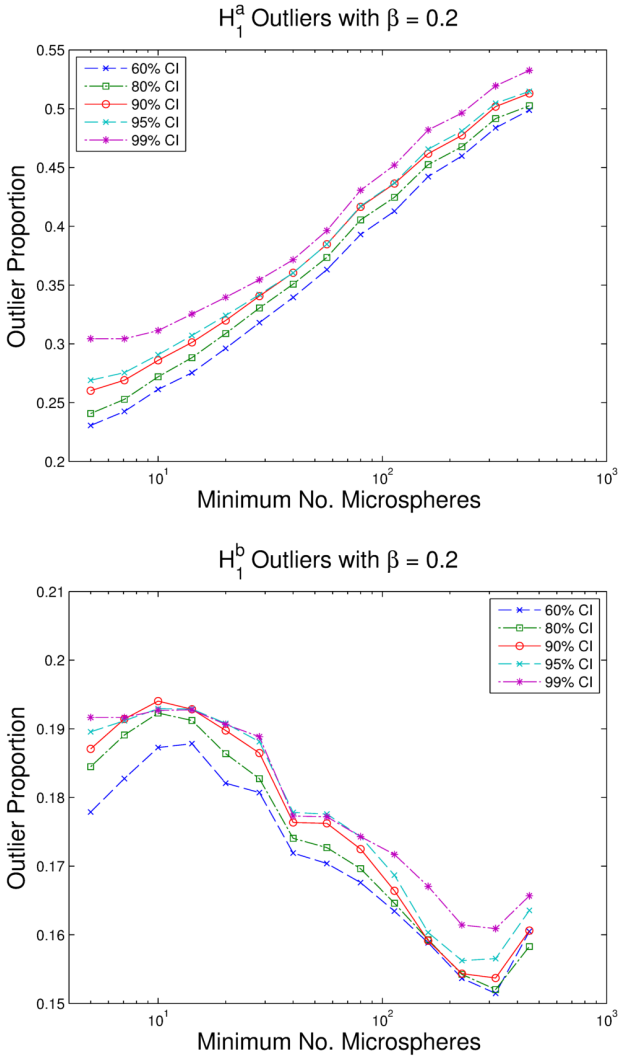

Figure 5.19: All CL viable space outlier proportions related to N_{min}. There is no significant difference between outlier proportions with $\beta = 0.2$ for bifurcations retained at different confidence levels.

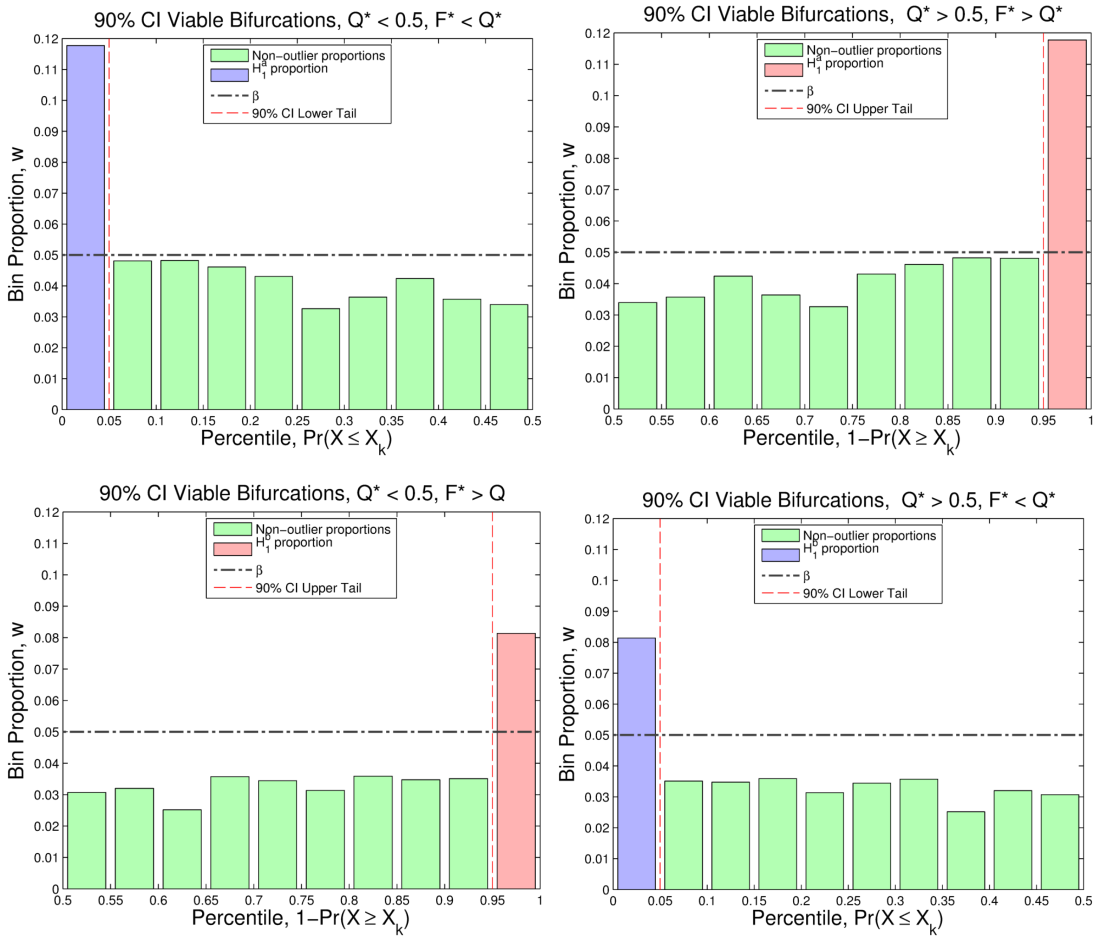

Figure 5.20: 90% CL viable space PPDs with interval width $\beta = 0.1$ and with $N_{min} = 5$. The top row shows symmetric PPDs for daughter vessel pairs tested for the anticipated phase separation H_1^a with Equations (5.16a) and (5.16b). Outliers of these tests make up the proportions of the blue and red bars respectively. Red bars indicate outliers for tests that $F^* > Q^*$, and blue bars indicate outliers for tests that $F^* < Q^*$. The bottom row shows symmetric PPDs for daughter vessel pairs tested for the opposite phase separation H_1^b with Equations (5.17a) and (5.17b). The outlier proportions of the two tests correspond to those enclosed in the dashed orange box in Figure 5.13.

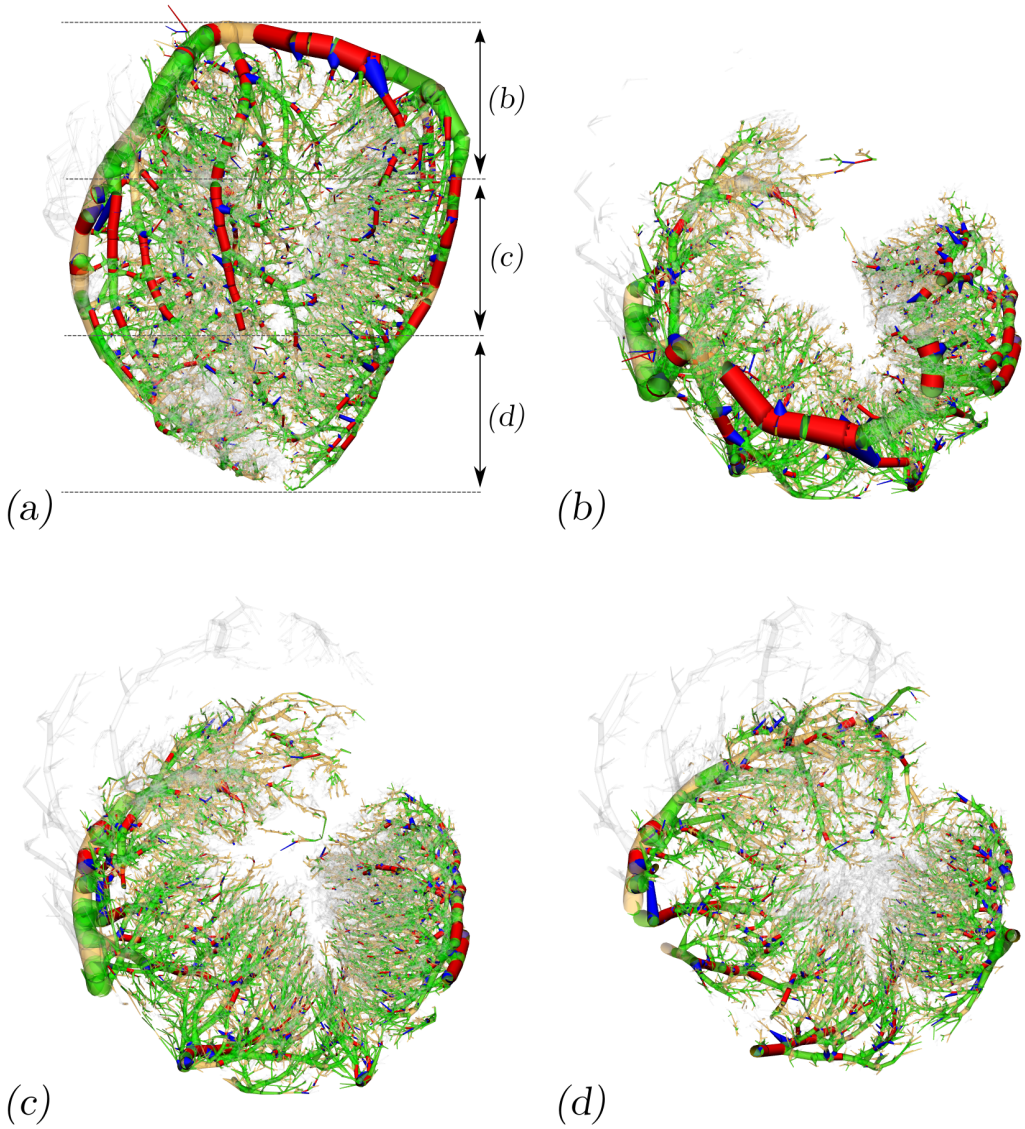

Figure 5.21: 90% CL viable space H_1^a outliers in vasculature with $N_{min} = 5$; (a) anterior long-axis view; (b) short-axis basal MIP; (c) short-axis mid-cavity MIP; (d) short-axis apical MIP. Daughter vessels in red receive more microspheres than expected and those in blue receive fewer microspheres than expected. Green vessels are in the viable space but are not outliers. Faded gold vessels and grey vessels are not in the viable space, although the former satisfy the N_{min} criterion but either form part of a discarded bifurcation (see previous chapter) or has a junction connectivity greater than 3 (e.g. a trifurcation).

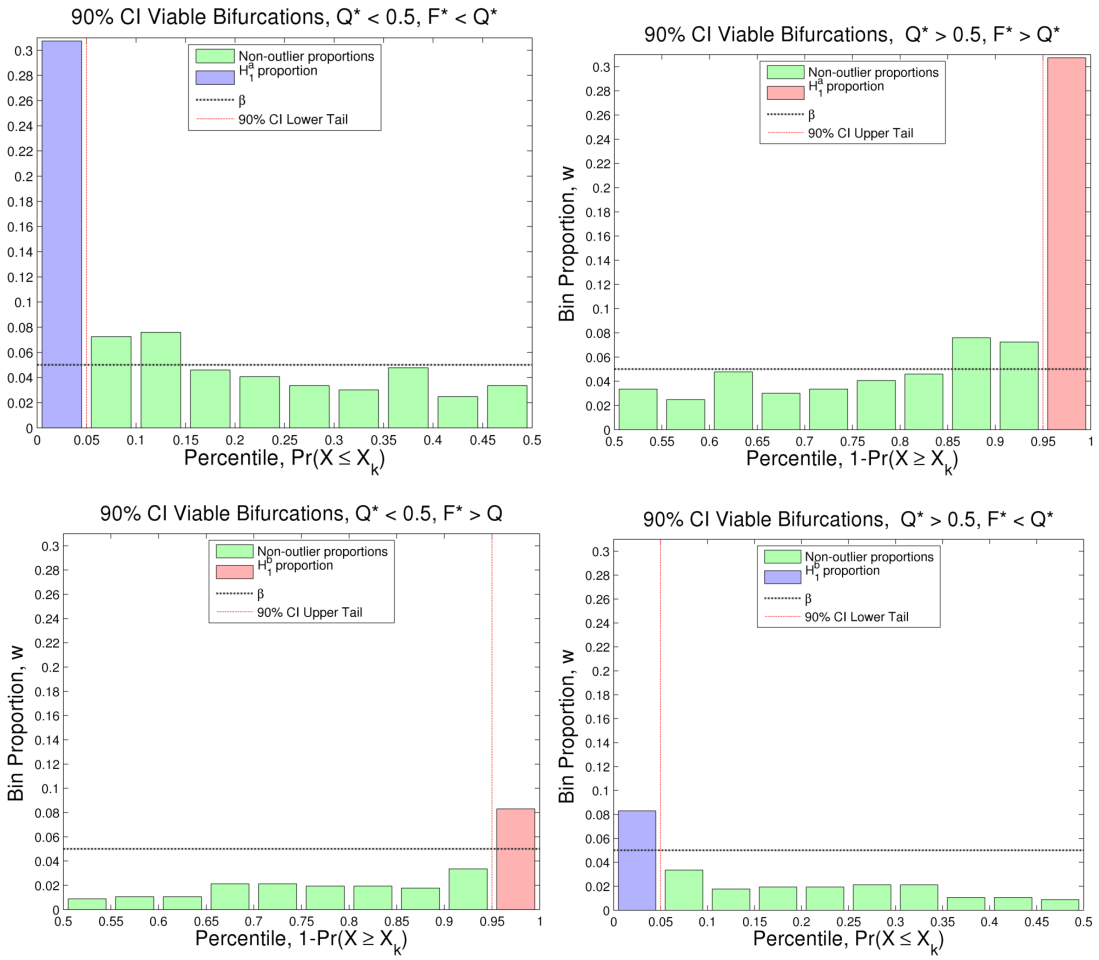

Figure 5.22: 90% CL viable space PPDs with interval width $\beta = 0.1$ and with $N_{min} = 320$. The top row shows symmetric PPDs for daughter vessel pairs tested for the anticipated phase separation H_1^a with Equations (5.16a) and (5.16b). Outliers of these tests make up the proportions of the blue and red bars respectively. Red bars indicate outliers for tests that $F^* > Q^*$, and blue bars indicate outliers for tests that $F^* < Q^*$. The bottom row shows symmetric PPDs for daughter vessel pairs tested for the opposite phase separation H_1^b with Equations (5.17a) and (5.17b). The outlier proportions of the two tests correspond to those enclosed in the dashed orange box in Figure 5.13.

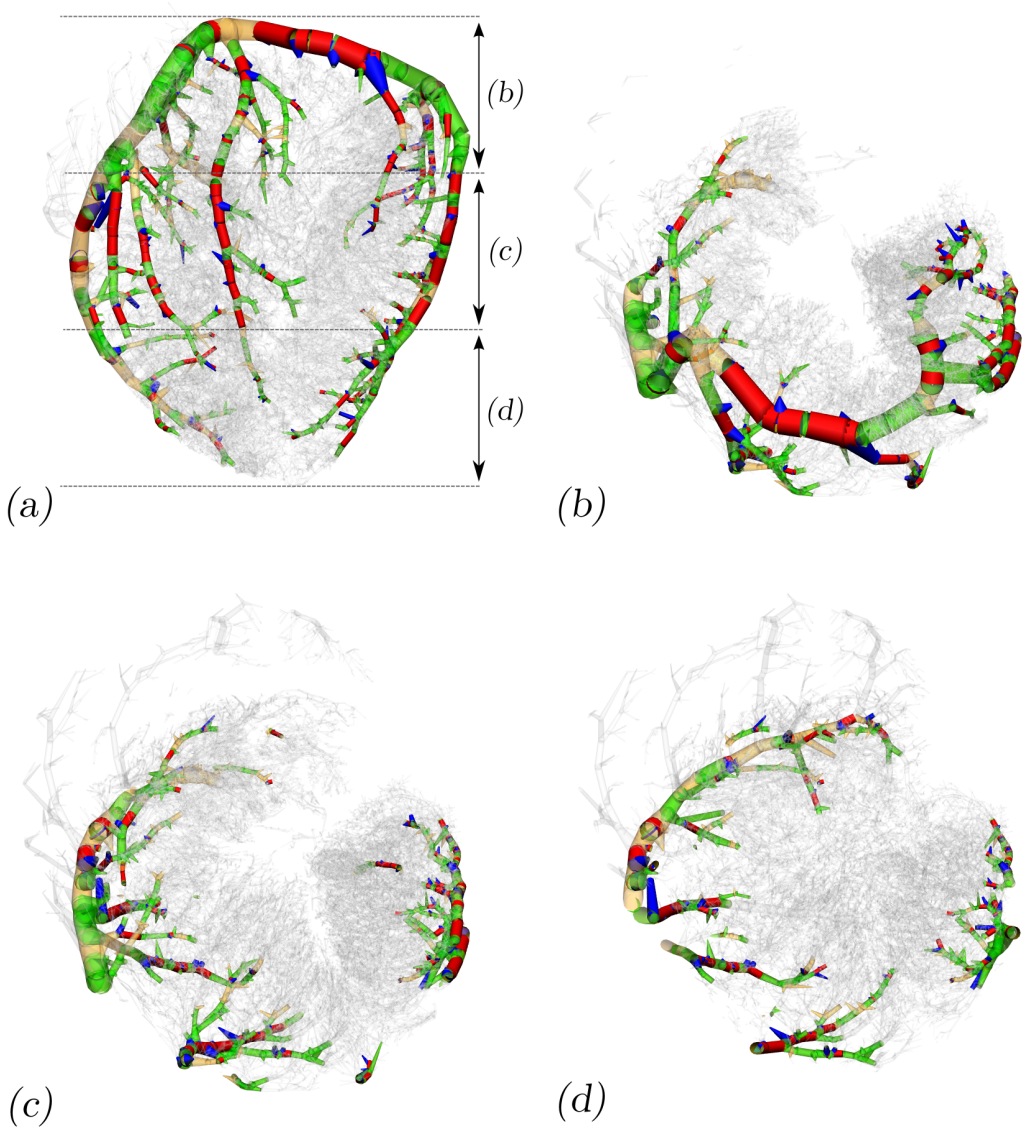

Figure 5.23: 90% CL viable space H_1^a outliers in vasculature with $N_{min} = 320$; (a) anterior long-axis view; (b) short-axis basal MIP; (c) short-axis mid-cavity MIP; (d) short-axis apical MIP. Daughter vessels in red receive more microspheres than expected and those in blue receive fewer microspheres than expected. Green vessels are in the viable space but are not outliers. Faded gold vessels and grey vessels are not in the viable space, although the former satisfy the N_{min} criterion but either form part of a discarded bifurcation (see previous chapter) or has a junction connectivity greater than 3 (e.g. a trifurcation).

5.3.4 Vessel Parameter Correlations

Statistical tests were performed to determine which vessel parameters differed significantly between outlier proportions and non-outlier proportions. The Mann-Whitney U-test was used to determine if the medians of vessel parameters were significantly different between vessels in different percentile proportions. Paired t-tests were not used since the parameters within each sample were not typically from a normal distribution (as tested with the Kolmogorov-Smirnov test). Five categories were compared for significant differences in parameter medians:

Sample S1: H_1^a outliers where (Q^*<0.5, F^*<Q^*)

Sample S2: H_1^a outliers where (Q^*>0.5, F^*>Q^*)

Sample S3: H_1^b outliers where (Q^*<0.5, F^*>Q^*)

Sample S4: H_1^b outliers where (Q^*>0.5, F^*<Q^*)

Sample S5: All non-outlier vessels.

The vessel parameters in each sample which were compared are listed below:

$$Q^* = \frac{Q_1}{Q_1 + Q_2} \tag{5.18a}$$

$$\theta^* = \frac{\theta_1}{\theta_1 + \theta_2} \tag{5.18b}$$

$$r_a^* = \frac{r_1}{r_1 + r_2} \tag{5.18c}$$

$$r_b^* = \frac{r_1}{r_p} \tag{5.18d}$$

$$L_p \tag{5.18e}$$

where subscripts 1 and 2 refer to the current daughter vessel and its complementary daughter vessel at a bifurcation respectively. Parameter θ is the angle between the centrelines of the parent and daughter vessel as shown below in Figure 5.24. Parameter r_a^* is the ratio of a daughter vessel's radius to the summed daughter vessel radii at a bifurcation, and r_b^* is the daughter-to-parent radius ratio. L_p is the

length of the parent vessel, which is related to upstream flow disturbance (Pries *et al.* , 1989; Carr & Wickham, 1990). The first three parameters Q^*, θ^* and r_a^* are all measures of branching asymmetry; values for those parameters of 0.5 would indicate equal flow distribution, equal daughter vessel branching angles, and equal daughter vessel radii at a bifurcation, respectively.

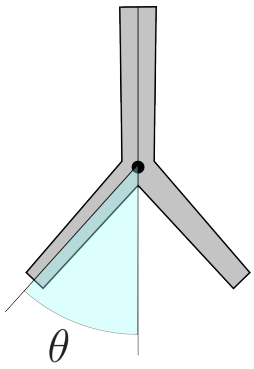

Figure 5.24: Branching angle, θ.

Table 5.3 shows the mean ± standard deviation of parameters in the five samples in the 90% CL viable space, as well as the number of vessels in each sample, N. For the asymmetry parameters Q^*, θ^* and r_a^*, samples S1 and S2 have means which sum to 1 and equal standard deviations, as do samples S3 and S4. Means for these asymmetry parameters in S5 are 0.5. Table 5.4 shows the p-values of two-tailed U-tests, revealing significant differences in sample parameter medians for every inter-sample comparison of the asymmetry parameters Q^*, θ^* and r_a^*.

Table 5.3: Means and standard deviations of sample parameters in 90% CL viable space.

Param.	S1	S2	S3	S4	S5
N	741	741	512	512	10,182
Q^*	0.222 ± 0.157	0.778 ± 0.157	0.289 ± 0.143	0.711 ± 0.143	0.5 ± 0.264
θ^*	0.670 ± 0.206	0.330 ± 0.206	0.602 ± 0.214	0.398 ± 0.214	0.5 ± 0.243
r_a^*	0.376 ± 0.135	0.624 ± 0.135	0.441 ± 0.101	0.559 ± 0.101	0.5 ± 0.125
r_b^*	0.601 ± 0.289	0.918 ± 0.136	0.740 ± 0.242	0.899 ± 0.145	0.812 ± 0.220
L_p	1.226 ± 1.1612	1.226 ± 1.162	1.096 ± 1.353	1.096 ± 1.353	0.980 ± 0.788

Table 5.4: U-test p-values for comparison of sample parameter medians in 90% CL viable space.

Param.	S1 *vs* S2	S1 *vs* S3	S1 *vs* S4	S1 *vs* S5	S2 *vs* S3
Q^*	< 0.01	< 0.01	< 0.01	< 0.01	< 0.01
θ^*	< 0.01	< 0.01	< 0.01	< 0.01	< 0.01
r_a^*	< 0.01	< 0.01	< 0.01	< 0.01	< 0.01
r_b^*	< 0.01	< 0.01	< 0.01	< 0.01	< 0.01
L_p	*NA*	< 0.01	< 0.01	< 0.01	< 0.01
Param.	S2 *vs* S4	S2 *vs* S5	S3 *vs* S4	S3 *vs* S5	S4 *vs* S5
Q^*	< 0.01	< 0.01	< 0.01	< 0.01	< 0.01
θ^*	< 0.01	< 0.01	< 0.01	< 0.01	< 0.01
r_a^*	< 0.01	< 0.01	< 0.01	< 0.01	< 0.01
r_b^*	0.016	< 0.01	< 0.01	< 0.01	< 0.01
L_p	< 0.01	< 0.01	*NA*	0.690	0.690

The daughter-to-parent radius ratio is also significantly different between all categories except for S2 *vs* S4. Parent vessel length is of course equal for S1 *vs* S2 and likewise for S3 *vs* S4, not significantly different for S3 and S4 *vs* S5, but is significantly different for all comparisons of S1 and S2 to other categories. Referring back to Table 5.3 the direction of these differences (an increase or a decrease) of parameter medians between samples can be determined. Parameters r_a^* and r_b^* like Q^* are significantly less in S1 than in any other sample, and parameter θ^* is significantly lower in S1 than in any other sample. The converse is true for all of these parameters when comparing S2 with any other samples. This suggests a correlation between the asymmetry parameters r_a^* and θ^* and model flow fraction Q^*. Parent vessel length L_p is significantly higher in S1 and S2 than in any other sample.

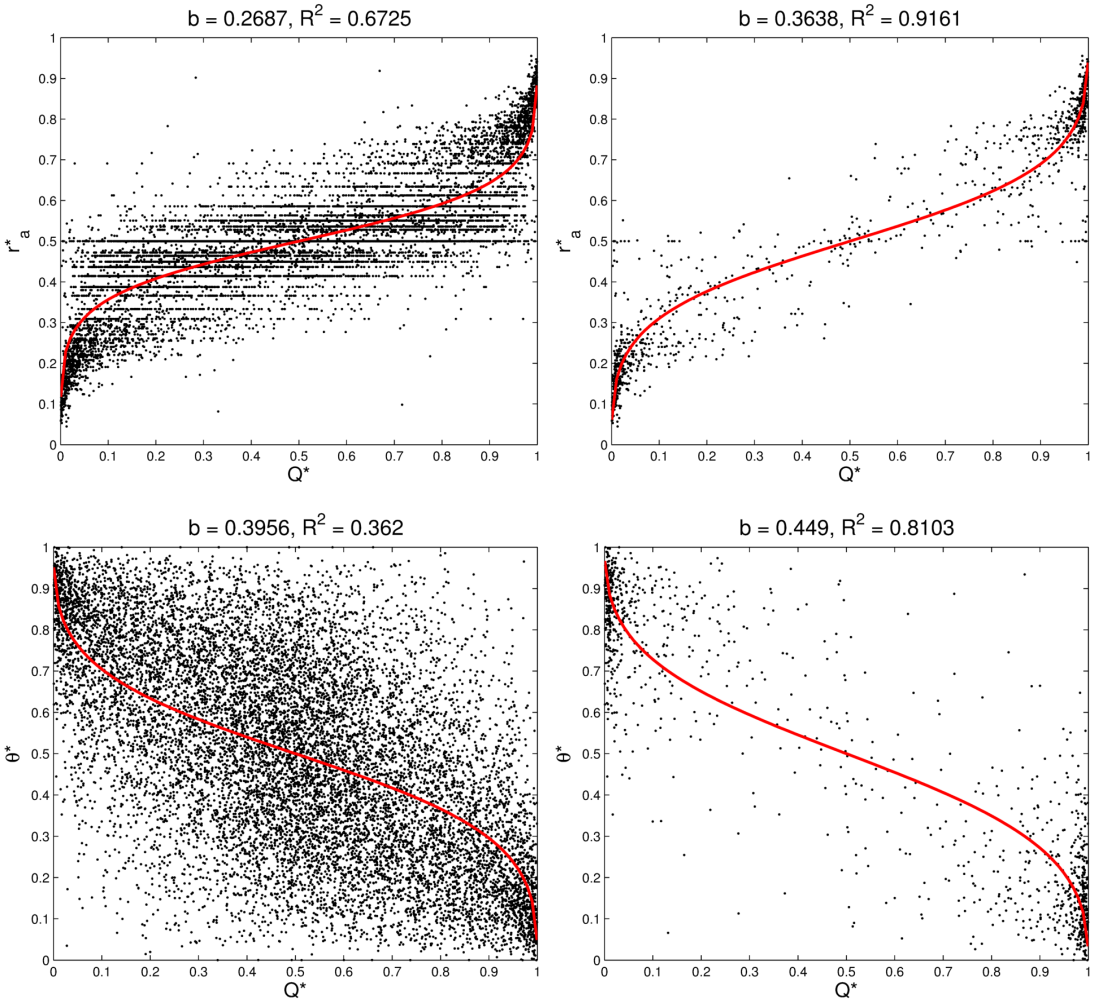

Figure 5.25: Asymmetry parameters r_a^* (above) and θ^* (below) correlated with Q^* for vessels in the 90% CL viable space. The left-hand column is for all vessels in the viable space, and the right-hand column is constrained by $N_{min} = 320$. Logistic functions fitted to the resulting data show a less sigmoidal and more accurate fit with bifurcations constrained by $N_{min} = 320$.

Asymmetry parameters r_a^* and θ^* are plotted against Q^* in Figure 5.25 with $N_{min} = 1$ on the left and $N_{min} = 320$ on the right. Sigmoidal fits are shown in red, with an improved fit in the higher generation vessels where the network is constrained to bifurcations with $N_{min} = 320$. There is a clear positive correlation of Q^* with r_a^* and r_b^*, and a negative correlation with θ^* in the data. This intuitively makes sense, referring back to Figures 5.21 and 5.23 for reference, since the high flow

daughter vessels tend to be part of a main vessel trunk with a larger radius and smaller branching angle than a side branch receiving less flow.

5.4 Discussion

Results demonstrate the prevalence of microsphere skimming particularly in the larger coronary arteries when comparing microspheres to a Poiseuille flow model with a homogeneous perfusion BC. More than expected H_1^a outliers are observed at all confidence levels (60% - 90%), in addition to which more than expected H_1^b outliers are observed at confidence levels from 80% - 99%.

Physiological myocardial tissue perfusion is highly heterogeneous, where a relative dispersion (RD) of perfusion of approximately 26.5% and 29.4% was computed from tissue segments with an average mass of 0.17g from 13 baboon hearts and 0.22g from 11 sheep hearts respectively (Bassingthwaighte *et al.* , 1989). The mean terminal vessel fed volume for the present study was approximately 3mm^3 (0.003g), at which scale relative dispersion of perfusion is likely to be between 60-80% by extrapolating the relationship of RD versus tissue sample mass (Bassingthwaighte *et al.* , 1989). Given that a homogeneous perfusion BC was assumed, conclusions which can be drawn need to be considered carefully. What is clear is that there are more than expected bifurcations at which microsphere flow fraction overestimates model flow fraction in the higher flow daughter vessel, with greater prevalence in the conduit arteries. To draw the conclusion that microsphere skimming indeed occurs in the conduit arteries let us consider several key factors:

1. The more proximal bifurcations to the root of the LCA network feed larger downstream tissue fed volumes;

2. The larger the downstream tissue volume, the closer the perfusion of the downstream tissue is likely to be to the mean perfusion of the LV* since perfusion heterogeneity reduces fractally with increasing tissue segment size (Bassingthwaighte *et al.* , 1989), thus the more suitable the homogeneous BC assumption;

*Recall that the RV-supplying vessels were removed from the analysis in the previous chapter.

3. Introducing terminal vessel perfusion heterogeity[†] in the previous chapter demonstrated that flow in the vessels supplying tissue regions ≥ 0.1g (constituting the largest 4,146 vessels) deviated by less than 2% from the flow computed from the homogeneous perfusion BC (see Figure 4.24 on page 133);

The results show that skimming is increasingly prevalent in the more proximal vessels, for which the homogeneous perfusion BC is a more suitable assumption than in more distal vessels. While many bifurcations were discarded due to failure to meet the observability criteria (Figure 5.12), a test for whether including more bifurcations by reducing the CL resulted in a greater outlier proportion revealed that this made no significant difference (Figure 5.19). Furthermore, even having discarded a large number of lower generation bifurcations with too few microspheres (Figure 5.19), there was still a considerably larger number of low generation bifurcations such that it did not affect the conclusion that skimming is more prevalent in the higher vessel generations (Figure 5.18). Model flows in the large conduit arteries are likely to be closer to physiological flows compared to vessels further downstream which supply smaller tissue regions with a higher associated perfusion heterogeneity. The perturbation analysis of terminal perfusion also demonstrated the insensitivity of proximal coronary arteries to terminal perfusion heterogeneity. It is therefore not unreasonable to assume that microsphere skimming is indeed occuring in the large conduit arteries as shown in Figure 5.23 on page 181.

The higher flow fraction vessels in which skimming occurs (namely the H_1^a outlier vessels with $Q^* > 0.5$) as a lumped category have a significantly higher flow fraction, lower daughter-daughter branching angle ratio θ^* (i.e. they are generally more parallel with the parent vessel), and larger radius ratios r_a^* and r_b^* than the non-outlier vessels (as well as naturally the H_1^a outlier vessels with $Q^* < 0.5$). As presented in the Background section in the Introduction, there are many factors which have been studied for their influence on phase separation. Flow fraction entering each daughter vessel has been established as the predominant cause of phase separation coupled with the phenomenon of axial streaming of suspended

[†]The perfusion heterogeneity introduced at the level of vessels supplying fed volumes of approximately 0.001g yielded $RD \approx 60\%$ as illustrated in Figure 4.25 on page 135.

particles resulting in non-uniform cross-sectional particle concentration (Schmid-Schönbein & Skalak, 1980). While phase separation is more likely to occur when particle diameter is closer to vessel diameter (Ofjord & Clausen, 1983), low particle concentrations amplify the effects of axial streaming and hence increase the severity of skimming (Fenton *et al.* , 1985). Thus low particle concentrations and high flow asymmetry in the conduit arteries may explain the prevalence of phase separation in the coronary arteries despite small particle size. Also while both *in vitro* and *in vivo* studies have shown that vessel branching angle is an insignificant influence for phase separation (Bugliarello & Hsiao, 1964; Palmer, 1965; Pries *et al.* , 1981; Fenton *et al.* , 1985), daughter radius ratio does have an influence because of changes in the non-linear flow profiles of fluid entering each daughter vessel (Fenton *et al.* , 1985; Pries *et al.* , 1989). This study shows that in the coronary arterial vessels of the porcine coronary circulation these parameters are correlated with Q^* with a sigmoid function (Figure 5.25 on page 185).

At higher confidence levels where the outlier percentile β was smaller, the proportion of outliers relative to the expected proportion (also given by β) increased, as shown in Figure 5.13 (page 170) and Table 5.2 (page 169). This implies that most of the outliers lie in a percentile very close to zero (or one hundred) making them very strong outliers in the binomial distribution representation. The PPDs of the 95% CL in Figure 5.14 (page 171) showed reasonably little variation in non-outlier percentile proportions (green bars) compared to the outlier proportions (red and blue bars). This suggests that the outlier bifurcations in which phase separation occurs are distinct, which has been shown in terms of geometry ratios and flow fractions.

The number of bifurcations retained for analysis with binomial distribution confidence intervals in each CL viable space was a matter of vessel observability, determined by flow fraction Q^* and the number of microspheres passing through each bifurcation, N. Viable spaces of higher confidence levels contained fewer bifurcations for the analysis as a result (Figure 5.12 on page 168), with 3,788 retained in the 99% CL viable space compared to 10,713 retained in the 60% CL viable space. Setting the outlier percentile to $\beta = 0.2$ a comparison of the outlier proportions

for bifurcations retained in each CL viable space revealed an increase in H_1^a outlier proportion with increasing CL, as shown in Figure 5.16 (page 173). The minimum value of N required in higher CL viable spaces increased to meet observability criteria, meaning proximal vessels in the network were preferentially retained in higher CL viable spaces. An increase in the proportion of vessels retained at higher CLs with more disparate flow fractions (i.e. closer to 0 or 1) as shown in Figure 5.17 (page 174) indirectly suggested that this greater flow asymmetry in the proximal circulation may have been an underlying cause of more prevalent phase separation.

Higher vessel generations were considered by restricting the network to bifurcations with a minimum number of microspheres passing through them, N_{min}. Considering the 90% CL viable bifurcations where $\beta = 0.05$, a linear increase in H_1^a outlier proportion was found with an increase in $log(N_{min})$, and H_1^b remained relatively constant (Figure 5.18 on page 174). This trend was consistent for all CL viable spaces when the outlier percentile was set at be $\beta = 0.2$. A higher CL viable space constrained by a given N_{min} (set A) contains fewer bifurcations than a lower CL viable space constrained by the same N_{min} (set B), because the observability constraint is more relaxed for set B resulting in more vessels with strongly asymmetric flow fractions being retained. One might expect this to result in a higher proportion of H_1^a outliers in set B compared to set A at a given N_{min} given high flow asymmetry is established as a cause for phase separation. However, the additional highly asymmetric bifurcations in lower CL viable spaces do not seem to result in a higher H_1^a outlier proportion at a given N_min, as illustrated in Figure 5.19 on page 177. The degree of skimming does not decrease by excluding the bifurcations with the most asymmetric flows, but rather slightly increases. This result seems counterintuitive, but given the increase is small[‡] it does warrant investigation.

Visualisation of the 3D network showing vessel segments corresponding to H_1^a outliers in the 90% CL viable space with $N_{min} = 5$ shows a high prevalence of H_1^a outlier bifurcations in the epicardial vessels, and along the transmural conduit arteries (Figure 5.20 on page 178). The vessel segments receiving high flow fractions

[‡]From Figure 5.19 there is an increase in H_1^a outlier proportion from 50% to 53% at $N_{min} = 320$ and $\beta = 0.2$ with a 60% CI and 99% CI, respectively.

along the conduit arteries receive a higher than expected fraction of microspheres, and the smaller branching segments fewer than expected. A 3D network visualisation at $N_{min} = 320$ (in Figure 5.22 on page 180) shows that the remaining network constitutes primarily epicardial arteries in which phase separation is most prevalent. The highly asymmetric epicardial and transmural conduit arteries transport blood generally from base to apex and from subepicardium to subendocardium, before feeding into resistance vessels which branch more symmetrically (Kalsho & Kassab, 2004; Marxen *et al.* , 2006). However the myocardium near the epicardial surface and the base of the heart are supplied by side-branches stemming directly from the large epicardial vessels, and have a lower vascular volume than the vessels which extend inward to the subendocardium (van Horssen *et al.* , 2014). The more proximal to the coronary ostia a side branch is, the lower the flow fraction it is likely to receive since blood in the main branch from which it stems needs to supply a much larger proportion of the myocardium. This provides a physiological explanation for the branching asymmetry in the proximal circulation.

There were also significant H_1^b outliers in the data, which represent the opposite effect of phase separation to what is generally observed. That is, low flow fraction daughter vessels receiving disproportionately high fractions of microspheres, and vice versa for high flow daughter vessels. This effect has previously been shown to result from upstream flow disturbance as a function of parent vessel length (Pries *et al.* , 1989) and flow velocity (Carr & Wickham, 1990). If the parent vessel is not long enough for a parabolic flow profile to be re-established, particles can become asymmetrically displaced in the downstream flow profile (see Figure A.4 in Background on page 210). In this study the H_1^b outlier vessels have a significant presence, more so than any non-outlier percentile proportions in the PPDs for all CLs from 80% to 99%. No single parameter has been identified as largely responsible for H_1^b outliers in this study, although it is plausible given the complex geometry of the vascular network that flow disturbances. There is also the possibility that these outliers are the result of cumulative errors between the Poiseuille model with homogeneous BCs and the microsphere allocation. The proportion of H_1^a outliers at each CL however is significantly larger than the H_1^b outliers suggesting that even if the H_1^b outliers were in part due to error in the model, it is

unlikely that phase separation indicated by the H_1^a outliers could be denied.

The observation that microsphere skimming becomes less prevalent in the smaller coronary arteries may be due to a combination of factors. Firstly perfusion heterogeneity is known to increase at smaller tissue sample sizes, which implies that the homogeneous perfusion BC is less valid further down the network. Additionally due to low microsphere counts many of the bifurcations with highly asymmetric flow fractions in lower vessel generations were not suitable for, and hence were discarded from, the analysis. These factors both add some degree of error to the analysis for skimming in lower vessel generations. On top of this, fed volumes assigned to terminal vessels are idealised and do not represent the true perfusion territories of each terminal vessel, although the inherent error of this volume assignment decreases in higher vessel generations as fed volumes of downstream vessels are summed. Both of these factors mean that further downstream vessels inherently have greater errors in their values of Q^* and F^*. Another point which supports the observation of lower skimming prevalence in smaller vessels is that branching becomes more symmetric towards lower vessel generations in terms of flow fractions, as well as ratios of area, vessel volume, resistances and lengths (Kalsho & Kassab, 2004). Given that skimming is known to occur in much smaller vessel diameters than available in this dataset, the increasing vessel symmetry at lower vessel generations is in agreement with the observation of less frequent phase separation.

The assumption of homogeneous perfusion BC disregards previous observations of heterogeneity in the myocardium (Bassingthwaighte *et al.* , 1989). However several studies have shown that in a vasodilated state the heart receives a more homogeneous distribution of blood (Gorman *et al.* , 1989; Bauer *et al.* , 2001; Chareonthaitawee *et al.* , 2001). Nonetheless, accurate assignment of terminal boundary conditions for truncated coronary networks remains an issue due to a lack of experimental data so other assumptions about coronary structure-function relations have been used in previous modelling studies. As demonstrated in the previous chapter, the volume-scaled downstream resistance BC (i.e. the heterogeneous perfusion BC) produced flows in the network which compared poorly with

the microsphere distributions. Another approach has been to generate vasculature down to the level of the capillaries where a constant outlet pressure BC could be imposed as in (Mittal *et al.* , 2005; Huo *et al.* , 2009), although this method employed a questionable 'copy and paste' approach using previously measured vessel bifurcations to replace missing subtrees of vessels between approximately 8-40μm in diameter.

Another approach which holds potential for more accurate boundary conditions is to use 'molecular microspheres' for unbiased flow measurements in small tissue segments using the imaging cryomicrotome, which have been mentioned in literature but not used in any studies to-date (Prinzen & Bassingthwaighte, 2000). Fluorescently labeled antibodies which target antigens in the capillary endothelium are supposedly under development for imaging with an epifluorescent cryomicrotome [§]. These molecular deposition markers could potentially allow for very precise quantification of myocardial blood flow to terminal vessels and would address the problem of assigning terminal BCs for such network simulations. They would also allow for assessment of the homogeneous BC's suitability, and could be used to confirm and/or derive laws relating branching geometry to outlet flow. Furthermore with accurate perfusion boundary conditions prescribed for vascular network model reconstructed from real data, branching heterogeneity and flow heterogeneity can be directly compared to gain insight into their relationship.

Bassingthwaighte made the observation of systematic over-deposition of 16.5μm diameter microspheres in regions of high flow as measured with IDMI, and a weak positive gradient of microsphere density from the subepicardium to the subendocardium (Bassingthwaighte *et al.* , 1987, 1990). An increasing subepicardial to subendocardial gradient of microsphere density was also observed when using particles of increasing diameter (Domenech *et al.* , 1969; Yipintsoi *et al.* , 1973; Utley *et al.* , 1974). The results of this study do not directly explain these previously observed effects, they do however reveal that skimming is strongly likely to occur in the conduit arteries (with a high branching asymmetry) which descend

[§]http://sbirsource.com/sbir/awards/94486-antibody-imaging-for-regional-flow-measurements

the heart walls and traverse the myocardium. Such observations support the hypotheses that microspheres preferentially distribute to higher flow regions, and preferentially distribute towards the subendocardium. These results also support the observations in the first chapter of microsphere deposition density gradients from the base-to-apex and from subepicardium-to-subendocardium. As previous animal studies have shown however, despite a systematic bias the microsphere method is reliable in tissue regions containing approximately 400 microspheres (Bassingthwaighte *et al.* , 1987, 1990).

Despite the identification of skimming in the proximal coronary circulation, in the study presented in Chapter 2 microsphere quantification in AHA regions for the validation of quantitative perfusion MRI is not confounded. At the very least, this finding suggests that as a precaution tissue segments used for flow quantification should not be divided too finely in a transmural direction (i.e. between the epicardium and endocardium), even if each region contains at least 400 microspheres, due to the observed deposition bias in tissue regions supplied by major conduit arteries which penetrate the myocardium transmurally.

5.5 Conclusions

A novel statistical approach has been developed and used to show the presence of phase separation in a porcine left coronary artery network. Phase separation appears to be most prevalent in the larger coronary arteries where there is a higher degree of branching and flow asymmetry. Branching asymmetry parameters Q^*, r_a^* and θ^* are significantly different in vessels in which phase separation occurs compared to those without phase separation. Furthermore although Q^* was assigned independently of r_a^* and θ^*, there is a strong correlation of Q^* with both of these parameters in the examined LCA network.

6 | Conclusions and Future Work

> *[Truth] is come at by a process, a coming into being of something; and that process is also, importantly, part of the truth. It is an act, a journey, not a thing. It has degrees. It is found by removing things, rather than by putting things together. [...] Truth as unconcealing is a progress towards something - the something is in sight, but never fully seen; whereas truth as correctness is given as a thing in itself, that can in principle be fully known.*
>
> – Ian McGilchrist (explaining Heidegger), *The Master and His Emissary*

The research outlined in the previous chapters describes a number of contributions to the understanding of coronary blood flow that have been made in this thesis. These are summarised as follows:

Chapter 2 Validation was provided for quantitative perfusion MRI using a gold standard of intra-organ perfusion measurement, microspheres. A novel method was developed involving image registration and cubic Hermite mesh fitting for quantifying myocardial blood flow (MBF) in AHA segments from microspheres, imaged with an epifluorescent CMT for the comparison to quantitative DCE-MRI algorithms. The strong correlations provide confidence in quantitative perfusion MRI measurements, and brings this technique a step closer to clinical application.

Chapter 3 The reconstruction and pruning of the LCA network of a pig heart from a stack of cryomicrotome images was achieved, to produce a vascular

network with approximately 10^5 vessel segments. This is the most detailed coronary arterial vascular network model reconstructed from imaging data to-date, which additionally was used for blood flow simulations. A more recent version of this network than used in this thesis can be found online: https://portal.vph-share.eu/resources/ae666741-66cb-4b1d-aa93-db4b34c0e9ce/.

Chapter 4 A novel outlet flow boundary condition which assumed homogeneous perfusion was developed to simulate Poiseuille flow throughout the LCA network. Simulated flow values were shown to be closer to microsphere-derived flows throughout the network compared to a previously proposed volume-scaled terminal resistance boundary condition. A novel method for identifying errors in the reconstructed network was developed using the distribution of microspheres for comparison, and allowed for the removal of erroneous branches from the network. The resulting network flow simulation produced an error relation with the microsphere distribution comparable to errors between two simultaneously injected microsphere samples. Physiological perfusion heterogeneity was achieved using the model upon introduction of random terminal vessel flow heterogeneity. This introduced perfusion heterogeneity resulted in only small changes in the model-microsphere error in the higher vessel generations, providing evidence for the suitability of the homogeneous perfusion BC for further analysis of skimming.

Chapter 5 A statistical method was developed to determine the prevalence of microsphere skimming in the network. Poiseuille flow was compared to microsphere-derived flow assuming a binomial distribution at each bifurcation in the network, and the higher generation arteries were identified as exhibiting the most prevalent microsphere skimming. Higher branching asymmetry was associated with bifurcations at which skimming occurred.

Specific directions for future work have previously been discussed in each chapter. Below these are summarised in the wider research context of the thesis as a whole.

Firstly automatic image registration of cryomicrotome and MRI data was hampered by the availability of only low-resolution MR images, with the additional

difficulty introduced by the high-contrast fluid in which the heart was partially submerged while mounted in the MRI-compatible Langendorff apparatus. Manual rigid registration of CMT data (both geometry and microsphere locations) with multiple MRI projections (short-axis perfusion, long-axis, and survey scan images) required careful examination of the overlap of bulk cardiac geometry and key anatomical points in the two datasets. While this approach was appropriate for the given dataset, an additional 3D MRI anatomical scan would provide higher resolution information of the cardiac geometry that may be suited for application of automated registration algorithms, saving time and potentially providing a registration of similar or greater accuracy.

The reconstruction of the LCA network, while currently one of the most detailed reconstructions of a vascular network from image data, suffers from limitations within the reconstruction pipeline. Specific inaccuracies in radius estimation could be addressed by validation of estimation algorithms using phantom tubes of known diameter imaged with the cryomicrotome, as well as applying radius estimation directly to the original image data using the Rayburst algorithm (Rodriguez *et al.* , 2006). There is also potential for improvement in the vessel filtering and thresholding stages; currently the Frangi filter fails to retain the junctions of many smaller vessels. To address these issues enhancements could be made by using combined gradient-morphology filters (Tankyevych & Talbot, 2009; Verdú-Monedero *et al.* , 2009) or a strain energy filter (Xiao *et al.* , 2011).

The proposed flow model in Chapter 4 relied on the assignment of terminal fed volumes for the prescription of terminal boundary conditions. One drawback with the use of this data was the absence of vascular cast in the right coronary artery (RCA), resulting in overestimated fed volume to terminal vessels of the LCA bordering the empty RCA territory. In future, the acquisition of a complete set of vascular data constrained by a myocardial segmentation would address this issue. However differences in regional perfusion would still need to be accounted for, specifically between the RV, LV and septal wall regions, all of which have differences in mean perfusions (Duncker & Bache, 2008).

While the homogeneous perfusion BC proved to produce a closer agreement between flows in the network with respect to the microspheres in comparison to the volume-scaled terminal resistance BC, there are several other boundary conditions which have been proposed for vascular network flow that do not depend on terminal tissue volume. While it makes sense to utilise tissue volume that is uniquely available in a dataset such as that provided from cryomicrotome imaging or micro-CT imaging (Marxen, 2004), a homogeneous perfusion BC disregards physiological regional perfusion heterogeneity. Additionally, while the heterogeneous perfusion BC produced worse agreement with microsphere-derived flows, this may have in part been a result of inaccuracies in the network reconstruction and resulting assigned terminal fed-volumes. By having a more complete vascular tree reconstruction (including the RCA for example), as well as more accurate terminal radii, terminal fed-volumes would likely become more uniform, and potentially improve results obtained with the heterogeneous BC. Marxen's comparison of microsphere and model flow in a rat kidney, shown in Figure 2 of (Marxen *et al.* , 2006), was far less asymmetric than the results obtained in this study (see Figure 4.7 on page 118). However, given the regional differences in branching structure and vascular density in the heart which are not observed in the kidney (Spaan *et al.* , 2005; van Horssen *et al.* , 2014), a global vascular scaling law seems less appropriate in the heart. Alternative BCs which could also be compared to the current method include (1) generation of the vascular tree to the capillary level based on morphometric data at which level a constant pressure BC is prescribed (Mittal *et al.* , 2005), and (2) application of a radius-dependent terminal vessel pressure (Hyde *et al.* , 2013a). Both of these methods would require accurate reconstruction of terminal vessels of the network, and would possibly necessitate the network to be truncated at a higher vessel generation for greater accuracy in terminal radius.

Finally there is potential to acquire accurate high-resolution images of regional perfusion from fluorescently-labelled molecular markers. This would provide (1) the opportunity to prescribe accurate, heterogeneous perfusion BC's for a network flow model, (2) allow for a more accurate model to compare with microsphere distribution, and (3) allow for network branching geometry and regional perfusion to be related, providing insight into the structure-function relationship, and finally

(3) a validation of the approach taken to identify microsphere skimming.

Impact

The method developed for the assessment of microsphere perfusion for comparison to perfusion MRI has allowed for validation of quantitative perfusion MRI in *ex vivo* porcine hearts. A further step is required to validate perfusion MRI in *in vivo* hearts before any clinical studies should be undertaken, particularly to ensure the additional *in vivo* factors such as cardiac contraction do not alter perfusion validation with microspheres. This may be achieved by comparing quantitative perfusion MRI of *in vivo* hearts with simultaneous microsphere injection to perfusion derived from microspheres imaged with cryomicrotome after excision. The current method with an extended image registration procedure can account for the deformation of the heart after excision. This validation could potentially provide a new clinical quantitative metric for cardiac perfusion, both for the purposes of monitoring disease progression and for the classification of disease severity.

The identification of microsphere skimming using the porcine LCA model provides evidence for a hypothesis which could not previously be tested. However, to have complete certainty in this result, more information must be made available regarding perfusion heterogeneity for the prescription of boundary conditions in our model, as discussed earlier. Given the strong likelihood of microsphere skimming being present and related to branching asymmetry particularly in the large coronary vessels, this would suggest that microspheres are preferentially distributed towards the subendocardium via the transmural conduit arteries. To validate perfusion MRI quantification in transmural segments, or at higher resolutions (e.g. pixel-wise quantification), this finding needs to be taken into consideration. Specifically a transmural microsphere distribution bias needs to be quantified in order to more accurately compute perfusion from microspheres. This may be achieved in the future by comparing microsphere distribution through the coronary network to a higher fidelity deposition marker such as IDMI, which current imaging methods would need to be modified for. This would provide greater confidence in the

flow model (with terminal flows parameterised by IDMI distribution) to derive relations between vessel branching properties and microsphere deposition locations with microsphere skimming. From these relations, a model to correct for microsphere distribution bias could be proposed and used to correct for the skimming bias in future high-resolution quantitative perfusion MRI validation studies.

Appendices

A | Determinants and Models of Skimming

A.1 Determinants of Skimming

In studies to validate the accuracy of microspheres for use in organ flow quantification, Bassingthwaighte compared microsphere and IDMI distributions in rabbit and sheep hearts (Bassingthwaighte *et al.* , 1987, 1990). His results demonstrated strong agreement between the two methods, but also revealed a slight systematic overestimation of IDMI flow by microsphere deposition in regions flow above the mean. Bassingthwaighte theorised that this systematic bias was due to phase separation. This phenomenon is where particles (including microspheres as well as red (RBC) and white blood cells (WBC)), distribute at a bifurcation disproportionately to the suspending medium. Particles enter higher-flow daughter vessels with a statistically higher frequency, and as a corollary they enter lower-flow daughter vessels with a statistically lower frequency. This phenemenon is a function of plasma flow fraction, feed haematocrit, vessel geometry and particle size. This phenomenon was first noted by Krogh who coined the term 'plasma skimming'* to describe the reduction of haematocrit (HCT) in contracting arterioles with the reduction in flow (Krogh, 1922). Plasma skimming has been studied extensively *in vitro* (Bugliarello & Hsiao, 1964; Palmer, 1965; Yen & Fung, 1978; Ofjord, 1981; Ofjord & Clausen, 1983; Dellimore *et al.* , 1983; Fenton *et al.* , 1985; Chien *et al.* , 1985; Carr & Wickham, 1990) with plastic particles, RBCs and hardened RBCs, and *in vivo* (Krogh, 1922; Svanes & Zweifach, 1968; Johnson, 1971; Johnson *et al.*

*this is used interchangeably in the literature with phase separation.

, 1971; Fung, 1973; Schmid-Schönbein & Skalak, 1980; Klitzman & Johnson, 1982; Pries *et al.* , 1989, 1992), with RBCs, WBCs and disk-like and spherical particles. These studies have collectively identified major determinants of phase separation, which are listed in table A.1 with key references.

Phase separation of RBCS *in vivo* is most pronounced in the capillaries, where RBCs are similar in diameter to the blood vessels and result in greater sensitivity to bias in distribution at bifurcations. Many *in vivo* studies have been carried out to characterise plasma skimming in the capillaries (Johnson, 1971; Johnson *et al.* , 1971; Fung, 1973; Schmid-Schönbein & Skalak, 1980; Klitzman & Johnson, 1982; Pries *et al.* , 1981, 1989). Furthermore at the scale of the capillaries the influences of cell-cell and cell-wall interactions as well as lateral cell migration on phase separation become important, for which recent computer simulation studies have sought to investigate. Given that the diameter of the smallest vessels extracted for the model presented in this thesis is $\geq 128\mu m$, such effects are considered not to be of great significance and the interested reader is directed to the following papers (Secomb *et al.* , 1985; Pries *et al.* , 1992; Secomb *et al.* , 1998; El-Kareh & Secomb, 2000; Pries & Secomb, 2005; Obrist *et al.* , 2010; Secomb *et al.* , 2007, 2009; Barber *et al.* , 2011).

Bulk flow fraction to a daughter vessel, Q^*, has been recognised as the primary determinant of phase separation in all studies, where flow fractions to daughter vessels at a bifurcation sum to 1. More specifically, phase separation most commonly occurs with unequal flow fractions, $Q^* < 0.5$ or $Q^* > 0.5$, and is more pronounced as $Q^* \rightarrow 0$ or $Q^* \rightarrow 1$. Investigators have over time elucidated contributing mechanisms and defined empirical relations to explain the non-linear, sigmoidal relation between Q^* and fractional particle distribution, F^*, for observations made at bifurcations. One of the earliest contributing factors to be identified for phase separation was 'axial streaming', where particles group towards the centre of a vessel creating a marginal zone near the wall absent of particles, and a gradient of increasing particle concentration towards the vessel's longitudinal axis (Taylor, 1955; Bayliss, 1959). This effect was further elucidated by Segré and Silberberg

Table A.1: Determinants of phase separation.

Determinant	Author/Year	Experiment details	
		Vessel type/diameter	Particle type/diameter
Flow fraction, Q_d/Q_p (dividing streamline)	(Krogh, 1922)	*in vivo* arterioles	RBCs
	(Bugliarello & Hsiao, 1964)	*in vitro* tubes	RBCs
	(Johnson *et al.* , 1971)	*in vivo* capillaries	RBCs
	(Ofjord, 1981)	*in vitro* slits	RBCs, μspheres/$10-15\mu m$
Diameter ratio, λ (of particle to vessel)	(Ofjord & Clausen, 1983)	*in vitro* T-junc. /$40-160\mu m$	RBCs, μspheres/$10-15\mu m$
	(Chien *et al.* , 1985)	*in vitro* T-junc./$1cm$	Spheres and disks/$0.32-0.79cm$
	(Fenton *et al.* , 1985)	*in vitro* tubes/$20-100\mu m$	RBCs
Parent conc., C_p (parent HCT, H_D)	(Bugliarello & Hsiao, 1964)	*in vitro* tubes	RBCs
	(Fenton *et al.* , 1985)	*in vitro* tubes/$20-100\mu m$	RBCs
	(Pries *et al.* , 1989)	*in vivo* vessels/$7.5-40\mu m$	RBCs
Flow history, z/Q	(Fung, 1973)	*in vivo* capillaries	RBCs
	(Pries *et al.* , 1989)	*in vivo* vessels/$7.5-40\mu m$	RBCs
	(Carr & Wickham, 1990)	*in vitro* tubes/$25-50\mu m$	RBCs
Eccentricity, e_x (effect of C_p and z/Q)	(Schmid-Schönbein & Skalak, 1980)	*in vivo* capillaries	RBCs and WBCs
	(Chien *et al.* , 1985)	*in vitro* T-junc./$1cm$	Spheres and disks/$0.32-0.79cm$
daughters diameter ratio D_1/D_2	(Pries *et al.* , 1989)	*in vivo* vessels/$7.5-40\mu m$	RBCs
	(Fenton *et al.* , 1985)	*in vitro* tubes/$20-100\mu m$	RBCs

who showed that particles experience a net force within a tube which causes them to concentrate in the tube's centre forming a parabolic flow profile (Segré, 1961; Segré & Silberberg, 1962). Measurements of the velocity profiles of platelets and RBCs in rabbit mesentery arterioles using video microscopy showed flattened profiles compared to an exact parabola, but still with a maximal flow in the centre of the profile approximately 1.5× that near the vessel wall (Tangelder *et al.* , 1986). Particles within a parabolic streaming profile have also been described in terms of *eccentricity*, denoted by e_x in table A.1, which is the radial distance of a particle from the centre of a vessel divided by the vessel radius; e_x was shown to be strongly related to the nonlinearity of the cell distribution profile in capillary branches in the rabbit ear chamber (Schmid-Schönbein & Skalak, 1980).

Another important concept developed to explain phase separation is the flow dividing streamline. This was introduced in (Bugliarello & Hsiao, 1964) as the boundary streamline which partitions fluid entering each daughter vessel at a bifurcation. Svanes illustrated diagrammatically how dividing streamlines in addition to axial streaming could explain non-linear phase separation at a bifurcation (Svanes & Zweifach, 1968); similar illustrations are shown in Figure A.1. The exact non-linear profile of the dividing streamline in a transverse vessel cross-section has also been characterised in relation to Q^* (Ofjord & Clausen, 1983; Chien *et al.* , 1985; Rong & Carr, 1990; Yan *et al.* , 1991), demonstrating increasingly non-linear bending of streamlines associated with smaller daughter-to-parent vessel diameter ratios. The flow dividing streamlines in Figure A.1 are represented in 2D within a longitudinal cross-section of a bifurcation (as in Svanes & Zweifach, 1968).

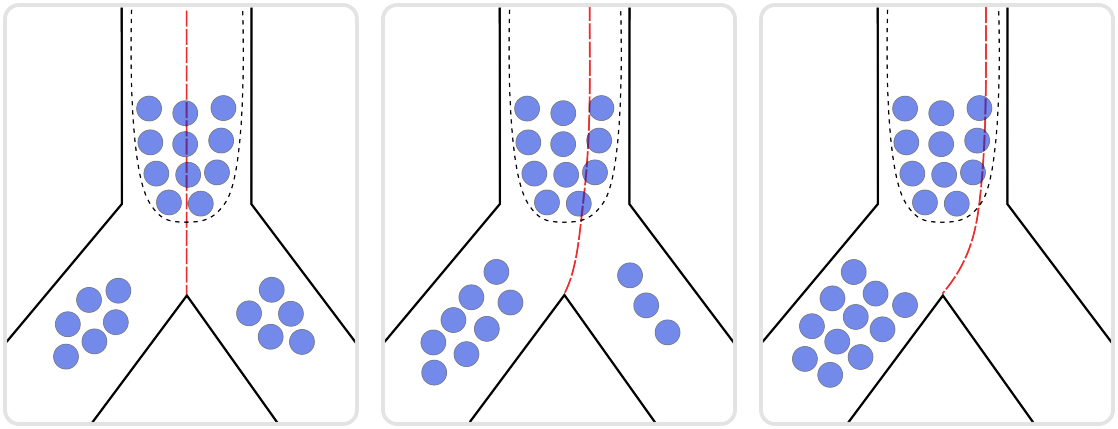

(a) (b) (c)

Figure A.1: The effects of flow fraction and axial drift on particle distribution at a bifurcation. Three fluid flow splitting profiles are indicated by flow dividing streamlines (long dashed red lines), either side of which particles distribute based on the relative position of their centre of mass. Particles stream axially in a flattened parabolic profile in all three cases (Tangelder *et al.* , 1986) (short dashed black lines). In (a) flow and particles are distributed approximately evenly to each daughter vessel. In (b) fluid is split approximately 2/3 to the left daughter vessel and 1/3 to the right, although particles are split 7/11 and 3/11 respectively. In (c) the flow dividing streamline is much nearer to the wall of the parent vessel, although still far away enough to accommodate a particle were there no parabolic streaming profile. Despite approximately 1/5 of the flow entering the right daughter vessel, all 11 particles enter the left daughter vessel due to axial streaming.

Another major determinant of phase separation is the particle-to-tube diameter ratio, λ, which has been shown to result in more pronounced phase separation as $\lambda \to 1$ in *in vitro* microsphere studies (Ofjord & Clausen, 1983; Chien *et al.* , 1985). The nonlinear relationship between Q^* and F^*, was investigated by Chien for example in a symmetric T-junction model using plastic spheres for values of $\lambda = 0.32$ to 0.79 (Chien *et al.* , 1985). For bulk flow fractions to a daughter vessel, $0 < Q^* < 1$, when Q^* (x-axis) was plotted against F^* (y-axis) a sigmoidal curve resulted, which became more linear for smaller values of λ. Furthermore they showed that $F^* = 0$ beneath a critical value of Q_c^* (where $Q_c^* < 0.5$), and that at greater values of λ, Q_c^* increases. A "wall-exclusion effect" was first described by Bayliss to explain Q_c^* as the situation where the flow dividing streamline in a parent vessel is within a single particle radius of the parent vessel wall facing a side branch, thus precluding any particles from entering the side branch (Bayliss,

1959). This was characterised by Ofjord whose *in vitro* experiments with 10-15μm microspheres demonstrated, assuming a parabolic flow profile, that the distance from the vessel wall of the particle exclusion zone corresponded well with the radius of the different sized particles (Ofjord, 1981). This is illustrated in Figure A.2b.

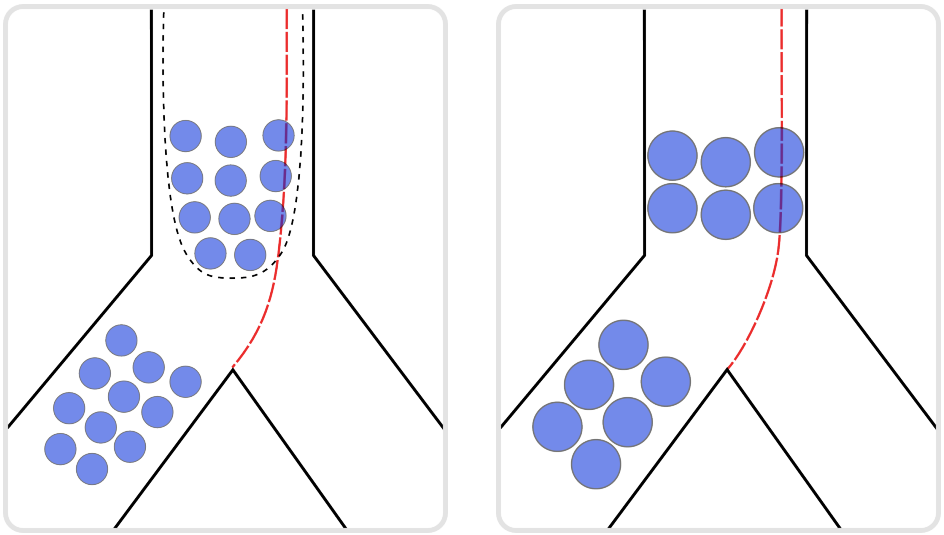

(a) (b)

Figure A.2: Dividing streamlines for critical flows Q_c^* with axial streaming (a) (reproduced from Figure A.1c) and without axial streaming (b). Figure (b) illustrates the (unphysiological) absence of axial streaming, where the distance of the dividing streamline from the vessel wall is less than one particle radius. This wall exclusion zone results in none of the particles entering the side branch (except for under certain conditions of flow disturbance).

Several *in vitro* experiments using microspheres demonstrated phase separation for values of λ between 0.083 (Ofjord, 1981) and 0.79 (Chien *et al.* , 1985). Ofjord using a slit model showed phase separation occured when passing 10μm diameter microspheres through 120μm channels ($\lambda = 8.33 \times 10^{-2}$) but not when using 3.5$\mu m$ diameter microspheres ($\lambda = 2.92 \times 10^{-2}$). They showed that for values of λ closer to 1, Q^* becomes a more dominant determinant of phase separation, since particles will partition along dividing streamlines according to the location of their centre of mass, as illustrated in Figure A.3a. Considering the extreme case of RBCs squeezing through capillaries ($\lambda = 1$), Johnson showed that at bifurcations

in cat mesenteric capillaries, Q^* to daughter vessels was the predominant factor causing plasma skimming at bifurcations (Johnson *et al.* , 1971; Johnson, 1971), and Fung showed that in a T-tube model of very narrow capillaries that all RBCs approaching a bifurcation entered the daughter vessel with higher flow (Fung, 1973). Dellimore showed using RBCs that even in $180\mu m$ diameter tubes, where $\lambda = 4.4 \times 10^{-2}$, phase separation effects were observed (Dellimore *et al.* , 1983).

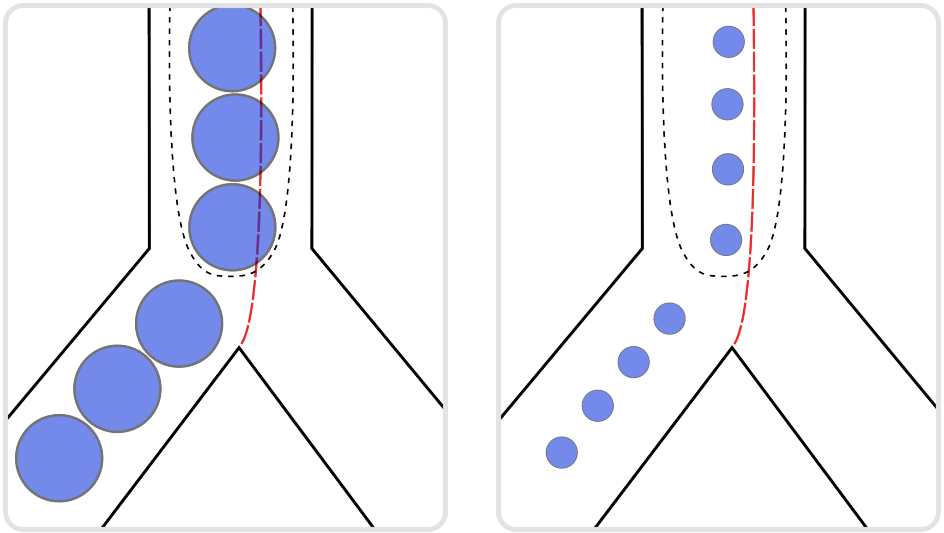

(a) (b)

Figure A.3: Figure (a) illustrates that with bulk flow fractions of 2/3 and 1/3 to the left and right daughter vessels respectively, given a sufficiently large particle-to-vessel diameter ratio, λ, particles may distribute entirely to one daughter vessel due to axial streaming. Figure (b) shows that when the concentration of particles is sufficiently low even at a considerably smaller λ, particles will tend to align in the centre of the flow profile and thus also distribute preferentially to the higher flow daughter vessel.

Another contributing factor to skimming is the particle concentration in the parent vessel[†], C_p, where a lower C_p results in more pronounced phase separation (Bugliarello & Hsiao, 1964; Johnson *et al.* , 1971; Yen & Fung, 1978; Dellimore *et al.* , 1983; Fenton *et al.* , 1985; Pries *et al.* , 1989). In other words, for a sufficiently low daughter vessel flow fraction $Q^* < 0.5$ such that $F^* < Q^*$, a decrease in C_p will result in a further decrease in F^*. It is hypothesised that this is at least in part due to more severe axial streaming as illustrated in Figure A.3b (compared to

[†]In *in vivo* studies with RBCs this is commonly given in terms of feeding vessel haemocrit H_f.

Figure A.1b), where with the resulting decreased e_x, particles become more prone to by-passing daughter vessels receiving a lower Q^*, and result in a higher critical flow (Fenton *et al.* , 1985). Another observation from both *in vivo* and *in vitro* experiments is that with lower values of C_p there is increased scatter in the relation between Q^* and F^* (summarised in Fenton *et al.* , 1985). The increased scatter may be due to a greater influence of flow disturbance on suspensions with low C_p. Flow disturbance in low Re networks are typically caused by close proximity of an upstream bifurcation (Pries *et al.* , 1989; Carr & Wickham, 1990). Figure A.4 shows how particles can be preferentially distributed into a daughter vessel receiving $Q^* = 0.5$; particles could also potentially be preferentially distributed to a daughter vessel receiving a *lower* Q^* under certain conditions of flow disturbance, leading to the increased scatter in the F^* vs Q^* relationship, especially when considering *in vivo* networks containing a range of vessel geometries and sizes. A further finding is the cumulative effect of HCT reduction in consecutive lower Q^* bifurcations throughout *in vivo* microvascular networks, which is partially responsible for the high HCT heterogeneity at the capillary level and has been termed the "network" Fahraeus effect (Pries *et al.* , 1986).

Rong, Carr and Wickham demonstrated the importance of flow history on phase separation in a simple tube network containing two consecutive bifurcations (Rong & Carr, 1990; Carr & Wickham, 1990). Flow disturbance at the upstream bifurcation could cause asymmetry in the flow profile of particles at the downstream bifurcation leading to skimming. This asymmetry was attenuated at greater values of z/Q (vessel length/flow) in the feeding vessel of the second bifurcation. Fenton observed in $20\mu m$ tubes using microphotometry to determine RBC profile that for very low haematocrits or extreme flow fractions, flow into a side branch would have the effect of shifting the RBC profile towards the side branch, creating a wider layer of plasma on the far wall of the main branch (Fenton *et al.* , 1985). If flow in the main branch reached a subsequent bifurcation before regaining a parabolic profile this effect would lead to additional phase separation. This builds on Lew and Fung's theoretical study of plasma flow in capillary-sized tubes where $Re \ll 1$ that it takes blood plasma about 0.65D[‡] along the length of a tube to

[‡]D = vessel diameter

readjust to a parabolic Poiseuille flow profile (Lew & Fung, 1969). Pries who used a microphotometric method to take measurements in cat mesentery arteriolar networks (containing vessels with a range of diameters from 10-40μm) showed that a symmetric flow profile was regained *in vivo* within a distance of 10 vessel diameters (Pries *et al.* , 1989).

Finally investigators found that phase separation increases with a difference in size of the daughter vessels (Fenton *et al.* , 1985; Pries *et al.* , 1989; Enden & Popel, 1994), where at $Q^* = 0.5$ the *smaller* daughter vessel received a higher haematocrit. Several investigators also examined the effects of bifurcation angle on phase separation and found no significant influence (Bugliarello & Hsiao, 1964; Palmer, 1965; Pries *et al.* , 1981; Fenton *et al.* , 1985). Parent vessel flow velocity was also shown to have no effect on phase separation (Palmer, 1965; Bugliarello & Hsiao, 1964), and more specifically for Reynolds numbers $Re < 3.0$ *in vitro* (Fenton *et al.* , 1985). Cell distensibility also was shown to have no effect on phase separation in 20-100μm tubes, where HRBCs and RBCs both produced the same F^* vs Q^* relations (Fenton *et al.* , 1985). Finally parent-to-daughter vessel diameter ratio also had no significant effect on phase separation (Carr & Wickham, 1990).

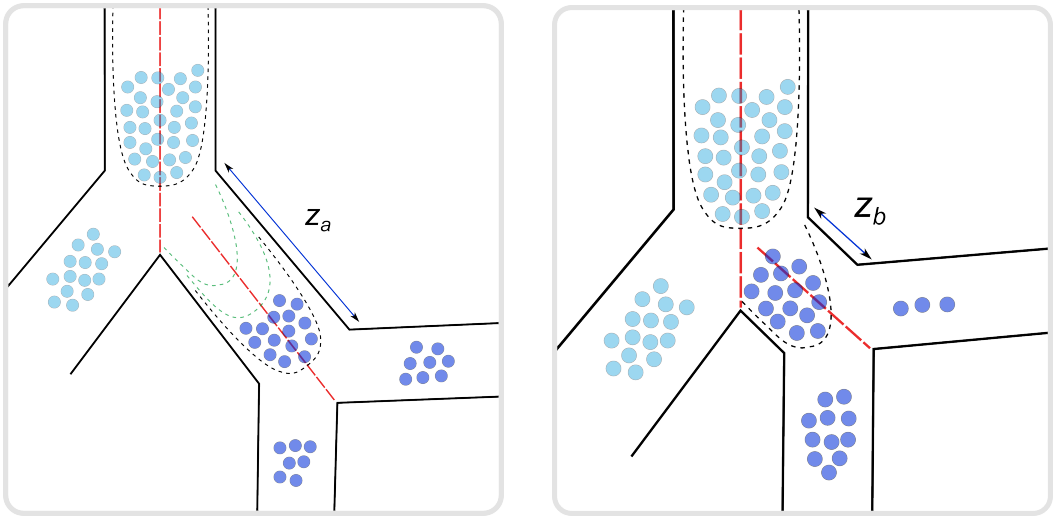

(a) (b)

Figure A.4: The effect of flow disturbance in consecutive bifurcations on particle flow profile and hence particle distribution in a secondary bifurcation. In both Figures (a) and (b), the bulk flow dividing streamlines indicate 50% of the bulk flow enters both daughter vessels, at both the first and second bifurcations. Figure (a) shows the recovery of a parabolic particle flow profile in the feeding vessel of the second bifurcation (dark blue spheres) allowing an approximately even distribution of particles into both daughter vessels. Figure (b) however shows a disturbed particle flow profile given only a short secondary bifurcation feeding vessel length, z_b, resulting in a particle distribution which is disproportionate to the bulk flow distribution.

This survey covers in brief the extensive work that has identified major determinants of phase separation with *in vivo*, *in vitro* and *in silico* experiments. Investigators have proposed both empirical and physical models to characterise phase separation, which have largely been fitted to data collected from capillary and arteriolar networks (Schmid-Schönbein & Skalak, 1980; Klitzman & Johnson, 1982; Pries *et al.* , 1989; Pries & Secomb, 2005). Models have also been proposed for *in vitro* studies using arteriole-sized tubes with limited degrees of freedom as compared to *in vivo* arteriolar networks (Ofjord & Clausen, 1983; Fenton *et al.* , 1985; Dellimore *et al.* , 1983; Chien *et al.* , 1985). These models are briefly summarised in the following section.

A.2 Models of Phase Separation

Several models have been proposed relating Q^* and F^* while accounting for the influence of factors such as feed haematocrit, axial streaming, particle-to-vessel diameter ratio and a cell-free marginal layer. Klitzman proposed an empirical fit using a logit function to represent the Q^* vs F^* relation of the form

$$-\operatorname{logit}(F^*) = \ln\left(\frac{1-F^*}{F^*}\right) = b \cdot \ln\left(\frac{1-Q^*}{Q^*}\right), \tag{A.1}$$

rearranged for fitting to data

$$F^* = \frac{(Q^*)^b}{(1-Q^*)^b + (Q^*)^b}. \tag{A.2}$$

The parameter b represents the non-linearity of the relation. When $b > 1$, the relation is non-linear favouring preferential flow of RBCs to high flow daughter vessels, and when $b < 1$, RBCs are preferentially distributed to low flow daughter vessels. Fitting this relation to observations made in 133 capillary bifurcations in hamster cremaster muscle a value of $b = 1.15 \pm 0.08$ was obtained, and when fitting to observations only where $Q^* > 0.75$, $b = 1.35 \pm 0.13$ (Klitzman & Johnson, 1982). Dellimore applied this logistic function to fit data collected from RBC and plasma flow through $180\mu m$ plastic tubes at HCTs of 42%, 30% and 20%. The parameter b was fitted for data collected across a range $0 \leq Q^* \leq 1$, where b demonstrated an inversely proportional relation to HCT, yielding 1.10, 1.28 and 1.58 for the high-to-low HCTs respectively. This indicated greater non-linearity of the function, and more pronounced phase separation at lower particle concentrations (Dellimore *et al.* , 1983).

Fenton proposed a two-phase physically-based model for fitting Q^* vs F^* from data collected from RBCs flowing through three sizes of tube bifurcations with diameters of $20\mu m$, $50\mu m$ and $100\mu m$ at two haematocrits, 20% and 40% (Fenton *et al.* , 1985). The model took into account the wall layer thickness which is the radial distance from the vessel wall devoid of particles, denoted by γ. A planar fluid dividing streamline was assumed whose perpendicular radial distance from

the tube centre was denoted by a, and parabolic velocity profiles were assumed for both fluid and particles. Parametric equations were used to relate Q^* and F^* to the parabolic velocity profile in terms of parent HCT, a and γ, where γ was the only fitted model parameter as HCT and a could be computed from measurements. Fenton's results revealed an increasing gap width γ and increasing critical flow fraction Q_c^* with decreasing HCT at a given tube diameter. Furthermore non-zero Q^* intercepts related to Q_c^* were found. Results were similar to those of Schmid-Schonbein which showed Q_c^* between 0.1 and 0.3 in capillaries (depending on cell eccentricity e_x) (Schmid-Schönbein & Skalak, 1980). Fitting the logistic function proposed by Klitzman, values for b ranged from 1.32 and 1.52 in $20\mu m$ diameter tubes, to 1.09 and 1.01 in $40\mu m$ diameter tubes, both at 40% and 20% HCT respectively.

Pries took into consideration the effect of Q_c^* and extended the empirical sigmoidal relation to a logit function of the form

$$\text{logit}(F^*) = a + b \cdot \text{logit}(Q^*) \tag{A.3}$$

where

$$\text{logit}(X) = \ln \frac{X}{1-X} \tag{A.4}$$

The final form of the equation used for fitting was

$$F^* = \frac{1}{1 + e^{-(a+b\cdot\text{logit}(0.5-S(0.5-Q^*)))}} \tag{A.5}$$

where the critical flow Q_c^* is related to a scaling factor S by

$$Q_c^* = 0.5 - \frac{0.5}{S} \tag{A.6}$$

The logit function in Equation (A.5) is valid for a range of Q^* between Q_c^* and $1 - Q_c^*$, above and below which Q^* is 0 and 1 respectively. Equation (A.5) was iteratively fit for S using data from 65 capillary and arteriolar bifurcations in rat mesentery with diameters of 10-30μm (Pries *et al.* , 1989). Downstream vessels were progressively occluded to reduce Q^* across a range of values at upstream

bifurcations. The variable a quantifies asymmetry of the cell distribution function between daughter vessels and b characterises the non-linearity of the sigmoid function. Average computed values came to $a = 0.018 \pm 0.24$, $b = 1.22 \pm 0.14$ and $Q_c^* = 0.02 \pm 0.023$, and a check for correlations between parameters confirmed their independence. Parameters b and Q_c^* showed a strong dependence on parent vessel diameter, with b also being dependent on parent vessel HCT, and a dependent on the ratio of daughter vessel diameters.

Flow history[§] also influenced both a and Q_c^*, where upstream flow disturbance perturbed the axisymmetric flow profile of RBCs entering a bifurcation. By relating the fitted logit function parameters to a theoretical model assuming a flat dividing streamline and parabolic flow profile (similar to Chien *et al.* , 1985; Fenton *et al.* , 1985), Pries showed Q_c^* was related to the width of the cell-free marginal zone and b related to the shape of the HCT concentration profile across the vessel cross-section. The relation of the logit function parameters and physical parameters were refined and presented in (Pries & Secomb, 2005) to account for a wider range of haematocrits as:

$$\text{logit}(F^*) = a + b\,\text{logit}\left[\frac{Q^* - Q_c^*}{1 - 2Q_c^*}\right], \tag{A.7}$$

where a, b and Q_c^* were related to physical parameters from linear regression fits to rat mesentery data (Pries *et al.* , 1989) to give:

$$a = -13.29\left[\frac{D_\alpha/D_\beta - 1}{D_\alpha/D_\beta + 1}\right]\frac{1 - H_D}{D_\alpha} \tag{A.8}$$

$$b = 1 + 6.98\frac{1 - H_D}{D_\alpha} \tag{A.9}$$

$$Q_c^* = 0.964\frac{1 - H_D}{D_\alpha} \tag{A.10}$$

where α and β denote the two daughter vessels at a bifurcaion, D the vessel diameter, and H_D the parent vessel discharge haematocrit.

[§]whether an upstream vessel was within 10 vessel diameters of a bifurcation and whether it was on the same or opposing side of the vessel to a daughter branch

Interestingly almost no phase separation was observed in bifurcations with feeding vessels greater than $40\mu m$ in diameter ($\lambda \approx 0.2$), where H_D was measured to lie on average between 43%-49%. This is in conflict with Dellimore's findings that RBC transport in glass tubes of $180\mu m$ diameter demonstrated persistent but decreasing phase separation for H_D ranging from 20% ($b = 1.58$) to 42% ($b = 1.10$) (Dellimore *et al.* , 1983). Fenton's experiments of RBC flow through $100\mu m$ tubes showed more mild phase separation at 20% ($b = 1.09$) and 42% ($b = 1.01$) H_D (Fenton *et al.* , 1985).

Pries' empirical formulae for phase separation do not address the issue of particle-to-vessel diameter ratio λ, nor do they hold true necessarily in the larger coronary arterioles and arteries which are the primary concern in the present study. More recent studies have focused on the microscopic interactions that influence phase separation on the scale of particle-to-particle and particle-to-wall interactions at the scale of the capillaries (Secomb *et al.* , 1998; El-Kareh & Secomb, 2000; Pries & Secomb, 2005; Secomb *et al.* , 2007, 2009; Obrist *et al.* , 2010; Barber *et al.* , 2011). There are no studies of phase separation in larger arterioles or arteries *in vivo*, let alone for microspheres with considerably lower blood volume fraction compared to RBCs. There is however reason to believe that phase separation effects do occur in the arterial and arteriolar coronary circulation, contributing to limitations in the microsphere technique, as investigated in this thesis.

B | Effect of Subtree Removal on Network Error

As demonstrated in Section 4.3.2 removal from the network flow error analysis of a high-error vessel subtree, along with its associated fed-volume and microspheres, could increase the flow error in another vessel subtree. Specifically, the removal of the first apex-feeding subtree (shown in Figure 4.19) caused an increase in error of another apex-feeding subtree (shown in Figure 4.22). Given that flow error in a vessel segment for the homogeneous perfusion BC model is dependent solely on tissue volume and number of microspheres, the effect of removing a subtree from the analysis on the remaining vessel segments can easily be derived analytically.

Removing a subtree affects the error in other subtrees because both tissue volume and FMS are removed from the analysis, and although the model flow Q_m is unchanged in non-proximal subtrees to the one removed, the FMS flow Q_f *is* changed, as a function of the fraction of tissue volume removed to the fraction of FMS removed. Recalling equation (4.19) for the flow error in a vessel segment i,

$$E^i = \frac{N^i}{V^i}\frac{V^T}{N^T} - 1,$$

The subtree segment shown in red in Figure 4.22 is not proximal to the previously excluded apex-feeding subtree (Figure 4.22 in dark blue), but extends separately from the LAD main trunk. In a subtree that is not proximal to a removed subtree the updated error, $\hat{E}^i$, can be computed exactly

$$\hat{E}^i = \frac{N^i}{V^i}\left[\frac{V^T - V^R}{N^T - N^R}\right] - 1, \tag{B.1}$$

where $V^R = \sum^{n^R} V^k$ is the removed FV associated with all of the removed terminal nodes n^R of the subtree, where each removed terminal is denoted by superscript k. Similarly for the removed number of FMS, $N^R = \sum^{n^R} N^k$. Using these equations an inequality can be derived relating the fractions of removed FV and FMS to the update in error in a vessel segment,

$$\text{if} \quad \frac{N_f^R}{N_f^T} > \frac{V^R}{V^T} \quad , \quad E^i < \hat{E}^i, \tag{B.2}$$

$$\text{if} \quad \frac{N_f^R}{N_f^T} < \frac{V^R}{V^T} \quad , \quad E^i > \hat{E}^i. \tag{B.3}$$

To put this verbosely, if the fraction of removed FMS to total FMS is greater than the fraction of removed FV to total FV (in a subtree which is not distal to the vessel segment in question, i), then the updated error $\hat{E}^i$ will be greater than the original error E^i.

As for bifurcations which *are* proximal to a removed subtree, the updated error $\hat{E}^i$ can be written as

$$\hat{E}^i = \frac{\hat{N}^i}{\hat{V}^i}\left[\frac{V^T - V^R}{N^T - N^R}\right] - 1, \tag{B.4}$$

where $\hat{N}^i = (N^i - N^R)$ and $\hat{V}^i = (V^i - V^R)$ are the updated number of FMS and FV in the vessel segment of interest, i.

Note that since the three major subnetworks of the LCA have been separately flow-normalised, removal of a smaller subnetwork of any of the LCx, LAD or LM networks will not affect errors in any of the other major subnetworks.

C | CMT Data Information

Heart #	stack dimensions, x,y,z	pixel size, $x \times y$ (μm)	slice thickness, z (μm)
1	2000 , 2000 , 1412	60×60	60
2	2000 , 2000 , 1284	60×60	64
3	2000 , 2000 , 1278	53.7×53.7	100
4	2000 , 2000 , 1231	53.7×53.7	100
5	2000 , 2000 , 1150	53.7×53.7	100
6	2000 , 2000 , 1030	53.7×53.7	100
7	2000 , 2000 , 1893	56.7×56.7	99.6
8	2000 , 2000 , 2052	56.5×56.5	59.4
9	2000 , 2000 , 2066	56.5×56.5	59.4
10	2000 , 2000 , 1352	56.5×56.5	59.4

Table C.1: Cryomicrotome image stack information for pig hearts. Note that the hearts are sectioned from base to apex, so image 1 is always of the most basal slice.

References

Agresti, A., & Coull, B. A. 1998. Approximate is better than "exact" for interval estimation of binomial proportions. *The American Statistician*, **52**(2), 119–126.

Alders, D. J. C., Groeneveld, A. B. J., de Kanter, F. J. J., & van Beek, J. H. G. M. 2004. Myocardial O2 consumption in porcine left ventricle is heterogeneously distributed in parallel to heterogeneous O2 delivery. *American journal of physiology. Heart and circulatory physiology*, **287**(3), H1353–61.

Austin, R. E., Aldea, G. S., Coggins, D. L., Flynn, A. E., & Hoffman, J. I. 1990. Profound spatial heterogeneity of coronary reserve. Discordance between patterns of resting and maximal myocardial blood flow. *Circulation Research*, **67**(2), 319–331.

Ballesteros, L. E., & Ramirez, L. M. 2008. Morphological expression of the left coronary artery: a direct anatomical study. *Folia morphologica*, **67**(2), 135–42.

Barber, J. O., Restrepo, J. M., & Secomb, T. W. 2011. Simulated Red Blood Cell Motion in Microvessel Bifurcations: Effects of Cell-Cell Interactions on Cell Partitioning. *Cardiovascular engineering and Technology*, **2**(4), 349–360.

Bassingthwaighte, J. B., & Bever, R. P. 1991. Fractal correlation in heterogeneous systems. *Physica D: Nonlinear Phenomena*, **53**, 71–84.

Bassingthwaighte, J. B., Malone, M. A., Meffett, T. C., King, R. B., Little, S. E., Link, J. M., & Krohn, K. A. 1987. Validity of microsphere depositions for regional myocardial flows. *American Journal of Physiology - Heart and Circulatory Physiology*.

Bassingthwaighte, J. B., King, R. B., & Roger, S. A. 1989. Fractal nature of regional myocardial blood flow heterogeneity. *Circulation Research*, **65**(3), 578–590.

Bassingthwaighte, J. B., Malone, M. A., Moffett, T. C., King, R. B., Chan, I. S., Link, J. M., & Krohn, K. A. 1990. Molecular and particulate depositions for regional myocardial flows in sheep. *Circulation Research*, **66**(5), 1328–1344.

Bauer, W. R., Hiller, K.-H., Galuppo, P., Neubauer, S., Kopke, J., Haase, a., Waller, C., & Ertl, G. 2001. Fast High-Resolution Magnetic Resonance Imaging Demonstrates Fractality of Myocardial Perfusion in Microscopic Dimensions. *Circulation Research*, **88**(3), 340–346.

Bayliss, L. E. 1959. The axial drift of the red cells when blood flows in a narrow tube. *The Journal of Physiology*, 593–613.

Beard, D. A., & Bassingthwaighte, J. B. 2000. The fractal nature of myocardial blood flow emerges from a whole-organ model of arterial network. *Journal of vascular research*, **37**(4), 282–296.

Beighley, P. E., Thomas, P. J., Jorgensen, S. M., & Ritman, E. L. 1997. 3D architecture of myocardial microcirculation in intact rat heart: a study with micro-CT. *Advances in experimental medicine and biology*, **430**, 165–175.

Blyth, C. R. 1986. Approximate binomial confidence limits. *Journal of the American Statistical Association*, **81**(395), 843–855.

Buckberg, G. D., Luck, J. C., Payne, D. B., Hoffman, J. I. E., Archie, J. P., & Fixler, D. E. 1971. Some sources of error in measuring regional blood flow with radioactive microspheres. *Journal of Applied Physiology*, 598–604.

Bugliarello, G., & Hsiao, G. C. C. 1964. Phase Separation in Suspensions Flowing through Bifurcations : A Simplified Hemodynamic Model. *Science*, **143**(3605), 469–471.

Caldwell, J. H., Martin, G. V., Raymond, G. M., & Bassingthwaighte, J. B. 1994. Regional myocardial flow and capillary permeability-surface area products are nearly proportional. *The American journal of physiology*, **267**(2 Pt 2), H654–66.

Camici, P. G., & Crea, F. 2007. Coronary microvascular dysfunction. *The New England journal of medicine*, **356**(8), 830–40.

Carr, R. T., & Wickham, L. L. 1990. Plasma skimming in serial microvascular bifurcations. *Microvascular research*, **190**, 179–190.

Cerqueira, M. D., Weissman, N. J., Dilsizian, V., Jacobs, A. K., Kaul, S., Laskey, W. K., Pennell, D. J., Rumberger, J. A., Ryan, T., & Verani, M. S. 2002. Standardized Myocardial Segmentation and Nomenclature for Tomographic Imaging of the Heart: A Statement for Healthcare Professionals From the Cardiac Imaging Committee of the Council on Clinical Cardiology of the American Heart Association. *Circulation*, **105**(4), 539–542.

Chareonthaitawee, P., Kaufmann, P. A., Rimoldi, O., & Camici, P. G. 2001. Heterogeneity of resting and hyperemic myocardial blood flow in healthy humans. *Cardiovascular research*, **50**(1), 151–61.

Chien, S., Tvetenstrand, C. D., Epstein, M. A., & Schmid-Schonbein, G. W. 1985. Model studies on distributions of blood cells at microvascular bifurcations. *American Journal of Physiology - Heart and Circulatory Physiology*, **248**(4), H568–H576.

Chilian, W. M., Layne, S. M., Klausner, E. C., Eastham, C. L., & Marcus, M. L. 1989. Redistribution of coronary microvascular resistance produced by dipyridamole. *The American journal of physiology*, **256**(2 Pt 2), H383–90.

Choy, J. S., & Kassab, G. S. 2008. Scaling of myocardial mass to flow and morphometry of coronary arteries. *Journal of applied physiology*, **104**(5), 1281–6.

Christian, T. F., Rettmann, D. W., Aletras, A. H., Liao, S. L., Taylor, J. L., Balaban, R. S., & Arai, A. E. 2004. Absolute Myocardial Perfusion in Canines Measured by Using Dual-Bolus First-Pass MR Imaging. *Radiology*, **232**(3), 677–684.

Clopper, C. J., & Pearson, E. S. 1934. The use of confidence or fiducial limits illustrated in the case of the binomial. *Biometrika*, **26**(4), 404–413.

Cookson, A. N., Lee, J., Michler, C., Chabiniok, R., Hyde, E., Nordsletten, D., Sinclair, M., Siebes, M., & Smith, N. P. 2012. A novel porous mechanical framework for modelling the interaction between coronary perfusion and myocardial mechanics. *Journal of biomechanics*, **45**(5), 850–5.

Crum, W. R., Hartkens, T., & Hill, D. L. G. 2004. Non-rigid image registration: theory and practice. *British Journal of Radiology*, **77**(2), S140–S153.

Decking, U. K. M., Skwirba, S., Zimmermann, M. F., Preckel, B., Thämer, V., Deussen, A., & Schrader, J. 2001. Spatial heterogeneity of energy turnover in the heart. *Pflügers Archiv: European journal of physiology*, **441**(5), 663–673.

Decking, U. K. M., Pai, V. M., Bennett, E., Taylor, J. L., Fingas, C. D., Zanger, K., Wen, H., & Balaban, R. S. 2004. High-resolution imaging reveals a limit in spatial resolution of blood flow measurements by microspheres. *American journal of physiology. Heart and circulatory physiology*, **287**(3), H1132–40.

Dellimore, J. W., Dunlop, M. J., & Canham, P. B. 1983. Ratio of cells and plasma in blood flowing past branches in small plastic channels. *The American journal of physiology*, **244**(5), H635–43.

Deussen, A. 1997. Local myocardial glucose uptake is proportional to, but not dependent on blood flow. *Pflügers Archiv: European journal of physiology*, **433**(4), 488–96.

Dole, W. P., Jackson, D. L., Rosenblatt, J. I., & Thompson, W. L. 1982. Relative error and variability in blood flow measurements with radiolabeled microspheres. *The American journal of physiology*, **243**(3), H371–8.

Dombe, D. D., Anitha, T., Dombe, P. A. G. S. D., & Ambiye, M. V. 2012. Clinically relevant morphometric analysis of left coronary artery. *International journal of of biological and medical research*, **3**(1), 1327–1330.

Domenech, R. J., Hoffman, J. I., Noble, M. I., Saunders, K. B., Henson, J. R., & Subijanto, S. 1969. Total and Regional Coronary Blood Flow Measured by Radioactive Microspheres in Conscious and Anesthetized Dogs. *Circulation Research*, **25**(5), 581–596.

Dougherty, R., & Kunzelmann, K.-H. 2007. Computing Local Thickness of 3D Structures with ImageJ. *Microscopy and Microanalysis*, **13**(S02).

Duncker, D. J., & Bache, R. J. 2008. Regulation of coronary blood flow during exercise. *Physiological reviews*, **88**(3), 1009–1086.

El-Kareh, A. W., & Secomb, T. W. 2000. A model for red blood cell motion in bifurcating microvessels. *International Journal of Multiphase Flow*, **26**(9), 1545–1564.

Enden, G., & Popel, A. S. 1994. A numerical study of plasma skimming in small vascular bifurcations. *Journal of biomechanical engineering*, **116**(1), 79–88.

Fåhræus, R., & Lindqvist, T. 1931. The viscosity of the blood in narrow capillary tubes. *American Journal of Physiology - Heart and Circulatory Physiology*, 562–568.

Fenton, B. M., Carr, R. T., & Cokelet, G. R. 1985. Nonuniform red cell distribution in 20 to 100 μm bifurcations. *Microvascular research*, **126**(1), 103–126.

Finegold, J. A., Asaria, P., & Francis, D. P. 2013. Mortality from ischaemic heart disease by country, region, and age: statistics from World Health Organisation and United Nations. *International journal of cardiology*, **168**(2), 934–45.

Frangi, A. F., Niessen, W. J., Vincken, K. L., & Viergever, M. A. 1998. Multiscale vessel enhancement filtering. *Medical Image Computing and Computer-Assisted Intervention*, **1496**, 130–137.

Franzen, D., Conway, R. S., Zhang, H., Sonnenblick, E. H., & Eng, C. 1988. Spatial heterogeneity of local blood flow and metabolite content in dog hearts. *The American journal of physiology*, **254**(2 Pt 2), H344–53.

Fritz-Hansen, T., Hove, J. D., Kofoed, K. F., Kelbaek, H., & Larsson, H. B. W. 2008. Quantification of MRI measured myocardial perfusion reserve in healthy humans: a comparison with positron emission tomography. *Journal of magnetic resonance imaging*, **27**(4), 818–24.

Fung, Y. C. 1973. Stochastic flow in capillary blood vessels. *Microvascular research*, **5**(1), 34–48.

Garcia-Sanz, A., Rodriguez-Barbero, A., Bentley, M. D., Ritman, E. L., & Romero, J. C. 1998. Three-Dimensional Microcomputed Tomography of Renal Vasculature in Rats. *Hypertension*, **31**(1), 440–444.

Glenny, R. W., Bernard, S., & Brinkley, M. 1993. Validation of fluorescent-labeled microspheres for measurement of regional organ perfusion. *Journal of Applied Physiology*, **74**(5), 2585–2597.

Gorman, M. W., Wangler, R. D., & Sparks, H. V. 1989. Distribution of perfusate flow during vasodilation in isolated guinea pig heart. *The American journal of physiology*, **256**(1 Pt 2), H297–301.

Goyal, A., Lee, J., Lamata, P., van den Wijngaard, J., van Horssen, P., Spaan, J., Siebes, M., Grau, V., & Smith, N. P. 2013. Model-based vasculature extraction from optical fluorescence cryomicrotome images. *IEEE transactions on medical imaging*, **32**(1), 56–72.

Hale, S. L., Vivaldi, M. T., & Kloner, R. A. 1986. Fluorescent microspheres: a new tool for visualization of ischemic myocardium in rats. *The American journal of physiology*, **251**(4 Pt 2), H863–8.

Heymann, M. A., Payne, B. D., Hoffman, J. I., & Rudolph, A. M. 1977. Blood flow measurements with radionuclide-labeled particles. *Progress in cardiovascular diseases*, **20**(1), 55–79.

Hildebrand, T., & Rüegsegger, P. 1997. A new method for the model-independent assessment of thickness in three-dimensional images. *Journal of microscopy*, **185**(November 1995), 67–75.

Hsu, L.-Y., Groves, D. W., Aletras, A. H., Kellman, P., & Arai, A. E. 2012. A quantitative pixel-wise measurement of myocardial blood flow by contrast-enhanced first-pass CMR perfusion imaging: microsphere validation in dogs and feasibility study in humans. *JACC. Cardiovascular imaging*, **5**(2), 154–66.

Hunter, P., & Pullan, A. 2001. *Fem/bem notes.*

Huo, Y., & Kassab, G. S. 2012. Intraspecific scaling laws of vascular trees. *Journal of the Royal Society, Interface / the Royal Society*, **9**(66), 190–200.

Huo, Y., Kaimovitz, B., Lanir, Y., Wischgoll, T.s, Hoffman, J. I. E., & Kassab, G. S. 2009. Biophysical model of the spatial heterogeneity of myocardial flow. *Biophysical journal*, **96**(10), 4035–43.

Huo, Yunlong, Wischgoll, Thomas, Choy, JS, & Sola, S. 2013. CT-based Diagnosis of Diffuse Coronary Artery Disease on the Basis of Scaling Power Laws. *Radiology*, **268**(3), 694–701.

Hyde, E. R., Cookson, A. N., Lee, J., Michler, C., Goyal, A., Sochi, T., Chabiniok, R., Sinclair, M., Nordsletten, D., Spaan, J., van den Wijngaard, J. P. H. M., Siebes, M., & Smith, N. P. 2013a. Multi-Scale Parameterisation of a Myocardial Perfusion Model Using Whole-Organ Arterial Networks. *Annals of biomedical engineering*, **42**(4), 797–811.

Hyde, E. R., Michler, C., Lee, J., Cookson, A. N., Chabiniok, R., Nordsletten, D. A., & Smith, N. P. 2013b. Parameterisation of multi-scale continuum perfusion models from discrete vascular networks. *Medical & biological engineering & computing*, **51**(5), 557–570.

Jerosch-Herold, M., Wilke, N., Stillman, A. E., & Wilson, R. F. 1998. Magnetic resonance quantification of the myocardial perfusion reserve with a Fermi function model for constrained deconvolution. *Medical Physics*, **25**(1), 73.

Jerosch-Herold, M., Hu, X., Murthy, N. S., Rickers, C., & Stillman, A. E. 2003. Magnetic resonance imaging of myocardial contrast enhancement with MS-325 and its relation to myocardial blood flow and the perfusion reserve. *Journal of magnetic resonance imaging : JMRI*, **18**(5), 544–54.

Johnson, P. C. 1971. Red cell separation in the mesenteric capillary network. *American Journal of Physiology*, **221**(1).

Johnson, P. C., Blaschke, J., Burton, K. S., & Dial, J. H. 1971. Influence of flow variations on capillary hematocrit in mesentery. *American Journal of Physiology*, **221**(1).

Jorgensen, S. M. 1998. Three-dimensional imaging of vasculature and parenchyma in intact rodent organs with X-ray micro-CT. *American Journal of Physiology - Heart and Circulatory Physiology*, **275**(3), 1103–1114.

Kaimovitz, B., Lanir, Y., & Kassab, G. S. 2005. Large-scale 3-D geometric reconstruction of the porcine coronary arterial vasculature based on detailed anatomical data. *Annals of biomedical engineering*, **33**(11), 1517–35.

Kalsho, G., & Kassab, G. S. 2004. Bifurcation asymmetry of the porcine coronary vasculature and its implications on coronary flow heterogeneity. *American Journal of Physiology - Heart and Circulatory Physiology*, **287**(6), 2493–2500.

Karch, R., Neumann, F., Podesser, B. K., Neumann, M., Szawlowski, P., & Schreiner, W. 2003. Fractal properties of perfusion heterogeneity in optimized arterial trees: a model study. *The Journal of general physiology*, **122**(3), 307–21.

Kassab, G. S. 2006. Scaling laws of vascular trees: of form and function. *American journal of physiology. Heart and circulatory physiology*, **290**(2), H894–903.

Kassab, G. S., & Fung, Y. C. 1994. Topology and dimensions of pig coronary capillary network. *The American journal of physiology*, **267**(1 Pt 2), H319–25.

Kassab, G. S., Rider, C. A., Tang, N. J., & Fung, Y. C. 1993. Morphometry of pig coronary arterial trees. *The American journal of physiology*, **265**(1 Pt 2), H350–65.

Kassab, G. S., Lin, D. H., & Fung, Y. C. 1994. Morphometry of pig coronary venous system. *American Journal of Physiology-Heart and Circulatory Physiology*, **267**(6 Pt 2), H2100–13.

Kassab, G. S., Berkley, J., & Fung, Y. C. 1997. Analysis of pig's coronary arterial blood flow with detailed anatomical data. *Annals of biomedical engineering*, **25**(1), 204–17.

Kelly, J. J., Ewen, J. R., Bernard, S. L., Glenny, R. W., & Barlow, C. H. 2000. Regional blood flow measurements from fluorescent microsphere images using an Imaging CryoMicrotome. *Review of Scientific Instruments*, **71**(1), 228.

King, R. B., Bassingthwaighte, J. B., Hales, J. R., & Rowell, L. B. 1985. Stability of heterogeneity of myocardial blood flow in normal awake baboons. *Circulation Research*, **57**(2), 285–295.

Klitzman, B., & Johnson, P. C. 1982. Capillary network geometry and red cell distribution in hamster cremaster muscle. *The American journal of physiology*, **242**(2), H211–9.

Kowallik, P., Schulz, R., Guth, B. D., Schade, A., Paffhausen, W., Gross, R., & Heusch, G. 1991. Measurement of regional myocardial blood flow with multiple colored microspheres. *Circulation*, **83**(3), 974–982.

Krogh, A. 1922. *The Anatomy and Physiology of Capillaries*. Yale University Press.

Kuhle, W. G., Porenta, G., Huang, S. C., Buxton, D., Gambhir, S. S., Hansen, H., Phelps, M. E., & Schelbert, H. R. 1992. Quantification of regional myocardial blood flow using 13N-ammonia and reoriented dynamic positron emission tomographic imaging. *Circulation*, **86**(3), 1004–1017.

Lamata, P., Niederer, S., Nordsletten, D., Barber, D. C., Roy, I., Hose, D. R., & Smith, N. P. 2011. An accurate, fast and robust method to generate patient-specific cubic Hermite meshes. *Medical image analysis*, **15**(6), 801–13.

Lamata, P., Sinclair, M., Kerfoot, E., Lee, A., Crozier, A., Blazevic, B., Land, S., Lewandowski, A. J., Barber, D., Niederer, St., & Smith, N. 2013. An automatic service for the personalization of ventricular cardiac meshes. *Journal of the Royal Society, Interface / the Royal Society*, **11**(91).

Lee, J., & Smith, N. P. 2008. Development and application of a one-dimensional blood flow model for microvascular networks. *Proceedings of the Institution of Mechanical Engineers, Part H: Journal of Engineering in Medicine*, **222**(4), 487–512.

Lee, J., & Smith, N. P. 2012. The multi-scale modelling of coronary blood flow. *Annals of biomedical engineering*, **40**(11), 2399–413.

Lee, J., Beighley, P., Ritman, E., & Smith, N. 2007. Automatic segmentation of 3D micro-CT coronary vascular images. *Medical image analysis*, **11**(6), 630–47.

Lee, J., Nordsletten, D., Cookson, A., Rivolo, S., & Smith, N. 2014. In silico Coronary Wave Intensity Analysis: Cardiac Function to Wave Generating Mechanisms. in review.

Lee, T. C., Kashyap, R. L., & Chu, C. N. 1994. Building skeleton models via 3-D medial surface axis thinning algorithms. *CVGIP: Graphical Models and Image Processing*, **56**(6), 462–478.

Lesage, D., Angelini, E. D., Bloch, I., & Funka-Lea, G. 2009. A review of 3D vessel lumen segmentation techniques: models, features and extraction schemes. *Medical image analysis*, **13**(6), 819–45.

Levine, G. N., Bates, E. R., Blankenship, J. C., Bailey, S. R., Bittl, J. A., Cercek, B., Chambers, C. E., Ellis, S. G., Guyton, R. A., Hollenberg, S. M., Khot, U. N., Lange, R. A., Mauri, L., Mehran, R., Moussa, I. D., Mukherjee, D., Nallamothu, B. K., & Ting, H. H. 2011. 2011 ACCF/AHA/SCAI Guideline for Percutaneous Coronary Intervention: a report of the American College of Cardiology Foundation/American Heart Association Task Force on Practice Guidelines and the Society for Cardiovascular Angiography and Interventions. *Circulation*, **124**(23), 574–651.

Lew, H. S., & Fung, Y. C. 1969. On the low-Reynolds-number entry flow into a circular cylindrical tube. *Journal of biomechanics*, **2**(1968), 105–119.

Lockie, T., Ishida, M., Perera, D., Chiribiri, A., De Silva, K., Kozerke, S., Marber, M., Nagel, E., Rezavi, R., Redwood, S., & Plein, S. 2011. High-resolution magnetic resonance myocardial perfusion imaging at 3.0-Tesla to detect hemodynamically significant coronary stenoses as determined by fractional flow reserve. *Journal of the American College of Cardiology*, **57**(1), 70–5.

Lopez, A. D., Mathers, C. D., Ezzati, M., Jamison, D. T., & Murray, C. J. L. 2006. Global and regional burden of disease and risk factors, 2001: systematic analysis of population health data. *Lancet*, **367**(9524), 1747–57.

Marxen, M. Sled, J. G., & Henkelman, R. M. 2009. Volume ordering for analysis and modeling of vascular systems. *Annals of biomedical engineering*, **37**(3), 542–51.

Marxen, M. 2004. *Fractal characteristics of vascular structure and modeling of blood flow in three dimensions*. Ph.D. thesis.

Marxen, M., & Henkelman, R. M. 2003. Branching tree model with fractal vascular resistance explains fractal perfusion heterogeneity. *American journal of physiology. Heart and circulatory physiology*, **284**(5), H1848–57.

Marxen, M., Sled, J. G., Yu, L. X., Paget, C., & Henkelman, R. M. 2006. Comparing microsphere deposition and flow modeling in 3D vascular trees. *American journal of physiology. Heart and circulatory physiology*, **291**(5), H2136–41.

Michler, C., Cookson, A. N., Chabiniok, R., Hyde, E., Lee, J., & Sinclair, M. 2012. A computationally efficient framework for the simulation of cardiac perfusion using a multi-compartment Darcy porous-media flow model. *International journal for numerical methods in biomedical engineering*, **29**, 1–17.

Miller, C. A., Naish, J. H., Ainslie, M. P., Tonge, C., Tout, D., Arumugam, P., Banerji, A., Egdell, R. M., Clark, D., Weale, P., Steadman, C. D., McCann, G. P., Ray, S. G., Parker, G. J. M., & Schmitt, M. 2014. Voxel-wise quantification of myocardial blood flow with cardiovascular magnetic resonance: effect of variations in methodology and validation with positron emission tomography. *Journal of cardiovascular magnetic resonance*, **16**(1), 11.

Mittal, N., Zhou, Y., Linares, C., Ung, S., Kaimovitz, B., Molloi, S., & Kassab, G. S. 2005. Analysis of blood flow in the entire coronary arterial tree. *American journal of physiology. Heart and circulatory physiology*, **289**(1), H439–46.

Morton, G., Chiribiri, A., Ishida, M., Hussain, S. T., Schuster, A., Indermuehle, A., Perera, D.and Knuuti, J., Baker, S., Hedström, E., Schleyer, Pa., O'Doherty,

M., Barrington, S., & Nagel, E. 2012. Quantification of absolute myocardial perfusion in patients with coronary artery disease: comparison between cardiovascular magnetic resonance and positron emission tomography. *Journal of the American College of Cardiology*, **60**(16), 1546–55.

Mosher, P., Ross, J., Mcfate, P. A., & Shaw, R. F. 1964. Control of Coronary Blood Flow by an Autoregulatory Mechanism. *Circulation Research*, **14**(3), 250–259.

Muehling, O., Jerosch-Herold, M., Panse, P., Zenovich, A., Wilson, B., Wilson, R., & Wilke, N. 2004. Regional Heterogeneity of Myocardial Perfusion in Healthy Human Myocardium: Assessment with Magnetic Resonance Perfusion Imaging. *Journal of Cardiovascular Magnetic Resonance*, **6**(2), 499–507.

Nekolla, S. G., Reder, S., Saraste, A., Higuchi, T., Dzewas, G., Preissel, A., Huisman, M., Poethko, T., Schuster, T., Yu, M., Robinson, S., Casebier, D., Henke, J., Wester, H. J., & Schwaiger, M. 2009. Evaluation of the novel myocardial perfusion positron-emission tomography tracer 18F-BMS-747158-02: comparison to 13N-ammonia and validation with microspheres in a pig model. *Circulation*, **119**(17), 2333–42.

Nolte, F., Hyde, E. R., Rolandi, C., Lee, J., van Horssen, P., Asrress, K., van den Wijngaard, J. P. H. M., Cookson, A. N., van de Hoef, T., Chabiniok, R., Razavi, R., Michler, C., Hautvast, G. L. T. F., Piek, J. J., Breeuwer, M., Siebes, M., Nagel, E., Smith, N. P., & Spaan, J. A. E. 2013. Myocardial perfusion distribution and coronary arterial pressure and flow signals: clinical relevance in relation to multiscale modeling, a review. *Medical & biological engineering & computing*, **51**(11), 1271–1286.

Nordsletten, D. A., Blackett, S., Bentley, M. D., Ritman, E. L., & Smith, N. P. 2006. Structural morphology of renal vasculature. *American Journal of Physiology - Heart and Circulatory Physiology*, **291**(1), 296–309.

Nose, Y., Nakamura, T., & Nakamura, M. 1985. The microsphere method facilitates statistical assessment of regional blood flow. *Basic research in cardiology*, **80**(4), 417–29.

Obrist, D., Weber, B., Buck, A., & Jenny, P. 2010. Red blood cell distribution in simplified capillary networks. *Philosophical transactions. Series A, Mathematical, physical, and engineering sciences*, **368**(1921), 2897–918.

Ofjord, E. S. 1981. Skimming of microspheres in vitro: implications for measurement of intrarenal blood flow. *American Journal of Physiology - Heart and Circulatory Physiology*, **241**(3), H342–7.

Ofjord, E. S., & Clausen, G. 1983. Intrarenal flow of microspheres and red blood cells: skimming in slit and tube models. *American Journal of Physiology-Heart and Circulatory Physiology*, **245**(3), H429–36.

Oosterhout, M. F. V., Wlligers, H. M. M., Reneman, R. S., & Prinzen, F. W. 1995. Fluorescent microspheres to measure organ perfusion: validation of a simplified sample processing technique. *American Journal of Physiology*, **269**(2), H725–H732.

Palmer, A. A. 1965. Axial drift of cells and partial plasma skimming in blood flowing through glass slits. *American Journal of Physiology*, **209**(6), 1115–1122.

Pärkkä, J. P., Niemi, P., Saraste, A., Koskenvuo, J. W., Komu, M., Oikonen, V., Toikka, J. O., Kiviniemi, T. O., Knuuti, J., Sakuma, H., & Hartiala, J. J. 2006. Comparison of MRI and positron emission tomography for measuring myocardial perfusion reserve in healthy humans. *Magnetic resonance in medicine*, **55**(4), 772–9.

Polissar, N. L., Stanford, D. C., & Glenny, R. W. 2000. The 400 microsphere per piece "rule" does not apply to all blood flow studies. *American Journal of Physiology-Heart and Circulatory Physiology*, **278**(1), H16–H25.

Pries, A. R., & Secomb, T. W. 2005. Microvascular blood viscosity in vivo and the endothelial surface layer. *American Journal of Physiology-Heart and Circulatory Physiology*, **289**, 2657–2664.

Pries, A. R., Albrecht, K. H., & Gaehtgens, P. 1981. Model studies on phase separation at a capillary orifice. *Biorheology*, **18**(3-6), 355–367.

Pries, A. R., Ley, K., & Gaehtgens, P. 1986. Generalization of the Fahraeus principle for microvessel networks. *The American journal of physiology*, **251**(6 Pt 2), H1324–32.

Pries, A. R., Ley, K., Claassen, M., & Gaehtgens, P. 1989. Red cell distribution at microvascular bifurcations. *Microvascular Research*, **101**, 81–101.

Pries, A. R., Fritzsche, A., Ley, K., & Gaehtgens, P. 1992. Redistribution of red blood cell flow in microcirculatory networks by hemodilution. *Circulation Research*, **70**(6), 1113–1121.

Pries, A. R., Secomb, T. W., Gessner, T., Sperandio, M. B., Gross, J. F., & Gaehtgens, P. 1994. Resistance to blood flow in microvessels in vivo. *Circulation Research*, **75**(5), 904–915.

Prinzen, F. W., & Bassingthwaighte, J. B. 2000. Blood flow distributions by microsphere deposition methods. *Cardiovascular research*, **45**(1), 13–21.

Proudfit, W. L., Shirey, E. K., & Sones, F. M. 1966. Selective Cine Coronary Arteriography: Correlation with Clinical Findings in 1,000 Patients. *Circulation*, **33**(6), 901–910.

Ritman, E. L. 2011. Current status of developments and applications of micro-CT. *Annual review of biomedical engineering*, **13**(Aug.), 531–52.

Rodriguez, A., Ehlenberger, D. B., Hof, P. R., & Wearne, S. L. 2006. Rayburst sampling, an algorithm for automated three-dimensional shape analysis from laser scanning microscopy images. *Nature protocols*, **1**(4), 2152–61.

Rong, F. W., & Carr, R. T. 1990. Dye studies on flow through branching tubes. *Microvascular research*, **202**, 186–202.

Rudolph, A. M., & Heymann, M. A. 1967. The Circulation of the Fetus in Utero: Methods For Studying Distribution of Blood Flow, Cardiac Output And Organ Blood Flow. *Circulation Research*, **21**(2), 163–184.

Salerno, M., & Beller, G. A. 2009. Noninvasive assessment of myocardial perfusion. *Circulation. Cardiovascular imaging*, **2**(5), 412–24.

Schindelin, J., Arganda-Carreras, I., Frise, E., Kaynig, V., Longair, M., Pietzsch, T., Preibisch, S., Rueden, C., Saalfeld, S., Schmid, B., Tinevez, J.-Y., White, D. J., Hartenstein, V., Eliceiri, K., Tomancak, P., & Cardona, A. 2012. Fiji: an open-source platform for biological-image analysis. *Nature methods*, **9**(7), 676–82.

Schmid-Schönbein, G. W., & Skalak, R. 1980. Cell distribution in capillary networks. *Microvascular Research*, **44**, 18–44.

Schuster, A., Grünwald, I., Chiribiri, A., Southworth, R., Ishida, M., Hay, G., Neumann, N., Morton, G., Perera, D., Schaeffter, T., & Nagel, E. 2010. An isolated perfused pig heart model for the development, validation and translation of novel cardiovascular magnetic resonance techniques. *Journal of cardiovascular magnetic resonance : official journal of the Society for Cardiovascular Magnetic Resonance*, **12**(Jan.), 53.

Schuster, A., Niloufar, Z., Ishida, M., Sinclair, M., ven den Wijngaard, P. H. M., Morton, G., Hautvast, L. T. F., Bigake, B., van Horssen, P., Smith, N., Spaan, J. A. E., Siebes, S., Chiribiri, A., & Nagel, E. 2014. Quantitative assessment of magnetic resonance derived perfusion measurements using advanced techniques: microsphere validation in an explanted pig heart system. *Journal of Cardiovascular MRI*, accepted.

Secomb, T. W., Skalak, R., Özkaya, N., & Gross, J. F. 1985. Flow of axisymmetric red blood cells in narrow capillaries. *Journal of Fluid Mechanics*, **163**(Apr.), 405.

Secomb, T. W., Hsu, R., & Pries, A. R. 1998. A model for red blood cell motion in glycocalyx-lined capillaries. *American Journal of Physiology*, **274**(21), H1016–H1022.

Secomb, T. W., Styp-Rekowska, B., & Pries, A. R. 2007. Two-dimensional simulation of red blood cell deformation and lateral migration in microvessels. *Annals of biomedical engineering*, **35**(5), 755–65.

Secomb, T. W., Barber, J. O., & Restrepo, J. M. 2009. Computational simulation of red blood cell motion in microvessel bifurcations. *Pages 1–4 of: International Conference on CFD in the Minerals and Process Industries*.

Segré, G. 1961. Radial particle displacements in Poiseuille flow of suspensions. *Nature*.

Segré, G, & Silberberg, A. 1962. Behaviour of macroscopic rigid spheres in Poiseuille flow. *Journal of Fluid Mechanics*.

Sinclair, M, Lee, J, Schuster, A, Chiribiri, A, van den Wijngaard, J, van Horssen, P, Siebes, M, Spaan, JAE, Nagel, E, & Smith, NP. 2014. Microsphere skimming in the porcine coronary arteries: implications for flow quantification. *Microcirculation Research*, in review.

Smith, N. P. 2004. A computational study of the interaction between coronary blood flow and myocardial mechanics. *Physiological Measurement*, **25**(4), 863–877.

Smith, N. P., Nickerson, D. P., Crampin, E. J., & Hunter, P. J. 2004. Multiscale computational modelling of the heart. *Acta Numerica*, **13**(June), 371.

Sonntag, M., Deussen, A., Schultz, J., Loncar, R., Hort, W., & Schrader, J. 1996. Spatial heterogeneity of blood flow in the dog heart. I. Glucose uptake, free adenosine and oxidative/glycolytic enzyme activity. *Pflügers Archiv: European journal of physiology*, **432**(3), 439–50.

Spaan, J. A. E., ter Wee, R., van Teeffelen, J. W. G. E., Streekstra, G., Siebes, M., Kolyva, C., Vink, H., Fokkema, D. S., & VanBavel, E. 2005. Visualisation of intramural coronary vasculature by an imaging cryomicrotome suggests compartmentalisation of myocardial perfusion areas. *Medical & biological engineering & computing*, **43**(4), 431–5.

Strahler, A. N. 1952. *Hypsometric (area-altitude) analysis of erosional topography*.

Svanes, K., & Zweifach, B. W. 1968. Variations in small blood vessel hematocrits produced in hypothermic rats by micro-occlusion. *Microvascular Research*, **220**, 210–220.

Tangelder, G. J., Slaaf, D. W., & Muijtjens, A. M. 1986. Velocity profiles of blood platelets and red blood cells flowing in arterioles of the rabbit mesentery. *Circulation*, **59**(5), 505–514.

Tankyevych, O., & Talbot, H. 2009. Spatially-variant morpho-hessian filter: Efficient implementation and application. *Mathematical Morphology and Its Application to Signal and Image Processing*, **5720**, 137–148.

Taylor, M. 1955. The flow of blood in narrow tubes. II. The axial stream and its formation, as determined by changes in optical density. *The Australian journal of experimental biology and medical science*.

Utley, J., Carlson, E. L., Hoffman, J. I. E., Martinez, H. M., & Buckberg, G. D. 1974. Total and Regional Myocardial Blood Flow Measurements with 25μ, 15μ, 9μ, and Filtered 1-10μ Diameter Microspheres and Antipyrine in Dogs and Sheep. *Circulation Research*, **34**(3), 391–405.

Van Bavel, E., & Spaan, J. A. 1992. Branching patterns in the porcine coronary arterial tree. Estimation of flow heterogeneity. *Circulation Research*, **71**(5), 1200–1212.

Van Beek, J. H., Roger, S. A., & Bassingthwaighte, J. B. 1989. Regional myocardial flow heterogeneity explained with fractal networks. *The American journal of physiology*, **257**(5), H1670–H1680.

van den Wijngaard, J. P. H. M. 2011. Porcine coronary collateral formation in the absence of a pressure gradient remote of the ischemic border zone. *American Journal of Physiology - Heart and Circulatory Physiology*, **300**(5), H1930–H1937.

van den Wijngaard, J. P. H. M., Schwarz, J. C. V. V., van Horssen, P., van Lier, M. G. J. T. B., Dobbe, J. G. G. G., Spaan, J. A. E., & Siebes, M. 2013. 3D Imaging of vascular networks for biophysical modeling of perfusion distribution within the heart. *Journal of Biomechanics*, **46**(2), 229–39.

van Horssen, P., Siebes, M., Hoefer, I., Spaan, J. A. E., & van den Wijngaard, J. P. H. M. 2010. Improved detection of fluorescently labeled microspheres and vessel

architecture with an imaging cryomicrotome. *Medical & biological engineering & computing*, **48**(8), 735–44.

van Horssen, P., van den Wijngaard, J. P. H. M., Brandt, M. J., Hoefer, I. E., Spaan, J. A. E., & Siebes, M. 2014. Perfusion territories subtended by penetrating coronary arteries increase in size and decrease in number toward the subendocardium. *American journal of physiology. Heart and circulatory physiology*, **306**(4), H496–504.

Verdú-Monedero, R., Angulo, J., & Serra, J. 2009. Spatially-variant anisotropic morphological filters driven by gradient fields. *Mathematical Morphology and Its Application to Signal and Image Processing*, 115–125.

Vinnakota, K. C., & Bassingthwaighte, J. B. 2004. Myocardial density and composition: a basis for calculating intracellular metabolite concentrations. *American journal of physiology. Heart and circulatory physiology*, **286**(5), H1742–9.

Waters, S. L., Alastruey, J., Beard, D. A., Bovendeerd, P. H. M., Davies, P. F., Jayaraman, G., Jensen, O. E., Lee, J., Parker, K. H., Popel, A. S., Secomb, T. W., Siebes, M., Sherwin, S. J., Shipley, R. J., Smith, N. P., & van de Vosse, F. N. 2011. Theoretical models for coronary vascular biomechanics: progress & challenges. *Progress in biophysics and molecular biology*, **104**(1-3), 49–76.

Weaver, M. E., Pantely, G. A., Bristow, J. D., & Ladley, H. D. 1986. A quantitative study of the anatomy and distribution of coronary arteries in swine in comparison with other animals and man. *Cardiovascular research*, **20**, 907–917.

West, G. B., Brown, J. H., & Enquist, B. J. 1997. A general model for the origin of allometric scaling laws in biology. *Science (New York, N.Y.)*, **276**(5309), 122–6.

Wischgoll, T., Choy, J. S., & Kassab, G. S. 2009. Extraction of morphometry and branching angles of porcine coronary arterial tree from CT images. *American journal of physiology. Heart and circulatory physiology*, **297**(5), H1949–55.

Wüsten, B., Buss, D. D., Deist, H., & Schaper, W. 1977. Dilatory capacity of the coronary circulation and its correlation to the arterial vasculature in the canine left ventricle. *Basic research in cardiology*, **72**(6), 636–50.

Xiao, C., Staring, M., Shamonin, D.and Reiber, J. H. C., Stolk, J., & Stoel, B. C. 2011. A strain energy filter for 3D vessel enhancement with application to pulmonary CT images. *Medical image analysis*, **15**(1), 112–24.

Yan, Z. Y., Acrivos, A., & Weinbaum, S. 1991. A three-dimensional analysis of plasma skimming at microvascular bifurcations. *Microvascular research*, **42**(1), 17–38.

Yen, R. T., & Fung, Y. C. 1978. Effect of velocity distribution on red cell distribution in capillary blood-vessels. *American Journal of Physiology*, **235**(2), H251–H257.

Yipintsoi, T., Dobbs, W. A., Scanlon, P. D., Knopp, T. J., & Bassingthwaighte, J. B. 1973. Regional distribution of diffusible tracers and carbonized microspheres in the left ventricle of isolated dog hearts. *Circulation research*, **33**(5), 573–87.

Yushkevich, P. A., Piven, J., Hazlett, H. C., Smith, R. G., Ho, S., Gee, J. C., & Gerig, G. 2006. User-guided 3D active contour segmentation of anatomical structures: significantly improved efficiency and reliability. *NeuroImage*, **31**(3), 1116–28.

Zarinabad, N., Chiribiri, A., Hautvast, G., Schuster, A., Sinclair, M., van den Wijngaard, J., Smith, N., Spaan, J., Siebes, M., Breeuwer, M., & Nagel, E. 2013. Modelling parameter role on accuracy of cardiac perfusion quantification. *Functional Imaging and Modeling of the Heart*, **7945**, 370–382.

Zou, K. H., Warfield, S. K., Bharatha, A., Tempany, C. M.C., Kaus, M. R., Haker, S. J., Wells, W. M., Jolesz, F. A., & Kikinis, R. 2004. Statistical validation of image segmentation quality based on a spatial overlap index. *Academic Radiology*, **11**(2), 178–189.